Elemental and isotope fingerprint of metal deficiency in soils

PhD Thesis

2018

Nils Thorsten Suhr

Trinity College Dublin
Coláiste na Tríonóide, Baile Átha Cliath
The University of Dublin

I declare that this thesis has not been submitted as an exercise for a degree at this or any other university and it is entirely my own work.

I agree to deposit this thesis in the University's open access institutional repository or allow the library to do so on my behalf, subject to Irish Copyright Legislation and Trinity College Library conditions of use and acknowledgment.

Nils Thorsten Suhr

Elemental and isotope fingerprint of metal deficiency in soils

Nils Thorsten Suhr

Abstract

Metal deficiency in soils is a frequently observed phenomenon in (sub)-tropical regions, and both natural and anthropogenic processes contribute to the depletion of soil reservoirs. Advanced chemical weathering, in old regolith, can lead to very severe natural depletion of metals in certain soil types, while soil over-cropping represents the human impact that increases the net offtake of metals from many soils. In both cases, the health of humans can suffer since many trace metals have vital functions in the human body. For example, nearly half the world population is affected by Zn deficiency symptoms caused by over-dependence on local crops that are grown on Zn deficient soils. This is all the more concerning in view of the anticipated rise in world population that will put additional demands on crop production with likely knock-on effects for essential metal depletion in soil.

This thesis presents petrographic, mineralogical and geochemical as well as isotopic investigations of two contrasting weathering profiles from the Deccan Traps, India to investigate the natural causes of metal deficiency in soils. Major- and trace elements (including essential metals), organic carbon (C) content, chemical weathering indices, uranium-series (U-series) systematics as well as zinc (Zn)- and chromium (Cr)- isotopes were analysed to quantify the mineralogical transformations, biogeochemical processes and environmental factors that lead to the loss of metals during soil formation. In addition, agricultural topsoil and animal manure samples were investigated from Zn deficient regions in India to compare and contrast their biogeochemical fingerprints to the findings from the weathering profiles.

The work revealed that actively weathering soils are strongly depleted in the isotope ^{234}U, hosted in labile sites in minerals. The chemical breakdown of metal-rich primary silicates and clay minerals in saprolite results in the mobilisation of substantial amounts of metals to aqueous solutions and plants. Ultimately, the breakdown of these minerals contributes to oceanic metal inventories, exemplified by the excess of ^{234}U in seawater. By contrast, strongly weathered soils (i.e. laterites) have lost their natural capacity to supply bio-available forms of metals to the environment and concentrations of residual essential metals such as Zn or redistributed Cr are mainly hosted in weathering resistant iron (Fe)-oxides. The isotopic fractionation of Zn and Cr is strongly affected by the formation of Fe-oxides, whereas the metal stable isotope ratios in actively weathering saprolite remain in the range of unweathered bedrocks. Hence, Zn isotopes can be used to distinguish between fertile and Zn deficient soils. Importantly, the geochemical fingerprints in the agricultural topsoils reveal that high concentrations of essential metals (Zn, copper (Cu), cobalt (Co), nickel (Ni), Cr) are also hosted in bio-unavailable oxide phases, whereas the bio-available pool in the inorganic soil constituents is much lower. Since the bio-available concentrations of metals in animal manure are too low to counterbalance essential metal deficiencies in Indian soils, their fertility status remains delicate without application of industrial metal fertilisers. Overall, the findings of this thesis suggest that geochemical and isotopic data can contribute to a deeper understanding of metal deficiency in soils and help in the development of more sustainable farming practices in (sub)-tropical regions.

Acknowledgements

I would like to express my sincere appreciation to my PhD supervisor Balz Kamber, for his support and mentorship throughout this project. Without his continued guidance, creativeness, unconventional way of thinking and understanding of the zeitgeist, this work would not have been possible. I would also like to thank all my colleagues in the TCD Geology Department for their encouragement and mental support as well as the good times outside of science. I am also grateful to Cora McKenna and Mark Kavanagh for their support and guidance in the laboratory. Thanks are due to the geology department's technical and administrative staff; Frank Hendron, Neil Kearney, Noel McGinley, Maura Morgan and Mags Duncan, for their support. I thank Claire Kamber for beautifully drafting figures for previous works that I could also use, and for her social support. I am also grateful to Dr Maja Tesmer for her support and to Prof. Dr Friedhelm von Blanckenburg for establishing the IsoNose network, which provided me with the opportunity to work on this PhD project. Thanks are due to Dr Dhananjay Mahendrakumar Mohabey and Dr Bandana Samant for their organisational help in India. I would also like to thank my internal examiner Dr Micha Ruhl and my external examiner Prof. Jérôme Gaillardet for the interesting and fruitful discussion during my viva voce.

Finally, I would like to thank my wife Yamirka for her endless encouragement and moral support.

Table of contents

Chapter 1: Introduction

1.1. Context of Thesis

In the geosciences, the term Critical Zone (CZ) describes the Earth's outermost layer, which extends from the lower limits of the groundwater zone up to the vegetation canopy (Brantley et al., 2007; Brantley et al., 2005). The CZ is the principal nutrient supplier for terrestrial life and a primary source of solutes to the oceans. Consequently, almost all life on Earth depends on this heterogeneous, near-surface environment, in which rock, soil, air, water and biota interact. The supply and exchange of nutrients throughout the CZ occur through (a)biotic chemical reactions where physical and chemical weathering of rocks catalysed by organisms and their metabolic products, release nutrients and energy to the terrestrial environment. Ultimately, these processes lead to the formation of soils that sustain natural and managed ecosystems and consequently impact on flora, fauna and humans.

Several metals (zinc (Zn), copper (Cu), iron (Fe), manganese (Mn), cobalt (Co), nickel (Ni), molybdenum (Mo)) are essential for the vital function of the human body at trace concentrations, and the importance of further metals (e.g., chromium (Cr)) is being discussed (e.g., Prashanth et al., 2015). Of these bio-essential elements, Zn is one of the most indispensable in human nutrition (e.g., Andersen, 2002) but between 20 and 50 percent of the world population is suffering from Zn deficiency symptoms. These include impairments in physical development and reduced immune system and brain function (Wessells and Brown, 2012; Cakmak, 2008). There is evidence that these Zn deficiency problems have links to crops that are grown on Zn deficient soils (Cakmak, 2008; Alloway, 2009), which exemplifies the importance of the emerging scientific field of medical geology. In the context of Zn, this involves a better understanding of metal exchange reactions within the part of the CZ where primary mineral matter is breaking down. Metal deficiency is particularly problematic in developing countries, where a large portion of the population relies on locally produced food. There, the impact of soil-crop relations on human health is receiving attention because it contributes to complex types of malnutrition – *hidden hunger* (e.g., Andersen, 2007). *Hidden hunger* describes micronutrient malnutrition of humans through a lack of essential metals such as Fe or Zn in their diet.

Nutritionists, the Food and Agriculture Organization of the United Nations as well as the World Health Organization have identified micronutrient malnutrition as a primary health care issue (Welch and Graham, 1999).

Despite the recognised importance of soil chemistry for crop production and human health, the origin of inherently low Zn and other vital trace metal contents is still relatively unexplored. Moreover, many of the mineralogical and chemical modifications within the CZ that cause metal deficiencies in soils have not yet been studied in detail by geologists. This is surprising given that geobiochemist are studying the origin and evolution of life in the context of the planetary cycles of bio-essential trace metals through geologic time (e.g., Zerkle et al., 2005; Hao et al., 2017). Several decades ago, Fyfe et al. (1983) noted that there was a need for more information exchange between geology and agricultural science in terms of nutrient deficiencies in soil. However, traditional administrative barriers, subdividing in natural sciences agricultural sciences have continued to inhibit scientific progress at the interface of these research disciplines. As a result, the potential of the inorganic components in soils to supply nutrients to plants have only been rarely addressed (Fyfe et al., 1983), even though at least historically, soil science was a discipline with foundational roots in geology (Wilding and Lin, 2006) that sought to understand the relationship of agriculture and geochemistry in terms of soil fertility (Jackson and Sherman, 1953). Regardless, in recent years prominent scientists (e.g., Brantley et al., 2005; Brantley et al., 2007; Brantley and Lebedeva, 2011; Jin et al., 2010) have begun to integrate soil studies with Earth's CZ investigations and new frontier disciplines such as geobiochemistry (Wilding and Lin, 2006) and medical geology opening a new chapter in understanding pedogenic processes and its effects on the environment.

Chemical weathering of rocks is one of the principal processes which modifies land surfaces and one of the most critical factors in the geochemical cycle of the earth (Kronberg et al., 1979). In (sub)-tropical regions, it dominates soil formation processes and often results in extreme geochemical partitioning of elements. Hence, the soil end-members are often characterised by severe elemental depletions and enrichments with knock-on effects on plant, animal and human health (Fyfe et al., 1983; Dissanayake and Chandrajith, 1999). Consequently, Zn and other micronutrient deficiencies in humans are prevalent in these climatic regions (e.g., Alloway, 2009). In the sub-tropics, the CZ typically attains thicknesses between 30-100 m (Xu and Liu, 2017) and permits separate studies of the deeper CZ, where rock weathers into saprolite (e.g., Buss et al., 2013), and

the upper CZ, where saprolite transforms into laterite (e.g., Viers et al., 2007). These targeted approaches can pinpoint the critical mineralogical and geochemical modifications that accompany the development of soils. The investigation of the CZ in (sub)-tropical regions could, therefore, be fundamental for understanding the natural depletion of Zn and other essential metals during pedogenesis. An improved knowledge of these processes could eventually help to develop strategies for more sustainable farming practices in tropical regions where impoverished soils conditions are prevalent.

Over the last two decades, analytical advances in multi-collector inductively-coupled-plasma mass-spectrometry (MC-ICP-MS) have opened the new research field of non-traditional stable isotopes (Maréchal et al., 1999; Halliday et al., 1995; Albarède and Beard, 2004). This technique has enabled measurement of the isotopic fractionation of essential metals, such as Zn, Cu, Fe, Cr, and Ni at high precision and accuracy. Isotopic fractionation of metals within the CZ is caused by many processes, including redox transformations, complexation, sorption, precipitation, dissolution, evaporation, diffusion, and biological cycling (Wiederhold, 2015). Hence, understanding of these isotopic signals has potential to distinguish between bio-available and inert species of metals. More informed insight into isotope fractionation within the CZ may eventually discover the key reasons for metal deficiency in soils with information that is inaccessible to chemical bulk soil data. The number of Zn isotope investigations of the CZ in (sub)-tropical regions is still limited (Guinoiseau et al., 2017; Vance et al., 2016; Viers et al., 2007) and the full potential of this isotopic tracer to explore the reasons for Zn deficiency in soils not yet fully explored.

It is clear that natural processes alone are not the sole cause for deficiency of essential metals within soils. Over the past three centuries, anthropogenic activity has impacted on 30-50% of the global land surface (Crutzen, 2002; Brantley et al., 2005). In developing countries, the most dramatic changes in land use begun in the late 1960s as a result of increasing population numbers that required higher crop productivity. This led to the agricultural revolution known as the “Green Revolution” (e.g., Hazell, 2009), which resulted in the expansion of the global production of staple food crops through the introduction of new cultivars, chemicals ranging from mineral fertilisers to pesticides to synthetic plant hormones, and mechanised machinery (Welch et al., 1999). This enormous international effort ultimately achieved adequacy in world food calorie production (Welch

et al., 1999), for example, supplying rice as the staple food to more than half of the world's population (e.g., Meng et al., 2005).

As a result of this success in higher crop production in (sub)-tropical regions, the reservoir of cultivated soils has experienced additional off-take of essential metals such as Fe or Zn (e.g., Andersen, 2007). It is important to recognise that producing enough food calories to maintain the world's population is in itself insufficient because billions of low-income people suffer from *hidden hunger* and will continue to live in poor health (Gregorio et al., 1999). This development will become an even greater concern in the face of growing world population, expected to reach 9.6 billion individuals by 2050 (Ray et al., 2013). To meet the food requirements of the rapidly expanding population new agricultural strategies are experimenting with crop cultivars that can take up higher concentrations of Fe and Zn from soils (Singh et al., 2017; Cakmak, 2008). Whereas such cultivars may alleviate essential metal deficiency in humans, it is self-evident that removal of such crops will further magnify the net output of essential metals from the soil reservoir. Sustainable strategies therefore require consideration of the size of the plant-available metal pools in soils (Cakmak, 2008).

In summary, natural processes and human land use trigger essential metal deficiencies in (sub)-tropical soils that remain poorly studied from a geochemical perspective. India is one of the most densely populated countries on Earth and given its (sub)-tropical climate it is neither surprising that Indian soils and crops often show Zn and other micronutrient deficiencies nor that its people suffer disproportionately from Zn deficiency (e.g., Cakmak, 2008). Furthermore, the expected continued rise in population (e.g., Bloom, 2011) suggests that the exhaustion of micronutrient reserves in Indian soils will continue and that in addition to existing deficiencies in Fe, Zn, and Mo new essential metals deficiencies will emerge (e.g., Singh, 2008). This outlook emphasises the need for the development of more sustainable agricultural and soil science strategies through the contribution from various research disciplines.

The aim of this thesis was to make a contribution to this topic with isotopic, geochemical and mineralogical investigations of a sub-recent saprolite and a fully evolved lateritic weathering profile from the Deccan Traps, India. Within these soil profiles, I sought to identify the processes that lead to metal loss and metal deficiency in crops grown on such substrate. The specific target of this work was the element Zn because of the

established soil-crop-human health relation. The information gained from the study of these weathering profiles was supplemented with a comparison of agricultural topsoils from Central India to detect similarities and contrasts between natural and anthropogenic processes that cause metal deficiency. This approach is a start towards bigger future investigations of how chemical weathering and farming practices in a densely populated part of the world affect Zn and other essential metal contents in soils.

1.2. Layout and Themes of the Thesis

This PhD project was designed as a number of thematically related peer-reviewed publications/manuscripts while also satisfying the remit of the European Initial Training Network ISONOSE funded under the EU FP7 Marie Curie Initial Training Network scheme, which provided the funding. Four individual sub-projects were defined and each of these forms a core chapter of the thesis. Because of the manuscript nature of these chapters, readers will find variably comprehensive introductions included in each. The conclusions of each chapter are also self-contained. After the final core chapter, readers are presented with summarising conclusions and an outlook. The publication status of each chapter is identified at the outset and each chapter has been formatted for the thesis, regardless of original journal formatting. In the following, a brief overview of all chapters is given.

Chapter 2 provides an investigation into the role of active weathering reactions and associated clay formation in saprolite for the supply of nutrients to aqueous solutions in the CZ and ultimately to rivers and oceans. My study focuses on how uranium-series (U-series) isotope systematics can be used as a tool to study active weathering reactions and associated metal-deficiency processes during soil formation and how to distinguish these reactions from those in fossilised palaeosols. The high-precision U-series data are supported by careful investigations of chemostratigraphical weathering trends in the Chhindwara saprolite profile and laser ablation inductively coupled plasma mass spectrometry (LA-ICP-MS) trace element maps of the protolith. A critical ambition of this chapter was to reconcile experimental findings of preferential ^{234}U loss during clay-mineral formation (e.g., Kigoshi, 1971) with empirical data from saprolitic weathering profiles to better understand the excess of ^{234}U in river waters (Chabaux et al., 2001; Dunk et al.,

2002) and oceans (Henderson, 2002). I made a U-series data compilation of the entire literature as well as mass balance calculations, which revealed that the fractionation of U isotopes in previous studies of weathering profiles is likely insufficient to explain the experimental and empirical hydrological findings. As a result, there is likely a lack of information evident in terms of U series fractionation during soil formation that should also affect other redox-sensitive metals and their isotope systematics. Hence, this chapter created a baseline for the interpretation of the elemental and isotopic data of Zn in the following chapter and helped to constrain possible processes that lead to fractionation of Zn. Finally, lessons from active weathering reactions exposed by U-series isotopes helped me to better pinpoint which mineralogical transformation are involved that cause metal-deficiency in soils.

Chapter 3 presents petrographic, mineralogical (X-ray diffraction (XRD)), LA-ICP-MS trace element maps, geochemical as well as new Zn isotope data on the saprolite profile described in Chapter 2 and additionally on a highly evolved laterite profile. I aimed to explore exchange reactions of Zn and associated mineral modifications within the full extent of the CZ that lead to Zn deficiency in (sub)-tropical regions. The Chhindwara saprolite and Bidar laterite profiles had previously been investigated for weathering intensity and associated trace element release by Babechuk et al. (2014). Several isotopic studies (lithium (Li), rhenium (Re), osmium (Os), neodynium (Nd) have also been conducted in the past on the fully evolved Bidar laterite profile (Kısakürek et al., 2004; Wimpenny et al., 2007; Babechuk et al., 2015), which helped to interpret the Zn-isotope data. The LA-ICP-MS trace element maps allowed me to identify into which minerals Zn was redistributed. This information was crucial to understanding how inherently low contents of Zn and other essential metals during soil formation in (sub)-tropical regions develop.

In Chapter 4, the silicon (Si)- and Cr-isotopic systematics of the same weathering profiles were investigated. The coupling of both stable isotope systems represented a relatively novel approach and aimed at understanding the aqueous redistribution and fractionation processes of both isotopic systems as a result of changing pH and Eh parameters as well as associated mineralogical transformation during soil formation. I am a co-author of this chapter, whose finding helped me to compare and contrast the elemental and isotopic data of Zn with Cr. This approach identified environmental factors that trigger metal deficiency in soils. The findings in the chapter were put into a broader context of

climate change and resulting elemental and isotopic fluxes of Si and Cr to rivers and oceans.

In the final core contribution of this thesis, Chapter 5, I investigated the essential trace metal composition of agricultural topsoil samples from Central India – an area with one of the highest percentage of Zn deficiency in soils on the Indian subcontinent. This study was motivated by the recognition that new additional types of metal deficiencies are likely to emerge in the next decades in India through intensified farming practices and soil over-cropping. With the findings from Chapters 2, 3 and 4 in mind I used geochemical data (major and trace elements) to identify which mineral phases host essential trace metals. This relatively unconventional approach helped me to distinguish between bio-available forms of metals and those which remain immobile in the soil reservoir. I used the diethylenetriamine pentaacetic acid (DTPA)-extraction method of Lindsay and Norvell (1978) to simulate plant-uptake of essential metals and to test the deficiency status of the sampled soils. Total organic carbon (C) measurements were also made to understand the relationship between plant-available pools of metals and organic soil constituents. Finally, I wanted to understand the benefits of farmyard manure (FYM) as soil fertiliser and its potential effects on trace metal cycles. In order to provide a broader context to the FYM data in terms of its potential as fertiliser to combat essential metal deficiencies that are caused by soil over-cropping, I made calculations to understand whether cow dung can balance the required annual amounts of metals that are needed in soils.

The concluding Chapter 6 is a synthesis of the insight gained from the research presented in the core chapters of the thesis and an essay on the wider implications of the new findings to the study of metal deficiency in soils and its links to metal deficiency in crops and ultimately in human diet.

1.3. Co-author Statement and Technical Support

The four core chapters (2-5) of this thesis consist of three published papers and one chapter that I intend to publish after the submission of the PhD thesis. All chapters are multi-authored. I am the lead author of three of these works and co-author of chapter 4. I wrote the lead-authored manuscripts in their entirety. The roles of the co-authors and technicians

consisted of: providing samples and understanding the geological and weathering profiles context; providing expert advice, guidance and conduction of analytical work (providing isotopic and chemical data) and help with putting my interpretations in Chapter 2 into a global context. The detailed roles are explained below.

Mike Widdowson, Hull University, United Kingdom, provided samples and field context of the Chhindwara and Bidar weathering profiles as well as editorial comments on Chapters 2 and 3. Moreover, he provided field guidance during the field trip to India in 2016.

Frank McDermott, University College Dublin, Ireland, was involved in the U-series aspects of Chapter 2 of this thesis, by providing guidance throughout stages of sample preparation, U and Th column calibration, and MC-ICP-MS analysis at University College Dublin. He performed the U-series isotope data reduction and provided editorial comments on Chapter 2.

Ronny Schoenberg, University of Tuebingen, Germany, was involved in the Zn isotope aspects of this thesis (Chapter 3). He provided the calibrated double spike and performed the MC-ICP-MS isotope analyses, reduced the data and provided editorial comments on Chapter 3.

David Chew, Trinity College Dublin, Ireland, performed all of the LA-ICP-MS analyses as well as data reductions of Chapters 2, 3 and 4 and made editorial comments on chapter 3.

Carolina Rosca, Trinity College Dublin, Ireland, conducted the column separation of Zn, assisted during the measurements as well as data reduction and made editorial comments on Chapter 3.

Martin Wille, University of Tuebingen, Germany, is the first author of the article that constitutes Chapter 4. My contribution of this paper was to perform detailed petrography and interpretations of the LA-ICP-MS trace element data with rock samples that Mike Widdowson and I collected during a revisit of the Chhindwara saprolite and Bidar laterite profile in January 2016. Furthermore, I crafted figures 4 and 5, provided editorial input into the manuscript and gave background information of the XRD data from Chapter 3.

Balz S. Kamber, my PhD advisor, was the main discussion partner for the interpretation of my data and provided editorial comments to all manuscripts. In addition, he analysed the U-series data as well as high precision trace elements of the Indian weathering profiles (Chapters 2, 3) on a quadrupole inductively coupled plasma mass spectrometer (Q-ICP-MS).

Finally, I would like to acknowledge the role of technicians that contributed to my PhD project. Michael Murphy at University College Dublin measured the U-series samples at a MC-ICP-MS (Chapter 2). Cora McKenna helped during the clean laboratory work (Chapters 2 and 5) and measured the trace elements of the cow dung samples on a Q-ICP-MS (Chapter 5). In addition, she assisted during the data reduction of the cow dung samples. Mark Kavanagh assisted during the measurements of the organic C content of the soil and cow dung samples of Chapters 3 and 5. Furthermore, he measured the essential metal contents of the DTPA-extracts of the soil samples (Chapter 5). Robbie Goodhue assisted with the XRD measurements of the weathering profile samples (Chapter 3).

Chapter 2: Th/U and U series systematics of saprolite: importance for the oceanic ^{234}U excess

Published in Geochemical Perspective Letters (2018, Vol. 6, 17-22)

Authors: Nils Suhr, Mike Widdowson, Frank McDermott, Balz S. Kamber

Abstract

The presence of excess uranium-234 (^{234}U) in seawater is a compelling argument for active delivery of solutes from the continents to the oceans. Previous studies found, however, that the complementary ^{234}U deficit on the continents is surprisingly modest, which would require protracted U loss from a large continental weathering pool. Our new compilation and statistical analysis of the published data, coupled with a mass balance calculation demonstrates that the apparent small ^{234}U deficit in the continental weathering pool implied by previous studies is insufficient to balance the observed oceanic excess. Our new data for a saprolite weathering profile developed on Deccan basalt reveal a very strong overall loss of U (elevated thorium/uranium (Th/U)) with a strong ^{234}U deficit attributable to chemical weathering. The U and ^{234}U deficits reported here from a geologically recent saprolite confirm the importance of the early stages of chemical weathering at the weathering front in the supply of nutrients to the oceans. Thus, as much as half the oceanic ^{234}U inventory is likely sourced from a thin active saprolite zone.

1. Introduction

One of the strongest pieces of evidence for active and ongoing delivery of chemical elements from the continents to the oceans is the presence of ^{234}U excess in seawater. The elevated ($^{234}U/^{238}U$) of seawater (~1.145), coupled with its relatively high U concentration and constancy of ($^{234}U/^{238}U$) over >780 kyr (Henderson, 2002) requires a continuous, quasi-steady input of U to the oceans. On long time scales, since the rise of free atmospheric oxygen, ca. 2.35 Gyr ago (Bekker et al., 2004) significant fluvial transport of soluble oxidised U(VI) from the continents to the oceans has occurred. The loss of U from the terrestrial realm to the oceans is primarily a consequence of rock weathering and is apparent from many lines of evidence (e.g., Partin et al., 2013).

The global mean ($^{234}U/^{238}U$) of dissolved river water U lies between 1.17-1.26 (Chabaux et al., 2001; Dunk et al., 2002). Excess ^{234}U in rivers and seawater implies that a corresponding deficit should exist through concomitant depletion within the weathered land surface. The short-lived nature of ^{234}U, the relatively short residence time of dissolved U in the oceans (300-500 kyr; Dunk et al., 2002) and the long-term stability of seawater ($^{234}U/^{238}U$) (Henderson, 2002) implies a steady release of U from continental weathering zones.

Here we present the first comprehensive compilation of data for terrestrial weathering products measured for U series systematics (Figure 1a) and calculate a mean global ($^{234}U/^{238}U$) of 0.992 ± 0.096 (1σ) (Supplemental Table 1; Supporting Information). The dispersion around the mean results from the large number of samples of weathering residues (n = 335) from different climatic and hydrological conditions. Regardless, statistical analysis shows that at the confidence level of 95 %, the data are tightly distributed (0.992 ± 0.010; Supplemental Equation 1) and that the mode is also close to secular equilibrium (1.04). The percentage cumulative frequency distribution (Supplemental Figure 1) shows that the calculated average ($^{234}U/^{238}U$) of 0.992 is not skewed by outliers with unusually high ($^{234}U/^{238}U$) and that there is no indication that it should not be representative of the global mean terrestrial weathering residue. At face value, this close-to-equilibrium ratio suggests that the average weathering residue records

only a modest ^{234}U loss, which, in turn, would imply that a very large mass of Earth surface material losing only a small fraction of its U at a slow rate.

However, soils with consistently low ($^{234}U/^{238}U$) values ≤0.90-0.55 (n = 20 samples) (Rosholt et al., 1966; Mathieu et al., 1995) (Figure 1a) do exist, and at least regionally, very strong U loss at high chemical weathering rates has been documented for the last 7-40 kyr (Ma et al., 2010). Thus, locally, rapid loss of U during active weathering does occur within the critical zone (CZ) and this may not be fully captured by the global mean ($^{234}U/^{238}U$) from previous studies of weathering residues (Figure 1a).

To describe the U cycle on the Earth's surface with a simple steady state model, it can be assumed that the seawater U inventory (ca. 4.7 x 10^{15} g) must have been released from the continents. Additionally, the ($^{234}U/^{238}U$) ratio in seawater (~1.145) suggests that an excess of ca. 3.74 x 10^{10} g of ^{234}U must be counterbalanced as a deficit on land. In our mass balance, 5.31 x 10^{10} g of ^{234}U per metre depth are concentrated in the Earth's surface (the CZ) on average. Taking into account possible ranges in ($^{234}U/^{238}U$) of terrestrial weathering products (Supplemental Table 1; Figure 1a) the average necessary depth of the weathering front can be calculated to balance the excess ^{234}U in seawater (Supplemental Table 2). The relationship between weathering depth and ($^{234}U/^{238}U$) is visualised on a binary plot (Figure 1b). Accordingly, a global mean ($^{234}U/^{238}U$) of 0.99 would require an average weathering depth on Earth of ca. 70 m. By contrast, if a ($^{234}U/^{238}U$) value of 0.90 is adopted as the representative value for residual weathered material, the required thickness reduces drastically to only 7 m. Furthermore, a ($^{234}U/^{238}U$) value of 0.75 for the terrestrial weathering products would be balanced with a weathering front of less than 3 m.

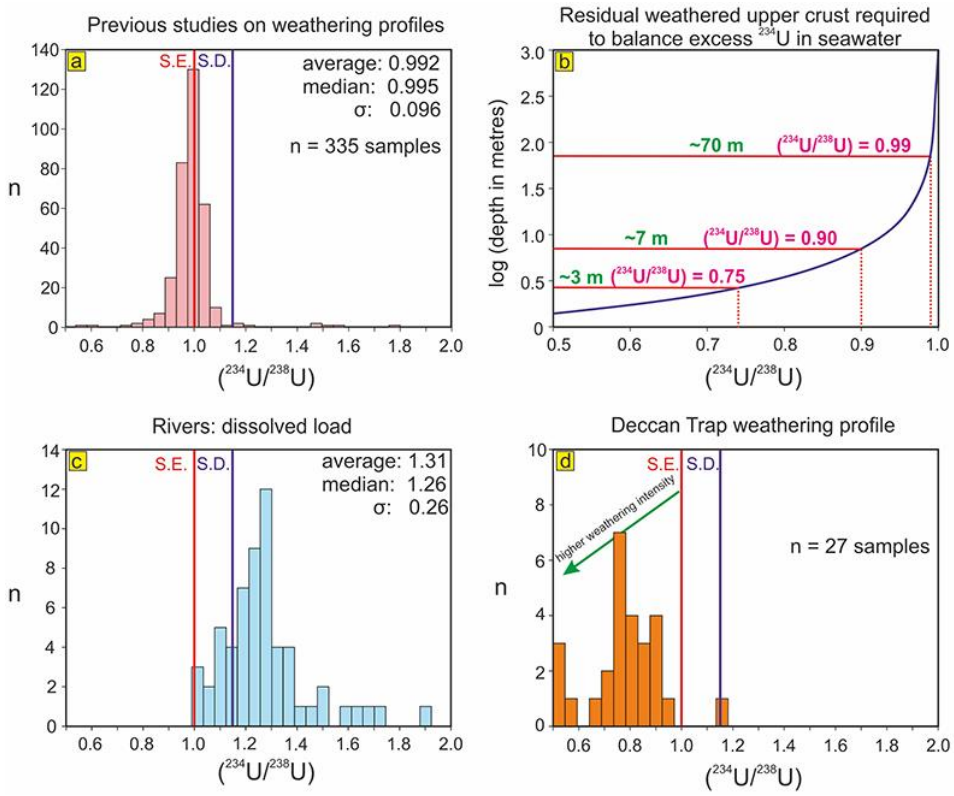

Figure 1. Histograms of ($^{234}U/^{238}U$). **(a)** Previously published data for weathering profiles. **(b)** Results of a simple mass balance calculation accounting for the observed ^{234}U excess in seawater in terms of weathering depth for various values of ($^{234}U/^{238}U$) in the residual weathered material. (**c)** Dissolved load in major rivers. **(d)** Weathering profile of this study. S.E. = secular equilibrium; S.D. = seawater dissolved ($^{234}U/^{238}U$). The average, median and standard deviation (σ) of each respective data set are illustrated in **(a,c)**. Data for **(a,c)** are compiled in Supplemental Table 1.

In view of the difficulty of reconciling the dissolved U budget of the ocean (requiring a mean global CZ thickness of ca. 70 m) with the observed mean CZ thickness of ca. 37 m (Xu and Liu, 2017), we here set out to test whether the solution to this discrepancy might be that the strongly weathered residue at the Earth's surface is underlain by a more actively weathering part of the CZ at greater depth, supplying U with a more severe ^{234}U deficit. This prospect prompted the investigation into the Th/U and U series systematics of an active weathering profile where primary mineral alteration has not yet progressed to the levels of oxide and hydroxide formation typical of laterites. The studied saprolitic smectite-dominated profile developed across an active weathering front on Deccan Trap basalt protolith. It is exposed to 640 cm depth in an artisan quarry east of Chhindwara, India on the very top of a flat-lying mesa, thus minimising effects of lateral element transport with water. The sampling area is also not subjected to significant atmospheric dust inputs (Babechuk et al., 2015), and the lack of an excessive vegetation

cover and biomass-dominated topsoil minimise the amount and effects of organic matter in the profile. The limited degree of weathering permits recognition of two basalt flows (Figure 2 and Supplemental Figure 2), whose morphology, vesicularity and joint patterns have controlled the location and extent of weathering. As a result, the weathering intensity increases downwards within the profile and remains relatively constant in the lower flow with Chemical Index of Alteration (CIA) values of 70-80. It, therefore, departs from simplified textbook examples of decreasing weathering intensity with depth. The profile has been the subject of very detailed earlier geochemical studies (Babechuk et al. 2014; 2015) in which sample context, mineralogy, geochemistry and weathering behaviour are documented. Here we analysed the same samples for U series compositions (27 samples, including 4 samples from a corestone) with a quadrupole inductively coupled plasma mass spectrometer (Q-ICP-MS) and representative samples of both flows with a high precision multi collector inductively coupled plasma mass spectrometer (MC-ICP-MS).

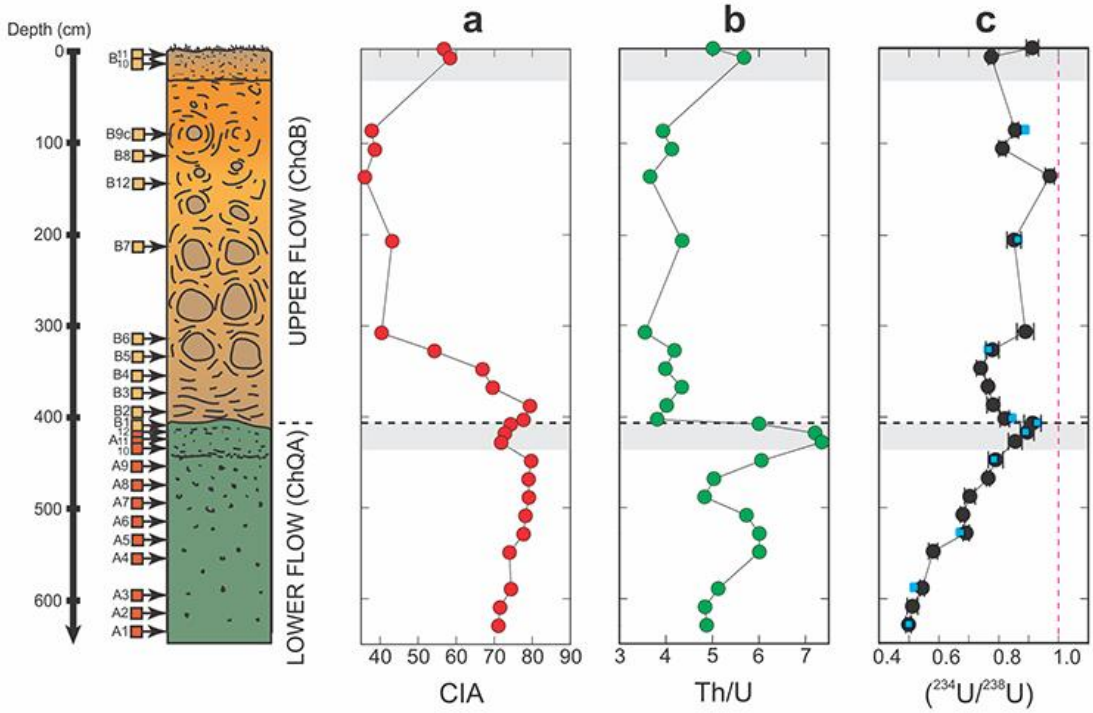

Figure 2. Vertical profile of volcanic flows and weathering characteristics. **(a)** CIA. **(b)** Th/U ratio. **(c)** ($^{234}U/^{238}U$), dashed purple line illustrates secular equilibrium, black dots = Q-ICP-MS data, blue squares = MC-ICP-MS data to test the accuracy of Q-ICP-MS data. Note that errors bars of MC-ICP-MS data are smaller than symbols; the contact between the two flows is shown on each plot as a horizontal dashed line. The modern soil surface and palaeo-flow surface are denoted by the horizontal shaded horizons.

2. Correlation between Weathering Indices and U/Th

Analytical methods and geochemical data, as well as additional descriptions of the weathering trends, are presented in the supporting information and in Supplemental Table 3. To assess weathering intensity, weathered material was compared to two samples of least weathered parental rock (ChQB12, CHQB9c). Overall, the saprolitic profile has progressed to an intermediate weathering intensity (Figure 2a), with CIA values ranging from 36 (fresh bedrock) to 80 (saprolite). Furthermore, nearly all samples show elevated Th/U ratios relative to the least weathered parent rock, indicating preferential elemental U release (Figure 2b). Importantly, all weathered samples also demonstrate clear preferential ^{234}U loss, resulting in ($^{234}U/^{238}U$) well below unity (Figure 2c), whereas the least weathered bedrock (ChQB12) has a ($^{234}U/^{238}U$) close to secular equilibrium (0.972). In the lower flow, ($^{234}U/^{238}U$) decreases quite smoothly from the top (0.914) towards the base (0.500). The preferential release of ^{234}U is strongly associated with loss of mobile over least mobile elements. For example, ($^{234}U/^{238}U$) and magnesium/titanium (Mg/Ti) are strongly positively correlated ($r^2 = 0.835$; Figure 3a). Thus, the chemical breakdown of Mg-silicates appears to occur concomitantly with the breakdown of glass and fine-grained matrix, resulting in the release of ^{234}U. This observation was contextualised with trace element maps (Supplemental Figure 3), showing that U and Th are enriched in glass and matrix occurring as interstitial material and inclusions in silicate minerals. The phenocrysts apparently form a crystalline mineral barrier whose breakdown by weathering then promotes accelerated chemical dissolution of glass and matrix. In both flows, there is also an anti-correlation between ($^{234}U/^{238}U$) and iron(III) oxide (Fe_2O_3) (Figure 3b), and the association between elevated Th/U and Fe_2O_3 identifies weathering intensity as the key control on U loss and U isotope systematics.

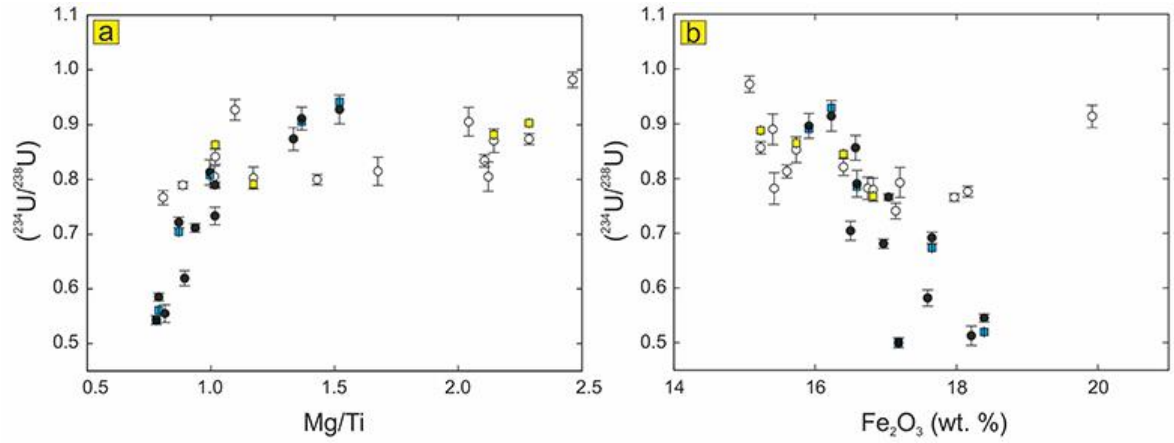

Figure 3. Bi-variate diagrams. **(a)** ($^{234}U/^{238}U$) vs. Mg/Ti. **(b)** ($^{234}U/^{238}U$) *vs*. Fe_2O_3. The decreasing Mg/Ti ratios correlate with ($^{234}U/^{238}U$), whereas Fe_2O_3 anti-correlates. White dots = Q-ICP-MS data of upper flow; black dots = Q-ICP-MS data of lower flow; yellow squares = MC-ICP-MS data of upper flow; blue squares = MC-ICP-MS data of lower flow.

3. Significance for the Dissolved Riverine U Flux and the Marine ^{234}U and U Inventories

The profile demonstrates that ^{234}U was lost preferentially over lattice-bound U. This finding is in agreement with experimental leaching studies that predict that ^{234}U should readily enter solutions because it resides in crystal defects caused by alpha recoil rather than bound within the crystal lattice (e.g., Kigoshi et al., 1971). These experimental observations provide the mechanism for observed ^{234}U excess in river waters (Dosseto et al., 2008a) and seawater (e.g., Chen et al., 1986) and explain why ($^{234}U/^{238}U$) values in the dissolved phases of the Deccan rivers are significantly higher than secular equilibrium (from 1.1 to 1.3) (e.g., Vigier et al., 2005). The main finding from the new saprolite data is that a significant proportion of the ^{234}U excess in dissolved river loads could originate from saprolitic zones, occurring as deep incipient weathering fronts at the base of the CZ (Figure 1).

To date, the only other studies that have documented strong loss of ^{234}U during weathering were performed on a thin soil profile developed on trachyte in Arizona (Rosholt et al., 1966) and across a soil-saprolite profile developed on a highly evolved Brazilian granite (Mathieu et al., 1995). In further agreement with these studies, our dataset suggests that ^{234}U loss was, at least on the scale of the entire profile, accompanied by

elemental U loss. It may seem surprising that many earlier empirical studies have not unequivocally documented stronger ^{234}U and U deficits in weathering profiles. However, the average thickness of the CZ across continental areas lies at more than 35 m (Xu and Liu, 2017), and in tropical regions weathering profiles can be >100 m thick (e.g., Buss et al., 2013). It is therefore likely that the zone of active weathering is often not readily accessible for sampling.

If the average CZ is composed of a narrow, actively weathering lower front and a more slowly weathering residue on top, their relative contributions to the marine ^{234}U can be calculated with relatively few assumptions. Taking an average global CZ of 36.8 m thickness, a ($^{234}U/^{238}U$) of ca. 0.76 in the actively weathering saprolite (samples from this study, n = 25; excluding the U-enriched corestone sample CHQB9d and least weathered parent rock CHQB12) and ($^{234}U/^{238}U$) of ca. 0.99 in the more strongly weathered CZ (n = 335; Figure 1a,b; Supplemental Tables 1, 2), the mass balance predicts that both layers contribute equally (ca. 50 %) to the oceanic ^{234}U excess (Figure 4). In this model calculation, the resulting average CZ is composed of 1.45 m saprolite, and 35.35 m of previously reacted residue above; proportions that are consistent with field observations (Supplemental Figure 4). In summary, the most parsimonious solution to the oceanic U inventory is that a very large pool of highly weathered CZ contributes roughly only half the U to the dissolved river load and the oceans, whereas a much narrower active zone of clay formation contributes the other half. In reality, there is a very strong longitudinal variability in CZ thickness and composition (Xu and Liu, 2017) but until better U constraints from different climatic settings exist, the first order conclusion is that a volumetrically minor deep actively weathering CZ is disproportionally important for supplying elemental fluxes from the continents.

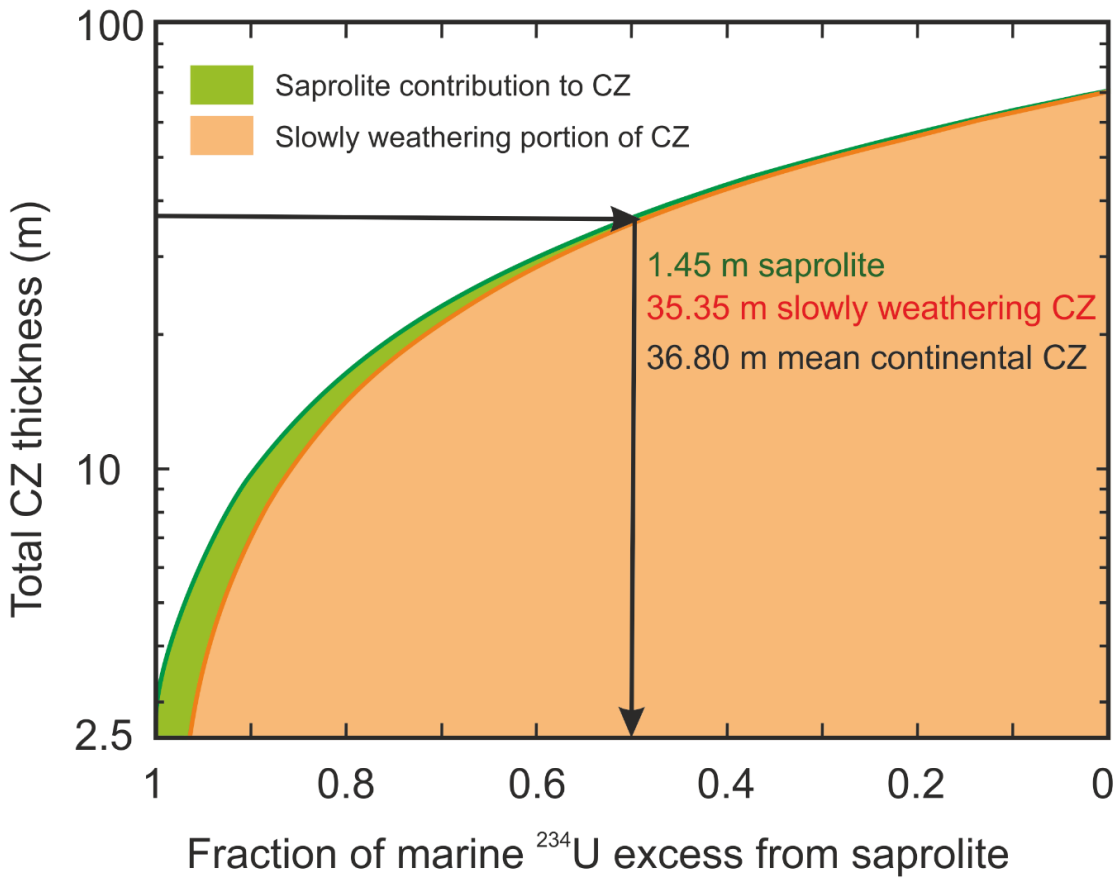

Figure 4. Total CZ thickness vs. fraction of marine ^{234}U excess from saprolite. For example, only 1.45 m of saprolite with ($^{234}U/^{238}U$) of ca. 0.76 is needed in steady state to contribute equally to the oceanic ^{234}U excess (50 %) as the more strongly weathered CZ (35.35 m) with ($^{234}U/^{238}U$) of ca. 0.99.

As might be expected from the relatively high standard deviation of the global mean ($^{234}U/^{238}U$), the elemental and isotopic systematics of Th and U are much more complex within the slowly weathering pool than in the saprolite (e.g., Dosseto et al., 2008b; Dequincey et al., 2002). Complexities arise from factors such as allochthonous input of U (e.g., Pett-Ridge et al., 2007) and Th (e.g., Pelt et al., 2013), biomass-related processes in topsoils (e.g., Rosholt et al., 1966), lateral U movement in down-hill topographies (e.g., Dosseto et al., 2008b) and formation of specific minerals, such as iron-aluminium (Fe-Al) oxides (e.g., Engel et al., 2016). Oxyhydroxide-rich horizons, for example, promote complicated redistribution because Fe hydroxides can retain ^{234}U (e.g., Dequincey et al., 2002).

Land surfaces in the tropics often consist of highly weathered and very old substrates, such as laterites which, on average, contain U close to secular equilibrium (Dequincey et al., 2002). In part, this is the result of the relatively short (246 kyr) half-life of ^{234}U (e.g., Dosseto, 2014), meaning that ^{234}U in the residuum of long-lived weathering profiles could return towards secular equilibrium with its parent nuclide (^{238}U) in less than 2 Myr. Furthermore, it is known that the bulk of the mobile elements and their isotopic signals have long been lost from laterites (e.g., Babechuk et al., 2015), and that they typically make a limited contribution to the present dissolved load of rivers. By contrast, the strongly weathered residue can still contribute a significant fraction of the suspended load (Supplemental Table 1; Supplemental Figure 5), as also suggested from strontium (Sr) isotope systematics (e.g., Allègre et al., 1996).

4. Conclusions

The continental dissolved flux of waters draining active weathering fronts of Deccan basalt are distinguished by elevated ($^{234}U/^{238}U$), thus leaving behind a residual ^{234}U-depleted residue. The calculated average ($^{234}U/^{238}U$) activity ratio of ca. 0.76 in this study for saprolite combined with mass balance calculations (Figures 1b, 4; Supplemental Table 2) suggests that active weathering fronts within the deeper CZ are crucial to understanding the global U systematics. These fronts supply disproportionally high amounts of dissolved elements (Buss et al., 2013; and references therein), including U (e.g., Ma et al., 2010), to the hydrosphere. The proposed scenario is corroborated by previously documented strong ^{234}U loss from weathering profiles (Rosholt et al., 1966; Mathieu et al., 1995) and suggests that the compiled global mean ($^{234}U/^{238}U$) of 0.992 ± 0.096 (1σ; n = 335 samples) (Figure 1a) for weathering residue is not fully representative. We propose that the discrepancy is due to the relative inaccessibility of the thin active (saprolitic) weathering zone at the rock-soil interface, having caused a sampling bias in favour of highly weathered residuum in many previous studies. Accordingly, the model envisaged here differs from the previous implicit assumption that a voluminous zone within the upper parts of the Earth surface dominantly supplies U to rivers and oceans. Our new data show that on the Deccan Traps basalts, strong preferential release of ^{234}U is restricted to relatively thin weathering zones of saprolite where primary minerals weather to clays close to the rock-soil interface. There, the significant isotopic fractionation processes of U predicted by experiments are related to

the preferential breakdown of glass and matrix. The study of elemental and stable isotope ratio systematics of other redox-sensitive elements (e.g., molybdenum (Mo), chromium (Cr), Fe, sulphur (S), zinc (Zn); e.g., Wille et al., 2018; Suhr et al., 2018) can benefit from focussing on comparable active weathering zones similarly exhibiting the U deficits required by mass balance, because the hydro-bio-geochemical cycles of these elements are known to have been affected by free oxygen in the atmosphere since the Precambrian (e.g., Partin et al., 2013; Bekker et al., 2004). Once the behaviour of these elements has been documented, deeper time studies can build on the new insights and help to reconstruct ancient Earth surface processes and associated ocean chemistry evolution.

Acknowledgements

This research is the contribution of the ISONOSE Marie Curie Research training network (www.IsoNose.eu) funded from the People Programme (Marie Curie Actions) of the European Union's Seventh Framework Programme FP7/2007-2013/ under REA grant agreement n° [608069]. We thank Cora McKenna for help during laboratory work and Michael Murphy at UCD for assistance during MC-ICP-MS analysis. We thank Dr David Chew for making the LA-ICP-MS trace element maps and four anonymous reviewers for their critical comments.

5. Supporting Information I

5.1. Additional descriptions of the weathering trends in profile

5.1.1. Chemical weathering indices

The CIA is useful to quantify early stages of weathering and predominantly tracks feldspar dissolution and the concomitant release of calcium (Ca), sodium (Na), and potassium (K) relative to Al, which is typically retained within pedogenetic clays. The CIA ranges from 36 in the least weathered sample (parent rock) to 79 in the most weathered portion of the upper flow. In the lower flow, the CIA is high, but relatively constant (71 to 80) (Supplemental Table 3).

Because U and Th are not principally hosted in feldspar but originally occurred in the micro-crystalline matrix (Supplemental Figure 3), the mafic index of alteration ($MIA_{(O)}$) (Supplemental Table 3), which incorporates Fe and Mg in the estimate of weathering intensity under oxic conditions (Babechuk et al., 2014), is also relevant for this study. The $MIA_{(O)}$ correlates well with the CIA ($r^2 = 0.900$; Babechuk et al., 2014) in these samples, confirming the similar bulk weathering behaviour of Mg, Ca, and Na in the Chhindwara profile. Both weathering indices demonstrate that the chemical breakdown of mafic minerals (Mg) and plagioclase (Ca, Na) accompanied the nearly congruent release of these major elements.

Regardless, it may seem surprising that the CIA and $MIA_{(O)}$ are not monotonously decreasing with depth. However, in basaltic weathering profiles, the lava flow morphology and texture (e.g., flow banding and vesicularity) have a strong control on fluid penetration, chemical attack, and, consequently, chemical weathering intensity (Babechuk et al., 2014). As a result, the deeper levels of the Chhindwara profile are currently stronger weathered than the massive section of the upper volcanic flow, explaining the lower CIA and MIA(o) values in this section. At the very advanced weathering stages (e.g., in laterites), these texturally controlled features disappear and a thick “textbook” profile develops that is characterised by upwards increasing weathering intensity.

5.1.2. Th/U systematics

The protolith ChQB12 has a Th/U of 3.66, which is typical for DVP tholeiite (e.g., Sheth et al., 2009). The remaining samples of the upper flow have a more variable but generally higher Th/U, averaging 4.22 ± 0.60, suggesting that U-loss in the upper part of the profile has not yet proceeded very far (Figure 2b). By contrast, the lower, more strongly weathered flow shows a significantly higher average Th/U of 5.76 in the central part, in agreement with the highest $MIA_{(O)}$ values in the profile. It is worth noting that this part of the flow originally had the greatest vesicularity and that the topmost layer of the lower flow, based on neodynium (Nd)-isotope ratios, may have seen deposition of a very small amount of extraneous material before the emplacement of the upper flow (Babechuk et al., 2015). Regardless of these minor volcanological variations, the elemental Th/U distribution in the studied profile is far simpler than any previous reported weathering profile. The simplicity of the profile presented here strongly argues against significant downward U (and Th) redistribution, such as documented in many laterite profiles (Dequnicey et al., 2002; Wimpenny et al., 2007).

5.1.3. U series systematics

In the upper flow, ($^{234}U/^{238}U$) is below unity with values ranging down to 0.740. Fewer correlations are found between ($^{234}U/^{238}U$) and chemical parameters than in the lower flow but there is a modest anti-correlation between ($^{234}U/^{238}U$) and CIA ($r^2 = 0.379$) and positive correlation with Mg/Ti ($r^2 = 0.315$; Figure 3a; excluding corestone sample ChQB9d). At these more modest levels of alteration, redistribution of minor quantities of leached weathering products apparently are an important factor. This is particularly evident in the elevated ($^{234}U/^{238}U$) of the least altered core of a corestone (sample CHQB9d), which has seen U addition. Regardless, at least in semi-quantitative terms, the lesser extent of preferential ^{234}U loss in the upper flow is consistent with its less advanced state of weathering.

Across the entire profile, ($^{230}Th/^{238}U$) is strongly correlated with ($^{234}U/^{238}U$). For most ($^{234}U/^{238}U$), the corresponding ($^{230}Th/^{238}U$) is higher, resulting in a systematic offset from

the equiline (Supplemental Figure 6). Excluding one least weathered parent rock (CHQB12), the data points of the upper profile define a straight line (r^2 = 0.774). In combination with the lower flow samples, an even stronger correlation is evident (r^2 = 0.951). The resulting ($^{230}Th/^{234}U$) is above unity, averaging 1.076 ± 0.050 in the lower flow and 1.107 ± 0.050 in the upper flow. Together, these observations suggest that the ^{230}Th-deficit resulted from a combination of ^{230}Th-loss during weathering and diminished production rate from depleted ^{234}U parent decay. No significant correlations are found between ($^{230}Th/^{234}U$) and other isotopic or chemical parameters in the lower flow. All samples have ($^{230}Th/^{232}Th$) much lower than 1. In the upper flow, ($^{230}Th/^{232}Th$) is anti-correlated (r^2 = 0.603) with Th/U. Finally, there is also an inverse, moderate correlation between Th/U and ($^{234}U/^{238}U$) evident (r^2 = 0.488 in the lower flow; r^2 = 0.336 in the upper flow). This suggests that ^{234}U is most easily lost during weathering, followed by lattice bound U and ^{230}Th.

5.2. Analytical details

5.2.1. Methodology and high-precision trace element analysis

Samples from the Chhindwara profile (n = 27; Babechuk et al., 2014) were powdered in an agate mill and analysed for their major elements by X-ray fluorescence (XRF) at Laurentian University (LU, Sudbury, Ontario). The trace element composition was determined at LU and Trinity College Dublin (TCD, Dublin, Ireland). The method of Eggins et al. (1997) was followed, incorporating modifications described in Kamber (2009) and Babechuk et al. (2010). For analysis, 100 mg of sample powder was digested with HF-HNO_3 (4:1) in closed Savillex Teflon® beakers at ~ 160 °C for 72-90 hours. Fluorides were then evaporated, and concentrated HCl (1 mL) was introduced to break down potential organic material, and then evaporated once more. Final conversion using two 1 mL aliquots of concentrated nitric acid (HNO_3) was performed and the nitrate residue was dissolved in a 20 % HNO_3 stock solution. Approximately 4 % of this stock was gravimetrically diluted to produce a 2 % HNO_3 solution with an internal standard mixture containing lithium-6 (^{6}Li), rhodium (Rh), rhenium (Re), bismuth (Bi), and ^{235}U for

solution Q-ICP-MS analysis. This was performed on a Thermo Scientific XSeriesII at LU and a Thermo Scientific iCap-Qs at TCD. Measurements on the latter instrument were repeat analyses of one batch of samples (23 of 61) that were undertaken due to detector-associated instability evident for some elements in the XSeriesII data from LU. Stock solutions prepared at LU were transported to TCD in their Savillex beakers, with an intermittent storage interval of ca. 22 months prior to the repeat analysis. During the analytical sessions in both laboratories, sample unknowns were preceded by blanks, calibration (USGS rock standard W-2a) and quality control standards (USGS rock standards BCR-2 and BIR-1), and bracketed with monitor samples (one every 5-7 unknowns) for external drift correction (Eggins et al., 1997). Method reproducibility and accuracy was assessed using the long-term average of USGS and GSJ standards run as unknowns. The concentrations of the high field strength elements (HFSE) (including U and Th) in basalt standards (BHVO-1, BHVO-2, BIR-1, BCR-2, JB-2) reproduced at 2 % RSD (1 sigma) or better, with the exception of BIR-1 which returns slightly higher RSD values due to very low incompatible element concentrations (Babechuk et al., 2014; 2015). The reproducibility for Mo is poor due to contamination of the second-generation USGS standards. Those data from Babechuk et al. (2014; 2015) that are relevant for our study are listed in Supplemental Table 3. At LU, accuracy and precision of the employed trace element method was tested by replicate analyses of the standard materials BCR-2 and TML. Nine digestions of USGS standard BCR-2 were analysed in 25 separate runs over a time period of 4 years. Long-term reproducibilities for the elements studied here (U and Th) were 1 % rsd (1 sigma). Blank levels were insignificant.

5.2.2. MC-ICP-MS analysis and details of U-series work

Approximately 70-100 mg of rock powder was weighed out for digestion. To this a known quantity of a calibrated mixed ^{229}Th-^{233}U-^{236}U spike solution was added before dissolution in high purity HNO_3/HF mixture. Following standard separation methods using UTEVA exchange chromatography, U and Th fractions for selected samples were analysed separately using a ThermoFinnigan Neptune MC-ICP-MS linked to a CETAC Aridus II Desolvating Nebulizer System at University College Dublin. Initial instrument set up and tuning was performed using an internal 4 ppb U standard. The ^{238}U ion beam for this

standard solution typically produced around 1.6 V on a Faraday collector. The major U isotopes (^{238}U, ^{235}U, ^{233}U and ^{236}U) were collected and measured in static mode using Faraday collectors, with the minor ^{234}U peak measured using a Secondary Electron Multiplier (SEM) in ion-counting mode. For U, the yield factor between the SEM and Faraday detectors was calculated using 50 measurement cycles, switching alternatively between measuring both ^{235}U and ^{238}U peaks on two Faraday cups and measuring ^{235}U on the SEM for the IRMM 3184 standard. Thorium fractions were measured in peak-jumping mode using the SEM for the minor isotopes ^{230}Th and ^{229}Th, while ^{232}Th was simultaneously measured in analogue mode in two Faraday collectors. Thorium measurements were performed using a single magnet-jump sequence of 60 measurement cycles with the SEM and Faraday cup, a 4.194 s integration time per cycle and 1 second idle time with ^{229}Th and ^{230}Th alternately collected in the central SEM. Ion-beam currents at half-masses 229.5 and 230.5 were measured using the SEM during the Th measurement cycle in order to correct for tailing effects from the large ^{232}Th peak. Quoted uncertainties in isotope ratios involving ^{230}Th have taken the uncertainties associated with this baseline correction into account. Each Th measurement was bracketed by a ^{235}U/^{238}U analysis of the IRMM 3184 standard to correct for mass-dependent fractionation using a linear interpolation. Between each sample or standard, a thorough cleaning of the sample inlet system with a solution of dilute HNO_3 (for U) and a hydrochloric-hydrofluoric (HCl-HF) solution (for Th) was performed to avoid cross-contamination. At the end of washout, the typical background count-rate was negligible (less than a few thousands CPS on the major ^{238}U and ^{232}Th isotopes). Mean values and standard deviations were calculated from the results once outliers were automatically removed (generally <10 % rejection) by the Neptune acquisition software. Measurements were subsequently processed using a Visual Basic Excel macro for mass-fractionation and baseline corrections.

5.2.3. Solution based Q-ICP-MS analysis and U series explanations

Uranium-series measurements for all studied samples were performed at Laurentian University, Canada, via solution quadrupole ICP-MS with an XSeriesII. All results are presented in Supplemental Table 3. For the quadrupole measurements, the remaining 98 %

of the stock solution of the trace element digest was dried down and redissolved for U and Th purification, using UTEVA resin. Two separate mass spectrometric analyses were performed on the purified U and Th solutions. For the first measurement, 5 % of the solution were gravimetrically diluted to 6 g 2 % HNO_3 together with a mixture of internal standards (10.6 ppb ^{6}Li and 4.4 ppb each indium (In), Re and Bi). This solution was analysed to determine the column yields for ^{232}Th and ^{238}U as well as the instrumental mass bias under the day's tuning conditions (via the $^{238}U/^{235}U$ ratio). Knowledge of column yields are not important for the ($^{234}U/^{238}U$) activity ratio but for ($^{230}Th/^{238}U$). The average column yields were 83 % for Th and 87 % for U. Propagation of Th and U concentration uncertainty introduces ca. 1/3 towards the final ($^{230}Th/^{238}U$) uncertainty estimated from repeat analyses of Table Mountain Latite (TML). The $^{238}U/^{235}U$ measured on 33 sample and standard solutions was 139.07 ± 0.29 (2 sigma) with a mean square weighted deviation (MSWD) of 0.45. The small mass bias of 0.00288 amu^{-1} was corrected with a linear law.

The remaining bulk of the purified U and Th solution was volumetrically diluted to 2 g of 2.5 % HNO_3 for measurements of the $^{230}Th/^{235}U$ and $^{234}U/^{235}U$ ratios (all signals in pulse count mode) using the quadrupole ICP-MS at exactly the same tuning and sample uptake conditions as for the column yield experiments. The instrument was operated in Xs-extraction mode using a standard impact bead spray chamber and a nominal 400 µl min^{-1} nebuliser to yield a sensitivity of 4.5 e6 cps ppb^{-1} at cerium oxide/cerium (CeO^{+}/Ce^{+}) of 1.7 %. The instrument background of <0.15 cps was monitored at mass 245. Mass 237 was analysed to estimate abundance sensitivity for correction of tailing of mass 235 onto mass 234 and mass 232 onto mass 230. It was determined to be 0.385 ± 0.076 ppm at 1 amu difference (^{238}U signal onto mass 237) similar to that reported by Pointurier et al. (2008), attesting to the ability of the XSeriesII ICP-MS for medium-precision U-isotope analysis (see also Shen et al., 2006 and Douville et al., 2010).

In terms of accuracy and external precision the concentrations in BCR-2 obtained for U (1.698 ± 0.016 ppm) and Th (5.785 ± 0.066 ppm) compare very favourably with isotope dilution literature data (e.g.,. Prytulak et al., 2008), and the reproducibility of the Th/U ratio (0.73 %) is also very similar to that (0.58 %) reported by Prytulak et al. (2008). The six individually analysed digests of TML returned somewhat inferior external errors. With respect to Th and U, we obtained concentrations of 30.35 ± 0.39 and 10.79 ± 0.13 ppm and a Th/U of 2.812 ± 0.022. This is again within the bandwidth of isotope dilution data, such as those reported by Kokfelt et al. (2003).

The ($^{234}U/^{238}U$) activity ratio was determined on three TML aliquots and averaged 1.0035 ± 0.0089 (Supplemental Table 4). This attests to the accuracy of the analysis (within uncertainty in secular equilibrium) and shows that, in terms of precision, the method is somewhat inferior to traditional thermal ionisation mass spectrometry data (e.g., Kokfelt et al., 2003) but adequate to measure the large expected deviations from secular equilibrium in weathering profiles. The ($^{230}Th/^{238}U$) activity ratio averaged 0.997 ± 0.012, which is also accurate within error, and in secular equilibrium. The ($^{230}Th/^{232}Th$) ratio averaged 1.082 ± 0.016, within the more precise magnetic sector mass spectrometer data (e.g., Kokfelt et al., 2003; Sims et al., 2008). Internal run precision for samples was always better than the external reproducibility of TML, which was therefore viewed as a more suitable measure of accuracy and precision.

To test the accuracy of the U-series data via Q-ICP-MS, the ($^{234}U/^{238}U$) ratios of the MC-ICP-MS measurement are compared to the respective ($^{234}U/^{238}U$) ratios of the Q-ICP-MS measurement. The agreement between both techniques was very good, with a correlation factor of 0.986 between the two methods (Supplemental Figure 7).

5.2.4. LA-ICP-MS trace element mapping

LA-ICP-MS elemental image maps were acquired using a Photon Machines Analyte Excite 193 nm ArF Excimer laser-ablation system with a Helex 2-volume ablation cell coupled to an Agilent 7900 ICPMS at the Department of Geology, TCD. The ICP-MS was tuned using NIST 612 standard glass to yield Th/U ratios of unity and low oxide production rates (ThO^+/Th^+ typically <0.15 %). 0.5 l/min helium (He) carrier gas was fed into the cell body and 0.2 l/min He was fed into the cup, and the aerosol was subsequently mixed with 0.56 l/min argon (Ar) make-up gas and a 6 ml/min volume of dinitrogen (N_2) to enhance signal sensitivity and reduce oxide formation. The Ar and N_2 were added in a ca. 1.5 cm^3 mixing bulb which results in a rapid washout for image mapping experiments. Ten isotopes (^7Li, ^{24}Mg, silicon-29 (^{29}Si), ^{52}Cr, ^{57}Fe, nickel-60 (^{60}Ni), copper-63 (^{63}Cu), ^{66}Zn, ^{232}Th and ^{238}U) were measured using a total duty cycle of 135 ms. A laser fluence of 3.3 J/cm^2s, a repetition rate of 30 Hz, a 12 μm spot size and a scan speed of 20 μm/s were employed. The LA-ICP-MS trace element image mapping procedure is similar to that described in Ubide et al. (2015) and outlined briefly below. Maps were made by covering

the sample under the ablation site with an array of adjacent lines, ablated in a successive manner. The final ablated area was rectangle-shaped to facilitate production of trace element maps using the "Image from Integrations" module in Iolite. Although the system has a fast washout (90 % signal reduction in less than 0.5 s), 10 seconds were allowed for washout between lines to avoid any carry-over from standards to samples and vice versa. NIST612 glass reference material was used as the calibration standard and ablated with the same parameters as the samples. Five NIST612 lines were analysed at the beginning and end of each experiment. Data reduction and production of trace element distribution maps was undertaken with the Iolite software (Paton et al., 2011) using the "Trace Elements" data reduction scheme in "Semi-Quantitative" mode (which in IOLITE corresponds to not employing an internal standard isotope). Following data reduction, trace element distribution maps were built with the Iolite module "Images From Integrations".

5.3. Analysis of quantitative loss of U from the Chhindwara profile

The respective loss and gain of an element in a sample is calculated after normalisation to an immobile or least-mobile element (expressed as ratio 'R') for both the sample and the parent rock (ChQB12) (Supplemental Equation 2) (Supplemental Table 3; e.g., Brimhall and Dietrich, 1987; Kurtz et al., 2000; Kisakürek et al., 2004; Babechuk et al., 2015)

$$\% \text{ change in R} = \left[\frac{(Rsample - Rprotolith)}{Rprotolith}\right] x\ 100 \qquad \text{Supplemental Equation 2}$$

By using this formula with niobium (Nb) as the immobile trace element (Babechuk et al., 2015), the U/Nb ratios indicate that the strongest loss of U in the Chhindwara profile lies around 40 % (Supplemental Table 3).

5.4. Supporting data

Supplemental Table 1. Literature data compilation of U concentrations and ($^{234}U/^{238}U$) activity ratios of rivers (dissolved load, suspended load) and weathering profiles.

Sample or Location	U (conc.)[1]	($^{234}U/^{238}U$)	Type	Source
Rivers				
Indus Thatta Bridge	4.94	1.026	Dissolved phase	Chabaux et al. (2001)[2]
Ganges Rajshahi	2.0	1.05	Dissolved phase	Chabaux et al. (2001)[2]
Yangtse Kiang	1.1	1.351	Dissolved phase	Chabaux et al. (2001)[2]
Brahmaputra Chilmari	1.0	1.034	Dissolved phase	Chabaux et al. (2001)[2]
Mississippi La Place	0.94	1.31	Dissolved phase	Chabaux et al. (2001)[2]
Huang Ho	7.5	1.318	Dissolved phase	Chabaux et al. (2001)[2]
Amazon Santarem	0.04	1.1	Dissolved phase	Chabaux et al. (2001)[2]
Rhine – Germany	2.48	1.29	Dissolved phase	Chabaux et al. (2001)[2]
Mackenzie – Canada	0.5	1.4	Dissolved phase	Chabaux et al. (2001)[2]
Saint Lawrence Quebec	0.29	1.18	Dissolved phase	Chabaux et al. (2001)[2]
Congo Zaïre	0.08	1.09	Dissolved phase	Chabaux et al. (2001)[2]
Godavari Rajahmundry	0.78	1.38	Dissolved phase	Chabaux et al. (2001)[2]
Zambezi Tete	0.26	1.19	Dissolved phase	Chabaux et al. (2001)[2]
Krishna Vijayawada	1.08	1.58	Dissolved phase	Chabaux et al. (2001)[2]
Rhône Arles	0.56	1.086	Dissolved phase	Chabaux et al. (2001)[2]

Sample or Location	U (conc.)[1]	($^{234}U/^{238}U$)	Type	Source
Wistula Poland	0.72	1.259	Dissolved phase	Chabaux et al. (2001)[2]
Garonne	0.75	1.16	Dissolved phase	Chabaux et al. (2001)[2]
Narbada Broach	0.84	1.39	Dissolved phase	Chabaux et al. (2001)[2]
Rio Grande	4.5	1.74	Dissolved phase	Chabaux et al. (2001)[2]
Mahanadi Asia	0.25	1.3	Dissolved phase	Chabaux et al. (2001)[2]
Limpopo Messina	2.8	1.5	Dissolved phase	Chabaux et al. (2001)[2]
Brazos America	1.6	1.22	Dissolved phase	Chabaux et al. (2001)[2]
Loire Nantes	0.37	1.145	Dissolved phase	Chabaux et al. (2001)[2]
Orange Upington[3]	0.79	2.59	Dissolved phase	Chabaux et al. (2001)[2]
Charente France	2.0	1.22	Dissolved phase	Chabaux et al. (2001)[2]
Cauveri Trichi	0.58	1.28	Dissolved phase	Chabaux et al. (2001)[2]
Seine Rouen	0.53	1.107	Dissolved phase	Chabaux et al. (2001)[2]
Tapti	0.36	1.26	Dissolved phase	Chabaux et al. (2001)[2]
Kalix Sweden	0.17	1.659	Dissolved phase	Chabaux et al. (2001)[2]
Suwannee Live Oak	0.15	1.9	Dissolved phase	Chabaux et al. (2001)[2]
Susquehannah Gettysburg	0.04	1.31	Dissolved phase	Chabaux et al. (2001)[2]
Fenland UK	0.92	1.276	Dissolved phase	Chabaux et al. (2001)[2]
Clyde UK	0.16	1.63	Dissolved phase	Chabaux et al. (2001)[2]
Forth UK	0.09	1.5	Dissolved phase	Chabaux et al. (2001)[2]

Sample or Location	U (conc.)[1]	($^{234}U/^{238}U$)	Type	Source
Tamar UK	0.04	1.44	Dissolved phase	Chabaux et al. (2001)[2]
Solimões	0.058	1.23	Dissolved phase	Dossetto et al. (2006)
Amazonas 07– LB	0.052	1.19	Dissolved phase	Dossetto et al. (2006)
Amazonas 07– M	0.050	1.22	Dissolved phase	Dossetto et al. (2006)
Amazonas 07– RB	0.049	1.23	Dissolved phase	Dossetto et al. (2006)
Amazonas 08	0.048	1.23	Dissolved phase	Dossetto et al. (2006)
Amazonas 10	0.051	1.23	Dissolved phase	Dossetto et al. (2006)
Amazonas 12	0.046	1.27	Dissolved phase	Dossetto et al. (2006)
Amazonas 14	0.052	1.23	Dissolved phase	Dossetto et al. (2006)
Madeira 03	0.030	1.27	Dissolved phase	Dossetto et al. (2006)
Madeira 04	0.033	1.26	Dissolved phase	Dossetto et al. (2006)
Negro	0.025	0.99	Dissolved phase	Dossetto et al. (2006)
Uatuma	0.040	1.14	Dissolved phase	Dossetto et al. (2006)
Trombetas	0.038	1.04	Dissolved phase	Dossetto et al. (2006)
Paraná do Ramos	0.028	1.39	Dissolved phase	Dossetto et al. (2006)
Arapiuns	0.024	2.04	Dissolved phase	Dossetto et al. (2006)
Tapajos	0.027	1.34	Dissolved phase	Dossetto et al. (2006)
Narmada – Deccan Traps	0.112	1.24	Dissolved phase	Vigier et al. (2005)

Sample or Location	U (conc.)[1]	($^{234}U/^{238}U$)	Type	Source
Tapti – Deccan Traps	0.157	1.19	Dissolved phase	Vigier et al. (2005)
Purna – Deccan Traps	0.151	1.15	Dissolved phase	Vigier et al. (2005)
Purna –Deccan Traps	n.d.	1.11	Dissolved phase	Vigier et al. (2005)
Pench – Deccan Traps	0.226	1.28	Dissolved phase	Vigier et al. (2005)
Mun – Deccan Traps	0.140	1.19	Dissolved phase	Vigier et al. (2005)
Jam – Deccan Traps	0.216	1.26	Dissolved phase	Vigier et al. (2005)
Wardha – Deccan Traps	0.128	1.2	Dissolved phase	Vigier et al. (2005)
Panjkra – Deccan Traps	0.422	1.21	Dissolved phase	Vigier et al. (2005)
Chotatawa – Deccan Traps	0.132	1.26	Dissolved phase	Vigier et al. (2005)
Solimões	3.42	0.99	Suspended load	Dossetto et al. (2006)
Amazonas 07– LB	3.55	0.99	Suspended load	Dossetto et al. (2006)
Amazonas 07– RB	3.26	1	Suspended load	Dossetto et al. (2006)
Amazonas 10	3.32	1	Suspended load	Dossetto et al. (2006)
Amazonas 12	3.27	0.979	Suspended load	Dossetto et al. (2006)
Amazonas 14	3.03	1	Suspended load	Dossetto et al. (2006)
Madeira 03	3.27	0.996	Suspended load	Dossetto et al. (2006)
Madeira 04	3.42	1	Suspended load	Dossetto et al. (2006)
Negro	3.21	1.033	Suspended load	Dossetto et al. (2006)
Uatuma	3.23	1.02	Suspended load	Dossetto et al. (2006)

Sample or Location	U (conc.)[1]	($^{234}U/^{238}U$)	Type	Source
Trombetas	4.13	1.027	Suspended load	Dossetto et al. (2006)
Paraná do Ramos	3.11	0.99	Suspended load	Dossetto et al. (2006)
Narmada – Deccan Traps	0.78	1.051	Suspended load	Vigier et al. (2005)
Tapti – Deccan Traps	0.85	0.989	Suspended load	Vigier et al. (2005)
Purna – Deccan Traps	1.28	1.104	Suspended load	Vigier et al. (2005)
Pench – Deccan Traps	0.99	0.978	Suspended load	Vigier et al. (2005)
Mun – Deccan Traps	0.89	1.00	Suspended load	Vigier et al. (2005)
Jam – Deccan Traps	0.94	1.093	Suspended load	Vigier et al. (2005)
Wainganga – Deccan Traps	3.13	1.00	Suspended load	Vigier et al. (2005)
Wagurr – Deccan Traps	0.88	0.952	Suspended load	Vigier et al. (2005)
Purna – Deccan Traps	n.d.	1.058	Suspended load	Vigier et al. (2005)
Weathering profiles				
Brasil – São Paulo – Paraná sedimentary basin	1.19	0.87	Soil	Bonotto and Jiménez-Rueda (2007)
Brasil – São Paulo – Paraná sedimentary basin	2.31	0.8	Soil	Bonotto and Jiménez-Rueda (2007)
Brasil – São Paulo – Paraná sedimentary basin	7.88	1.17	Soil	Bonotto and Jiménez-Rueda (2007)
Brasil – São Paulo – Paraná sedimentary basin	9.1	1.06	Soil	Bonotto and Jiménez-Rueda (2007)
Brasil – São Paulo – Paraná sedimentary basin	6.71	0.97	Soil	Bonotto and Jiménez-Rueda (2007)

Sample or Location	U (conc.)[1]	($^{234}U/^{238}U$)	Type	Source
Brasil – São Paulo – Paraná sedimentary basin	7.6	1.06	Soil	Bonotto and Jiménez-Rueda (2007)
Réunion Island – basalt	0.573	0.998	Corestone	Claude et al. (2016)
Réunion Island – basalt	1.37	1.019	Red shell	Claude et al. (2016)
Réunion Island – basalt	2.34	1.006	Red fine intermediate matrix	Claude et al. (2016)
Réunion Island – basalt	0.605	0.999	Core	Claude et al. (2016)
Réunion Island – basalt	0.608	0.998	Gray shell	Claude et al. (2016)
Réunion Island – basalt	0.608	1.005	Gray shell	Claude et al. (2016)
Réunion Island – basalt	0.665	1.005	Gray shell	Claude et al. (2016)
Réunion Island – basalt	1.18	1.01	Red shell	Claude et al. (2016)
Réunion Island – basalt	1.35	1.005	Red shell	Claude et al. (2016)
Réunion Island – basalt	1.39	1.005	Red shell	Claude et al. (2016)
Réunion Island – basalt	1.54	1.006	Red shell	Claude et al. (2016)
Puerto Rico – Rio Icacos watershed – diorite	0.336	1.023	Corestones	Chabaux et al. (2013)
Puerto Rico – Rio Icacos watershed – diorite	0.33	1.022	Corestones	Chabaux et al. (2013)
Puerto Rico – Rio Icacos watershed – diorite	0.334	1.013	Corestones	Chabaux et al. (2013)
Puerto Rico – Rio Icacos watershed – diorite	0.275	1.019	Corestones	Chabaux et al. (2013)

Sample or Location	U (conc.)[1]	($^{234}U/^{238}U$)	Type	Source
Puerto Rico – Rio Icacos watershed – diorite	0.325	1.031	Corestones	Chabaux et al. (2013)
Puerto Rico – Rio Icacos watershed – diorite	0.218	1.02	Corestones	Chabaux et al. (2013)
Puerto Rico – Rio Icacos watershed – diorite	0.408	1.02	Corestones	Chabaux et al. (2013)
Puerto Rico – Rio Icacos watershed – diorite	0.407	1.022	Corestones	Chabaux et al. (2013)
Puerto Rico – Rio Icacos watershed – diorite	0.508	1.024	Rindlets	Chabaux et al. (2013)
Puerto Rico – Rio Icacos watershed – diorite	0.439	1.018	Rindlets	Chabaux et al. (2013)
Puerto Rico – Rio Icacos watershed – diorite	0.39	1.017	Rindlets	Chabaux et al. (2013)
Puerto Rico – Rio Icacos watershed – diorite	0.57	1.022	Rindlets	Chabaux et al. (2013)
Puerto Rico – Rio Icacos watershed – diorite	0.275	1.019	Rindlets	Chabaux et al. (2013)
Puerto Rico – Rio Icacos watershed – diorite	0.866	1.021	Lower saprolite	Chabaux et al. (2013)
Puerto Rico – Rio Icacos watershed – diorite	0.689	1.033	Lower saprolite	Chabaux et al. (2013)
Puerto Rico – Rio Icacos watershed – diorite	0.886	1.021	Lower saprolite	Chabaux et al. (2013)
Puerto Rico – Rio Icacos watershed – diorite	0.808	1.029	Lower saprolite	Chabaux et al. (2013)
Puerto Rico – Rio Icacos watershed – diorite	0.646	1.018	Lower saprolite	Chabaux et al. (2013)

Sample or Location	U (conc.)[1]	($^{234}U/^{238}U$)	Type	Source
Puerto Rico – Rio Icacos watershed – diorite	0.707	1.029	Lower saprolite	Chabaux et al. (2013)
Puerto Rico – Rio Icacos watershed – diorite	0.641	1.03	Lower saprolite	Chabaux et al. (2013)
Puerto Rico – Rio Icacos watershed – diorite	0.51	1.045	Upper saprolite	Chabaux et al. (2013)
Puerto Rico – Rio Icacos watershed – diorite	0.51	1.049	Upper saprolite	Chabaux et al. (2013)
Puerto Rico – Rio Icacos watershed – diorite	0.602	1.042	Upper saprolite	Chabaux et al. (2013)
Puerto Rico – Rio Icacos watershed – diorite	0.578	1.026	Upper saprolite	Chabaux et al. (2013)
Puerto Rico – Rio Icacos watershed – diorite	0.607	1.022	Soil	Chabaux et al. (2013)
Burkina Faso	6.1	0.963	Laterite	Dequincey et al. (2002)
Burkina Faso	5.3	1.002	Laterite	Dequincey et al. (2002)
Burkina Faso	5.8	1.024	Laterite	Dequincey et al. (2002)
Burkina Faso	4.7	0.99	Laterite	Dequincey et al. (2002)
Burkina Faso	3.6	0.973	Laterite	Dequincey et al. (2002)
Burkina Faso	2.1	1.047	Laterite	Dequincey et al. (2002)
Burkina Faso	1.7	1.042	Laterite	Dequincey et al. (2002)
Burkina Faso	1.7	1.029	Laterite	Dequincey et al. (2002)
Burkina Faso	1.3	1.014	Laterite	Dequincey et al. (2002)

Sample or Location	U (conc.)[1]	($^{234}U/^{238}U$)	Type	Source
Burkina Faso	1.5	1.025	Laterite	Dequincey et al. (2002)
Burkina Faso	1.1	1.053	Laterite	Dequincey et al. (2002)
Burkina Faso	1.1	1.058	Laterite	Dequincey et al. (2002)
Burkina Faso	1.9	1.022	Laterite	Dequincey et al. (2002)
Burkina Faso	1.3	1.025	Laterite	Dequincey et al. (2002)
Burkina Faso	0.9	1.022	Laterite	Dequincey et al. (2002)
Burkina Faso	1.3	0.99	Laterite	Dequincey et al. (2002)
SE Australia – Nunnock River catchment	1.99	0.942	Soil	Dosseto et al. (2008b)
SE Australia – Nunnock River catchment	2.00	0.944	Soil	Dosseto et al. (2008b)
SE Australia – Nunnock River catchment	1.97	0.969	Soil	Dosseto et al. (2008b)
SE Australia – Nunnock River catchment	1.62	0.935	Soil	Dosseto et al. (2008b)
SE Australia – Nunnock River catchment	1.71	0.975	Soil	Dosseto et al. (2008b)
SE Australia – Nunnock River catchment	1.59	0.969	Soil	Dosseto et al. (2008b)
SE Australia – Nunnock River catchment	1.84	0.968	Soil	Dosseto et al. (2008b)
SE Australia – Nunnock River catchment	2.05	0.971	Soil	Dosseto et al. (2008b)

Sample or Location	U (conc.)[1]	($^{234}U/^{238}U$)	Type	Source
SE Australia – Nunnock River catchment	1.64	0.954	Soil	Dosseto et al. (2008b)
SE Australia – Nunnock River catchment	2.34	0.98	Soil	Dosseto et al. (2008b)
SE Australia – Nunnock River catchment	2.04	1.005	Soil	Dosseto et al. (2008b)
SE Australia – Nunnock River catchment	2.25	0.991	Soil	Dosseto et al. (2008b)
SE Australia – Nunnock River catchment	2.13	0.982	Soil	Dosseto et al. (2008b)
SE Australia – Nunnock River catchment	2.51	0.967	Soil	Dosseto et al. (2008b)
SE Australia – Nunnock River catchment	2.19	1.027	Saprolite	Dosseto et al. (2008b)
SE Australia – Nunnock River catchment	2.98	1.083	Saprolite	Dosseto et al. (2008b)
SE Australia – Nunnock River catchment	3.35	0.968	Saprolite	Dosseto et al. (2008b)
SE Australia – Nunnock River catchment	3.35	0.968	Saprolite	Dosseto et al. (2008b)
Puerto Rico – volcaniclastic bedrock	1.18	1.17	Regolith	Dosseto et al. (2012)
Puerto Rico – volcaniclastic bedrock	1.37	1.8	Regolith	Dosseto et al. (2012)
Puerto Rico – volcaniclastic bedrock	1.89	1.14	Regolith	Dosseto et al. (2012)

Sample or Location	U (conc.)[1]	($^{234}U/^{238}U$)	Type	Source
Puerto Rico – volcaniclastic bedrock	2.03	1.02	Regolith	Dosseto et al. (2012)
Puerto Rico – volcaniclastic bedrock	0.55	1.1	Regolith	Dosseto et al. (2012)
Puerto Rico – volcaniclastic bedrock	0.51	1.1	Regolith	Dosseto et al. (2012)
Puerto Rico – volcaniclastic bedrock	0.80	1.07	Regolith	Dosseto et al. (2012)
Puerto Rico – volcaniclastic bedrock	1.26	1.05	Regolith	Dosseto et al. (2012)
Puerto Rico – volcaniclastic bedrock	2.07	1.05	Regolith	Dosseto et al. (2012)
Puerto Rico – volcaniclastic bedrock	1.43	1.07	Regolith	Dosseto et al. (2012)
Puerto Rico – volcaniclastic bedrock	1.80	1.06	Regolith	Dosseto et al. (2012)
French Guadeloupe – Deshaies watershed – andesitic bedrock	1.75	1.003	Weathering rind	Engel et al. (2016)
French Guadeloupe – Deshaies watershed – andesitic bedrock	1.96	1.008	Weathering rind	Engel et al. (2016)
French Guadeloupe – Deshaies watershed – andesitic bedrock	2.05	1.014	Weathering rind	Engel et al. (2016)
French Guadeloupe – Deshaies watershed – andesitic bedrock	2.22	0.996	Weathering rind	Engel et al. (2016)
French Guadeloupe – Deshaies	2.14	1.002	Weathering rind	Engel et al. (2016)

Sample or Location	U (conc.)[1]	($^{234}U/^{238}U$)	Type	Source
watershed – andesitic bedrock				
French Guadeloupe – Deshaies watershed – andesitic bedrock	1.98	0.991	Weathering rind	Engel et al. (2016)
French Guadeloupe – Deshaies watershed – andesitic bedrock	1.87	0.991	Weathering rind	Engel et al. (2016)
French Guadeloupe – Deshaies watershed – andesitic bedrock	1.88	0.992	Weathering rind	Engel et al. (2016)
French Guadeloupe – Deshaies watershed – andesitic bedrock	2.44	1.013	Weathering rind	Engel et al. (2016)
French Guadeloupe – Deshaies watershed – andesitic bedrock	2.06	0.989	Weathering rind	Engel et al. (2016)
French Guadeloupe – Deshaies watershed – andesitic bedrock	2.2	0.989	Weathering rind	Engel et al. (2016)
French Guadeloupe – Deshaies watershed – andesitic bedrock	2.5	0.998	Weathering rind	Engel et al. (2016)
French Guadeloupe – Deshaies watershed – andesitic bedrock	1.6	0.991	Weathering rind	Engel et al. (2016)
French Guadeloupe – Deshaies watershed – andesitic bedrock	1.88	0.987	Weathering rind	Engel et al. (2016)
French Guadeloupe – Deshaies watershed – andesitic bedrock	1.71	0.986	Weathering rind	Engel et al. (2016)
French Guadeloupe – Deshaies	1.47	0.983	Weathering rind	Engel et al. (2016)

Sample or Location	U (conc.)[1]	($^{234}U/^{238}U$)	Type	Source
watershed – andesitic bedrock				
French Guadeloupe – Deshaies watershed – andesitic bedrock	1.65	0.989	Weathering rind	Engel et al. (2016)
French Guadeloupe – Deshaies watershed – andesitic bedrock	1.65	0.984	Weathering rind	Engel et al. (2016)
French Guadeloupe – Deshaies watershed – andesitic bedrock	1.91	0.99	Weathering rind	Engel et al. (2016)
French Guadeloupe – Deshaies watershed – andesitic bedrock	2.11	0.986	Weathering rind	Engel et al. (2016)
French Guadeloupe – Deshaies watershed – andesitic bedrock	1.92	0.982	Weathering rind	Engel et al. (2016)
USA – Sierra Nevada –batholith	2.31	0.99	Residual soil	Hansen and Stout (1968)
USA – Sierra Nevada –batholith	1.07	1.04	Residual soil	Hansen and Stout (1968)
USA – Sierra Nevada –batholith	0.99	1.00	Residual soil	Hansen and Stout (1968)
USA – Sierra Nevada –batholith	0.82	1.09	Residual soil	Hansen and Stout (1968)
USA – Sierra Nevada –batholith	0.69	1.00	Residual soil	Hansen and Stout (1968)
USA – Sierra Nevada –batholith	0.62	0.98	Residual soil	Hansen and Stout (1968)
USA – Sierra Nevada –batholith	3.0	1.00	Residual soil	Hansen and Stout (1968)
USA – Sierra Nevada –batholith	3.0	1.00	Residual soil	Hansen and Stout (1968)
USA – Sierra Nevada –batholith	3.1	1.00	Residual soil	Hansen and Stout (1968)

Sample or Location	U (conc.)[1]	($^{234}U/^{238}U$)	Type	Source
USA – Sierra Nevada –batholith	2.4	1.00	Residual soil	Hansen and Stout (1968)
USA – Sierra Nevada –batholith	1.5	1.00	Residual soil	Hansen and Stout (1968)
USA – Sierra Nevada –batholith	3.9	1.05	Residual soil	Hansen and Stout (1968)
USA – Sierra Nevada –batholith	4.6	1.00	Residual soil	Hansen and Stout (1968)
USA– New Mexico – Rhyolitic volcaniclastics and tuff	2.2	0.97	O-horizon	Huckle et al. (2016)
USA – New Mexico – Rhyolitic volcaniclastics and tuff	2.6	0.96	A-horizon	Huckle et al. (2016)
USA – New Mexico – Rhyolitic volcaniclastics and tuff	2.3	0.95	B1-horizon	Huckle et al. (2016)
USA – New Mexico – Rhyolitic volcaniclastics and tuff	2.4	0.91	B2-horizon	Huckle et al. (2016)
USA – New Mexico – Rhyolitic volcaniclastics and tuff	2.4	0.92	B3-horizon	Huckle et al. (2016)
USA – New Mexico – Rhyolitic volcaniclastics and tuff	4.9	1.56	O-horizon	Huckle et al. (2016)
USA – New Mexico – Rhyolitic volcaniclastics and tuff	7.8	1.49	A-horizon	Huckle et al. (2016)
USA – New Mexico – Rhyolitic volcaniclastics and tuff	9.5	1.53	AB-horizon	Huckle et al. (2016)
USA – New Mexico – Rhyolitic	7.5	1.48	B1-horizon	Huckle et al. (2016)

Sample or Location	U (conc.)[1]	($^{234}U/^{238}U$)	Type	Source
volcaniclastics and tuff				
USA – New Mexico – Rhyolitic volcaniclastics and tuff	3.48	1.00	B2-horizon	Huckle et al. (2016)
USA – New Mexico – Rhyolitic volcaniclastics and tuff	3.42	0.95	B3-horizon	Huckle et al. (2016)
USA – New Mexico – Rhyolitic volcaniclastics and tuff	3.05	1.00	O-horizon	Huckle et al. (2016)
USA – New Mexico – Rhyolitic volcaniclastics and tuff	3.72	0.97	A-horizon	Huckle et al. (2016)
USA – New Mexico –Rhyolitic volcaniclastics and tuff	3.67	0.97	AB-horizon	Huckle et al. (2016)
USA – New Mexico – Rhyolitic volcaniclastics and tuff	4.13	0.97	B-horizon	Huckle et al. (2016)
USA – New Mexico – Rhyolitic volcaniclastics and tuff	3.86	0.92	BC-horizon	Huckle et al. (2016)
USA – New Mexico –Rhyolitic volcaniclastics and tuff	2.09	0.97	O-horizon	Huckle et al. (2016)
USA – New Mexico – Rhyolitic volcaniclastics and tuff	2.6	0.98	A-horizon	Huckle et al. (2016)
USA – New Mexico – Rhyolitic volcaniclastics and tuff	2.34	0.96	B1-horizon	Huckle et al. (2016)
USA – New Mexico –Rhyolitic	2.26	0.90	B2-horizon	Huckle et al. (2016)

Sample or Location	U (conc.)[1]	($^{234}U/^{238}U$)	Type	Source
volcaniclastics and tuff				
USA – New Mexico – Rhyolitic volcaniclastics and tuff	2.77	0.95	B3-horizon	Huckle et al. (2016)
USA – California – alluvial terraces – Merced River	2.375	1.017	Soil	Keech et al. (2013)
USA – California – alluvial terraces – Merced River	2.917	1.008	Soil	Keech et al. (2013)
USA – California – alluvial terraces – Merced River	2.856	0.994	Soil	Keech et al. (2013)
USA – California – alluvial terraces – Merced River	2.833	1.003	Soil	Keech et al. (2013)
USA – California – alluvial terraces – Merced River	5.81	1.008	Soil	Keech et al. (2013)
USA – California – alluvial terraces – Merced River	2.377	1.016	Soil	Keech et al. (2013)
USA – California – alluvial terraces – Merced River	3.549	1.007	Soil	Keech et al. (2013)
USA – California – alluvial terraces – Merced River	2.169	1.01	Soil	Keech et al. (2013)
USA – California – alluvial terraces – Merced River	2.396	0.994	Soil	Keech et al. (2013)
USA – California – alluvial terraces – Merced River	2.375	0.992	Soil	Keech et al. (2013)
USA – California – alluvial terraces – Merced River	1.523	0.993	Soil	Keech et al. (2013)

Sample or Location	U (conc.)[1]	($^{234}U/^{238}U$)	Type	Source
USA – California – alluvial terraces – Merced River	1.658	0.989	Soil	Keech et al. (2013)
USA – California – alluvial terraces – Merced River	1.619	0.984	Soil	Keech et al. (2013)
USA – California – alluvial terraces – Merced River	1.917	0.978	Soil	Keech et al. (2013)
USA – California – alluvial terraces – Merced River	2.79	0.952	Soil	Keech et al. (2013)
USA – California – alluvial terraces – Merced River	1.988	0.964	Soil	Keech et al. (2013)
USA – California – alluvial terraces – Merced River	2.103	0.95	Soil	Keech et al. (2013)
USA – California – alluvial terraces – Merced River	1.666	0.992	Soil	Keech et al. (2013)
USA – California – alluvial terraces – Merced River	1.573	1.006	Soil	Keech et al. (2013)
USA – California – alluvial terraces – Merced River	5.26	0.985	Soil	Keech et al. (2013)
USA – California – alluvial terraces – Merced River	3.196	1.009	Soil	Keech et al. (2013)
USA – California – alluvial terraces – Merced River	2.837	0.976	Soil	Keech et al. (2013)
USA – California – alluvial terraces – Merced River	3.2	0.997	Soil	Keech et al. (2013)
USA – California – alluvial terraces – Merced River	4.24	0.972	Soil	Keech et al. (2013)

Sample or Location	U (conc.)[1]	($^{234}U/^{238}U$)	Type	Source
USA – Shale Hills catchment	2.728	0.936	Regolith	Ma et al. (2010)
USA – Shale Hills catchment	2.78	0.943	Regolith	Ma et al. (2010)
USA – Shale Hills catchment	2.777	0.951	Regolith	Ma et al. (2010)
USA – Shale Hills catchment	2.733	0.934	Regolith	Ma et al. (2010)
USA – Shale Hills catchment	2.768	0.942	Regolith	Ma et al. (2010)
USA – Shale Hills catchment	2.8	0.958	Regolith	Ma et al. (2010)
USA – Shale Hills catchment	2.844	0.972	Regolith	Ma et al. (2010)
USA – Shale Hills catchment	3.046	0.957	Regolith	Ma et al. (2010)
USA – Shale Hills catchment	2.958	0.968	Regolith	Ma et al. (2010)
USA – Shale Hills catchment	2.644	0.973	Regolith	Ma et al. (2010)
USA – Shale Hills catchment	2.799	0.966	Regolith	Ma et al. (2010)
USA – Shale Hills catchment	2.746	0.996	Regolith	Ma et al. (2010)
USA – Shale Hills catchment	3.022	1.019	Regolith	Ma et al. (2010)
USA – Shale Hills catchment	3.106	1.061	Regolith	Ma et al. (2010)
USA – Shale Hills catchment	3.209	1.072	Regolith	Ma et al. (2010)
USA – Shale Hills catchment	3.152	1.058	Regolith	Ma et al. (2010)
USA – Shale Hills catchment	3.134	0.995	Bedrock	Ma et al. (2010)
USA – Shale Hills catchment	3.026	0.997	Bedrock	Ma et al. (2010)

Sample or Location	U (conc.)[1]	($^{234}U/^{238}U$)	Type	Source
Guadaloupe – andesite	0.332	0.999	Drilled core	Ma et al. (2012)
Guadaloupe – andesite	0.33	1.009	Drilled core	Ma et al. (2012)
Guadaloupe – andesite	0.338	1.003	Drilled core	Ma et al. (2012)
Guadaloupe – andesite	0.336	0.997	Core powders	Ma et al. (2012)
Guadaloupe – andesite	0.326	1.003	Core powders	Ma et al. (2012)
Guadaloupe – andesite	0.327	1.002	Core powders	Ma et al. (2012)
Guadaloupe – andesite	0.737	1.031	Drilled rind	Ma et al. (2012)
Guadaloupe – andesite	0.741	1.012	Drilled rind	Ma et al. (2012)
Guadaloupe – andesite	0.907	1.011	Drilled rind	Ma et al. (2012)
Guadaloupe – andesite	1.211	1.016	Drilled rind	Ma et al. (2012)
Guadaloupe – andesite	0.878	1.009	Drilled rind	Ma et al. (2012)
Guadaloupe – andesite	0.936	1.003	Drilled rind	Ma et al. (2012)
Guadaloupe – andesite	1.122	1.009	Drilled rind	Ma et al. (2012)
Guadaloupe – andesite	1.225	1.001	Drilled rind	Ma et al. (2012)
Guadaloupe – andesite	1.284	1.015	Drilled rind	Ma et al. (2012)
USA – Shale-Hill	2.548	0.93	Regolith	Ma et al. (2013)
USA – Shale-Hill	2.96	0.94	Regolith	Ma et al. (2013)
USA – Shale-Hill	2.844	0.98	Regolith	Ma et al. (2013)
USA – Shale-Hill	3.034	0.96	Regolith	Ma et al. (2013)
USA – Shale-Hill	3.005	0.97	Regolith	Ma et al. (2013)
USA – Shale-Hill	2.566	0.94	Regolith	Ma et al. (2013)

Sample or Location	U (conc.)[1]	($^{234}U/^{238}U$)	Type	Source
USA – Shale-Hill	2.796	0.94	Regolith	Ma et al. (2013)
USA – Shale-Hill	2.944	0.95	Regolith	Ma et al. (2013)
USA – Shale-Hill	2.996	0.96	Regolith	Ma et al. (2013)
USA – Shale-Hill	2.99	0.96	Regolith	Ma et al. (2013)
USA – Shale-Hill	2.816	0.97	Regolith	Ma et al. (2013)
USA – Shale-Hill	2.71	0.95	Regolith	Ma et al. (2013)
USA – Shale-Hill	2.881	0.95	Regolith	Ma et al. (2013)
USA – Shale-Hill	2.932	0.95	Regolith	Ma et al. (2013)
USA – Shale-Hill	2.9	0.96	Regolith	Ma et al. (2013)
USA – Shale-Hill	2.936	0.96	Regolith	Ma et al. (2013)
Brasil – Amazonia – Pitinga river basin – granite	9.6	0.87	Clay rich topsoil	Mathieu et al. (1995)
Brasil – Amazonia – Pitinga river basin – granite	9.9	0.89	Clay rich topsoil	Mathieu et al. (1995)
Brasil – Amazonia – Pitinga river basin – granite	9.3	0.96	Saprolite	Mathieu et al. (1995)
Brasil – Amazonia – Pitinga river basin – granite	7.3	1.07	Saprolite	Mathieu et al. (1995)
Brasil – Amazonia – Pitinga river basin – granite	9.4	1.02	Saprolite	Mathieu et al. (1995)
Brasil – Amazonia – Pitinga river basin – granite	13	0.97	Saprolite	Mathieu et al. (1995)
Brasil – Amazonia – Pitinga river basin – granite	7.5	0.88	Saprolite	Mathieu et al. (1995)
Brasil – Amazonia – Pitinga river basin – granite	9.2	0.83	Saprolite	Mathieu et al. (1995)
Brasil – Amazonia – Pitinga river basin – granite	7.6	0.84	Saprolite	Mathieu et al. (1995)

Sample or Location	U (conc.)[1]	($^{234}U/^{238}U$)	Type	Source
Brasil – Amazonia – Pitinga river basin – granite	6.8	0.91	Saprolite	Mathieu et al. (1995)
Brasil – Amazonia – Pitinga river basin – granite	11.4	0.98	Completely kaolinised vein	Mathieu et al. (1995)
Brasil – Amazonia – Pitinga river basin – granite	53.4	0.54	Completely kaolinised vein	Mathieu et al. (1995)
Brasil – Amazonia – Pitinga river basin – granite	13	1.05	Saprolite	Mathieu et al. (1995)
Brasil – Amazonia – Pitinga river basin – granite	10.3	0.93	Saprolite	Mathieu et al. (1995)
Brasil – Amazonia – Pitinga river basin – granite	9.4	0.81	Saprolite	Mathieu et al. (1995)
Brasil – Amazonia – Pitinga river basin – granite	6.2	0.93	Completely kaolinised vein	Mathieu et al. (1995)
Brasil – Amazonia – Pitinga river basin – granite	n.d.	0.87	Saprolite	Mathieu et al. (1995)
Brasil – Amazonia – Pitinga river basin – granite	4.1	0.89	Ferruginous nodules	Mathieu et al. (1995)
Brasil – Amazonia – Pitinga river basin – granite	9.2	0.83	Ferruginous nodules	Mathieu et al. (1995)
Australia – New South Wales – basalt	1.009	0.997	Regolith	Menozzi et al. (2016)
Australia – New South Wales – basalt	1.245	0.998	Regolith	Menozzi et al. (2016)
Australia – New South Wales – basalt	1.903	1.004	Regolith	Menozzi et al. (2016)

Sample or Location	U (conc.)[1]	($^{234}U/^{238}U$)	Type	Source
Australia – New South Wales – basalt	1.901	1.009	Regolith	Menozzi et al. (2016)
Australia – New South Wales – basalt	2.123	1.02	Regolith	Menozzi et al. (2016)
Luxembourg – Ardennes Massif	0.33	0.933	Regolith	Moragues-Quiroga et al. (2017)
Luxembourg – Ardennes Massif	3.14	0.961	Regolith	Moragues-Quiroga et al. (2017)
Luxembourg – Ardennes Massif	3.09	0.949	Regolith	Moragues-Quiroga et al. (2017)
Luxembourg – Ardennes Massif	3.82	1.053	Regolith	Moragues-Quiroga et al. (2017)
Luxembourg – Ardennes Massif	5.22	1.038	Regolith	Moragues-Quiroga et al. (2017)
Luxembourg – Ardennes Massif	5.84	0.953	Regolith	Moragues-Quiroga et al. (2017)
Luxembourg – Ardennes Massif	3.83	0.947	Regolith	Moragues-Quiroga et al. (2017)
Brasil – River Preto basin – granulite	2.89	0.93	Ferralitic Soil profile	Moreira-Nordemann (1980)
Brasil – River Preto basin – granulite	1.07	0.93	Ferralitic Soil profile	Moreira-Nordemann (1980)
Brasil – River Preto basin – granulite	1.21	0.96	Ferralitic Soil profile	Moreira-Nordemann (1980)
Brasil – River Preto basin – granulite	1.75	0.95	Ferralitic Soil profile	Moreira-Nordemann (1980)
Brasil – River Preto basin – granulite	1.6	0.94	Ferralitic Soil profile	Moreira-Nordemann (1980)
Costa Rica – alluvial terrace – basaltic clast	0.23	1.008	Weathering rind	Pelt et al. (2008)
Costa Rica – alluvial terrace – basaltic clast	0.27	1.002	Weathering rind	Pelt et al. (2008)

Sample or Location	U (conc.)[1]	($^{234}U/^{238}U$)	Type	Source
Costa Rica – alluvial terrace – basaltic clast	0.25	1.014	Weathering rind	Pelt et al. (2008)
Costa Rica – alluvial terrace – basaltic clast	0.23	1.002	Weathering rind	Pelt et al. (2008)
Costa Rica – alluvial terrace – basaltic clast	0.4	1.013	Weathering rind	Pelt et al. (2008)
Costa Rica – alluvial terrace – basaltic clast	0.6	1.026	Weathering rind	Pelt et al. (2008)
Costa Rica – alluvial terrace – basaltic clast	0.58	1.032	Weathering rind	Pelt et al. (2008)
Costa Rica – alluvial terrace – basaltic clast	0.58	1.044	Weathering rind	Pelt et al. (2008)
Costa Rica – alluvial terrace – basaltic clast	0.71	1.04	Weathering rind	Pelt et al. (2008)
Costa Rica – alluvial terrace – basaltic clast	n.d.	1.003	Weathering rind	Pelt et al. (2008)
Costa Rica – alluvial terrace – basaltic clast	0.191	1.015	Weathering rind	Pelt et al. (2008)
Costa Rica – alluvial terrace – basaltic clast	0.23	1.008	Weathering rind	Pelt et al. (2008)
Costa Rica – alluvial terrace – basaltic clast	0.271	1.004	Weathering rind	Pelt et al. (2008)
Costa Rica – alluvial terrace – basaltic clast	0.594	1.017	Weathering rind	Pelt et al. (2008)
Costa Rica – alluvial terrace – basaltic clast	0.722	1.035	Weathering rind	Pelt et al. (2008)
Costa Rica – alluvial terrace – basaltic clast	0.674	1.045	Weathering rind	Pelt et al. (2008)

Sample or Location	U (conc.)[1]	($^{234}U/^{238}U$)	Type	Source
Costa Rica – alluvial terrace – basaltic clast	0.669	1.055	Weathering rind	Pelt et al. (2008)
Costa Rica – alluvial terrace – basaltic clast	0.717	1.062	Weathering rind	Pelt et al. (2008)
Mount Cameroon volcano – Pyroclastic deposits	0.97	1.012	Soil profile	Pelt et al. (2013)
Mount Cameroon volcano – Pyroclastic deposits	0.9	1.004	Soil profile	Pelt et al. (2013)
Mount Cameroon volcano – Pyroclastic deposits	1.54	1.008	Soil profile	Pelt et al. (2013)
Mount Cameroon volcano – Pyroclastic deposits	1.48	1.00	Soil profile	Pelt et al. (2013)
Mount Cameroon volcano – Pyroclastic deposits	2.09	1.016	Soil profile	Pelt et al. (2013)
Mount Cameroon volcano – Pyroclastic deposits	2.06	1.002	Soil profile	Pelt et al. (2013)
Mount Cameroon volcano – Pyroclastic deposits	1.64	1.027	Soil profile	Pelt et al. (2013)
Mount Cameroon volcano – Pyroclastic deposits	0.99	1.005	Soil profile	Pelt et al. (2013)
Mount Cameroon volcano – Pyroclastic deposits	1.67	1.011	Soil profile	Pelt et al. (2013)
UK – River Witham	0.87	1.025	Regolith	Plater et al. (1988)
UK – River Witham	0.48	0.98	Regolith	Plater et al. (1988)
UK – River Witham	1.04	1.01	Regolith	Plater et al. (1988)
UK – River Witham	0.72	1.09	Regolith	Plater et al. (1988)

Sample or Location	U (conc.)[1]	($^{234}U/^{238}U$)	Type	Source
UK – River Witham	1.03	0.99	Regolith	Plater et al. (1988)
UK – River Witham	0.92	0.94	Regolith	Plater et al. (1988)
France – Mercantour Massif	n.d.	0.96	Soil	Rezzoug et al. (2009)
France – Mercantour Massif	n.d.	0.96	Soil	Rezzoug et al. (2009)
France – Mercantour Massif	n.d.	0.96	Soil	Rezzoug et al. (2009)
France – Mercantour Massif	n.d.	0.96	Soil	Rezzoug et al. (2009)
France – Mercantour Massif	n.d.	0.96	Soil	Rezzoug et al. (2009)
France – Mercantour Massif	n.d.	0.93	Soil	Rezzoug et al. (2009)
France – Mercantour Massif	n.d.	0.97	Soil	Rezzoug et al. (2009)
USA – Minnesota – loess	3.17	0.947	A-horizon	Rosholt et al. (1966)
USA – Minnesota – loess	3.22	0.922	B-horizon	Rosholt et al. (1966)
USA – Minnesota – loess	3.27	0.908	B-horizon	Rosholt et al. (1966)
USA – Minnesota – loess	3.07	0.891	B-horizon	Rosholt et al. (1966)
USA – Minnesota – loess	3.03	0.928	C-horizon	Rosholt et al. (1966)
USA – Minnesota – loess	2.57	0.926	C-horizon	Rosholt et al. (1966)
USA – Minnesota – loess	2.33	0.937	A-horizon	Rosholt et al. (1966)
USA – Minnesota – loess	2.66	0.903	B-horizon	Rosholt et al. (1966)
USA – Minnesota – loess	2.49	0.909	B-horizon	Rosholt et al. (1966)
USA – Minnesota – loess	2.37	0.902	B-horizon	Rosholt et al. (1966)

Sample or Location	U (conc.)[1]	($^{234}U/^{238}U$)	Type	Source
USA – Minnesota – loess	2.21	0.906	C-horizon	Rosholt et al. (1966)
USA – Minnesota – loess	2.2	0.915	C-horizon	Rosholt et al. (1966)
USA – Minnesota – loess	2.04	0.909	C-horizon	Rosholt et al. (1966)
USA – Minnesota – till	3.24	0.993	A-horizon	Rosholt et al. (1966)
USA – Minnesota – till	3.45	0.977	B-horizon	Rosholt et al. (1966)
USA – Minnesota – till	2.18	0.869	B-horizon	Rosholt et al. (1966)
USA – Minnesota – till	1.92	0.867	C-horizon	Rosholt et al. (1966)
USA – Minnesota – till	2.06	0.880	C-horizon	Rosholt et al. (1966)
USA – Utah – Cretaceous shale	6.00	1.20	A-horizon	Rosholt et al. (1966)
USA – Utah – Cretaceous shale	5.76	0.949	B-horizon	Rosholt et al. (1966)
USA – Utah – Cretaceous shale	6.34	0.916	C-horizon	Rosholt et al. (1966)
USA – Utah – till	3.12	1.06	A-horizon	Rosholt et al. (1966)
USA – Utah – till	2.87	1.00	B-horizon	Rosholt et al. (1966)
USA – Utah – till	3.46	0.980	A-horizon	Rosholt et al. (1966)
USA – Utah – till	3.18	0.946	B-horizon	Rosholt et al. (1966)
USA – Arizona – trachyte	3.02	0.739	A-horizon	Rosholt et al. (1966)
USA – Arizona – trachyte	2.7	0.769	B-horizon	Rosholt et al. (1966)
USA – Arizona – trachyte	4.18	0.584	C-horizon	Rosholt et al. (1966)
USA – Mississippi – sand	1.88	0.962	A-horizon	Rosholt et al. (1966)
USA – Mississippi – sand	2.09	0.954	B-horizon	Rosholt et al. (1966)
USA – Mississippi – sand	1.99	0.938	B-horizon	Rosholt et al. (1966)

Sample or Location	**U (conc.)[1]**	**($^{234}U/^{238}U$)**	**Type**	**Source**
USA – Mississippi – sand	0.78	0.960	C-horizon	Rosholt et al. (1966)
USA – Wyoming – alluvium	5.06	0.938	A-horizon	Rosholt et al. (1966)
USA – Wyoming – alluvium	188	0.946	A-horizon	Rosholt et al. (1966)
Australia – Frogs Hollow	4.27	0.958	Soil	Suresh et al. (2013)
Australia – Frogs Hollow	5.14	0.981	Soil	Suresh et al. (2013)
Australia – Frogs Hollow	5.73	0.987	Soil	Suresh et al. (2013)
Australia – Frogs Hollow	6.53	0.997	Soil	Suresh et al. (2013)
Australia – Frogs Hollow	8.66	1.016	Soil	Suresh et al. (2013)
Australia – Frogs Hollow	7.00	0.936	Soil	Suresh et al. (2013)
Australia – Frogs Hollow	6.86	0.965	Soil	Suresh et al. (2013)
Australia – Frogs Hollow	7.87	0.978	Soil	Suresh et al. (2013)
Australia – Frogs Hollow	9.42	0.999	Soil	Suresh et al. (2013)
Australia – Frogs Hollow	11.4	1.006	Soil	Suresh et al. (2013)
Average of all soil samples	**3.418**	**0.992**		
Median of all soil samples	**2.127**	**0.995**		

(1) Note that the U concentrations in river samples are tabulated in ppb and the concentrations in the suspended load of rivers and soil samples in ppm; (2) and references therein; (3) not shown in Figure 1c. n.d. = not determined.

Supplemental Table 2. Calculation of CZ thickness required to balance the excess of ^{234}U in seawater.

LAND SURFACE		
	Land surface of the Earth (km^2)	1.49E+08
	Land surface of the Earth (cm^2)	1.49E+18
	Continental crust density (g/cm^3) in (upper crust)	2.5
	Mass of rock per **metre depth** over surface of Earth (grammes)	3.72E+20
	Uranium content of unweathered rock (ppm)*	2.60E+00
	Mass of ^{238}U AVAILABLE in weathered material (grammes)	9.68E+14
	Mass of ^{234}U AVAILABLE in weathered material (grammes)	5.31E+10
	Activity ratio of residual weathered upper crust (this is an input variable)	0.76
	Mass of ^{234}U removed to ocean by weathering (grammes)	**1.28E+10**
	Metres of rock (vertical) affected by weathering to balance excess ^{234}U in oceans	***2.94***
OCEAN WATER		
	Volume of ocean water km^3	1.36E+09
	Volume of ocean water cm^3	1.36E+24
	Density of ocean water	1.024
	Mass of ocean water in g	1.39264E+24
	Concentration of uranium in seawater mg/m^3	3.3
	Concentration of uranium in seawater mg/ml	0.0000033
	Concentration of uranium in seawater mg/g	3.3792E-06
	Concentration of uranium in seawater (ppm)	0.0033792
	Total amount of U in seawater (grammes)	4.70601E+15
	Total amount of ^{234}U in seawater at equilibrium (grammes)	2.58E+11
	Total amount of ^{234}U in seawater at equilibrium (grammes)	2.96E+11
	Excess ^{234}U in seawater (grammes)	**3.74E+10**

*Taylor, S.R., McLennan, S.M. (1995) The geochemical evolution of the continental crust. Reviews of Geophysics 33, 241-265.

Supplemental Table 3. Major (wt.%) and trace (ppb) element concentrations, elemental ratios, relative % loss R of U/Nb and U series activity ratios.

Sample name	ChQA1	ChQA2	ChQA3	ChQA4	ChQA5	ChQA6	ChQA7	ChQA8	ChQA9	ChQA10	ChQA11	ChQA12	ChQB1	ChQB2	ChQB3	ChQB4	ChQB5	ChQB6	ChQB7	ChQB8	ChQB9a	ChQB9b	ChQB9c	ChQB9d	ChQB10	ChQB11	ChQB12
Al_2O_3	13.19	12.46	12.5	12.28	12.66	12.87	13.08	12.86	13.23	11.53	11.72	12.44	15.16	15.85	14.99	15.14	14.48	13.39	13.7	12.98	13.22	13.11	13.03	13.69	14.92	15.17	12.93
Fe_2O_3	17.18	18.21	18.39	17.59	17.65	16.97	16.5	17.04	16.59	16.57	15.91	16.23	16.4	16.74	17.97	17.14	16.82	15.4	15.73	15.6	17.2	15.42	15.23	13.36	18.16	19.92	15.07
MgO	2.3	2.45	2.43	2.69	2.68	2.72	2.94	2.94	3.01	3.34	3.3	3.43	2.61	2.74	2.28	2.14	2.97	4.71	4.75	4.92	3.88	4.87	5.09	5.03	3.95	3.62	5.46
CaO	2.62	2.47	2.2	2.23	1.91	1.97	2.05	1.9	1.88	1.53	1.39	1.4	1.97	1.92	2.92	3.29	5.39	9.06	8.43	9.48	6.88	9.38	9.9	10.16	5.43	5.57	10.55
Na_2O	0.55	0.43	0.26	0.22	0.02	<0.01	<0.01	<0.01	<0.01	<0.01	<0.01	<0.01	0.3	0.26	0.84	1.04	1.59	2.11	1.81	2.26	1.57	2.25	2.33	2.49	0.68	0.91	2.43
K_2O	0.27	0.36	0.41	0.43	0.58	0.42	0.25	0.32	0.33	1.79	1.82	1.69	0.64	0.48	0.31	0.29	0.26	0.31	0.18	0.22	0.19	0.22	0.23	0.23	0.12	0.29	0.28
Th	2752	2878	2911	2879	2894	2858	2752	2846	2910	2625	2604	2406	1824	1964	1817	1837	1727	1573	1470	1619	1557	1507	1494	1549	1930	2642	1485
U	565	595	568	479	482	499	570	566	481	357	361	401	478	489	419	460	413	443	338	392	400	411	380	640	340	527	406
Th*(ppm)	2.70		2.75		2.72				2.66		0.97	2.40	1.73				1.64		1.42				1.43				
±	0.00		0.00		0.00				0.02		0.00	0.00	0.00				0.00		0.00				0.001				
U*(ppm)	0.56		0.54		0.46				0.45		0.35	0.40	0.46				0.40		0.33				0.37				
±	0.00		0.00		0.00				0.00		0.00	0.00	0.00				0.00		0.00				0.000				
% in $R_{U/Nb}$	-9.69	-9.79	-15.26	-28.11	-27.01	-21.23	-8.3	-12.45	-27.19	-36.99	-32.65	-18.15	-0.84	-2.94	-12.74	-5.63	-10.56	4.35	-13.91	-10.07	-4.97	1.14	-6.38	53.07	-32.85	-9.06	-
MIA(O)	64	63	63	68	69	68	69	70	68	70	68	68	57	56	50	41	40	39	41	38	44	42	56	67	56	57	38
CIA	71	72	74	74	78	78	79	79	80	72	73	74	78	79	70	67	54	40	43	39	47	39	38	38	58	57	36
Mg/Ti	0.78	0.81	0.79	0.89	0.87	0.94	1.02	1.02	1.00	1.33	1.37	1.52	1.02	1.01	0.89	0.81	1.17	2.04	2.14	2.11	1.68	2.12	2.29	2.14	1.43	1.10	2.46
Th/U	4.88	4.84	5.13	6.01	6.01	5.73	4.83	5.03	6.06	7.35	7.21	6.00	3.81	4.02	4.34	3.99	4.18	3.55	4.35	4.13	3.89	3.66	3.93	2.42	5.68	5.01	3.66
$(^{234}U/^{238}U)$	0.500	0.512	0.545	0.582	0.692	0.681	0.704	0.766	0.790	0.856	0.896	0.914	0.821	0.782	0.765	0.740	0.780	0.890	0.852	0.813	0.793	0.782	0.856	1.160	0.776	0.913	0.972
±	0.009	0.018	0.007	0.015	0.010	0.008	0.017	0.006	0.025	0.023	0.023	0.028	0.015	0.020	0.007	0.014	0.021	0.028	0.023	0.012	0.028	0.029	0.011	0.010	0.010	0.020	0.015
	0.4999		**0.5193**		**0.6736**				**0.7853**		**0.8906**	**0.9292**	**0.8444**				**0.7673**		**0.8644**				**0.8876**				
	0.0003		**0.0003**		**0.0003**				**0.0003**		**0.0004**	**0.0004**	**0.0003**				**0.0003**		**0.0004**				**0.0004**				
$(^{230}Th/^{234}U)$	0.927	1.034	1.090	0.972	1.028	1.091	0.965	1.141	1.177	1.144	1.137	1.208	1.112	1.144	1.066	1.111	1.059	1.086	1.099	1.145	1.042	1.093	1.145	1.182	1.207	1.210	0.900
±	0.053	0.027	0.019	0.068	0.065	0.089	0.045	0.063	0.026	0.077	0.047	0.022	0.014	0.034	0.107	0.016	0.077	0.096	0.065	0.031	0.046	0.042	0.042	0.019	0.032	0.038	0.042
	1.047		**1.086**		**1.077**				**1.261**		**n.d.**	**1.207**	**1.097**				**1.065**		**1.060**				**1.088**				
	0.017		**0.016**		**0.017**				**0.070**			**0.021**	**0.009**				**0.014**		**0.012**				**0.003**				
$(^{230}Th/^{238}U)$	0.463	0.530	0.594	0.566	0.711	0.743	0.680	0.874	0.931	0.979	1.018	1.104	0.913	0.894	0.815	0.822	0.825	0.967	0.937	0.931	0.826	0.854	0.980	1.371	0.937	1.105	0.875
±	0.028	0.015	0.011	0.042	0.048	0.065	0.034	0.052	0.022	0.070	0.045	0.021	0.012	0.028	0.087	0.013	0.064	0.091	0.059	0.027	0.039	0.035	0.038	0.024	0.026	0.037	0.043
	0.524		**0.564**		**0.726**				**0.990**		**n.d.**	**1.121**	**0.926**				**0.817**		**0.917**				**0.965**				
	0.009		**0.008**		**0.011**				**0.055**			**0.020**	**0.008**				**0.011**		**0.010**				**0.002**				
$(^{230}Th/^{232}Th)$	0.368	0.373	0.378	0.321	0.383	0.445	0.495	0.527	0.473	0.404	0.459	0.565	0.744	0.706	0.583	0.631	0.602	0.835	0.670	0.691	0.645	0.713	0.782	1.758	0.499	0.677	0.802
±	0.023	0.011	0.008	0.024	0.026	0.039	0.025	0.031	0.012	0.029	0.021	0.012	0.012	0.023	0.062	0.011	0.047	0.079	0.043	0.021	0.031	0.030	0.031	0.034	0.014	0.024	0.041
	0.328		**0.341**		**0.373**				**0.516**		**n.d.**	**0.569**	**0.744**				**0.604**		**0.650**				**0.757**				
	0.005		**0.005**		**0.006**				**0.029**			**0.010**	**0.006**				**0.008**		**0.007**				**0.002**				
$(^{232}Th/^{238}U)$	1.566	1.555	1.646	1.930	1.930	1.841	1.552	1.616	1.945	2.362	2.315	1.928	1.225	1.290	1.394	1.282	1.344	1.140	1.397	1.326	1.249	1.177	1.275	0.777	1.824	1.610	1.175
±	0.022	0.022	0.023	0.027	0.027	0.026	0.022	0.023	0.027	0.033	0.032	0.027	0.017	0.018	0.020	0.018	0.019	0.016	0.020	0.019	0.017	0.016	0.001	0.011	0.026	0.023	0.016
	1.594		**1.656**		**1.944**				**1.917**		**n.d.**	**1.971**					**1.354**		**1.410**				**1.275**				
	0.001		**0.001**		**0.001**				**0.003**			**0.001**					**0.001**		**0.001**				**0.001**				

*MC-ICP-MS measurements. Note that the bold activity ratios represent MC-ICP-MS measurements, whereas all other values were determinded by Q-ICP-MS. Corestone samples ChQB9a, b, d are not shown in figure 2. CHQB9d is also not shown in figure 3. n.d. = not determined due to operator error.

Supplemental Table 4. Trace element (ppb) concentration and isotopic ratios determined for standards.

	TML-1	TML-2	TML-3	TML-4	TML-5	TML-6	Average	stddev	rsd	BCR-2	stdev	rsd
Th	29803	30695	30911	30288	30185	30233	30352	394	1.3	5785	66	1.1
±	94	81	106	61	69	173	97					
rsd	0.316	0.264	0.344	0.201	0.227	0.572	0.32					
U	10624	10915	10921	10695	10887	10710	10792	130	1.2	1698	16	0.9
±	95	79	46	89	106	47	77					
rsd	0.890	0.721	0.425	0.832	0.971	0.438	0.71					
Th/U	2.81	2.81	2.83	2.83	2.77	2.82	2.812	0.022	0.8	3.404	0.025	0.7
(^{234}U/^{238}U)	1.0024	0.9998	1.0085				1.0035	0.0089	0.9			
±	0.0093	0.0054	0.0033									
(^{230}Th/^{234}U)	0.9899	1.0048	0.9873				0.9940	0.0188	1.9			
±	0.003	0.0083	0.0048									
(^{230}Th/^{238}U)	0.9983	1.0106	1.0017				1.0035	0.0127	1.3			
±	0.0038	0.0091	0.0056									
(^{230}Th/^{232}Th)	1.0876	1.0983	1.0816				1.0892	0.0169	1.6			
±	0.0094	0.0130	0.0103									

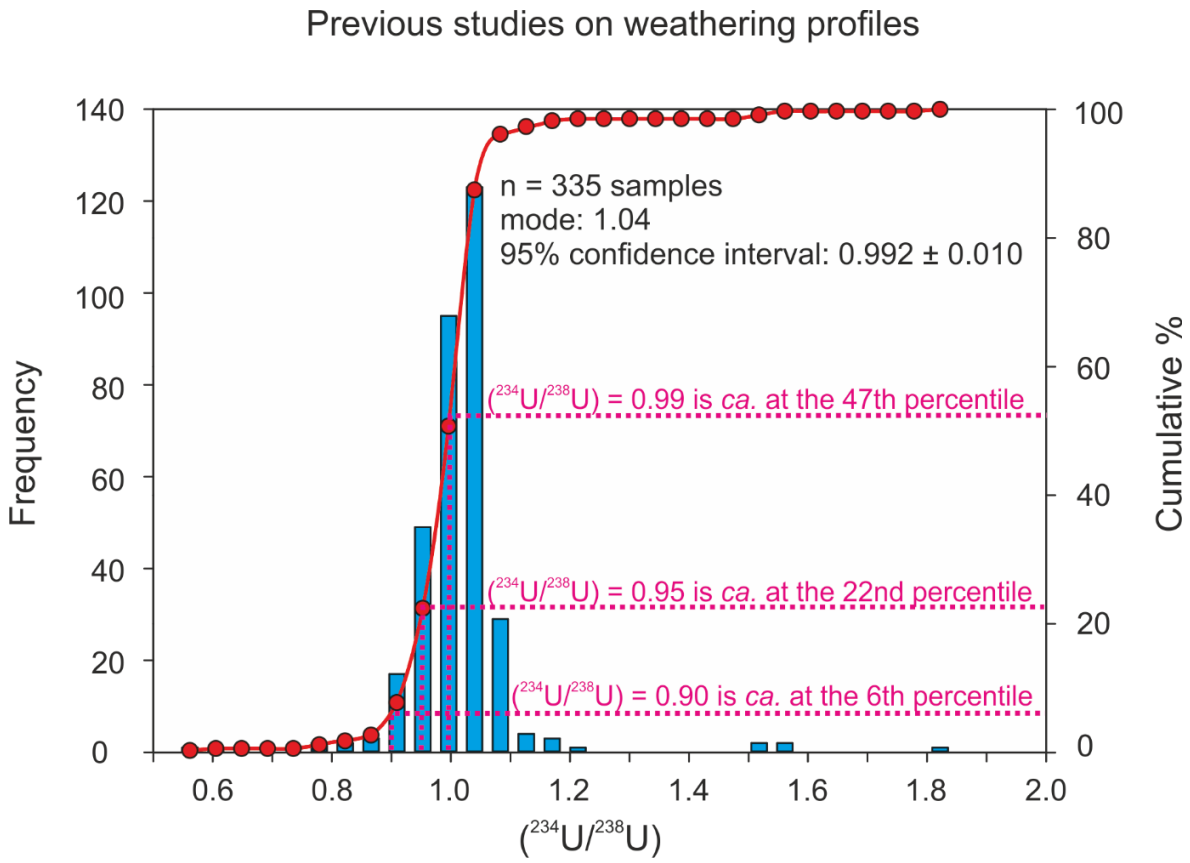

Supplemental Figure 1. Histogram of (^{234}U/^{238}U) in compiled published weathering residues. In addition, the mode, the 95 % confidence interval and the 6th, the 22nd, as well as the 47th percentile from the percentage cumulative frequency of the (^{234}U/^{238}U) dataset, are illustrated (Supplemental Table 1; n = 335

samples). The mode shows that the most frequent ($^{234}U/^{238}U$) ratio (n = 123 samples) lies at *ca.* 1.04. The percentiles demonstrate that less than 6 % of the published ($^{234}U/^{238}U$) data are below 0.90. Furthermore, *ca.* 78 % of the presently published literature has ($^{234}U/^{238}U$) ratios >0.95, whilst 53 % of the ($^{234}U/^{238}U$) data are >0.99. The confidence interval was calculated using the formula: $\bar{x} \pm Z \frac{\sigma}{\sqrt{n}}$ (Supplemental Equation 1). Where $\bar{x}$ represents the sample mean; Z the value (1.960) to calculate the 95 % confidence interval; σ the standard deviation and n the number of samples. The 95 % confidence interval provides evidence that the true mean of ($^{234}U/^{238}U$) is likely to lie between 0.982 and 1.002. Summarised, the statistical evaluations strengthen the idea that the calculated ratio of *ca.* 0.99 is representative as the best current estimate of the global mean average ($^{234}U/^{238}U$) continental weathering residue.

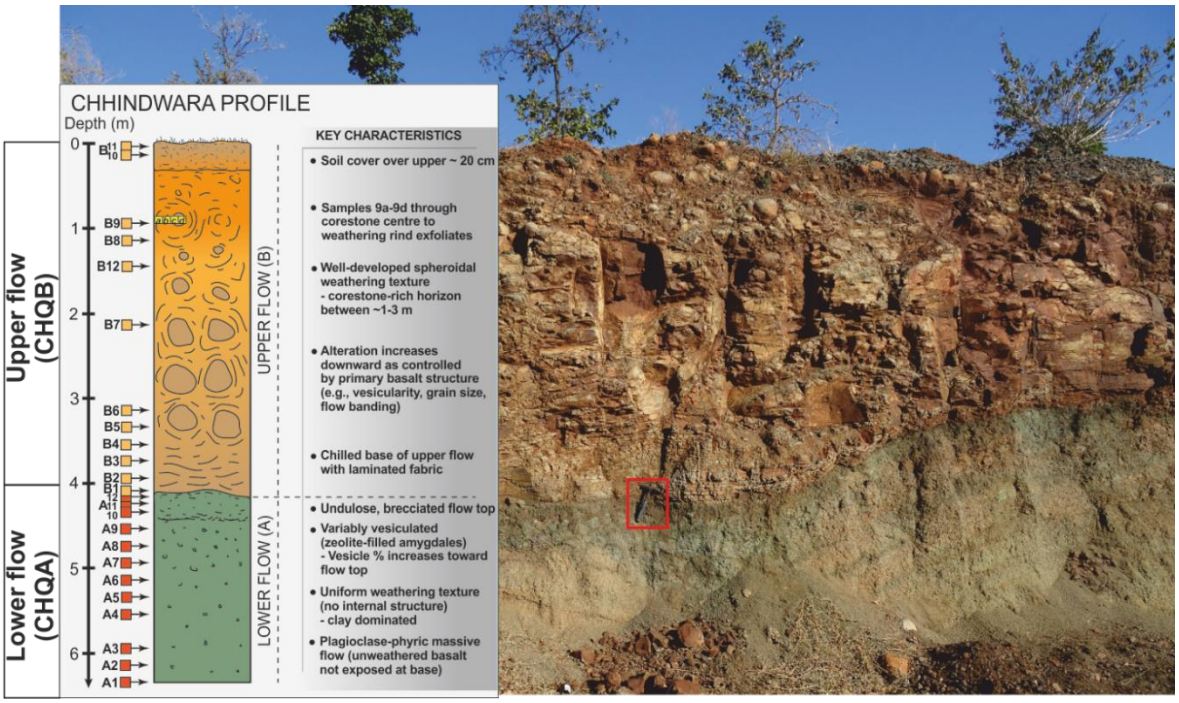

Supplemental Figure 2. Geological sketch section with key characteristics and sample heights (Babechuk et al., 2014) next to a field photograph of the Chhindwara weathering profile. The red rectangle marks the position of a geological hammer as scale (ca. 35 cm). The weathering profile is exposed in a roadside quarry. Note the colour change marking the transition for the upper flow (CHQB) to the lower flow (CHQA). Note also that this photo was taken in January 2016, whereas the samples of this study were taken in 2009 several meters away from the picture scene.

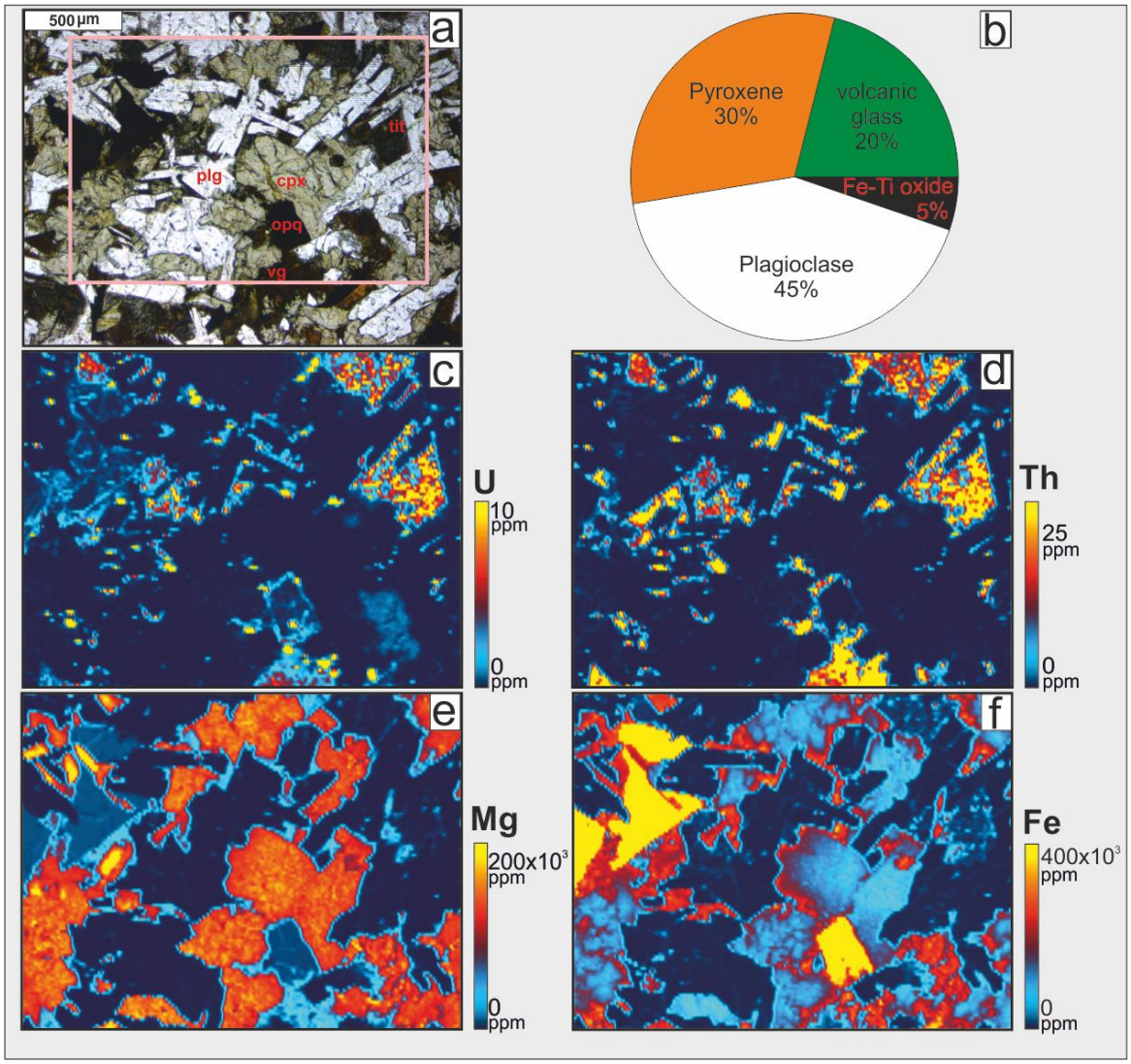

Supplemental Figure 3. (a) Photomicrograph of doleritic parent rock under ppl showing clinopyroxene (cpx), volcanic glass (vg), plagioclase (plg), primary Fe-Ti oxide (opq = opaque) and titanite (tit). Volcanic glass occurs as inclusions in all silicate minerals and as the interstitial matrix. The pink frame delineates the area that was laser ablated. **(b)** Pie chart with modal % of the primary minerals in the protolith. **(c)** Semi-quantitative LA-ICP-MS compositional maps of U, **(d)** Th, **(e)** Mg, **(f)** and Fe. It is obvious that volcanic glass is most U and Th enriched and that weathering resistant primary Fe-Ti oxide hosts minor amounts of U that is unlikely to be released during weathering. In addition, titanite is enriched in U and Th but occurs only as accessory phase in the protolith. Chemical breakdown of pyroxene and plagioclase appears to happen with the concomitant breakdown of volcanic glass, consequently resulting in the release of U.

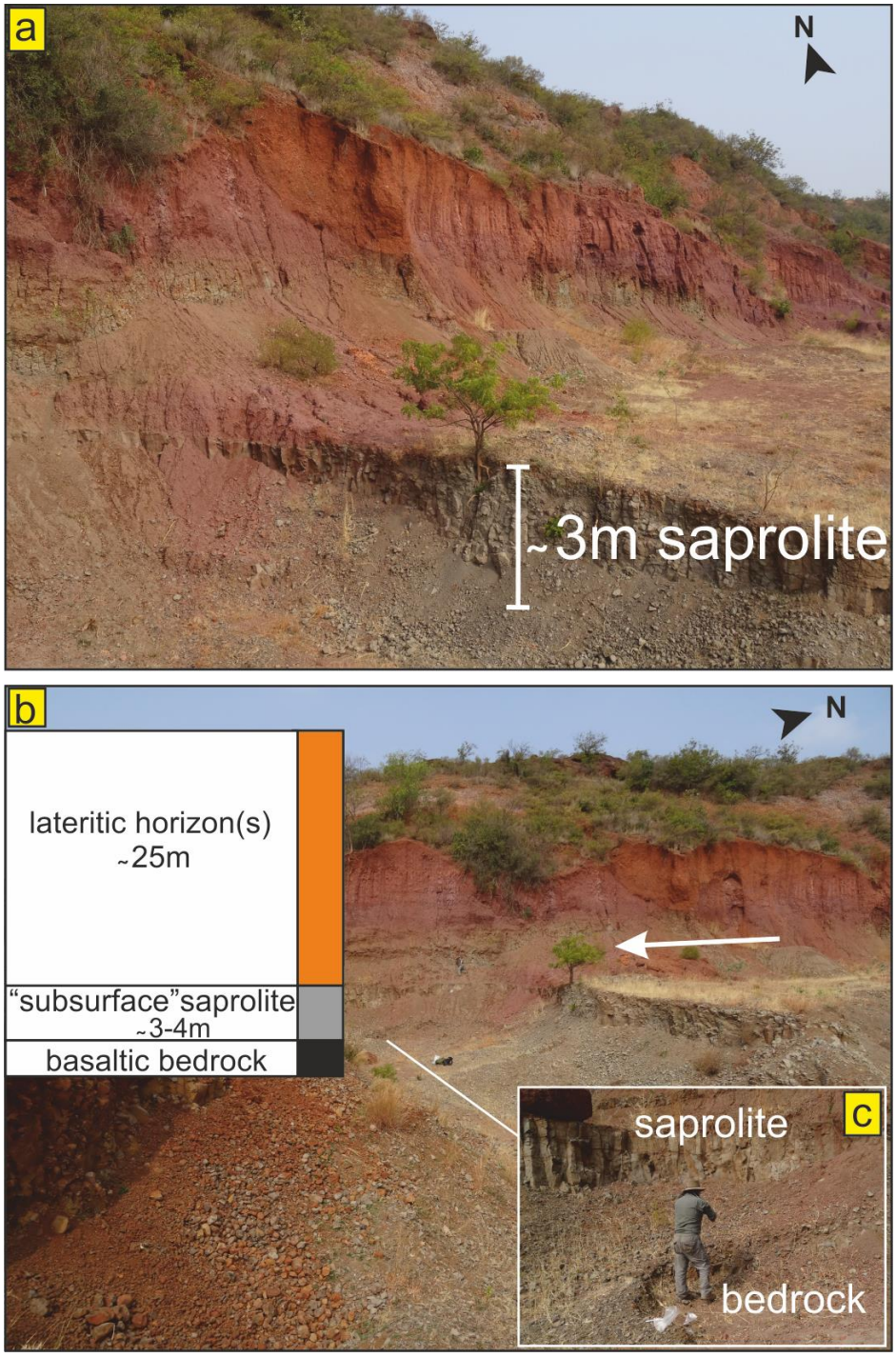

Supplemental Figure 4. (a) Highly evolved lateritic weathering profile in a road stone quarry near Bidar, India. The saprolitic weathering front was not exposed to the surface before quarry work. **(b)** Cross section of the same profile (including the meter scales of the lateritic horizons (ca. 25m) and the "subsurface" saprolite (ca. 3-4m)) shows the full extent of the lateritic weathering profile. White arrow is marking the position of a tree that can be seen in **(a)**. Note that the black arrow in **(a)** and **(b)** illustrates the direction towards north. **(c)** Photograph of the saprolite and the bedrock much closer to the weathering profile. From the observations in **(a)**, **(b)** and **(c)** it can be inferred that the actively weathering saprolite zone of primary weathering in lateritic profiles is very thin and often not exposed to the surface.

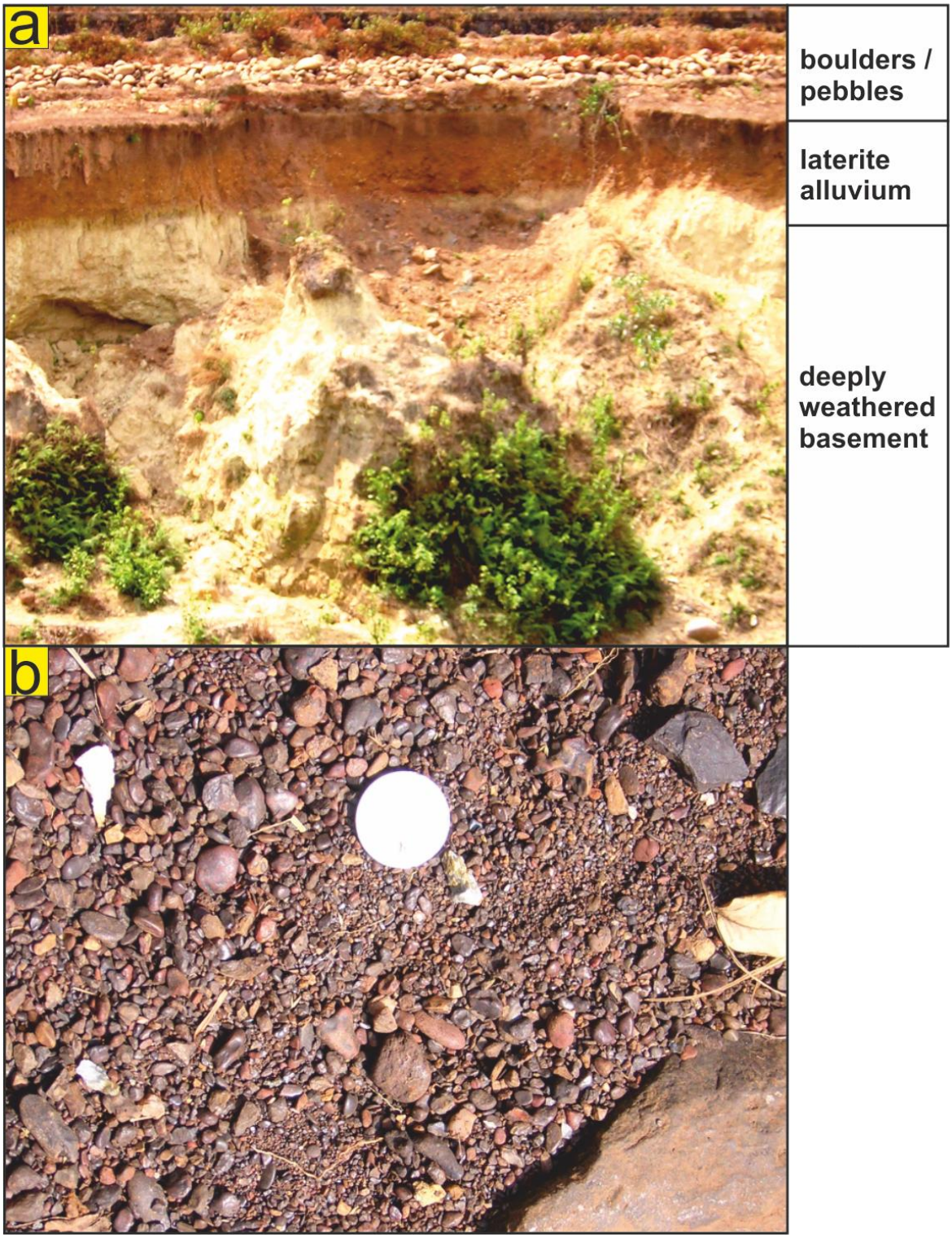

Supplemental Figure 5. (a) Cross section through the lateritic alluvium of an old river channel on the Konkan of Goa, India. On top, the major scour consists of boulders and pebbles, whereas the laterite alluvium is located beneath the surface. Below the laterite alluvium, the deeply weathered basement is exposed. **(b)** Lateritic gravel bed load from a Goa river tributary that consists of a mixture of more angular bed rock fragments, and smaller, rounded laterite gravel.

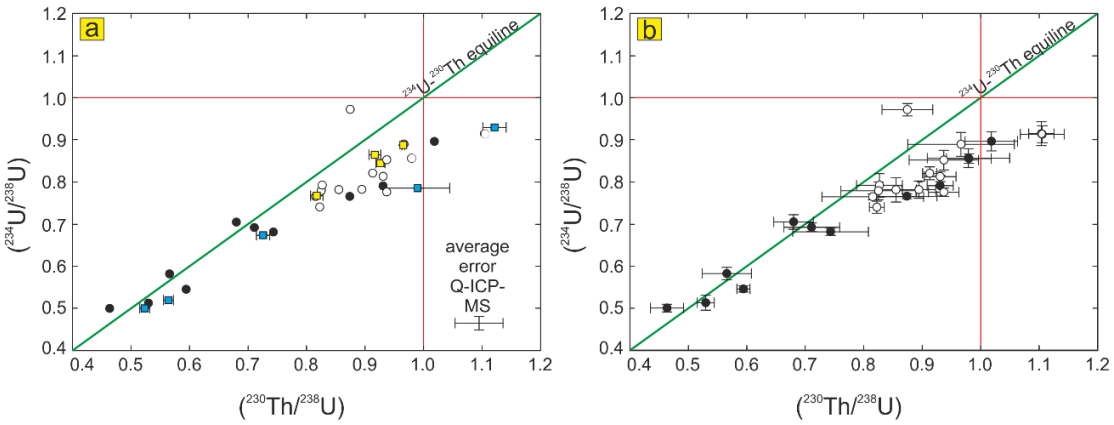

Supplemental Figure 6. Bi-variate diagrams. **(a)** (^{234}U/^{238}U) vs. (^{230}Th/^{238}U) activities show a strong positive correlation. White dots = Q-ICP-MS data of upper flow; black dots = Q-ICP-MS data of lower flow; yellow squares = MC-ICP-MS data of upper flow; blue squares = MC-ICP-MS data of lower flow. **(b)** Q-ICP-MS data of **(a)** with individual error of each sample.

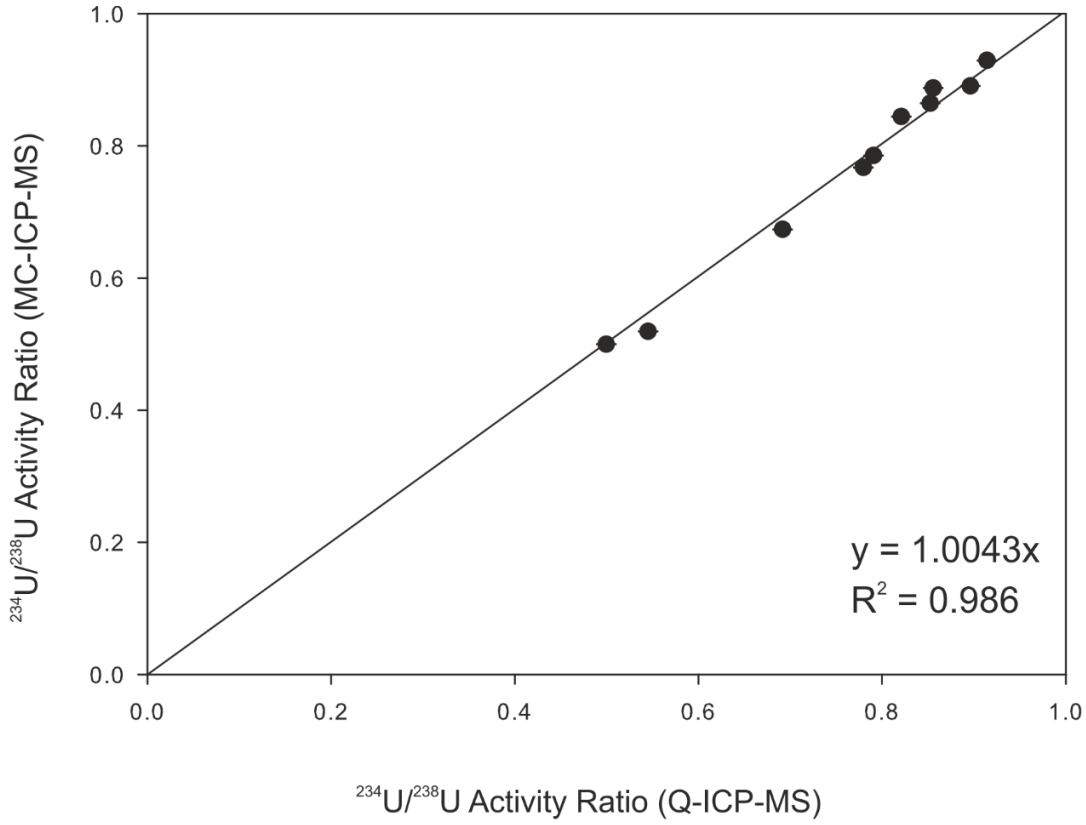

Supplemental Figure 7. Comparison of the $^{234}U/^{238}U$ activity ratio measurement by MC-ICP-MS and Q-ICP-MS on representative samples from different weathering sections. Both measurement techniques correlate very well with each other, yielding an R^2 value of 0.986 (forced through origin).

6. Supporting Information II

6.1. Anion-exchange column calibration for U and Th separation from basaltic rocks using AG 1X8 Resin

6.1.1. Introduction

The following sections describe a calibration scheme for basaltic rocks using AG 1X8 Resin 200-400 mesh (BioRad) for the elution of U and Th with HNO_3 (U-separation) and HCl (Th-separation). The calibration scheme was modified from a recipe that was provided by University College Dublin for the separation of U and Th from carbonates. Precise information is presented on the elution peak shapes and positions for the collection of U and Th. The correct volume of resin and molarity of acids is crucial for the pre-concentration of actinides and matrix removal prior to analysis by MC-ICP-MS.

6.1.2. Experimental preparation

The solutions were prepared from 100 mg of whole rock standards of the US Geological Survey (Basalt, Columbia River - 2 (BCR-2); Andesite (AGV-2)). The standard sample powders were digested with HF-HNO_3 (4:1) in closed, Savillex Teflon® beakers at ~ 160 °C for 72-90 hours. Final conversion using two 1 mL aliquots of concentrated HNO_3 was performed, and the nitrate residue product was dissolved in 2 ml of 7 M HNO_3 prior to loading on the columns. All experiments were measured on a Thermo Scientific iCAP Q-ICP-MS at TCD. For the column calibration, R1040 2.5 ml Columns with frits from RockbourneScientific as well as additional reservoirs were used. Before the calibration, columns and reservoirs were cleaned in 0.5 M HNO_3 overnight and after that rinsed with H_2O-Milli-Q. Columns were marked at the one cm and four cm scale to assure that the right volume of resin was inserted. The anion resin was three times suspended in H_2O-Milli-Q and the supernatant decanted after the resin settled. The same procedure followed once in 6 M HCl and after that at least twice in H_2O-Mili-Q to ascertain that no acid was left on the resin. After the cleaning steps, the resin was added dropwise into the columns

that were filled with a few ml of H_2O-Mili-Q. The resin bed was washed with 6 M HCl and subsequently with H_2O-Mili-Q, 6 M HCl, and twice with H_2O-Mili-Q (1 ml of resin is washed in 3 ml of solution in each step). After this procedure and shortly before the samples were loaded, the resin was conditioned by adjusted volumes of HNO_3 (3 ml of HNO_3 for 1 ml of resin). The sample solutions were loaded onto the columns drop by drop in two steps a 0.5 ml. After the loading of the samples, they were eluted with HNO_3 to separate the matrix and the U fractionation. After that, an elution with 6 M HCl followed to separate Th. The single elution steps in the experiments were conducted with an acid volume of 0.5 ml to get very detailed information on the elution profiles.

6.1.3. Results and discussion

In order to reach very high Th and U yields, several column calibrations were conducted with the BCR-2 standard and varying conditions of resin volume and molarity of HNO_3. The usage of 1 ml of resin volume and conditioning of the resin with 7 M HNO_3 resulted in a successful separation of U. However, a strong Th washout occurred directly at the beginning of the experiment so that the later elution of Th with 6 M HCl resulted in a too low yield. In the second separation experiment, the volume of resin was increased to 4 ml in one column with the aim to reach a better retention of Th on the resin (Supplemental Figure 8a,b). Furthermore, in a second column the resin bed was conditioned with 7.5 M HNO_3 (Supplemental Figure 8c,d) to test if the usage of a stronger acid would lead to a higher equilibrium adsorption of Th, as it is suggested in other column calibrations with this resin type (Bunney et al., 1959). In a fourth column calibration attempt, we eluted U with 7.5 M HNO_3 to see the effects on Th (Supplemental Figure 9).

Conditioning of the resin with 7 M HNO_3 and 7.5 M HNO_3 resulted in recovery yields of U that exceeded 90% and a clear separation from the matrix. However, the recovery yields of Th in both column experiments were <30% (Supplemental Figure 8a,c). Additionally, the conditioning of the resin and elution with 7.5 M HNO_3 in the fourth column calibration experiment resulted in an even higher Th loss, so that the recovery yields of Th were <10% (Supplemental Figure 9). In the last attempt, the resin bed was conditioned by using a higher volume of 7 M HNO_3 (20 ml instead of 12 ml) to guarantee

that the chloride form was completely converted and soaked in HNO_3 (Supplemental Figure 10).

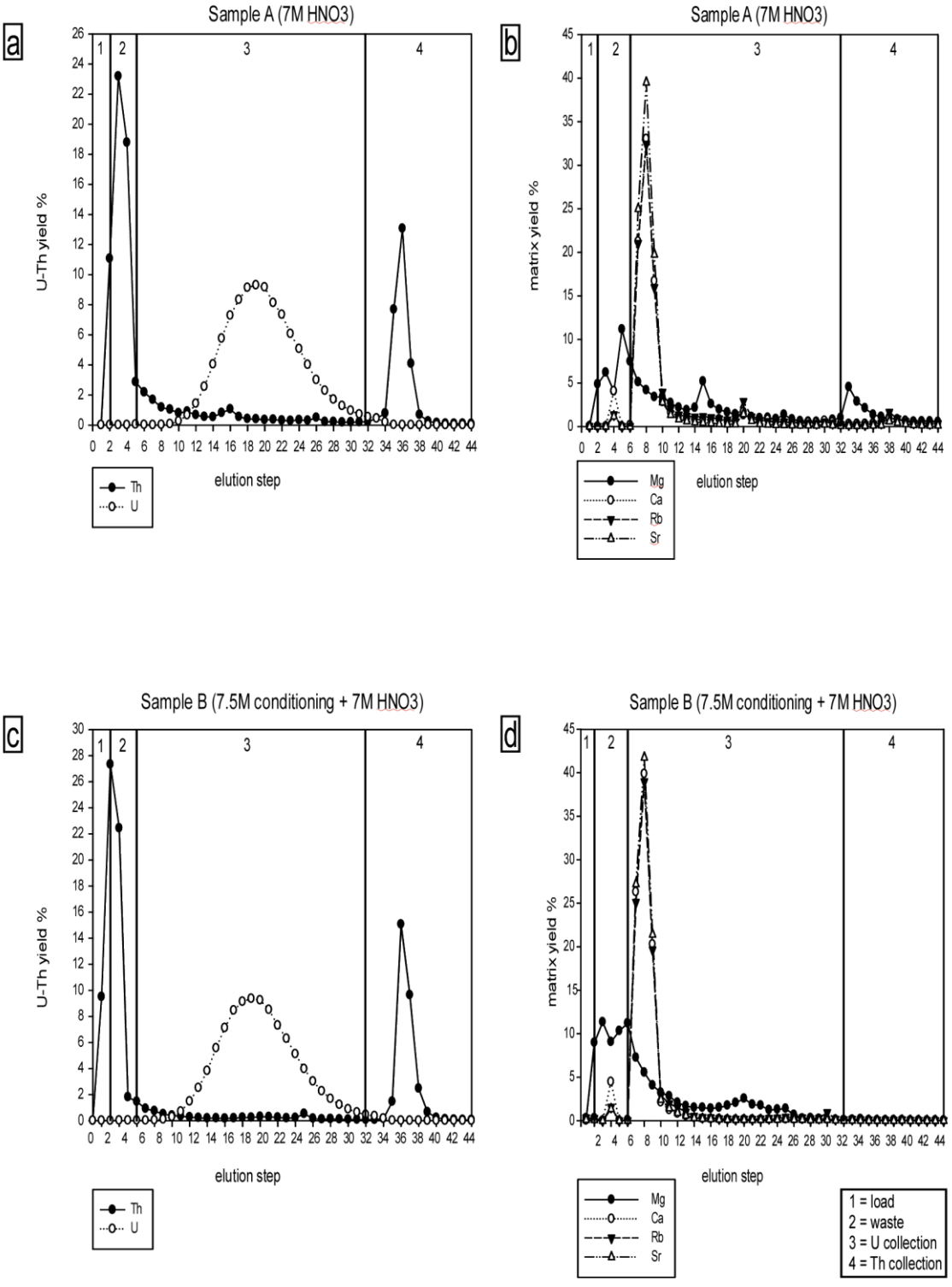

Supplemental Figure 8. Column calibration with 4 ml of resin (BCR-2). **(a)** Conditioning of the resin and U yields with 7 M HNO_3, **(b)** Conditioning of resin bed and matrix separation with 7 M HNO_3, **(c)**

Conditioning of resin bed with 7.5 M HNO_3 and elution of U with 7 M HNO_3, **(d)** Conditioning of resin bed with 7.5 M HNO_3 and matrix separation with 7 M HNO_3.

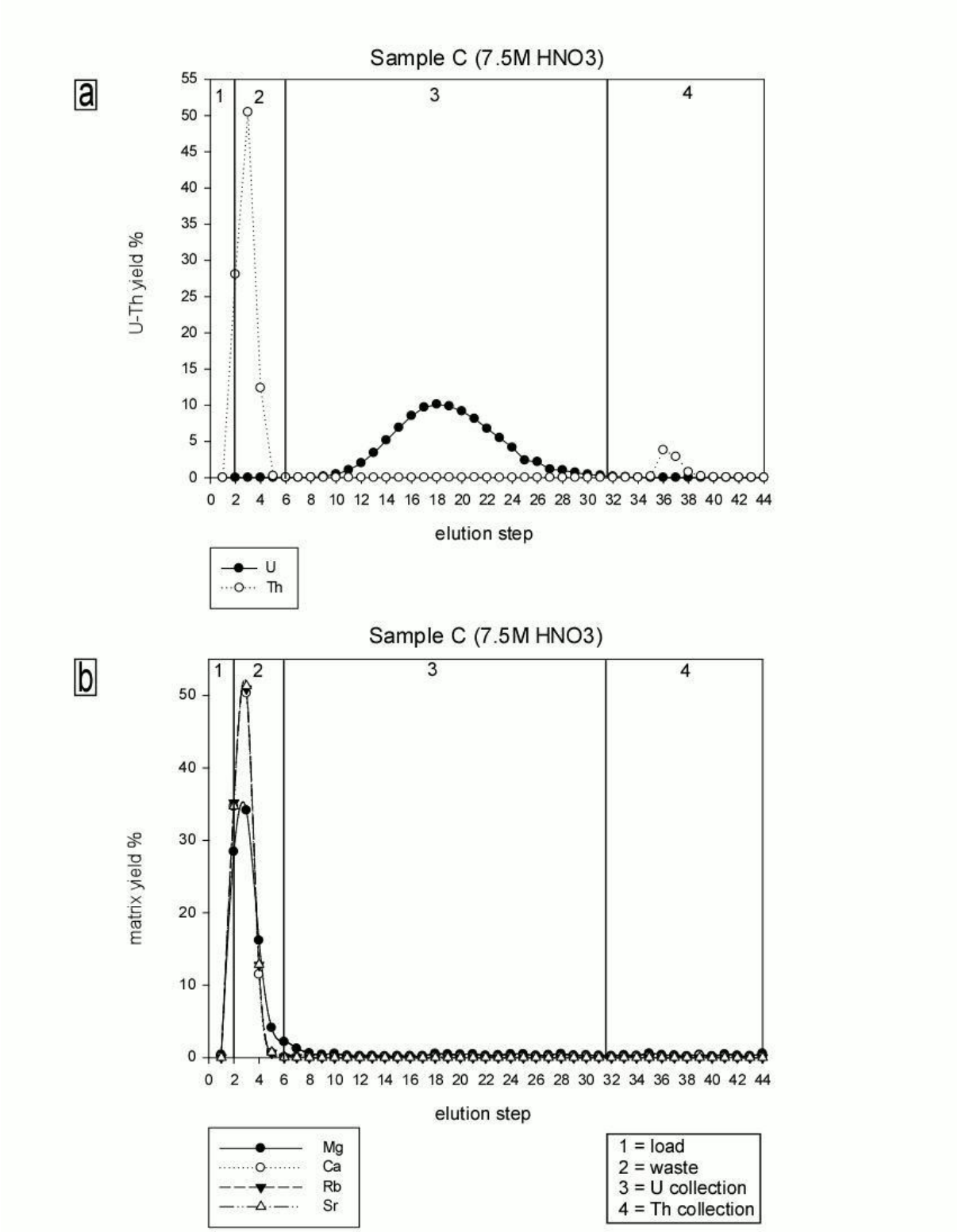

Supplemental Figure 9. Column calibration with 4 ml of resin and 7.5 M HNO_3 for conditioning of the resin bed and elution of the matrix and U (BCR-2). **(a)** U-Th yields, **(b)** matrix separation.

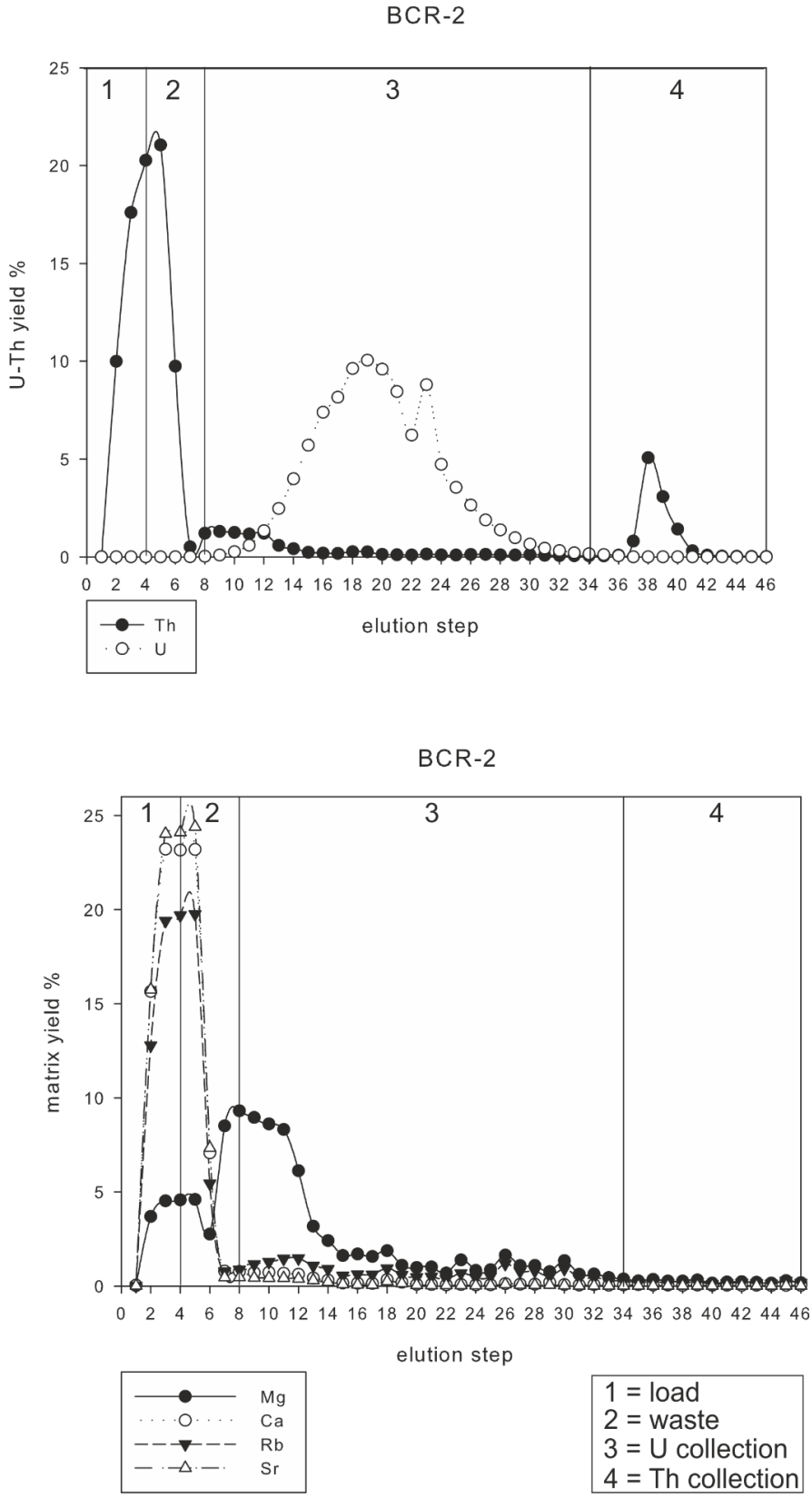

Supplemental Figure 10. Column calibration with 4 ml of resin and 20 ml of 7 M HNO_3 for the conditioning of the resin bed. 7 M HNO_3 was used for the elution of the matrix and U. **(a)** U-Th yields, **(b)** matrix separation.

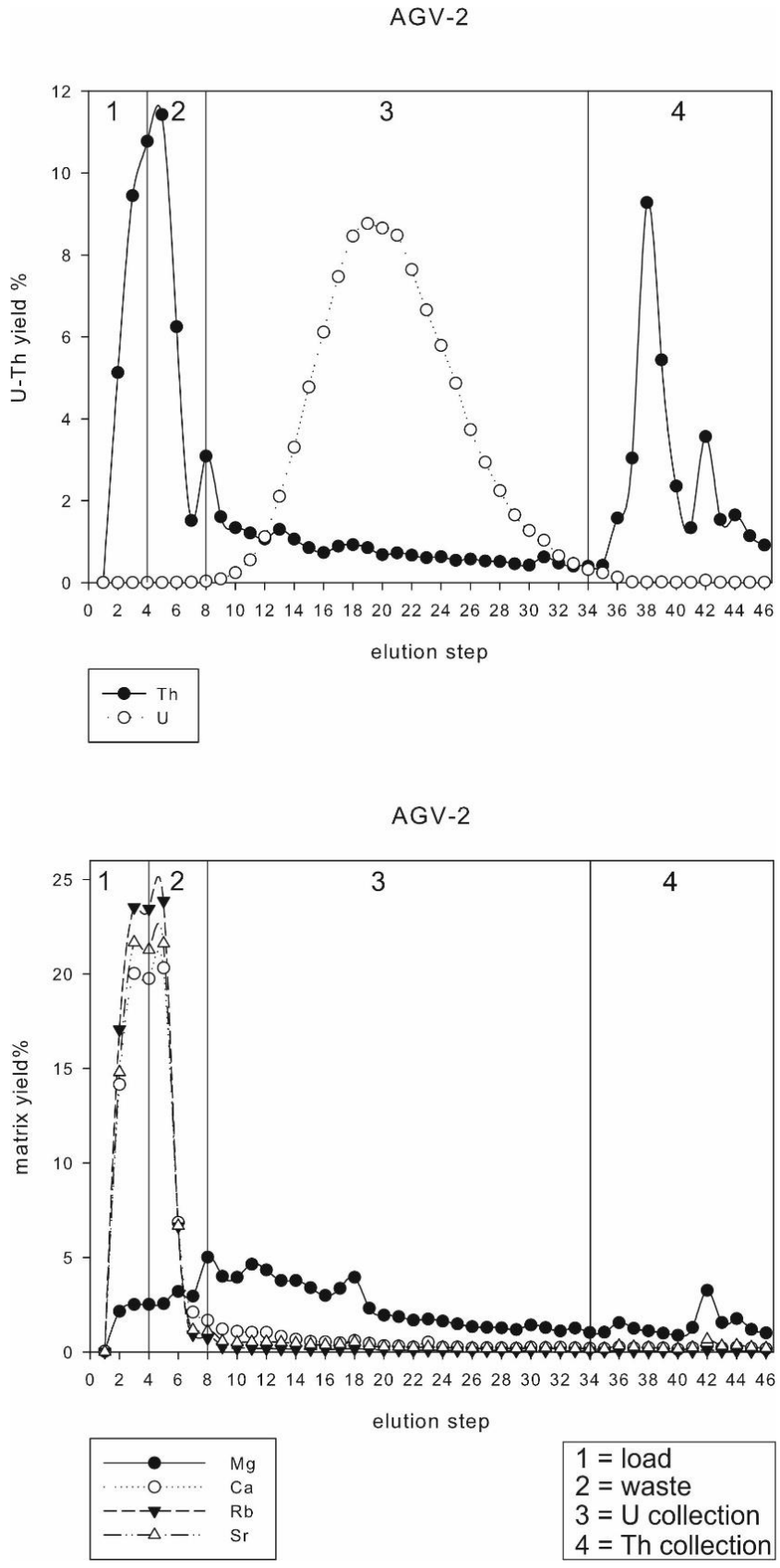

Supplemental Figure 11. Column calibration with 4 ml of resin and 20 ml of 7 M HNO_3 for the conditioning of the resin bed. 7 M HNO_3 was used for the elution of the matrix and U. **(a)** U-Th yields, **(b)** matrix separation.

This approach resulted in a lower yield of Th in comparison to previous experiments (Supplemental Figure 8). However, the same experiment was conducted with the rock standard AGV-2 (Supplemental Figure 11) and resulted in a Th yield >30%. This suggests that the rock matrix likely has an influence on the retention of Th on the resin bed. Overall, the findings in the experiments are in agreement with Yokoyama et al. (1999), who demonstrated that the recovery yield of Th from basalt is not >30% due to matrix effects. Thus, AG 1X8 Resin is not useful for the separation of U and Th from basalts.

6.1.4. Conclusions

The separation of U and Th from the BCR-2 standard resulted in a high purification of U (>90%), but much lower Th yields (<30%). Different resin volumes and changes in the molarity of HNO_3 (7 M, 7.5 M) always resulted in a successful separation of U from the matrix. However, the use of 7.5 M HNO_3 resulted in very low Th yields. Thus, the usage of AG 1X8 Resin (BioRad) for column calibrations of basaltic rocks and soils, similar in composition to the BCR-2 rock standard, is not useful for the separation of Th. The results also demonstrate that the Th yields depend on the basaltoid type and consequently the rock matrix. This is illustrated by the difference of the Th yields in case that it is isolated from different rock types (Supplemental Figures 10; 11).

6.2. Separation of U and Th from basaltic rock and soil samples using UTEVA resin

6.2.1. Introduction

In order to overcome the issue with AG 1X8 Resin 200-400 mesh (BioRad) and to separate Th with yields >90%, a column procedure with UTEVA resin was established. The resin was purchased from Triskem-International, France, as pre-packed 2-cm^3 columns. The separation of U and Th from the BCR-2 standard followed a method that was developed by Gadu and Kamber (2008). This method was originally used for Cu- and/or caesium (Cs) rich samples and is based on findings of Fujiwara et al. (2007) but modified with respect to the molarity of the HNO_3 solution. An 8M HNO_3 solution was used to obtain very high yields for Th and U. A concern by Gadu and Kamber (2008) that this increase in acid concentrations might prevent some of the other elements before Th, to completely be stripped from the columns, was not confirmed. Thus, a replication of this experiment should result in complete matrix separation and yields of Th and U >90%.

6.2.2. Sample preparation and experimental details

For analysis, 100 mg of sample powder (BCR-2) was digested with HF-HNO_3 (4:1) in closed, Savillex Teflon® beakers at ~160 °C for 72-90 hours. Final conversion using two 1 mL aliquots of concentrated HNO_3 was performed, and the nitrate residue product was dissolved in 1 ml of 8M HNO_3 prior to loading on the column. Both experiments were measured on a Thermo Scientific iCAP Q ICP-MS at TCD. Every elution step was collected in microtubes. The resin bed was cleaned with 30 ml of 0.1 M HNO_3 and then conditioned by 1.5 ml of 4 M HNO_3. After the loading of the sample (drop by drop), a wash-in followed in three steps using 0.2 ml of 4 M HNO_3. Major elements were eluted in five steps a 1 ml with 4 M HNO_3. A change in molarity to 0.1 M HNO_3 followed and after three steps a 1 ml, the Th collection started. To identify best possible separation of Th and U four elution steps a 0.5 ml with 0.1 M HNO_3 were introduced (elution steps fourteen to

seventeen; Supplemental Figures 12a, b). After that, 1 ml aliquots were used again, and 6 ml of 0.1 M HNO_3 were needed to separate all U. After the separation experiments, the resin was put in 0.1 M HNO_3.

6.2.3. Results and discussion

The results show excellent retention for both U and Th, while the major elements were completely eluted by this time (Supplemental Figures 12; 13). In the first experiment, an intersection between U and Th in elution steps 15-17 (Supplemental Figure 12a) indicates that they have not been perfectly separated from each other. In the second experiment, however, all Th was completely eluted before U stripped from the column (Supplemental Figure 12b). Regardless, the omission of elution step 16 in both experiments results in U and Th yields >90% that are required to avoid abundance sensitivity issues during the MC-ICP-MS measurement. This demonstrates that the method by Gadu and Kamber (2008) is useful for U and Th separations from basalt and soils that derived from basaltic substrate.

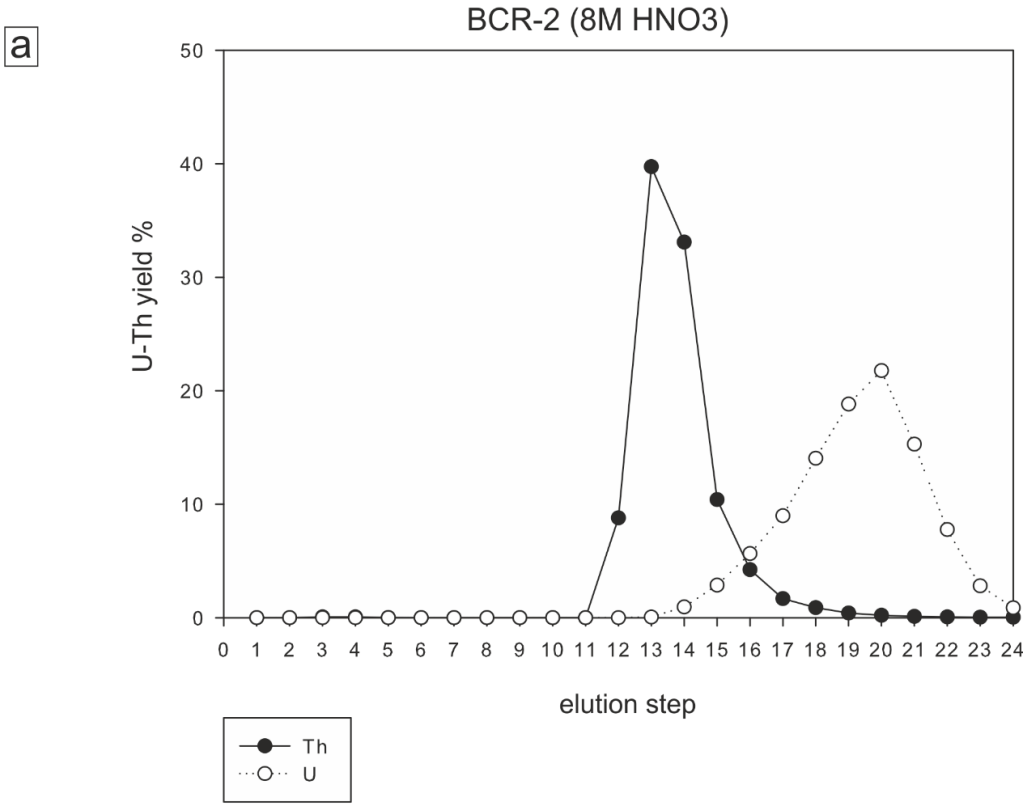

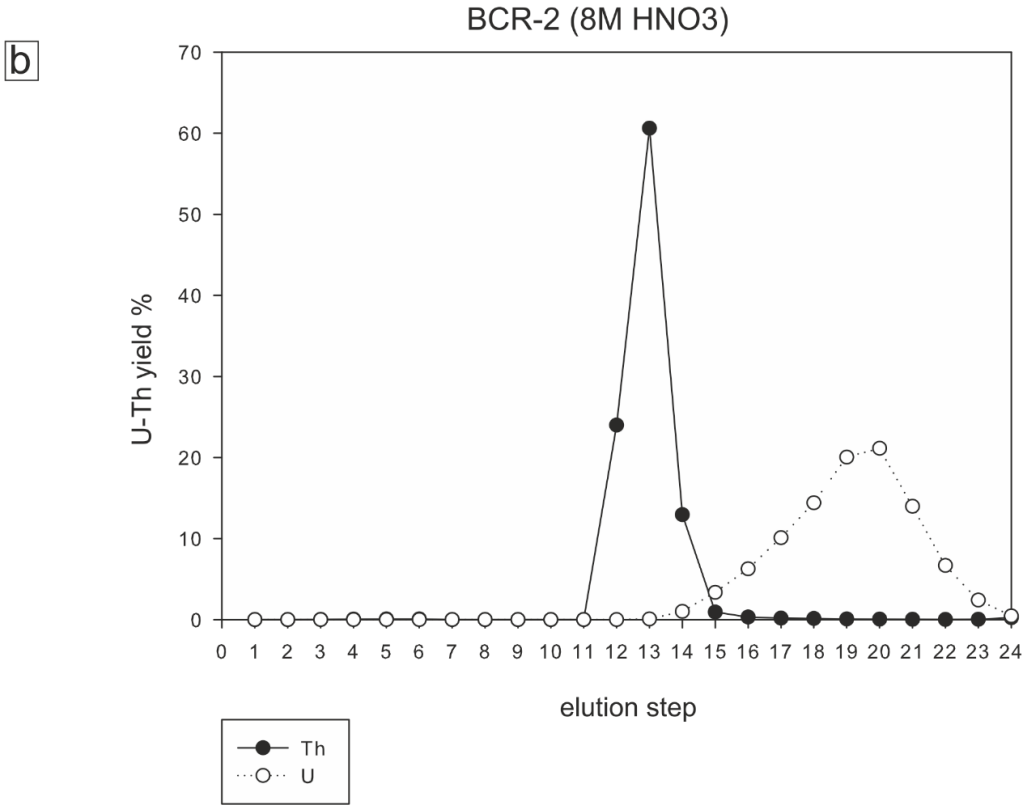

Supplemental Figure 12. Column calibration with UTEVA resin. **(a)** U-Th yields in the 1st experiment **(b)** U Th yields in the 2nexperiment.

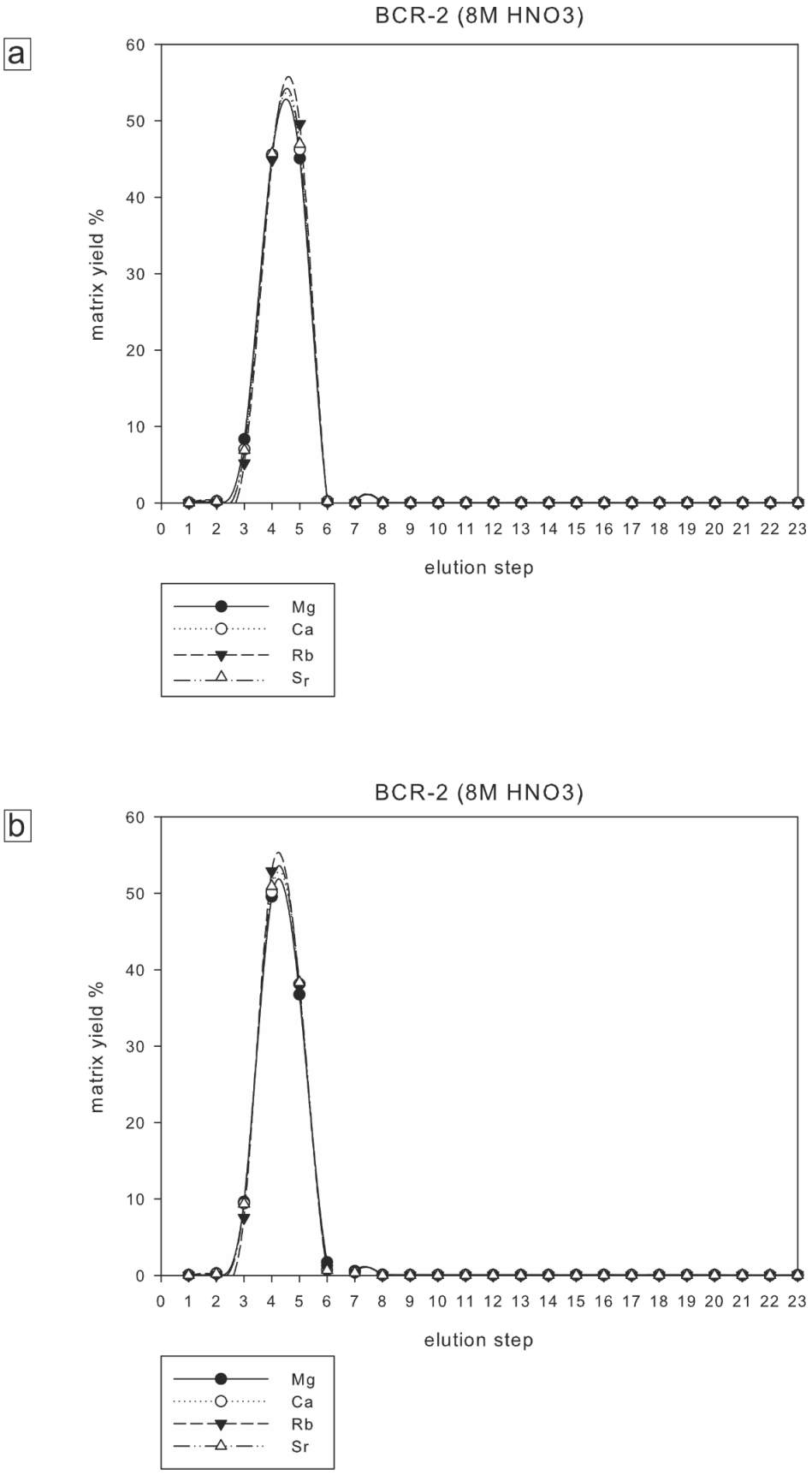

Supplemental Figure 13. Column calibration with UTEVA resin. a) Matrix yields in the 1st experiment b) Matrix yields in the 2nd experiment.

6.2.4. Conclusions

Based on the above-presented experiments, UTEVA is confirmed as an excellent resin for the separation of U and Th from basalt and basaltic soil. As a result, the developed method is useful for subsequent U series measurements.

Chapter 3: Elemental and isotopic behaviour of Zn in Deccan basalt weathering profiles: Chemical weathering from bedrock to laterite and links to Zn deficiency in tropical soils

Published in Science of The Total Environment (2018, Vol. 619-620, 1451-1463)

Authors: Nils Suhr, Ronny Schoenberg, David Chew, Carolina Rosca, Mike Widdowson, Balz S. Kamber

Abstract

Zinc (Zn) is a micronutrient for organisms and essential for plant growth, therefore knowledge of its elemental cycling in the surface environment is important regarding wider aspects of human nutrition and health. To explore the nature of Zn cycling, we compared its weathering behaviour in a sub-recent regolith versus an ancient laterite profile of the Deccan Traps, India – an area of known soil Zn deficiency. We demonstrate that progressive breakdown of primary minerals and the associated formation of phyllosilicates and iron oxides leads to a depletion in Zn, ultimately resulting in a loss of 80% in lateritic residues. This residue is mainly composed of resistant iron oxides and hydroxides ultimately delivering insufficient amounts of bio-available Zn. Morever, (sub)-tropical weathering in regions experiencing extended tectonic quiescence (e.g., cratons) further enhance the development of old and deep soil profiles that become deficient in Zn. This situation is clearly revealed by the spatial correlation of the global distribution of laterites, cratons (Africa, India, South America and Australia) and known regions of Zn deficient soils that result in health problems for humans whose diet is derived from such land.

We also investigate whether this elemental depletion of Zn is accompanied by isotope fractionation. In the saprolitic horizons of both weathering profiles, compositions of $\delta^{66}Zn_{JMC\text{-}Lyon}$ lie within the "crustal average" of $+0.27 \pm 0.07‰$ $\delta^{66}Zn_{JMC\text{-}Lyon}$. By contrast, soil horizons enriched in secondary oxides show lighter isotope compositions. The isotopic signature of Zn ($\Delta^{66}Zn_{sample\text{-}protolith}$ up to $\sim -0.65‰$) during the formation of the studied ferruginous-lateritic weathering profile likely resulted from a combination of biotically-

and kinetically-controlled sorption reactions on iron (Fe)-oxyhydroxides. Our findings suggest that oxide rich soil types/horizons in sub-(tropical) regions likely exert a control on riverine Zn isotope compositions such that these become heavier than the crustal average. This isotopic behaviour invites a broader study of global soils to test whether light isotope composition alone could serve as an indicator for reduced bioavailability of Zn.

1. Introduction

Zinc is an essential metal for humans, animals and higher plants because it is a structural constituent and regulatory co-factor in enzymes and proteins involved in many biochemical pathways. It is required in a wide range of macromolecules including hundreds of enzymes, and is the only metal involved in all six classes of enzymes (e.g., Alloway, 2009). In humans, Zn plays a key role in physical growth and development, the functioning of the immune system, reproductive health, sensory function and neurobehavioural development. Children suffering from Zn deficiency often show stunted linear growth, pneumonia or diarrhoea (e.g., Hotz and Brown, 2004) and it is estimated that as many as ca. 100,000 children die each year due to Zn malnutrition (Black et al., 2013). Widespread Zn deficiency is a problem in many developing countries and around 2 billion individuals of the world's human population has diets which lack in Zn (Prasad, 2012).

Zinc deficiency is considered to be the most pervasive micronutrient problem in world crops (e.g., Alloway, 2009), and the relationship to Zn deficiency in soils has been known for decades (e.g., Viets et al., 1954). In tropical and sub-tropical regions chemical weathering of rocks is the main driver for soil formation, and responsible for the release of most elements, including micronutrients such as Zn; thus, weathering profiles in (sub)-tropical latitudes make promising targets in which to explore and document processes that cause substantial element loss during soil formation. Basalts are highly reactive during weathering (e.g., Berner and Berner, 1996) and contain high concentrations of redox-sensitive metals, many of which are bio-essential. Of all common igneous rocks, basalt has the highest Zn concentration (Krauskopf and Bird, 1967; Wedepohl and Correns, 1969; Alloway, 2008), typically hosted in ferromagnesian minerals including augite, hornblende, and biotite, where it substitutes for Fe^{2+} or magnesium (II) Mg^{2+} (Alloway, 2008).

The exchange and release of elements and isotopes in terrestrial ecosystems is determined by the complex interplay between rock, soil, biota, water, and atmosphere within the "*Critical Zone*" (CZ), which extends from the actively cycling groundwater zone up to the vegetation canopy (e.g., Brantley et al., 2007). Insight into the chemical behaviour of Zn within the CZ is essential because this zone comprises the reservoirs of soils that provide plants with nutrients. Despite the obvious role of Zn in the environment,

surprisingly little is known about its elemental and isotopic behaviour during weathering. It is well documented that (bio)-geochemical cycling of metals in natural systems is often accompanied by stable isotope fractionation, and that processes including redox transformations, complexation, sorption, precipitation, dissolution, evaporation, diffusion, and biological cycling are similarly important in metal stable isotope fractionation (Wiederhold, 2015). Accordingly, stable isotope ratios have been effectively employed as geochemical tracers of pedogenic processes and associated element cycling.

Although the apparent riverine flux of Zn from unpolluted sites overlaps with the "crustal average" Zn isotope composition (Little et al., 2014, 2016; Vance et al., 2016), several studies have documented deviations in Zn isotope ratios within weathering residues. Viers et al. (2007) investigated weathering horizons of soil profiles developed on granodiorite and granite, and identified isotope fractionation leading to saprolite being ca. +0.2 permil heavier and ferruginous soil horizons being ca. -0.6 permil lighter compared to the parent granodiorite. Opfergelt et al. (2017) conducted a study of Icelandic soils derived from basalt and proposed that soil organic matter (SOM) controlled modest (0.1 permil) Zn isotope fractionation. Guinoiseau et al. (2017) studied laterite and podzol soils from the Amazon Basin and found lighter Zn in lateritic soils ($\delta^{66}Zn_{\text{JMC-Lyon}} = -0.11‰$ and $-0.14‰$). By contrast, soils developed on Hawaiian basalt and Scottish granodiorite apparently show no evidence for enhanced Zn isotope fractionation (Vance et al., 2016). To date, it has remained unclear whether soil Zn isotope ratios could serve as an indicator for the extent of Zn loss and for limited bioavailability.

Here, the weathering behaviour of Zn and its isotopes on Deccan Traps basalt, India is detailed. Two weathering profiles were selected to compare their contrasting mineralogical stages of soil formation. The first is a saprolite near Chhindwara that has progressed only to a low-intermediate stage of weathering. The other is a laterite profile near Bidar, representing extreme weathering, with its uppermost levels now being almost devoid of silicates and instead replaced by a secondary mixture of chemically resistant oxides and hydroxides. The similarity of the bedrock in both weathering profiles allows a direct comparison of the isotopic behaviour of Zn from the incipient to extreme stages of basalt alteration. Both weathering profiles have already been investigated in terms of elemental enrichment and depletion patterns, as well as with isotopic tracers (lithium (Li), rhenium (Re), osmium (Os), neodymium (Nd)) (Kısakürek et al., 2004; Wimpenny et al., 2007; Babechuk et al., 2014; Babechuk et al., 2015), these examples provide a well-

characterised opportunity to investigate elemental behaviour of Zn and Zn isotopes. The latter point is important, because previous Zn isotope studies (e.g., Viers, et al., 2007; Vance et al., 2016; Opfergelt et al., 2017) have hinted at the complex interplay of rock, soil, biota, water and atmosphere within the CZ in various climates, regions and environments on exchange reactions of Zn and Zn isotopes.

2. Geological overview, background and weathering profile descriptions

2.1. Geological overview and background

The Deccan Traps are a continental flood basalt province (CFBP) situated in northwest peninsular India; the thick lava stack was erupted onto the complex Archean–Proterozoic basement of the Dharwar craton over a period of ca. 3 to 4 Ma across the Cretaceous-Paleogene (K-Pg) boundary (Figure 1; e.g., Courtillot et al., 1988; Widdowson et al., 2000; Chenet et al., 2007; Hooper et al., 2010; Cucciniello et al., 2015; Schoene et al., 2015). The characteristic chemical variability and isotopic signatures of this basaltic succession are well-documented and provide the basis for a detailed chemostratigraphy of 12 formations (Fm) (Mitchell and Widdowson, 1991; Widdowson et al., 2000; Vanderkluysen et al., 2011, and references therein). The Ambenali Fm, is one of the uppermost stratigraphical units, and the most geographically extensive and volumetric; importantly it is also the most compositionally homogeneous (Widdowson et al., 2000), and thus makes a very suitable candidate for case studies comparing chemical alteration and weathering processes on basalt (Kısakürek et al., 2004). Both the weathering profiles used in this study were developed on Ambenali Fm lava flow units.

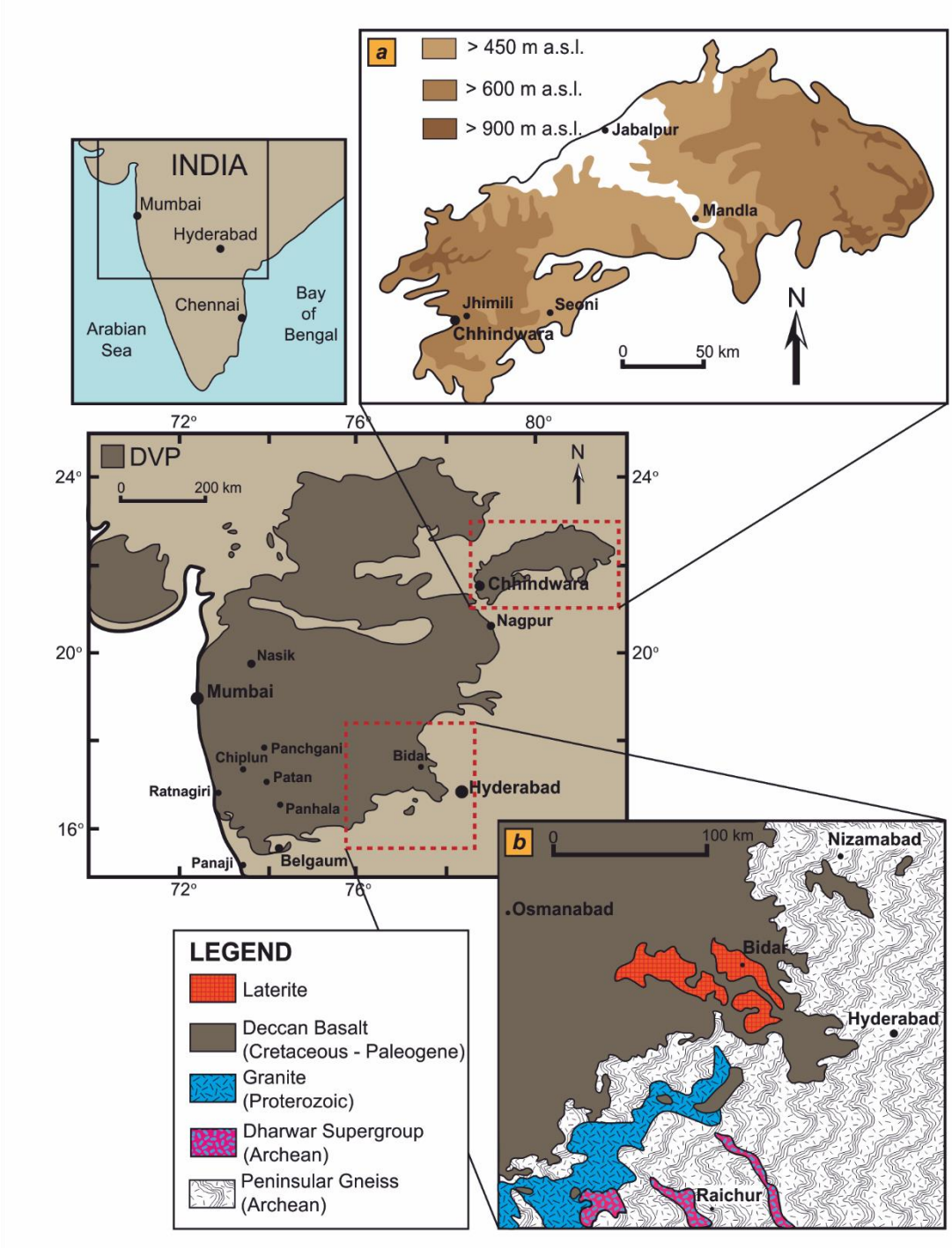

Figure 1. Simplified geological map showing the extent of the Deccan Volcanic Province (DVP) within peninsular India and the geomorphology of the weathered basaltic terrane. Inset maps show **(a)** the mesa topography near Chhindwara in the Madya Pradesh district and **(b)** the more detailed geology of the SE lobe of the DVP, including the extent of the thick laterite that hosts the Bidar profile (Babechuk et al., 2014). DVP geology maps are modified from Borger and Widdowson (2001), Kısakürek et al. (2004) and Babechuk et al. (2014).

2.1.1. Aggressive, tropical weathering and lateritisation of Deccan Traps basalt

The northward drift of India during the Late Cretaceous to early Cenozoic passed through equatorial latitudes (Klootwijk and Peirce, 1979; Ganerød et al., 2011) and exposed peninsular India and the Deccan Traps to aggressive tropical weathering. Extensive rainfall led to the establishment of stable water tables within the near-surface units of the neo-formed Deccan Traps flood terrain (Widdowson and Cox, 1996). This phase of alteration and widespread lateritisation likely continued throughout the Palaeogene (Bonnet et al., 2014), diminishing by the mid- Oligocene (~25 Ma) possibly as a consequence of regional uplift coinciding with collision of India with Eurasia (Molnar and Stock, 2009) or associated regional tectonic rearrangement (Schmidt et al., 1983; Richards et al., 2016) and/or the erosive uplift of the rifted margin of Western India (Beck et al., 1995; Widdowson, 1997). As a result, these earlier developed weathering profiles were subsequently raised above the water table and dissected during the Neogene (Widdowson, 1997).

At Bidar (Figure 1), the units of the Ambenali Formation were lateritised relatively soon after eruption (Kısakürek et al., 2004; Wimpenny et al., 2007a). Several studies have found that this Bidar profile contains dust derived from extraneous sources (Kısakürek et al., 2004; Wimpenny et al., 2007; Babechuk et al., 2014; Babechuk et al., 2015), and inputs from allochthonous groundwater only occurred during the main developmental phase of the Bidar profile: Further, any groundwater input is likely to have been locally sourced only from essentially the same, widespread basaltic units. In effect, the elevated position of the Bidar area and its remote, intracontinental location, isolates the profile from the influence of basement lithologies or marine influence (Kısakürek et al., 2004). Therefore, since influence of any compositionally different or extraneous sources has been established as negligible, the Bidar laterite profile makes an excellent candidate to investigate element mobility and its associated isotopic behaviour during advanced *in situ* weathering.

2.1.2. Active, (sub)-tropical weathering and geologically recent saprolitisation of Deccan Traps basalt

Large areas of the current exposure of the Deccan have not progressed to laterite, and these more recently weathered Deccan basalts are instead the result of a change to wetter climate (i.e., 'modern' monsoonal) conditions in peninsular India during the late Neogene and Quaternary (Wang et al., 2005; Spicer et al., 2017). During these Periods rivers responded by deepening and enlarging their channels, promoting increased denudation and the development of river terraces (e.g., Clift et al., 2002; Kale, 2002; Babechuk et al., 2014). The mesa-like topography of these profiles is the result of the Pleistocene–Holocene fluvial processes that incised into the flat lying, ca. 4–10 m thick basaltic flows. These fluvial processes further eroded the lateritised Palaeocene duricrust from most of the topographic highs, thus permitting variable weathering of the basalt that became exposed in the wake of climate change associated with Quaternary glacial-interglacial cycles. Currently, approximately >90% of the Deccan basalt outcrops consist of variably weathered basalt within saprolite-type weathering profiles 1–10 m thick.

Such a Quarternary saprolite weathering profile is exposed near Chhindwara (Figure 1), allowing study of the incipient to intermediate stages of active basalt weathering; locally, there are no higher elevations that might unduly complicate elemental and isotopic signals resulting from the in-situ alteration processes (Babechuk et al., 2014), and only very minor input of aeolian dust has contaminated the lava flow surface during basalt emplacement. These latter have effected minimal modification of geochemical signature (Babechuk et al., 2015).

2.2. Weathering profile descriptions

Previous investigation of the Chhindwara and Bidar profiles has yielded valuable information regarding the stages of basalt chemical weathering (Babechuk et al., 2014, 2015). To provide necessary context for the current study, these may be summarised as follows:

2.2.1. Chhindwara, Deccan Traps, India (Quaternary: Sub-recent profile)

This weathering profile (Figures 1; 2a) is developed across two basalt flows exposed in a quarry east of Chhindwara, India (22° 04.213′ N, 79° 01.393′ E); its morphology and chemical composition are described in detail by Babechuk et al. (2014; 2015). Field observations show that the weathering intensity does not decrease uniformly with depth, but was partially controlled by the structure and porosity (i.e. fracturing and primary vesicularity) of the original lava flows. Accordingly, weathering is more intense at the finer-grained and banded base of the upper flow (ChQB), while the thicker, more massive central part of the upper flow is spheroidally weathered and still retains core-stones within the altered clay-rich matrix; top soil is thin with limited vegetation cover. The lower flow (ChQA) has a thick (ca. 10 m) massive core (now exposed by recent quarrying) which becomes progressively vesicular upwards; in the topmost 1–2 m these vesicles contain zeolitic amygdules.

Regardless of these physical variations, the upper parts of both the lower and upper flows exhibit essentially similar immobile element (niobium (Nb), tantalum (Ta), zirconium (Zr), hafnium (Hf)) patterns and allow an interpretation of chemical weathering trends (Babechuk et al., 2014; 2015). The least weathered samples (ChQB12, CHQB9c) are taken here as being representative of the protolith composition: ChQB9c was sampled from a corestone along with three more samples taken at increasing distance (and degree of alteration) from the corestone centre (ChQ9a, b, d). Enhanced formation of secondary phases (smectite, hydroxides of iron, manganese oxide) is evident in the lower part of the upper flow (sample CHQB6 and downwards); examination of the overlying top soil reveals similar secondary alteration products. Similarly, these secondary phases increase towards the bottom of the lower flow with concomitant loss of primary mineralogy (clinopyroxene and plagioclase). These documented mineralogical reactions correspond with the trends of weathering indices (Babechuk et al., 2014), and demonstrate that the profile has progressed to an intermediate weathering intensity: chemical index of alteration (CIA) values of 35–80 and oxidative mafic index of alteration [$MIA_{(O)}$] values of 38–71 (Table 1).

Table 1. Major (wt%) and trace element (µg/g) concentrations, weathering indices ($MIA_{(O)}$, CIA)[a], relative % loss (R) of Mn[b], Zn, as well as Zn isotope compositions of the Chhindwara and Bidar profiles.

Chhindwara saprolite profile

Sample	Description	Depth (cm)	MgO	Zn/Nb	Mn /Nb	$MIA_{(O)}$	CIA	Fe^{2+}/Nb	Fe^{3+}/Nb	∑Fe/Nb	$R_{Mn\%}$	Zn	$R_{Zn\%}$	$\delta^{66}Zn_{IRMM-3702}$	$\delta^{66}Zn_{JMC-Lyon}$	2SE	$\Delta^{66}Zn_{sample-protolith}$
			wt%					*molar*	*molar*	*molar*	*/Nb*	*(µg/g)*	*/Nb*				
ChQB11	Topsoil	0	3.62	11.43	190.14	57	57	59.23	144.95	204.18	− 8.69	139.63	− 13.78	− 0.022	0.268	0.020	0.008
ChQB10	Topsoil	10	3.95	13.60	174.17	56	58	64.82	148.30	213.13	− 16.36	145.15	2.62	− 0.031	0.259	0.019	− 0.001
ChQB9d	Corestone	90	5.03	13.90	175.60	67	38	74.32	169.90	244.22	− 15.67	112.09	4.89				
ChQB9c	Least weathered corestone	90	5.09	13.58	198.90	56	38	106.92	118.54	225.46	− 4.48	114.77	2.45				
ChQB9b	Corestone	90	4.87	13.38	207.73	42	39	116.87	105.58	222.45	− 0.24	116.32	0.98				
ChQB9a	Corestone	90	3.88	12.62	218.05	44	47	102.67	85.77	188.44	4.71	122.63	− 4.76				
ChQB8		110	4.92	13.77	193.73	38	39	105.97	106.53	212.50	− 6.97	126.64	3.91				
ChQB12	Parent rock	140	5.46	13.25	208.23	38	36	158.65	62.00	220.65	0	113.38	0.00	− 0.030	0.260	0.018	−
ChQB7		210	4.75	13.68	205.81	41	43	103.91	134.07	237.98	− 1.16	113.25	3.21				
ChQB6		310	4.71	13.28	181.59	39	40	95.89	119.46	215.35	− 12.8	118.91	0.17				
ChQB5		330	2.97	12.72	206.99	40	54	34.63	181.93	216.56	− 0.6	123.77	− 4.00	− 0.038	0.252	0.022	− 0.009
ChQB4		350	2.14	12.42	233.47	41	67	14.89	193.87	208.76	12.12	127.69	− 6.31	− 0.053	0.237	0.015	− 0.023
ChQB3		370	2.28	12.59	237.31	50	70	16.23	206.23	222.47	13.96	127.33	− 5.04				
ChQB2		390	2.74	13.10	277.01	56	79	7.86	189.49	197.35	33.03	139.16	− 1.17				
ChQB1		405	2.61	12.83	296.98	57	78	6.43	195.53	201.96	42.62	130.44	− 3.24	− 0.085	0.205	0.012	− 0.055
ChQA12		410	3.43	11.59	150.04	68	74	11.06	185.85	196.91	− 27.95	119.65	− 12.55				
ChQA11		420	3.3	9.17	150.66	68	73	10.46	165.74	176.20	− 27.65	103.68	− 30.83				
ChQA10		430	3.34	9.17	116.71	70	72	10.72	163.02	173.74	− 43.95	109.53	− 30.82	− 0.096	0.194	0.013	− 0.067
ChQA9		450	3.01	10.42	139.16	68	80	13.81	135.54	149.34	− 33.17	144.93	− 21.41				
ChQA8		470	2.94	10.00	125.11	70	79	14.00	142.71	156.72	− 39.92	136.12	− 24.59				
ChQA7		490	2.94	10.38	159.64	69	79	13.18	144.59	157.77	− 23.34	135.96	− 21.68				
ChQA6		510	2.72	9.06	127.63	68	78	15.33	143.89	159.21	− 38.71	121.01	− 31.61				
ChQA5		530	2.68	8.47	83.47	69	78	16.40	142.43	158.84	− 59.92	117.90	− 36.09	− 0.001	0.289	0.020	0.029
ChQA4		550	2.69	9.28	115.75	68	74	16.94	139.85	156.79	− 44.41	130.38	− 29.99				
ChQA3		590	2.43	9.72	142.52	63	74	17.83	145.19	163.02	− 31.56	137.30	− 26.68				
ChQA2		610	2.45	9.65	139.30	63	72	15.12	148.97	164.09	− 33.1	134.06	− 27.23				
ChQA1		630	2.3	9.94	123.39	64	71	18.06	145.19	163.25	− 40.74	130.95	− 25.04	− 0.100	0.190	0.024	− 0.070

Bidar laterite profile

Sample	Description	Depth (cm)	Zn/Nb	$MIA_{(O)}$	CIA	Fe_2O_3	TOC	Zn	$R_{Zn\%}$	$\delta^{66}Zn_{IRMM-3702}$	$\delta^{66}Zn_{JMC-Lyon}$	2SE	$\Delta^{66}Zn_{sample-protolith}$
						wt%	*wt%*	*(µg/g)*	*/Nb*				
BB-9	Nodular laterite	200	2.27	99.3	99.7	77.53	0.32	31.83	− 79.91	− 0.573	− 0.283	0.012	− 0.514
BB-8	Vermiform laterite	500	4.10	99.4	99.7	38.37	0.15	69.33	− 63.70	− 0.174	0.116	0.019	− 0.115
BB-7	Base of laterite	600	3.58	98.6	99.9	27.7	0.11	51.83	− 68.35	− 0.072	0.218	0.014	− 0.013
BB-6	Base of laterite/top of saprolite	1100	39.78	99.4	100	84.81	0.18	224.59	252.07	− 0.719	−0.429	0.020	− 0.660
BB-5	Saprolitised basalt (grey/blue colour)	1300	2.24	98.8	99.9	36.95	0.15	52.57	− 80.18	− 0.150	0.140	0.013	− 0.091
BB-4	Reddened saprolite	1500	4.31	91.3	90.4	21.64	0.51	80.10	− 61.88	− 0.537	− 0.247	0.012	− 0.478
BB-3	Deeply weathered basalt (saprolite)	2600	6.02	97.8	99.9	24.1	0.11	114.03	− 46.72	0.026	0.316	0.020	0.085
BB-2	Basalt with minor alterations	3500	11.09	35.5	36	12.63	0.18	113.15	− 1.83	− 0.018	0.272	0.016	0.041
BB-1	Unaltered basalt	4700	11.30	35	36.5	13.4	0.07	104.64	-	− 0.059	0.231	0.014	−

[a] Major elements, trace elements, $MIA_{(O)}$ and CIA values described in detail in Babechuk et al. (2014). [b] Mn is only presented for the Chhindwara profile

2.2.2. Bidar laterite profile

The Bidar laterite is a deep (~50 m) weathering profile and located at a mesa edge near Bidar, India (17°54.87′ N, 77°32.39′ E) (Figures 1; 2b). By contrast to the Chhindwara profile it exhibits a far more advanced weathering stage (Borger and Widdowson, 2001; Kısakürek et al., 2004; Babechuk et al., 2014), and is characterised by upwardly increasing degrees of alteration exposing a typical 'lateritic' weathering progression from bedrock to surface: This may be summarised as unweathered basalt (> 40 m depth) passing into a saprolitic horizon (~ 35–30 m), advancing into saprolite with Fe-rich mottles and segregations (30–25 m); above this level primary silicates have been almost entirely transformed into secondary minerals (~ 25–15 m), and irregular Fe-rich agglomerations become dominant (with concomitant decrease in silicon (Si) and aluminium (Al) concentrations); between 15 and 10 m depth, a zone with anomalously high Fe and trace metal concentrations is interpreted as marking the position of a former water table (Kısakürek et al., 2004; Babechuk et al., 2014; 2015); at the top the profile progresses upward from tabular, semi-indurated laterite (10–4 m) and finally into an indurated laterite cap that represents the most extreme stage of weathering. In effect, secondary clays have transformed into kaolinite, goethite and hematite in the upper portions of the profile (Figure 2b).

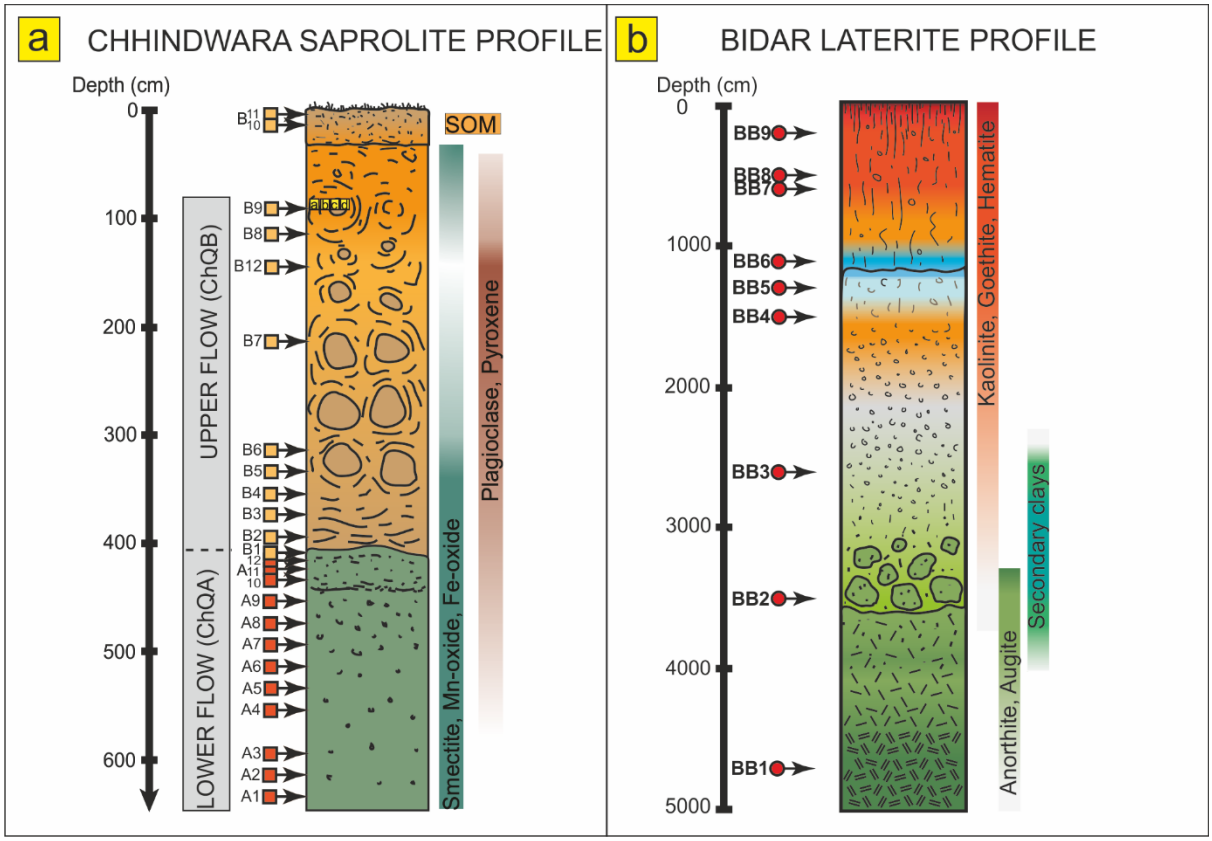

Figure 2. Geological sketch section of the: **(a)** Chhindwara weathering profile **(b)** Bidar laterite (modified from Kısakürek et al., 2004 and Widdowson, 2007). The mineralogy in the weathering progression accompany the schematic of each profile and is discussed in the next chapters.

The two profiles described above may be compared in the Bidar saprolite zone (BB2-BB3) where mineralogical transformations are similar to those observed throughout as in the Chhindwara profile.

3. Methods

3.1. XRD analyses

X-ray diffraction (XRD) analyses were performed with a Bruker D5000 at Trinity College Dublin (TCD), Ireland. Three samples of the Chhindwara profile had previously been measured with a Phillips PW 1729 X-ray diffractometer at Central Analytical Facility

(CAF) at Laurentian University, Sudbury, Ontario, Canada. The methodology, analytical description, detailed descriptions of the results, quantitative mineralogy (Supplemental Figures 1–3) and petrographic descriptions of the Chhindwara bedrock samples and the Bidar laterite profiles (Supplemental Figures 4–5) can be found in the supporting information.

3.2. LA-ICP-MS element mapping

Whereas most other analytical techniques such as elemental analysis were performed on existing samples (e.g. from the Babechuk et al., 2014 study), new samples were collected in 2016 for LA-ICP-MS trace element maps of the Chhindwara bedrock and Bidar laterite profile. LA-ICP-MS elemental image maps were acquired using a Photon Machines Analyte Exite 193 nm ArF Excimer laser-ablation system with a Helex 2-volume ablation cell coupled to an Agilent 7900 ICPMS at the Department of Geology, TCD. The ICP-MS was tuned on NIST 612 glass as described by Ubide et al. (2015), with thorium oxide/thorium (ThO^+/Th^+) ratios < 0.15% and thorium/uranium (Th/U) ratios close to unity. Argon (Ar) carrier gas and dinitrogen (N_2) (to boost signal sensitivity) were mixed with the helium (He)-laser aerosol from the cell in a ca. 1.5 cm^3 mixing bulb which affords a rapid washout for image mapping experiments. Ten isotopes (lithium-7 (^{7}Li), magnesium-24 (^{24}Mg), silicon-29 (^{29}Si), chromium-52 (^{52}Cr), ^{57}Fe, nickel-60 (^{60}Ni), copper-63 (^{63}Cu), ^{66}Zn, ^{232}Th and ^{238}U) were measured using a total duty cycle of 135 ms. A laser fluence of 3.3 J/cm^2s, a repetition rate of 31 Hz, a 12 μm spot size and a scan speed of 20 μm/s were employed. Similar to Ubide et al. (2015), image maps were made by "rastering" the sample under the ablation site. To produce the full map, adjacent lines (or "rasters") were ablated in a successive manner. The final ablated area was rectangle-shaped to facilitate production of trace-element maps using the "Image from Integrations" module in Iolite. NIST612 glass reference material was used as the calibration standard. Data reduction and production of trace element distribution maps was undertaken with the Iolite software (Paton et al., 2011) using the "Trace Elements" data reduction scheme in "Semi-Quantitative" mode (which in IOLITE corresponds to not employing an internal standard isotope). Following data reduction, trace element distribution maps were built with the Iolite module "Images From Integrations".

3.3. Elemental analysis

Samples from the Chhindwara profile (n = 27; Babechuk et al., 2014) were powdered in an agate mill while the powders for the Bidar profile were prepared in a tungsten carbide mill. The major element composition of both profiles was determined by X-ray fluorescence (XRF) following a loss-on-ignition (LOI) measurement; the Bidar XRF data were obtained at the Open University (UK) and were reported previously (Kısakürek et al., 2004; Widdowson, 2007). The Chhindwara XRF data were obtained at Geoscience Laboratories (Sudbury, Ontario). Ferrous iron measurements were also obtained on Chhindwara samples at the Geoscience Laboratories via potentiometric titration with potassium permanganate ($KMnO_4$) and were reported in Babechuk et al. (2014). All trace element data were obtained via solution quadrupole ICP-MS analysis at the Department of Earth Sciences at Laurentian University (LU) with a Thermo Scientific XSeriesII (LU) and at TCD with a Thermo Scientific iCap-Qs. Tantalum, tungsten (W), and molybdenum (Mo) data were not reported for the Bidar samples due to potential contamination from the tungsten carbide mill, but all other trace elements are unaffected (Babechuk et al., 2015). For further information on sample preparation and analysis, readers are referred to the original studies (Kısakürek et al., 2004; Babechuk et al., 2014; 2015). Total organic carbon (TOC %) analyses were undertaken using an Elementar vario EL cube instrument at the Trinity Centre for the Environment, TCD.

3.4. Analytical technique for zinc isotope determination

Zinc isotope analyses were performed at the Isotope Geochemistry Group, Eberhard Karls University Tuebingen, Germany. The protocol for Zn purification is detailed in (Moeller et al., 2012). Powder aliquots of soil samples and USGS rock reference materials containing at least 1 µg of Zn were spiked with an appropriate amount of purified ^{64}Zn–^{67}Zn double-isotope tracer prior to digestion with hydrofluoride-nitric acids (HF-HNO_3) (Moeller et al., 2012). The double-spike technique allows the in-run correction of instrumental mass-bias effects but also accounts for Zn isotopic fractionation caused by anion-exchange chemistry (Bermin et al., 2006). The digests were converted to chloride for ion chromatography using

self-made Teflon shrink columns loaded with 1.1 mL of BioRad DOWEX AG MP-1, 100-200 mesh anion resin. Procedural blanks were below 1 ng total Zn and therefore were negligible.

Zinc isotope ratio measurements were performed on a ThermoFischer Scientific NeptunePlus multiple collector inductively coupled plasma mass spectrometer (MC-ICP-MS), in low resolution mode, coupled to a Cetac ARIDUS II. The Aridus II desolvating nebulizer system greatly reduces potential metal-oxide interferences on Zn masses in the analyte solutions, such as chromium(II) oxide/vanadium(II) oxide/titanium(II) oxide ($^{51}V^{16}O/ {}^{50}Cr^{16}O/{}^{50}V^{16}O/{}^{50}Ti^{16}O$) on ^{66}Zn, $^{52}Cr^{16}O$ on ^{68}Zn, on ^{67}Zn, and $^{48}Ti^{16}O$ on ^{64}Zn, although impurities of Ti, V, and Cr have never been detected. To avoid any metal-nitride formation the Aridus II was run without additional dinitrogen (N_2) gas. Signals of $^{64}Zn^+$, $^{66}Zn^+$, $^{67}Zn^+$, $^{68}Zn^+$ and $^{70}Zn^+$ together with the interference monitors $^{62}Ni^+$ (for correction of $^{64}Ni^+$ on $^{64}Zn^+$) and germanium-72 ($^{72}Ge^+$) (for correction of $^{70}Ge^+$ on $^{70}Zn^+$) were detected simultaneously. Small background signals (e.g. very small signals from long-term memory of the uptake system, the Ni cones or the sample carrier solution) were corrected with on-peak zero measurements of the sample carrier solution prior to each measurement. A 10^{10} Ω resistor was used to detect the highly abundant ^{64}Zn signal (49.2% natural abundance plus enriched ^{64}Zn from the double spike), a 10^{12} Ω resistor was used to detect the least abundant ^{70}Zn (0.61% natural abundance) and all other signals were detected using 10^{11} Ω resistors on the respective amplifiers. The double spike deconvolution was performed using measured abundances of the ^{64}Zn, ^{66}Zn, ^{67}Zn and ^{68}Zn isotopes. The lowest signal intensities are detected on $^{68}Zn^+$ when using a ^{64}Zn-^{67}Zn double spike and 1:1 sample to DS ratios. During the course of this study signals detected on $^{68}Zn^+$ ranged between 1.5 and 6.4 V using an amplifier resistor of 10^{11} Ω allowing for high-precision Zn isotope ratio analyses.

Isotopic data are reported in the δ notation relative to the certified $\delta^{66/64}Zn_{IRMM\text{-}3702}$ solution standard. For ease of reference, they are also tabulated (Table 1) relative to the "JMC-Lyon" solution standard using an offset of +0.29 ± 0.05‰ (Moeller et al., 2012). The external 2 s.d. reproducibility for $\delta^{66}Zn$ on IRMM-3702 during the course of this study was better than 0.03‰. Accuracy was controlled by interspersed analyses of an in-house solution standard prepared from an "Alfa Aeser" Pura-tronic Zn wire yielding an average $\delta^{66}Zn$ of − 10.295 ± 0.026‰ (2SD, n = 8), within the laboratory long-term reproducibility of − 10.278 ± 0.051‰ (n = 21). The USGS standards BCR-2, BHVO-2, and BIR-1a

yielded average $\delta^{66/64}Zn_{JMC\text{-}Lyon}$ values of 0.280 ± 0.036‰ (n = 3), 0.315 ± 0.036‰ (n = 3) (see table in supporting information), and 0.236 ± 0.028‰ (n = 6), respectively. These are within the range reported in previous studies (Sossi et al., 2015), demonstrating the accuracy of this dataset.

4. Results

4.1. XRD data

The quantitative XRD mineralogy of the Chhindwara profile (Figure 3a) shows that minor amounts of smectite developed at the base (ChQB6) of the upper flow. Further down the weathering profile, in the lower volcanic flow, the amount of smectite increases, whereas the amounts of primary clinopyroxene and plagioclase decrease. The amount of smectite decreases somewhat only in the deepest levels of the lower volcanic flow probably as a result of the textural control on the extent of weathering (Babechuk et al., 2014). In general, identification and quantification of those phases which have undergone moderate weathering can be challenging; here materials consists of amorphous clays, secondary oxides and volcanic glass that cause strong background signals (see supporting information for more information in the diffractograms). Results should, therefore, be interpreted only as a qualitative estimate of the mineralogical composition.

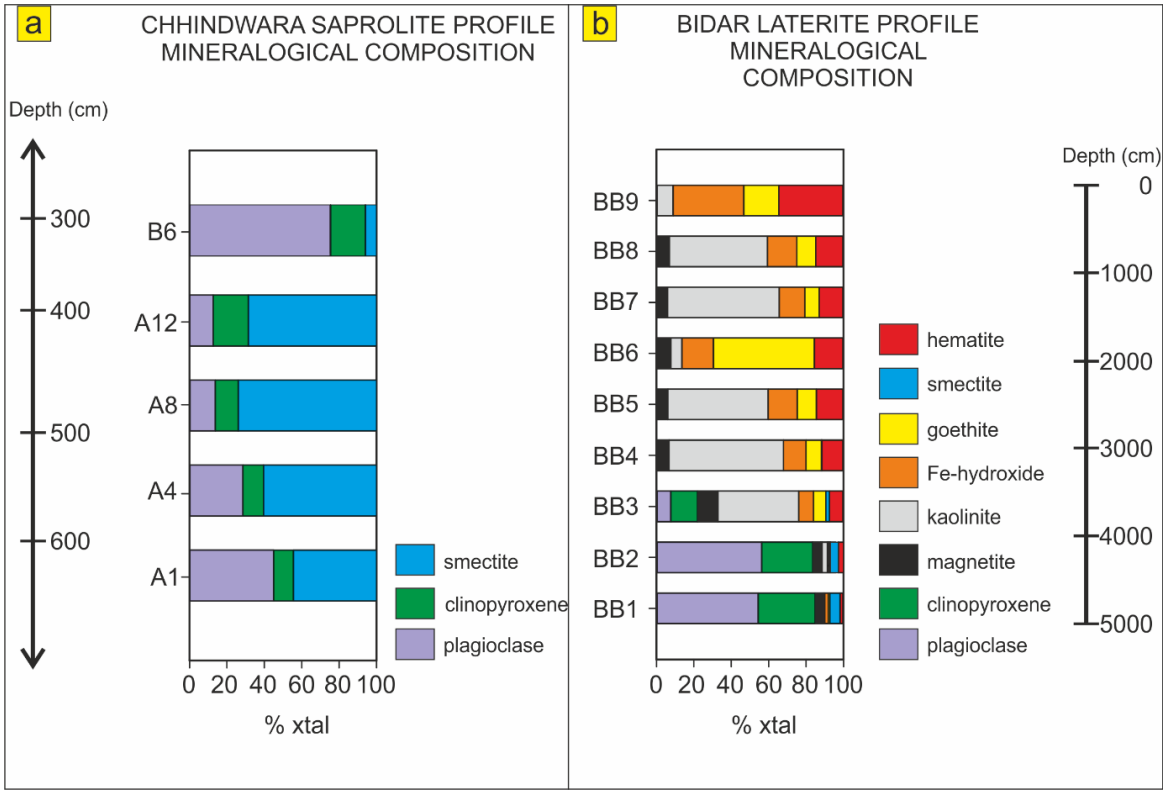

Figure 3. Quantitative XRD bulk mineralogical determination of the Chhindwara saprolite profile **(a)** and Bidar laterite profile **(b)**. The stacked horizontal bar charts represent the identified mineral phases and their respective quantities in each weathering section. Note that the quantities in Chhindwara are unlikely to reflect the correct quantities of the identified minerals, due to strong background signals as a result of amorphous phases (some clays and secondary oxides). Regardless, high quantites of smectite have been identified and agree to the findings of previous studies (Babechuk et al., 2014; 2015). For further information see also the supporting information.

In the Bidar profile, plagioclase, clinopyroxene and magnetite are the primary mineral phases (Figure 3b). In sample BB3, enhanced formation of kaolinite is evident, whilst in sample BB4, primary silicates have been transformed entirely to secondary clays (mainly kaolinite) and Fe-oxides (hematite, goethite, Fe-oxyhydroxides). From section BB4 to BB5, slightly higher quantities of Fe-oxides were measured, whereas at the palaeo-water table sample (BB6) > 90% of Fe-oxides, particularly goethite, are recorded. Above this level, the weathering progresses as expected, with kaolinite decreasing as Fe-oxides increase upwards to the tubular/nodular cap (BB9). This nodular cap contains ≥ 90% Fe-oxides.

4.2. LA-ICP-MS element maps

Thin section petrography shows that the parent dolerite rock of the lower flow is mainly composed of clinopyroxene, plagioclase, volcanic glass, and Fe-Ti oxide (Supplemental Figures 4; 6). The LA-ICP-MS element maps show that Zn was mainly hosted within the primary Fe-Ti oxide, pyroxene and volcanic glass (Supplemental Figure 6b). The concentration of Zn and Mg are lower in the weathered Mg-Fe silicate (Supplemental Figure 7) than in unaltered clinopyroxene (Supplemental Figure 6), whereas the concentration of Fe is higher. In the bedrock of the Bidar laterite, Zn is mainly hosted within pyroxene and primary Fe-Ti oxide (Supplemental Figure 8a). In the palaeo-water table sample, Zn is enriched in the Fe-oxyhydroxides (Supplemental Figure 8b). In the nodular cap on top of the profile (Supplemental Figure 8c), Zn is mainly depleted in Fe-oxyhydroxide rich areas, with the exception of a small vein that exhibits similar Zn enrichment as the Fe-oxyhydroxides in the palaeo-water table sample.

4.3. Transition metals (Zn, Fe^{III}/Fe^{II}, Mn) and MgO (wt%) in the Chhindwara saprolite profile

Various transition metal ratios and MgO abundances are presented in Table 1 and Figure 4. Babechuk et al. (2015) showed that the high field strength element (HFSE) ratios of Zr/Hf and Nb/Ta do not deviate by ≥ 3% in all samples within both flows of the Chhindwara profile. Niobium and Ta were found to be the least-mobile elements for mass calculations (see also Kurtz et al., 2000). Therefore, Zn, Fe and manganese (Mn) concentrations were normalised to Nb. In contrast to Nb, Zn exhibits greater mobility within both flows of the Chhindwara profile and in most cases the Zn/Nb ratios of the weathered samples are lower compared to the Zn/Nb ratios of unweathered protolith (ChQB12; Table 1).

Overall, the chemostratigraphical trends of Zn/Nb and MgO (wt%) are similar (Figure 4a, b). This is particularly obvious at the weakly banded base of the upper flow (lowermost 80 cm), where diminished release of MgO (wt%) is accompanied by a minor loss of Zn (samples ChQB3 and ChQB2). Enrichment of Fe(III) and Mn also occurred in this weakly banded base (Figure 4 c, d). By contrast, in both top soil samples from this

flow (ChQB10 and ChQB11), Mn/Nb is depleted, whereas Zn/Nb in ChQB10 is slightly enriched. In the less weathered formerly columnar central section of the upper flow, a modest enrichment in Zn/Nb is linked to slightly higher MIA values of 41 and 50 in samples ChQB7 and CHQB9d respectively. In the lower flow, from top to bottom of the profile, Zn/Nb as well as MgO (wt%) are more strongly depleted than in the less weathered upper flow. However, fluctuations in the depletion trend of Zn/Nb are found which correlate with the weathering trend of Mn/Nb.

Weathering trends based on elemental mass-balance calculations are listed in Table 1, whereby the change in an element of interest is expressed relative to the least-weathered parent rock (ChQB12). The respective loss and gain of an element in a sample is calculated after normalisation to an immobile or least-mobile element for both the sample and the parent rock in the formula (Table 1; e.g., Brimhall and Dietrich, 1987; Kurtz et al., 2000; Kisakürek et al., 2004; Babechuk et al., 2015).

$$\% \text{ change in R} = \left[\frac{(Rsample - Rprotolith)}{Rprotolith}\right] x\ 100$$

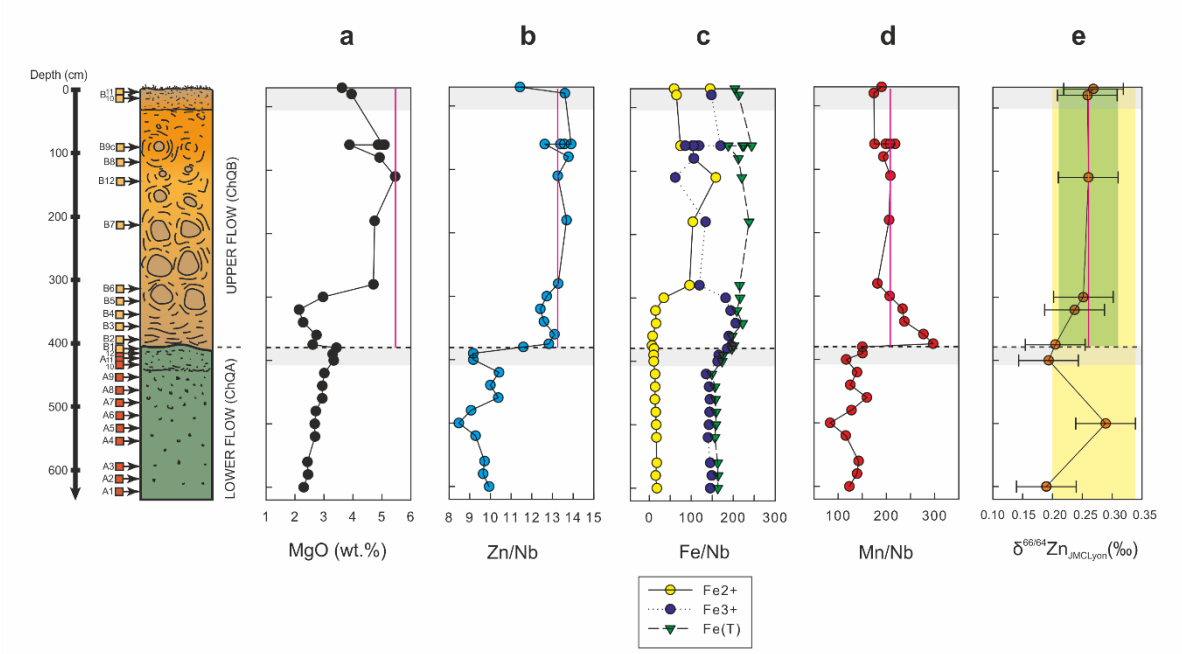

Figure 4. Chhindwara saprolite profile: **(a)** MgO (wt%); **(b)** Zn; **(c)** molar Fe; **(d)** molar Mn; **(e)** Zn isotope ratios ($\delta^{66/64}Zn_{JMCLyon}$); Zn **(b)**, Fe **(c)** and Mn **(d)** represent ratios normalised to Nb. All diagrams are plotted against depth below the soil surface. Profile sketch from Babechuk et al. (2014). The contact between the two

flows (ChQA and ChQB) is illustrated. Sample ChQB9a-d at a depth of 90 cm represent a corestone transect from centre (9d) to rim (9a). The uppermost three samples in the lower flow (ChQA10-ChQA12) constitute the porous, paleo-flow top. The pink vertical line in **(a) (b) (d) (e)** represents the protolith composition/ratio (ChQB12). The green bar in **(e)** represents the analytical uncertainty (2SD) of the protolith and also the analytical uncertainty of each sample is illustrated. The yellow field in **(e)** represents the compositional range of the crustal average of $\delta^{66}Zn_{JMC\text{-}Lyon}$ (+ 0.27 ± 0.07‰, 1SD) (Little et al., 2016).

The Zn/Nb ratio within the upper flow indicates a deviation from the protolith of ~ − 14% to + 5%. Stronger fluctuations are evident for Mn of ~ -16% to +43%. A sharp depletion trend of Zn and Mn marks the transition between the upper (ChQB) and lower flow (ChQA) and the enhanced release of Zn correlated with increased weathering intensity is evident. The loss corresponds to deviation from the protolith of between ~ − 13% to − 36% for Zn and − 23% to − 60% for Mn, respectively.

4.4. Transition metals (Zn, Mn) and Fe_2O_3 (wt%) in the Bidar profile

The Zn and Fe_2O_3 (wt%) results are presented in Table 1 and Figure 5, with Zn normalised to Nb. Fe_2O_3 (wt%) is not plotted *vs* an immobile element, since it itself is an immobile element in the oxidative environment. From the bedrock upwards into the indurated laterite cap, an overall depletion trend in Zn/Nb is evident. The exception is the iron dominated palaeo-water table sample, where Zn/Nb is enriched. Generally, with strengthening weathering intensity, the amount of Fe_2O_3 (wt%) increases, resulting in a maximal enrichment of Fe_2O_3 (77.5 wt. %) in the strongest weathered section, i.e. the top of the nodular cap (BB9). Excluding the palaeo-water table sample (BB6), Zn concentrations are moderately anti-correlated with Fe_2O_3 (wt%) ($r^2 = 0.65$; not shown). When expressed relative to the least-weathered parent rock, a maximum loss of ca. 80% in Zn is calculated for the most weathered section of the lateritic profile (BB9), whereas the palaeo-water table (BB6) is enriched by ~ 250% (Table 1). In general, the TOC is low in the Bidar profile (Table 1; Figure 5d). Starting from the bedrock sample (BB1) with a TOC of 0.07%, TOC increases moderately upwards with the exception of samples BB4 (0.51%) and BB9 (0.32%) that are relatively enriched compared to the protolith.

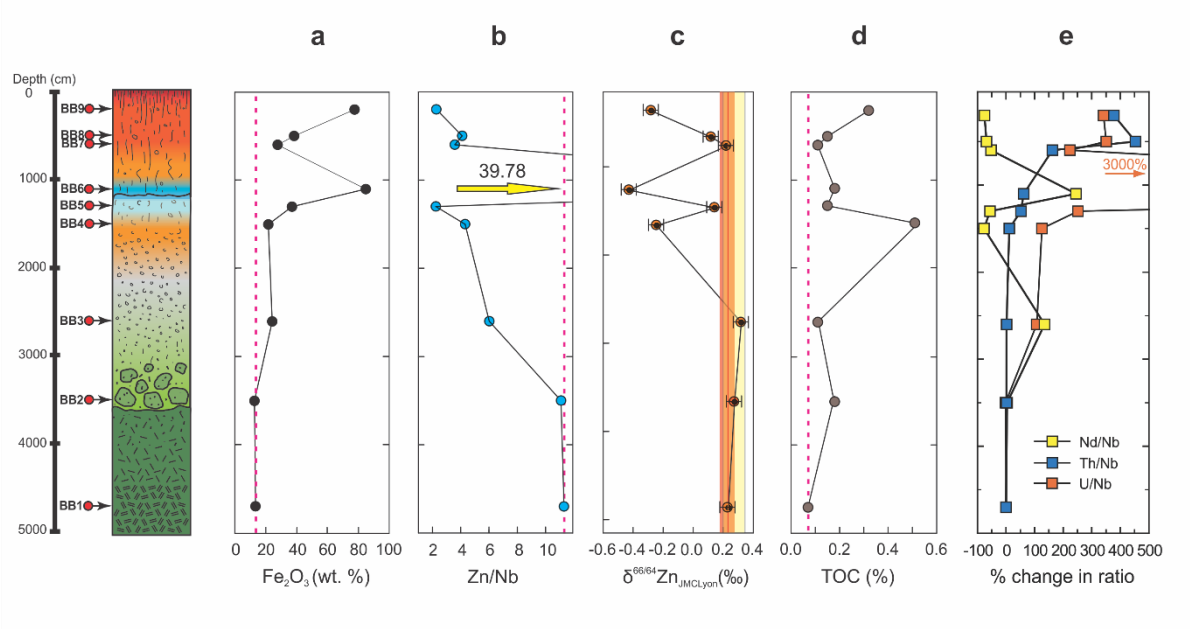

Figure 5. Bidar laterite profile: **(a)** Fe_2O_3 (wt%); **(b)** Zn ratios normalised to Nb; **(c)** Zn isotope ratios ($\delta^{66/64}Zn_{JMCLyon}$); **(d)** TOC (%); **(e)** % change in ratio of dust derived elements (Nd, Th, U) (normalised to Nb) relative to the protolith (Babechuk et al., 2015); The dashed purple vertical line in **(a)**, **(b)**, **(d)** represents the protolith composition/ratio (BB1). The red bar in **(c)** represents the analytical uncertainty (2SD) of the protolith. The yellow field in **(c)** represents the compositional range of the crustal average of $\delta^{66}Zn_{JMC\text{-}Lyon}$ (+ 0.27 ± 0.07‰, 1SD) (Little et al., 2016).

4.5. Zn isotopic composition in both profiles

The Zn isotope data are presented in Table 1 and Figures 4 and 5. Differences in the $\delta^{66}Zn_{JMC\text{-}Lyon}$ composition relative to the protolith ($\delta^{66}Zn_{sample}$ - $\delta^{66}Zn_{protolith}$) are expressed as $\Delta^{66}Zn_{sample\text{-}protolith}$ and tabulated (Table 1). In the Chhindwara saprolite profile (Figure 4e), the parent basalt has a $\delta^{66}Zn$ value of +0.260 ± 0.018‰ (2 SE) relative to JMC Lyon standard. The values of $\delta^{66}Zn_{JMC\text{-}Lyon}$ in the Chhindwara saprolite profile range from + 0.190 ± 0.024‰ to + 0.289 ± 0.020‰. The degree of isotope fractionation across the entire profile is very low outside of external reproducibility.

In the Bidar laterite profile (Figure 5c), the parent basalt has a $\delta^{66}Zn_{JMC\text{-}Lyon}$ value of + 0.231 ± 0.014‰ (2SE), very similar to the Chhindwara bedrock. The saprolitic, clay-rich zones (BB2-BB3) also exhibit a very low degree of isotope fractionation, respectively, whereas in the more strongly weathered, secondary Fe-oxide rich part, lighter Zn compositions are found. In particular, the palaeo-water table (BB6) and nodular cap (BB9)

samples that are very strongly enriched in Fe-oxides are depleted, with $\Delta^{66}Zn_{sample\text{-}protolith}$ values of − 0.660‰ and − 0.514‰, respectively. Furthermore, sample BB4 exhibits a lighter Zn isotopic composition with a $\Delta^{66}Zn_{sample\text{-}protolith}$ value of − 0.478‰, while samples BB5 (− 0.091‰), BB7 (− 0.013‰) and BB8 (− 0.115‰) show less fractionated Zn isotope compositions compared to the protolith value. In summary, the Bidar profile becomes enriched in lighter Zn isotopes towards the top, even though excursions within this overall depletion trend are evident. All Zn isotope data are interpreted using the laboratory long-term reproducibility of the in-house solution standard (2SD = ± 0.051‰) to apply the highest analytical uncertainty.

5. Discussion

In the following sections, elemental and isotopic trends of Zn in both profiles are interpreted in conjunction with the quantitative XRD mineralogy (Figure 3), the LA-ICP-MS element maps (Supplemental Figures 6−8), weathering indices (CIA, $MIA_{(O)}$) as well as selected major element abundances (Fe, Mn; Table 1). As the Bidar profile involves an older, more complex and more prolonged weathering history, additional chemostratigraphic information (TOC values and previously published elemental dust signatures (Nd, Th, U) (Figure 5e) from Babechuk et al. (2015) are also compared to the Zn isotope systematics, to help elucidate the different environmental processes that were involved in laterite formation and to understand which mineral reactions promoted Zn mobility. In the final section, we discuss the relevance of the observed Zn behaviour within the hydrosphere and anthroposphere.

5.1. Chhindwara saprolite profile- Zn and Zn isotopes

The LA-ICP-MS maps of the Chhindwara bedrock provide evidence that primary Fe-Ti oxides host the highest concentrations of Zn. They are unlikely to contribute to Zn loss because of their strong resistance to weathering (e.g., Nesbitt and Wilson, 1992). By contrast, clinopyroxene is a major carrier and volcanic glass a minor carrier of Mg, where

Zn^{2+} substituted at trace concentrations for Mg^{2+}. The breakdown of pyroxene and volcanic glass resulted in release of both elements beginning with incipient weathering (Supplemental Figures 6; 7). This explains the coupled behaviour of Zn/Nb ratios with MgO% in the upper flow of the profile. In the lower flow, greater amounts of Zn and MgO% have been released, but Zn/Nb correlates with Mn/Nb ratios, which points to a minor association of Zn with a Mn-rich phase (Figure 4). Additionally, the minor release of Zn in areas of Mn/Nb and Fe^{III} enrichment at the weakly banded base of the upper flow, suggests coupled behaviour between Zn and secondary oxides.

Regardless, the release of Zn is mainly associated with the chemical breakdown of the Mg-rich phases (pyroxene: ~ 120 µg/g and volcanic glass: < 40 µg/g) that became converted into smectite and secondary oxides (Figures 3a; 4; and Supplemental Figures 6; 7). Overall, this means that a net loss of Zn occurred as a result of these mineral transformations. This is also confirmed by the CIA values that lie within the range of smectite in the more strongly weathered sections (values between 70 and 85) (Nesbitt and Young, 1982; Nesbitt and Wilson, 1992) and its correlation with the MIA(o) (Table 1; Figure 4, indicating the similar bulk weathering behavior of Mg, calcium (Ca), and sodium (Na) in the profile ($R^2 = 0.9$; Babechuk et al., 2014). As a result of this alteration, ca. 35% of the mobile Zn fraction was lost from the more strongly weathered part of the saprolite.

In the top soil, biological processes might explain the very slight enrichment of Zn (CHQB10) via adsorption or complexation with soil organic matter (SOM), while Zn depletion (ChQB11) was possibly caused by preferential uptake into vegetation. Atmospheric inputs into the top soil are unlikely because the addition of dust to the profile was minimal (Babechuk et al., 2015).

Zn isotopic fractionation remains within the analytical uncertainty (2SD) of the protolith and overlaps with the "crustal average" of $\delta^{66}Zn_{JMC\text{-}Lyon}$ (+ 0.27 ± 0.07‰) (Little et al., 2016). This implies that the flux of elemental Zn to the hydrosphere from saprolite and incipient weathering fronts of Deccan basalt (deeper CZ) has an isotopic composition within the range of "lithospheric" Zn (e.g., Little et al., 2014).

5.2. Bidar laterite profile - Zn and Zn isotopes

The lower sections of the profile (BB2-BB3) display similar elemental and isotopic weathering behaviour of Zn comparable to the Chhindwara profile and only a slightly higher loss of Zn (ca. 45%) in BB3 is evident. By contrast, the more extreme weathering intensity in the upper sections of the Bidar profile resulted in a Zn loss of up to 80% (BB5, BB9) and lighter Zn isotope compositions developed. Based on the quantitative mineralogical analyses (Figure 3b), the loss of the additional 35% of Zn in the upper sections of the Bidar profile must be related to the transformation from smectite to kaolinite and Fe-oxides (hematite, goethite, and Fe-oxyhydroxides). The critical role of the mineralogical transformations from bedrock to laterite can be further visualised by detailed petrography and the LA-ICP-MS trace element maps, which illustrate that the secondary Fe-oxides exhibit an inherently low Zn content in the lateritic weathering residue (Supplemental Figures 5; 8a, c). This is also confirmed by the enrichment in Fe_2O_3 (wt%) and decreasing Zn/Nb ratios towards the top of the profile (Figure 5). An exception to the overall depletion trend of Zn is represented by the palaeo-water table (Figures 3b; 5; Supplemental Figure 8b), where anomalous Zn enrichment of 252% is evident (sample BB6, Table 1). This is explained by the iron oxide enrichment in this sample that likely resulted from a significant net input of groundwater-transported Fe^{2+} and oxic rainwater, which facilitated the oxidation to Fe^{3+} and subsequent precipitation as ferric oxides (e.g. Kısakürek et al., 2004). Thus, the same process may have resulted in the enrichment of Zn.

The relationship between Fe-oxide development and Zn mobility is also reflected by the Zn isotopic fractionation in horizons that are enriched in Fe_2O_3 (wt%) (Table 1). Fractionation resulted in depleted values up to 13 times larger than analytical uncertainty (2SD). Excluding sample BB4, increasing lighter Zn isotope ratios correlate strongly with Fe_2O_3 (wt%) ($R^2 = 0.944$; Figure 6a), whereas a moderate correlation is evident for all samples ($R^2 = 0.622$). The oxyhydroxide development may be associated with the retention of lighter Zn ($\Delta^{66}Zn_{sample\text{-}protolith}$ of up to − 0.660‰ in the palaeo-water table) (Figures 3b; 5a-c; Supplemental Figure 8; Table 1).

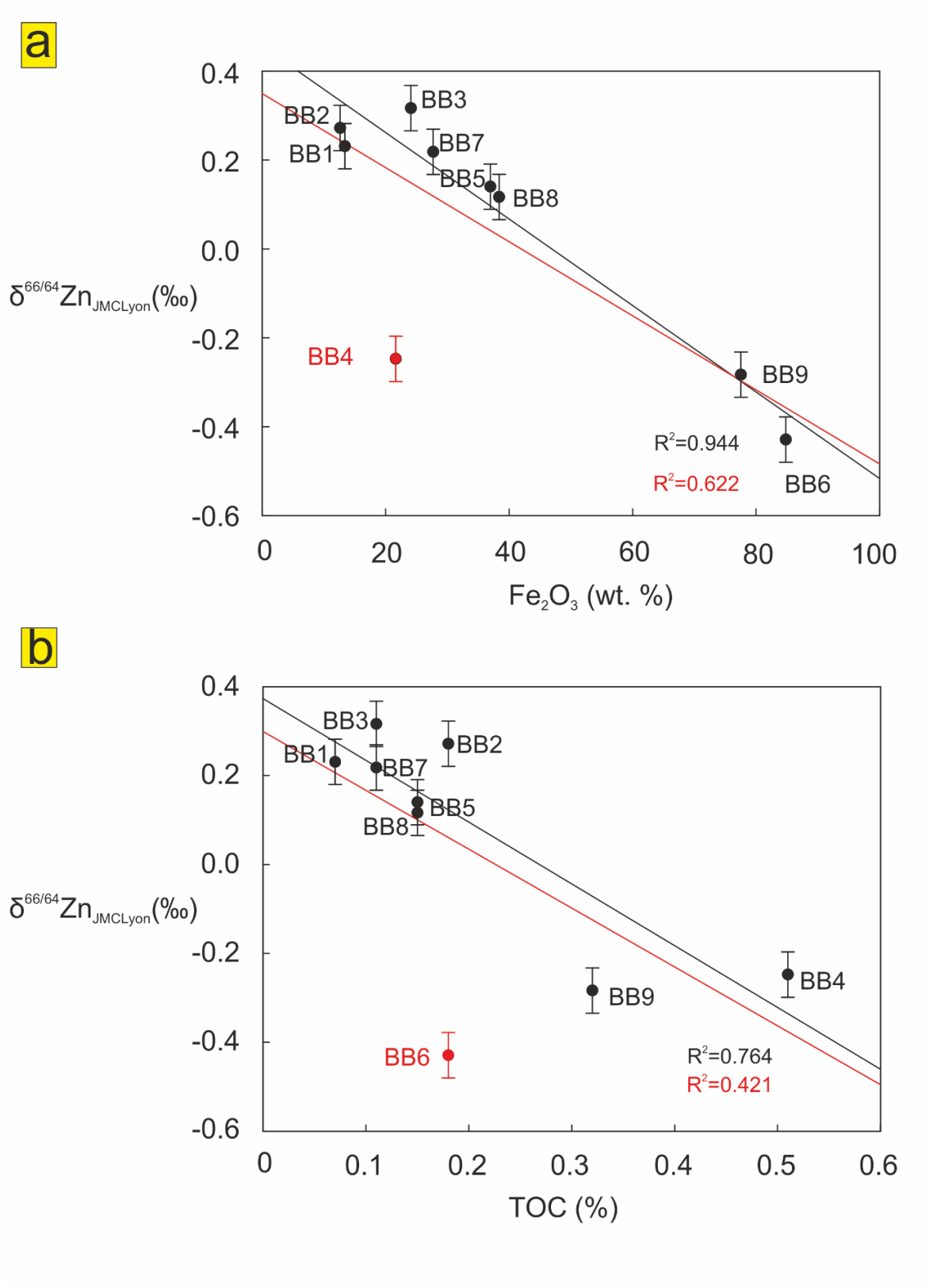

Figure 6 (a) Binary diagram of $\delta^{66/64}Zn_{JMCLyon}$ (‰) and Fe_2O_3 (wt%) of the Bidar laterite profile. Excluding sample BB4, a very good correlation ($R^2 = 0.944$) between $\delta^{66/64}Zn_{JMCLyon}$ (‰) and Fe_2O_3 (wt%) is evident, whereas under consideration of all samples a regression line is defined that indicates a moderate correlation ($R^2 = 0.622$). Analytical uncertainty of $\delta^{66/64}Zn_{JMCLyon}$ (‰) = 2SD. **(b)** Cross plot of $\delta^{66/64}Zn_{JMCLyon}$ (‰) and

TOC (wt%) for samples from the Bidar laterite profile. Excluding sample BB6, a strong correlation (R^2 = 0.764) is evident, whereas the complete dataset results in a much more modest correlation (R^2 = 0.421). Analytical uncertainty of $\delta^{66/64}Zn_{JMCLyon}$ (‰) = 2SD.

However, the deviation of sample BB4 from the correlation trend (Figure 6a) suggests that a first order relationship between oxyhydroxide development and the extent of fractionation towards lighter $\delta^{66}Zn_{JMC\text{-}Lyon}$ is not necessarily always linked. In the following section, the possible pedological processes in laterite are discussed and contrasted with the sub-recent, clay-rich Chhindwara saprolite profile.

5.3. Processes affecting the Zn isotope composition in laterite

5.3.1. The impact of abiotic weathering processes on isotopic Zn

In general, the preferential adsorption of lighter Zn on secondary oxides in weathering profiles (Viers et al., 2007; Vance et al., 2016; this study) contradicts most experimental studies. In such studies, heavier Zn isotopes adsorb on Fe-oxyhydroxide (Juillot et al., 2008; Pokrovsky et al., 2005). Only in the early stages of such experiments is adsorption of isotopically lighter Zn on the surface sites observed and explained by short-lived kinetic isotope effects. After a relatively short time, however, the experiments evolve to steady state (*i.e.* equilibrium fractionation) and to high ionic strength, with preference to heavier Zn on the mineral surfaces. Since the ionic strength in laterites is low (e.g., Robson and Gilkes, 1980, Dolling and Ritchie, 1985, Chairidchai and Ritchie, 1990), the preferential adsorption of lighter Zn on the surface sites of secondary oxides is possible. Such a pedological process might also cause the incorporation of lighter Zn into secondary oxides. However, the strong fractionation towards lighter Zn in the metal enriched palaeo-water table sample (BB6) is not explainable with this process, so we propose that two different mechanisms might be responsible for the enrichment in lighter Zn isotopes.

Firstly, pH-dependent sorption experiments (3 < pH < 8) on goethite surfaces (Pokrovsky et al., 2005) showed enrichment of lighter Zn by about 0.2‰ with decreasing pH values. Lateritic soils develop in low pH (2−5) environments (e.g., Wimpenny et al.,

2007) and the oxidation of Fe^{2+} to Fe^{3+} results in a release of protons into solutions. This means that the formation of secondary Fe-oxides exerts a control on decreasing pH and may explain the isotope fingerprint in the goethite-rich palaeo-water table (Figure 3b and Supplemental Figure 8b) or nodular cap (BB9) of the Bidar profile. However, it must be noted that the adsorption of lighter Zn on goethite might be alternatively related to short-lived kinetic effects (Moynier et al., 2017) and that it was not confirmed in other pH experiments (e.g., Julliot et al. 2008). Secondly, changes in the redox state of the Bidar profile might have caused the lighter Zn composition in the palaeo-water table sample (BB6). For instance, spinel and chromite have lighter Zn compositions (Luck et al., 2005; Chen et al., 2013). The dissolution of Fe^{2+} from such refractory phases in reducing environments below the water table could have vertically transported lighter Zn upwards the profile where it precipitated with Fe-oxides.

Regardless of the mechanisms responsible for the formation of Fe-oxyhydroxides in laterite, the absence of such processes in younger, clay-rich weathering substrates from the deeper CZ (Chhindwara profile and Bidar saprolite) might explain the lack of Zn isotope composition departing significantly from the crustal average (Little et al., 2016). The enhanced formation of Fe-oxyhydroxides is therefore one key process to explain Zn isotope fractionation towards lighter values.

5.3.2. The significance of biotic processes on isotopic Zn in the Bidar laterite profile

The increasingly open and porous structure of the profile upwards from BB4 to BB9 (Babechuk et al., 2015) provides pathways for mobile colloidal particles in percolating meteoric water, and the chemostratigraphical trends of TOC and $\delta^{66}Zn_{JMC\text{-}Lyon}$ demonstrate a likely association (Figure 5c, d). This relationship is as also evident from the inverse correlation of lighter $\delta^{66}Zn_{JMC\text{-}Lyon}$ with higher TOC ($r^2 = 0.421$; and $r^2 = 0.764$, excluding the palaeo-water table sample BB6; Figure 6b). The reddened, kaolinite rich saprolite section of the Bidar profile (BB4) contains the highest TOC % of all samples and departs from the positive correlation trend of lighter $\delta^{66}Zn_{JMC\text{-}Lyon}$ with Fe_2O_3 (wt%) (Figure 6a).

Hence, biochemical reactions likely affect fractionation of Zn isotopes and possibly its association with specific soil minerals.

Zinc is normally complexed to organic ligands in soil solutions and Vance et al. (2016) and Opfergelt et al. (2017) suggested that they can preferentially transport heavier Zn out of soils. This is in agreement with experimental studies which have shown that Zn adsorbs on humic acids, resulting in a Zn pool heavier than the corresponding free aqueous ion by 0.25‰ (Jouvin et al., 2009). Apart from that, Houben et al. (2014) demonstrated that heavier Zn isotopes are preferentially retained in roots of plants ($\Delta^{66}Zn_{root-shoot}$ = +0.24 to +0.40‰). As a result, the residual soil solution contains isotopically lighter Zn that may adsorb on mineral surfaces. The loss of heavier Zn through mobilisation of solid organic material (Vance et al., 2016) and lighter Zn soil solutions are potential mechanisms to explain the lighter Zn composition in the ferruginous sections of the Bidar profile. However, the previously outlined abiotic fractionation mechanisms suggest that biotic fractionation alone is unlikely to explain the lighter compositions in samples BB4 and BB9 ($\Delta^{66}Zn_{sample-protolith} \sim -0.5$‰).

5.3.3. Dust addition and redistribution of elemental and isotopic Zn

Aeolian dust input is a likely means of altering elemental and isotopic compositions in the Bidar profile, especially where input material is of significantly different composition and antiquity to that of the basalt protolith. Further, the documented extent of dust addition is not limited to the top soil (Babechuk et al., 2015), and dust appears to have been washed into the porous and tubular layers that characterise the upper portions of the laterite profile. Potentially, Zn, as well as Fe could at least partly be derived from aeolian dust sources (e.g., Taylor et al., 1983; Gallet et al., 1996; McLennan, 2001). Importantly, inspection of the trace element maps of Fe and Zn from the nodular cap (BB9) reveals a strong enrichment of both elements on the microscale in Fe-oxide rich veins (Supplemental Figure 8c). These could represent segregation pathways of dust-derived material into the laterite (Widdowson, 2007).

Several sections (BB 3, 4, 5, 6, 7, 8, 9) of the Bidar laterite show complex enrichment and redistribution trends of U, Nd, and Th, which were at least in part attributed to dust input (Figure 5e; Babechuk et al., 2015). Zinc concentration shows a relationship to Th in the topmost samples of the laterite (BB7–BB9). In combination, the trace element maps and chemostratigraphical trends therefore suggest that whilst dust-derived Zn has likely entered the profile, it did so without causing the relative enrichment intensities observed for other elements.

According to Little et al. (2014; 2016), average dust $\delta^{66}Zn_{JMC\text{-}Lyon}$ values lie between + 0.33 and + 0.37‰. These values are similar to the Bidar bedrock within analytical uncertainty, whereas aerosols from tropical latitudes can be ca. + 0.2‰ heavier (Little et al., 2014). An "isotopic overprint" from such sources might explain why the $\delta^{66}Zn_{JMC\text{-}Lyon}$ of BB7 is nearly indistinguishable from the Bidar bedrock or why sample BB3 illustrates a slight offset from the linear regression line towards heavier Zn isotope value (Figure 6a). Regardless, the palaeo-water table sample (BB6) is characterised by the highest allochthonous input to the profile and exhibits the lightest Zn isotope composition in the profile. In summary, despite evidence for aeolian input, the previously described in situ pedological processes likely dominated the isotopic evolution of Zn in most sections of the Bidar profile.

5.4. Relevance for Zn deficiency in crops grown in (sub)-tropical environment

Mineralogical transformations in the weathering process ultimately lead to inherently low Zn contents in laterite and, depending on the type of soil classification system, also in ferralsols and oxisols elsewhere (Figures 5a, b; 7a, b).

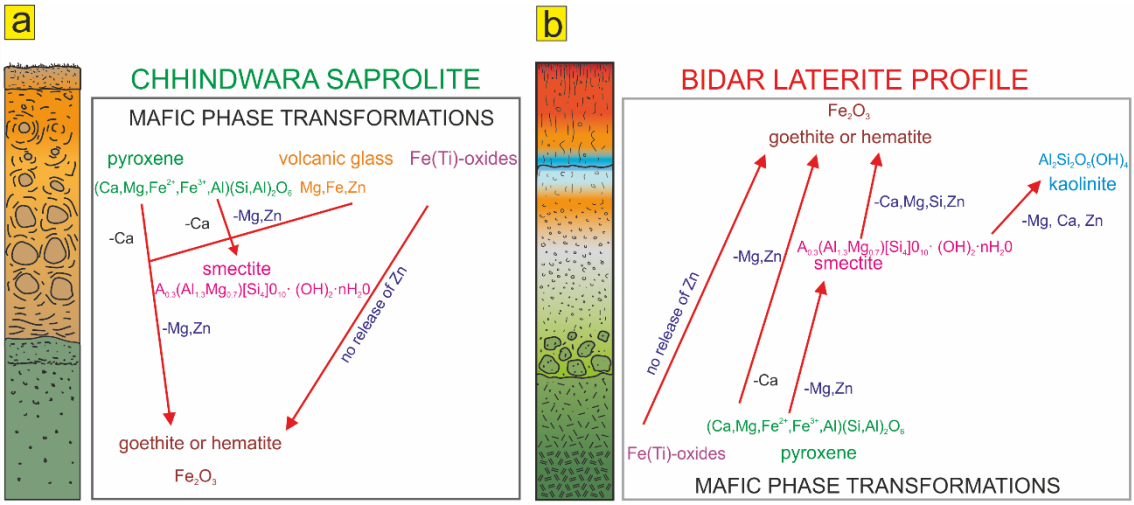

Figure 7. (a) Mineralogical transformations of primary mafic phases (pyroxene, volcanic glass) in the process of saprolitisation; **(b)** Mineralogical transformations of pyroxene and smectite in the process of lateritisation (Anand, 2005; Noack et al., 1993). The weathering resistance of the primary Fe-Ti oxides results in the retention of some amounts of Zn with respect to the overall soil budget. All other minerals undergo mineralogical transformations that result in a loss of Zn, so that an inherently low content of Zn in the weathering residue/soil develops. Note that the "weathering vectors" in Chhindwara **(a)** and Bidar **(b)** differ, since the incipient to intermediate weathering stages in basalt are still texturally controlled, whereas the weathering progression in the stronger weathered Bidar laterite profile increases upwards the profile, likewise to " typical textbook" soil profiles.

With respect to the availability of Zn to plants, it is noteworthy that much of the remaining residual pool of Zn remains bound in refractory phases: either within primary oxides, or in the weathering products hematite, goethite, and Fe-oxyhydroxides (Figures 3b; 5a, b; Supplemental Figure 8) (e.g., Nesbitt and Wilson, 1992). As a result, the supply of Zn to plants can be severely limited on lateritic soils, even when a residual Zn pool is present. This is one reason why even Zn-rich bedrock, such as basalt, can develop into a residue with inherently low bioavailable Zn.

The trace element maps presented in this study illustrate this scenario (Supplemental Figures 6−8). In samples where Zn is hosted by refractory minerals, measurement of the subsoil Zn concentration via assay alone is not sufficient to determine the quantity of bioavailable Zn. The relatively spare available data, including the results from this study, suggest that light Zn isotope composition in subsoil may be an indication of poor bio-availability of Zn. By contrast, subsoil Zn isotope ratios within the crustal average (e.g., Little et al., 2014; 2016) may show that the inorganic pool of bio-available Zn has not been

evacuated from the soil reservoir. Thus, there is potential that Zn isotopes may eventually serve to fingerprint subsoils with poor Zn bioavailability.

A striking result of global geochemical and soil distribution atlases is that the CZ in many tropical and subtropical regions is strongly depleted in most bio-essential elements (Fyfe et al., 1983). We propose that this is not solely due to the climatic control on the type of weathering but also because stable continental regions (cratons) underlie these soils. Cratons are characterised by remarkable tectonic quiescence with resulting low denudation rates (e.g., Hewawasam et al., 2013). In (sub)-tropical regions, they are typically covered by laterite residues. Fresh bedrock and/or smectite rich regolith of the deeper CZ is only rarely exposed at the surface of cratonic regions of India, Africa, South America, and Australia. The development of widespread and stable laterite in such areas severely limits the natural re-supply of Zn from fresher rock material at depth.

We further propose that it is not a coincidence that Zn deficient soils, highly depleted weathering residues (i.e. lateritic soils), and cratons show general geographic superposition within the tropical belt (Figure 8a, b, c). Agricultural cultivation in these areas may therefore be inherently challenging in terms of micronutrients, with knock-on effects such as growth abnormalities (e.g., Alloway, 2009); including stunted growth, small leaves and sterility, increased susceptibility to damage by high light intensity, as well as propensity for fungal infection (e.g., Cakmak, 2000; Alloway, 2009). Zn deficiency in subsistence farmers in subtropical-tropical cratonic areas may be magnified by their over-dependence on crops local for diet (Figure 8d; Wessells and Brown, 2012; Andersen, 2002).

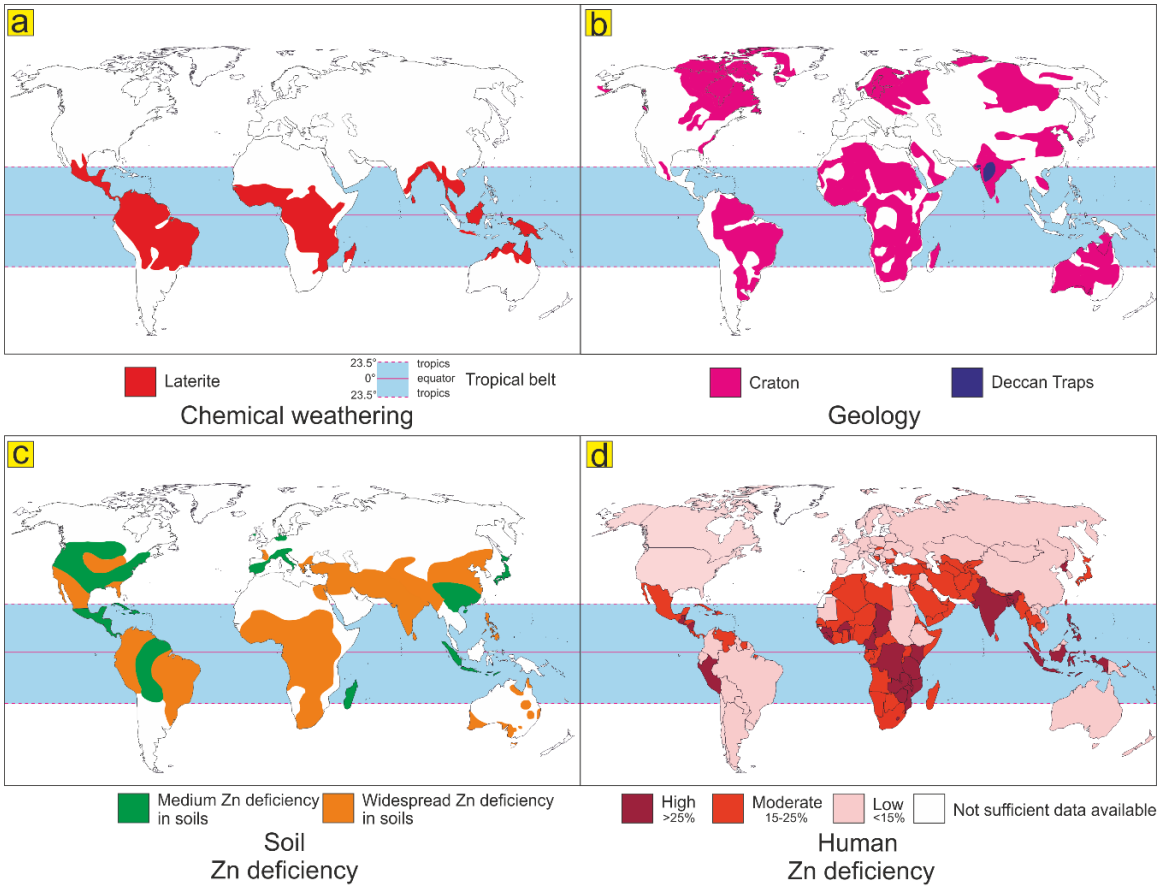

Figure 8. Geographical overlap between the global distribution of **(a)** laterite soils (Gidigasu, 2012 and references therein), **(b)** cratons (USGS, 1997; Tang et al., 2013) and **(c)** Zn deficient soils (Alloway, 2008). The correlation demonstrates that the tectonic stability of cratons (India, Africa, South America and Australia) in the tropics (blue defines the tropical region) hinders the exposure of Zn rich bedrock to the surface, potentially explaining why world crops in tropical regions lack in Zn (Alloway, 2008); **(d)** Human Zn deficiency (Wessells and Brown, 2012).

Finally, at least in some areas (e.g. the Amazon) the isotopically light Zn of weathering residues is possibly mirrored by heavy values in the dissolved load of rivers (e.g., $\delta^{66}Zn_{JMC\text{-}Lyon}$ ca. + 0.5−0.6‰; Little et al., 2014). This suggests that analysis of (sub)-tropical river waters might be an alternative and logistically feasible way to gain valuable information on soil Zn deficiency in entire catchments from geologically challenging areas.

6. Conclusions

Our new elemental Zn and Zn isotope systematics from two contrasting weathering profiles from India have resulted in the following main findings:

1) In the sub-recent, smectite-rich Chhindwara saprolite only a small fraction of bio-available Zn has been evacuated, and Zn isotopes remained almost unchanged during weathering. By contrast, Zn is strongly fractionated in the highly weathered upper sections of the Bidar laterite, likely from a number of (a)biotic processes ($\Delta^{66}Zn_{sample\text{-}protolith}$ up to ca. -0.65‰). Enhanced formation of secondary Fe-oxyhydroxides is a requirement for fractionation towards lighter Zn ratios, while the TOC in a ferruginous, kaolinite rich section of the profile suggests that biotic processes exert control on the Zn isotope systematics as well. In both scenarios, the fractionation towards lighter Zn ratios in the subsoil develops in the absence of fertile rock debris and smectite.

2) LA-ICP-MS trace element maps are a powerful tool to investigate the mineral hosts of bio-essential trace elements in the CZ. In the Bidar laterite profile, high quantities of Zn are locked away in weathering resistant primary oxides and refractory secondary oxide phases. Hence, bulk soil analyses and depletion factors alone are not reliable indicators by which to assess the amount of bio-available Zn in soils.

3) Even on originally Zn rich bedrock, subtropical-tropical cratonic soils may experience Zn deficiency, as evident from world maps. Surface layers become severely leached and, depending on the bedrock, soils will be dominated by minerals such as gibbsite, Fe-oxides, kaolinite and quartz (see Fyfe et al., 1983). Due to the tectonic quiescence of cratonic areas, they remain covered by severely leached surface layers in the subtropics and tropics. Geology and weathering history evidently contribute to human Zn deficiency in areas where the population relies on local crops.

4) Because the Zn isotope ratios in the Chhindwara saprolite and strongly weathered upper sections of the Bidar laterite differ, Zn isotopes could eventually serve as new tool to evaluate the overall loss of Zn and storage of bio-unavailable Zn in oxides. The investigation of Zn isotopes in subsoils and rivers that drain these areas might therefore help to improve sustainable farming practices in subtropical-tropical cratonic regions where vast areas are covered by challenging soils.

Acknowledgements

This work is a contribution from the Marie Curie Initial Training Network IsoNose (www.IsoNose.eu) that is funded by the People Programme (Marie Curie Actions) of the European Union's Seventh Framework Programme FP7/2007-2013/ under REA grant agreement no [608069]. Dr. Robbie Goodhue assisted in XRD measurements and Mr. Mark Kavanagh in TOC measurements. We thank Dr. Michael G. Babechuk for Zn concentration measurements and the editorial input of Prof. Mae Sexauer Gustin. The final manuscript significantly benefitted from the suggestions of three anonymous reviewers.

7. Supporting Information

7.1. Bulk rock X-Ray diffraction patterns

7.1.1. Methodology and analytical description

The Bruker D5000 in Trinity College Dublin Geochemistry (Ireland) has a 2.2 kW Cu long fine focus (0.4 x 12mm filament), with the following optical configuration: 2.5° primary soller, 1 mm aperture diaphragm, 1 mm scattered radiation diaphragm, no secondary soller, 0.2 mm detector diaphragm and a secondary curved graphite monochromator ahead of the scintillation counter. A scan of sample was made from 3 to 40° 2θ at a speed of 1 seconds / 0.02° step at 40 kV and 40 mA. Sample rotation was applied. The bulk powder XRD patterns are reported as the relative intensity (I/Io) vs. 2Θ angle (copper (Cu) Kα). Bruker AXS, Diffrac.EVA software (2012 Release, Version 3.0) was used to interpret the trace and the International Centre for Diffraction Data, Pennsylvania, PDF-4 3+ database to provide phase matching. Further, standardless semiquantitative phase abundances were obtained applying the RIR (reference intensity ratios) method. Clay mineral identification were conducted using the techniques described by Hillier (2002) and Starkey et al. (1984) and were best in agreement to Hillier et al. (2002). For clay mineral analyses, a representative 1 g portion of each sample was placed in 50 ml graduated cylinder and DI water added up to the 50 ml mark. The sample was shaken thoroughly, subjected to ultrasound for 5 minutes and then allowed to stand for 3 hours. (Where flocculation occurred, 0.5 ml of 0.1M sodium hexametaphosphate ($(NaPO_3)_6$) was added and the dispersion process repeated). After 3 hours, a nominal <2 µm fraction was removed (from 39 mm below the surface as per Stokes' Law) using a thin diameter glass pipette and pipetted onto the surface of a Si wafer ('zero-background') and allowed to dry overnight at room temperature. The sample was run on the XRD and then placed in an ethylene glycol ($(CH_2OH)_2$) vapour (at 60 °C) overnight, before being rerun so a comparison between the air dried and glycol-solvated sample could be made.

Samples ChQB2, ChQB3 and ChQB10 were selected for qualitative XRD analysis and measured in the Central Analytical Facility at Laurentian University (Sudbury,

Ontario, Canada). All patterns were obtained from dry, untreated powders. No attempt at detailed phyllosilicate analysis (e.g., ethylene glycol treatment or heating) was made. The XRD measurement was performed with a Phillips PW 1729 X-ray diffractometer operated at 40 kV/30 mA using Fe filtered cobalt (Co) Kα radiation. The powders were scanned from 5° to 75° (2Θ) with a step-size of 0.02° and a dwell time of 2 s at each step. Phase identification was performed using PANalytical's X'Pert HighScore.

7.1.2. Results of bulk rock X-ray diffraction patterns

7.1.2.1. Chhindwara saprolite profile

Eight samples from different sample heights and weathering degrees were selected for qualitative XRD analyses (Supplemental Figures 1; 2). Additionally, the XRD patterns of Supplemental Figure 1 were used for quantitative XRD analyses. The XRD patterns in Supplemental Figure 1 follow in the progression of their weathering intensity, starting with the least weathered sample CHQB6 at the bottom of the figure. The XRD patterns show that the primary mineral phases in both flows of the Chhindwara profile consist of plagioclase and clinopyroxene. The peak intensities, however, differ in the measured samples. Generally, the peak intensities of plagioclase and clinopyroxene decrease with higher degrees of weathering. By contrast, secondary phases of smectite (nontronite) and Fe-oxide increase in the stronger weathered samples. Amorphous phases in the samples can be inferred from the background intensities. They also increase in samples that are characterised by higher intensities of weathering. The degree of formation of secondary phases is lower in the upper volcanic flow in comparison to the lower volcanic flow. Moreover, both flows in the Chhindwara profile comprise the same mineral phases that only differ in their abundance, except for sample ChQB10 where C was detected as an additional phase. Unfortunately, the techniques applied to identify different phases of clay minerals (Starkey et al., 1984) were not able to deliver better data compared to the bulk XRD analysis and confirmed that the peaks of smectite match best with nontronite. Likely, high quantities of amorphous clay minerals and oxides complicate attempts in identifying the different mineral phases in relatively low weathered soil sections (i.e., in saprolite),

since XRD analyses are most suitable for the identification of crystalline mineral phases. In addition, the Chhindwara bedrock in the lower volcanic flow derived from a dolerite sill and consist of ca. 20% volcanic glass (see also Chapter 2), which further complicates attempts in identifying the mineral phases. Hence, the quantification of smectite, plagioclase and clinopyroxene represents an estimate of the mineral phase abundance in the different sections of the Chhindwara profile.

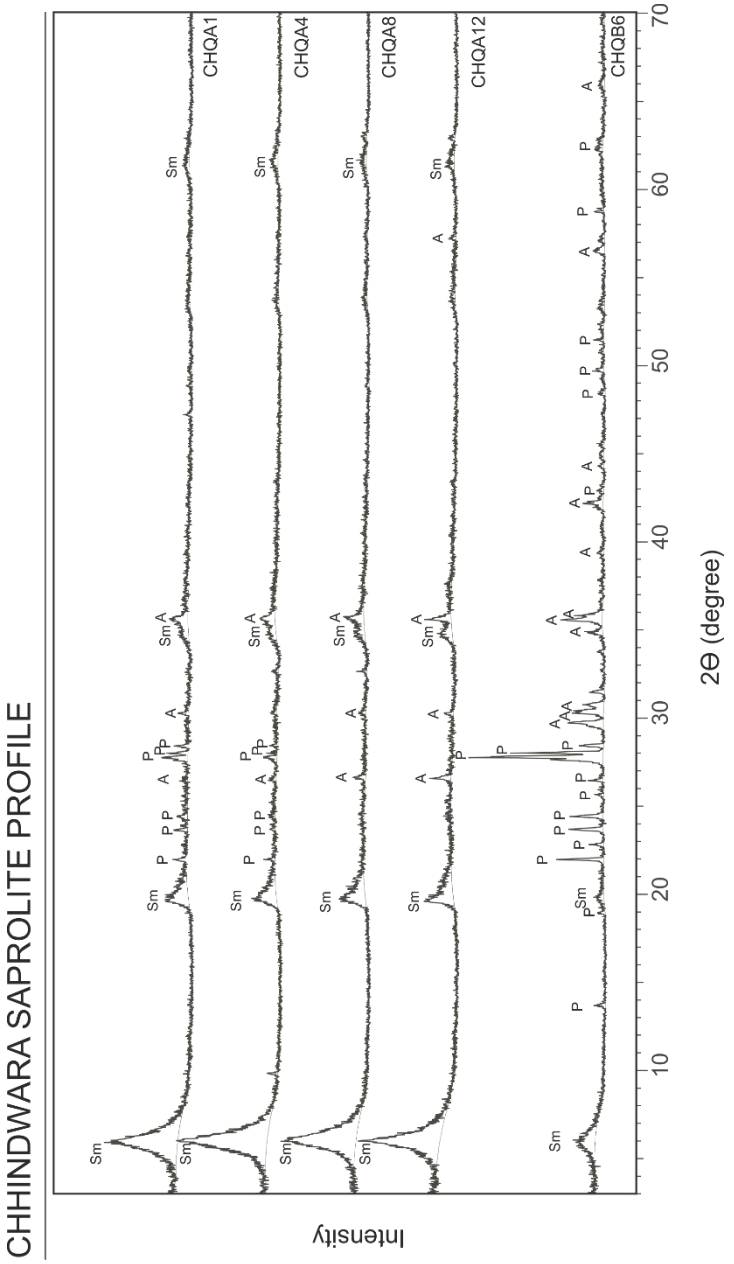

Supplemental Figure 1. Bulk powder XRD patterns of representative samples (CHQB6, CHQA12, CHQA8, CHQA4 and CHQA1) of the Chhindwara saprolite profile. P, plagioclase; A, augite; Sm, smectite.

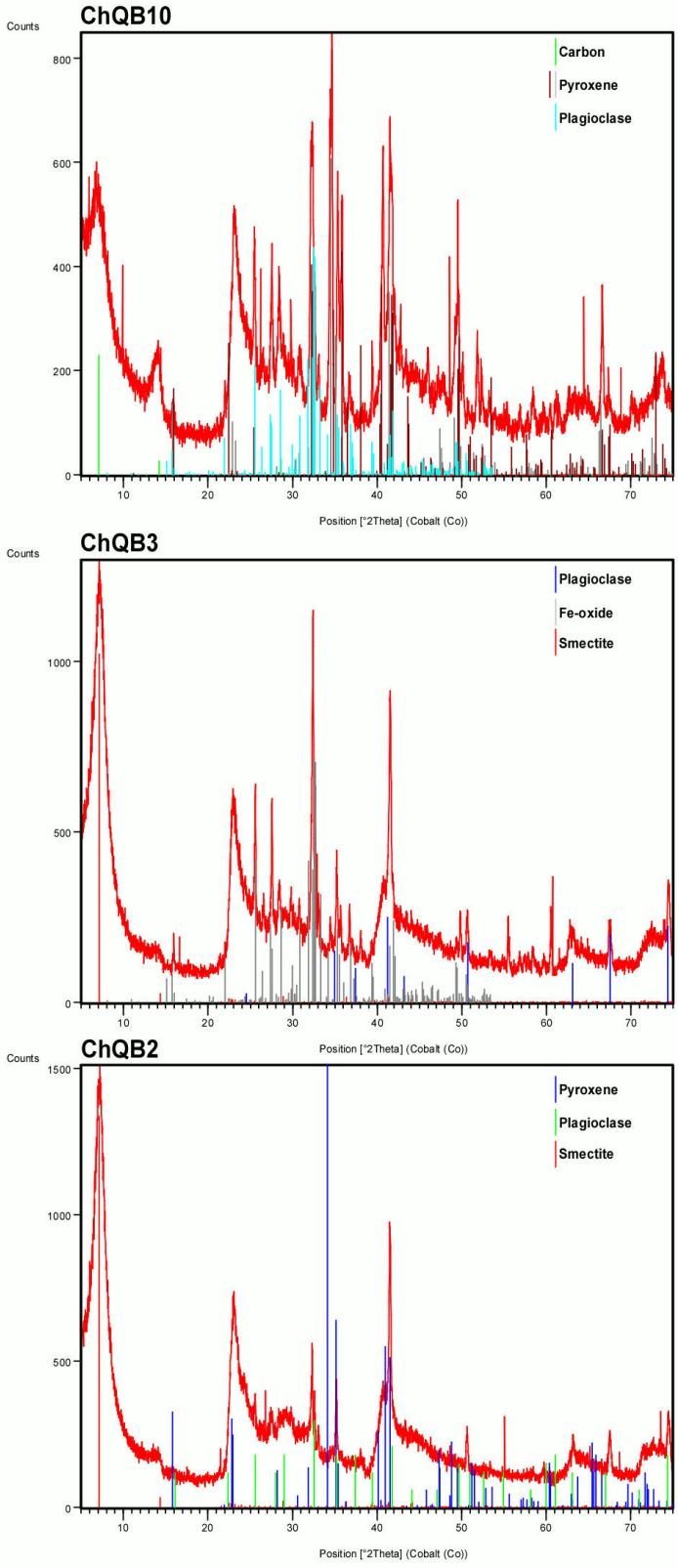

Supplemental Figure 2. Representative XRD diagrams of samples ChQB10, ChQB3, and ChQB2.

7.1.2.2. Bidar laterite profile

All nine samples of the Bidar profile were selected for qualitative XRD analysis. The patterns were collected on dry, untreated powders. No attempt at detailed phyllosilicate analysis (e.g., ethylene glycol treatment or heating) was made. The XRD patterns of all 9 samples are illustrated in Supplemental Figure 3 and in order of increasing sample height. For smectite, the best phase matches were nontronite and montmorillonite and detected in samples BB1-BB2. Further, plagioclase, clinopyroxene (augite) and magnetite were identified as primary mineral phases. In samples BB3-BB5, the primary phases have been almost completely replaced by secondary mineral phases and the formation of kaolinite, goethite, iron-hydroxide and hematite is evident. An exception is represented by sample BB6 (palaeo-water table), where goethite dominates. In addition, hematite, iron-hydroxide, and minor amounts of magnetite and kaolinite were identified. Above the palaeo-water table, kaolinite is significantly enriched, but the peak intensity of kaolinite decreases with the intensity of chemical depletion towards the nodular cap (BB9), whereas the peak intensities of hematite, goethite, and iron-hydroxide increase.

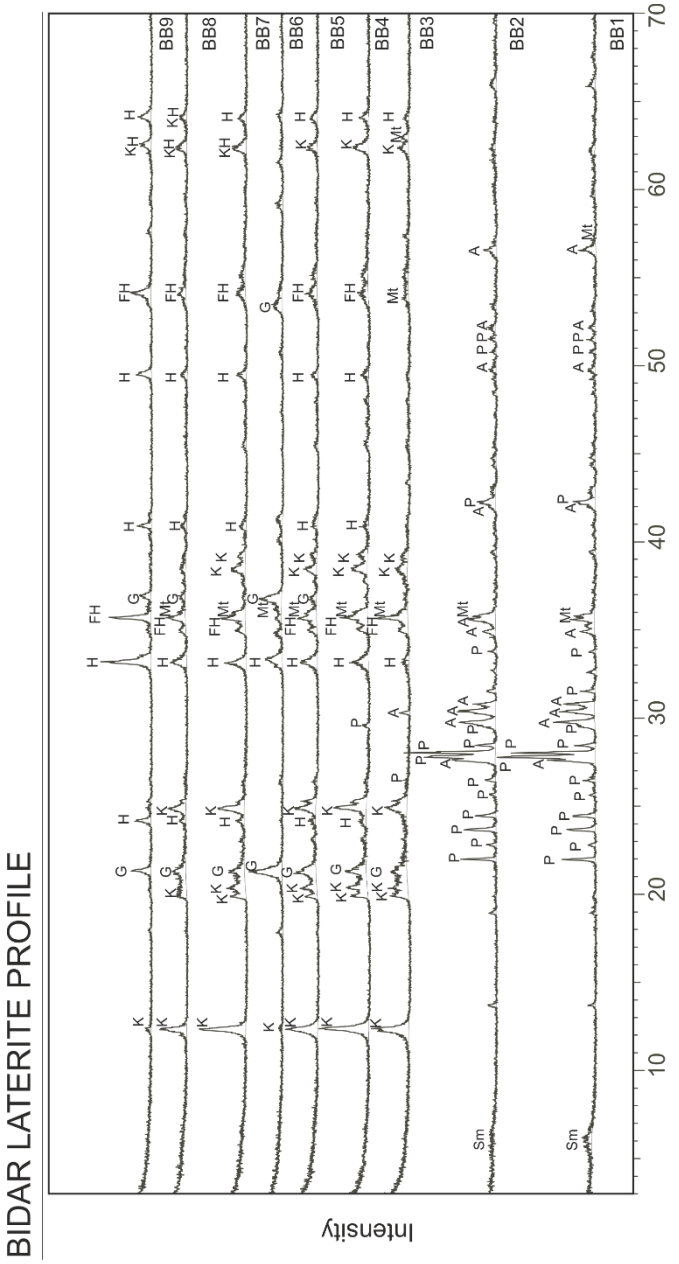

Supplemental Figure 3. Bulk powder XRD patterns of all samples of the Bidar laterite profile. P, plagioclase; A, augite; Mt, magnetite; Sm, smectite; K, kaolinite; G, goethite; FH, Fe-hydroxide (hematite); H, hematite.

7.2. Petrography

7.2.1. Microscopy of the Chhindwara and Bidar bedrock

The following two subsections include thin section descriptions of the Chhindwara and Bidar bedrock that were recently sampled (January 2016). Thin section photomicrographs include plane polarised light (PPL) and cross polarised light (XPL) images. Overall, the modal abundance of the identified minerals in thin section correlates with the quantitative XRD analyses of the Bidar bedrock. In addition, the modal abundance of clinopyroxene and smectite of the Chhindwara bedrock are similar to the calculated values from the RIR method, except for plagioclase. Our petrographic observations therefore confirm the reliability of the applied RIR method, notably for the Bidar laterite profile.

7.2.2. Chhindwara bedrock

This thin section consists of plagioclase (ca. 45%), clinopyroxene (25%; augite), 5% orthopyroxene (hypersthene) and primary Fe-Ti oxide (5 %) (Supplemental Figure 4). The grain sizes are relatively homogenous, and plagioclase and clinopyroxene crystals typically have sizes of 400-600 μm. In places, they even reach sizes of up to 1000 μm. Furthermore, volcanic glass (20%) has sizes of up to 400-600 μm in the thin section and occurs also as small inclusions within pyroxene, plagioclase and the matrix. The large aggregates of volcanic glass are already altered and have developed clay coatings. In addition, a minor amount of isotropic material around a few clinopyroxene rims indicates the presence of altered glass. Particularly in the centre of the volcanic glass, clay particles are oriented perpendicular to the pore walls, which confirms their authigenic origin Kühn et al. (2010). Moreover, the occurrence of primary minerals within the altered glass aggregates supports an authigenic origin. Weathering products also formed along cracks in clinopyroxene. Moreover, subgrain formation and atypical interference colours provide evidence of minor alteration in clinopyroxene. In total, these weathering products comprise 5% of the thin section. Secondary weathering products consist also of hematite, goethite, and oxy-hydroxides, but occur only as accessory phases in the rock.

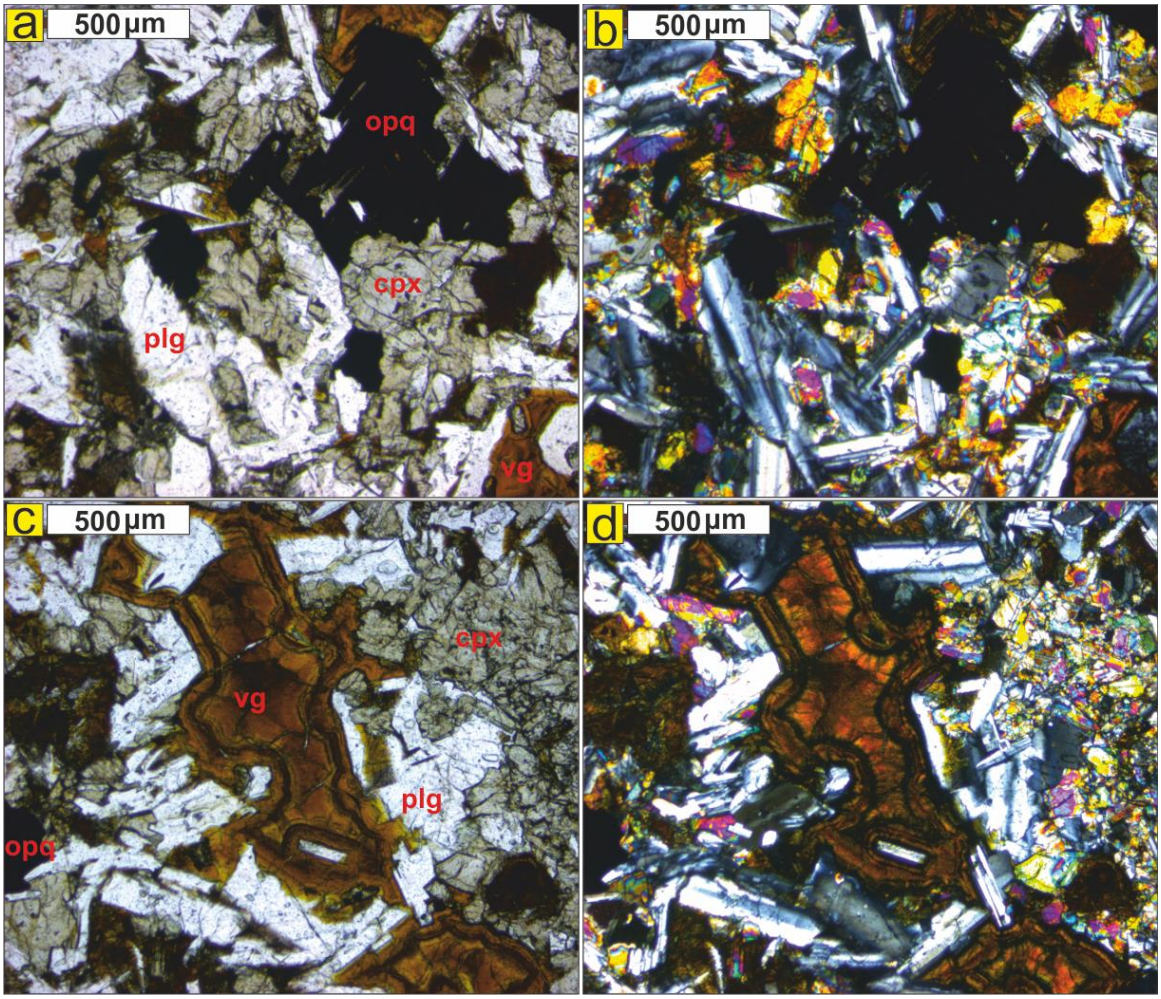

Supplemental Figure 4. Photomicrographs of the Chhindwara saprolite bedrock under ppl **(a, c)** and xpl **(b, d)**. All major phases in the profile are illustrated in the images. Plg = plagioclase; cpx = clinopyroxene; vg= volcanic glass; opq = Fe-Ti oxide.

7.2.3. Bidar bedrock

The bedrock is composed of a fine grained matrix that consists of euhedral-subhedral shaped, twinned plagioclase laths (ca. 55 %), augite and minor amounts of hypersthene (30%), primary Fe-Ti oxide (5 %) and glass (ca. 5-10 %) (Supplemental Figure 5). In places, phenocrysts of augite and plagioclase occur. In a few places within the matrix, minor amounts of plagioclase and augite have been replaced by clay minerals. In particular, volcanic glass has been altered to clays and secondary Fe-Mn oxides. Furthermore, a few minerals have been completely altered.

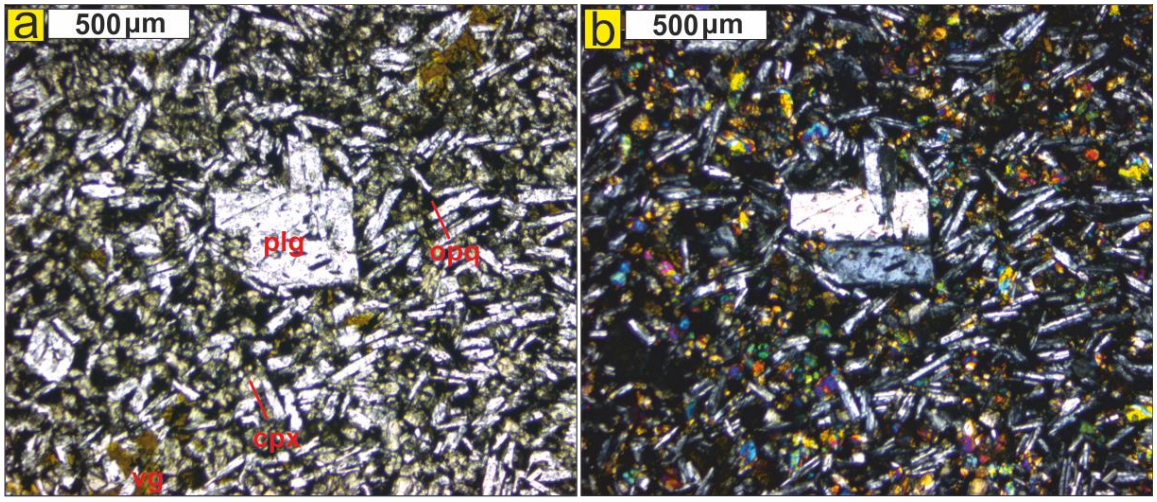

Supplemental Figure 5. Photomicrographs of the Bidar laterite bedrock under ppl **(a)** and xpl **(b)**. In the centre, a phenocryst of plagioclase is surrounded by a fine grained matrix of pyroxene, plagioclase, primary Fe-Ti oxide and volcanic glass. Plg = plagioclase; cpx = clinopyroxene; vg= volcanic glass; opq = Fe-Ti oxide.

7.3. LA-ICP-MS element maps of Zn, Mg and Fe distribution

7.3.1. Chhindwara bedrock

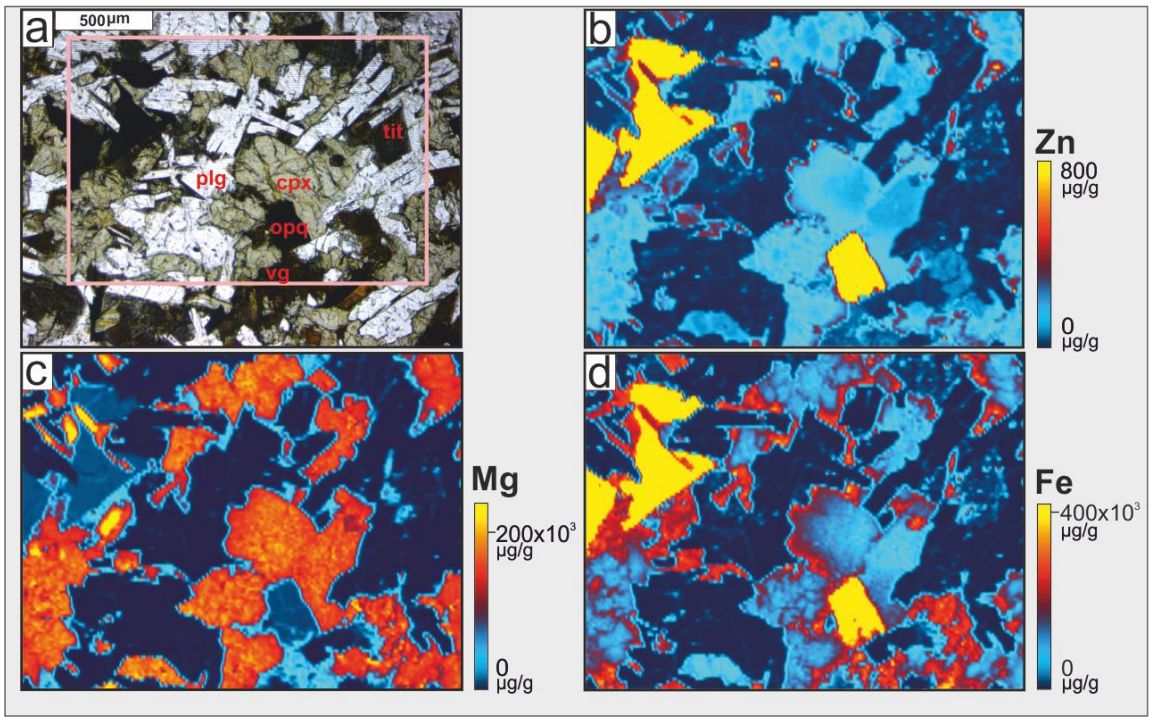

Supplemental Figure 6. (a) Photomicrograph under ppl of Fe-Mg rich clinopyroxene (cpx), volcanic glass (vg), plagioclase (plg), primary Fe-Ti oxide (opq = opaque) and titanite (tit). Volcanic glass occurs as inclusions in all silicate minerals and the matrix. The pink frame delineates the area that was laser ablated. **(b)** Semi-quantitative LA-ICP-MS compositional maps of Zn, **(c)** Mg and **(d)** Fe. It is obvious that weathering resistant primary Fe-Ti oxide is most Zn enriched and that clinopyroxene and volcanic glass host moderate amounts of Zn. In addition, titanite contains minor amounts of Zn but occurs only as accessory phase in the Chhindwara bedrock. Zinc from the primary Fe-Ti oxide is unlikely to be released during weathering. Chemical breakdown of the Fe-Mg silicates appears to happen with the concomitant breakdown of volcanic glass, so that Mg and Zn are simultaneously released from the weathering front, whereas oxidised Fe remains in the profile.

7.3.2. Altered silicate minerals and volcanic glass of Chhindwara bedrock

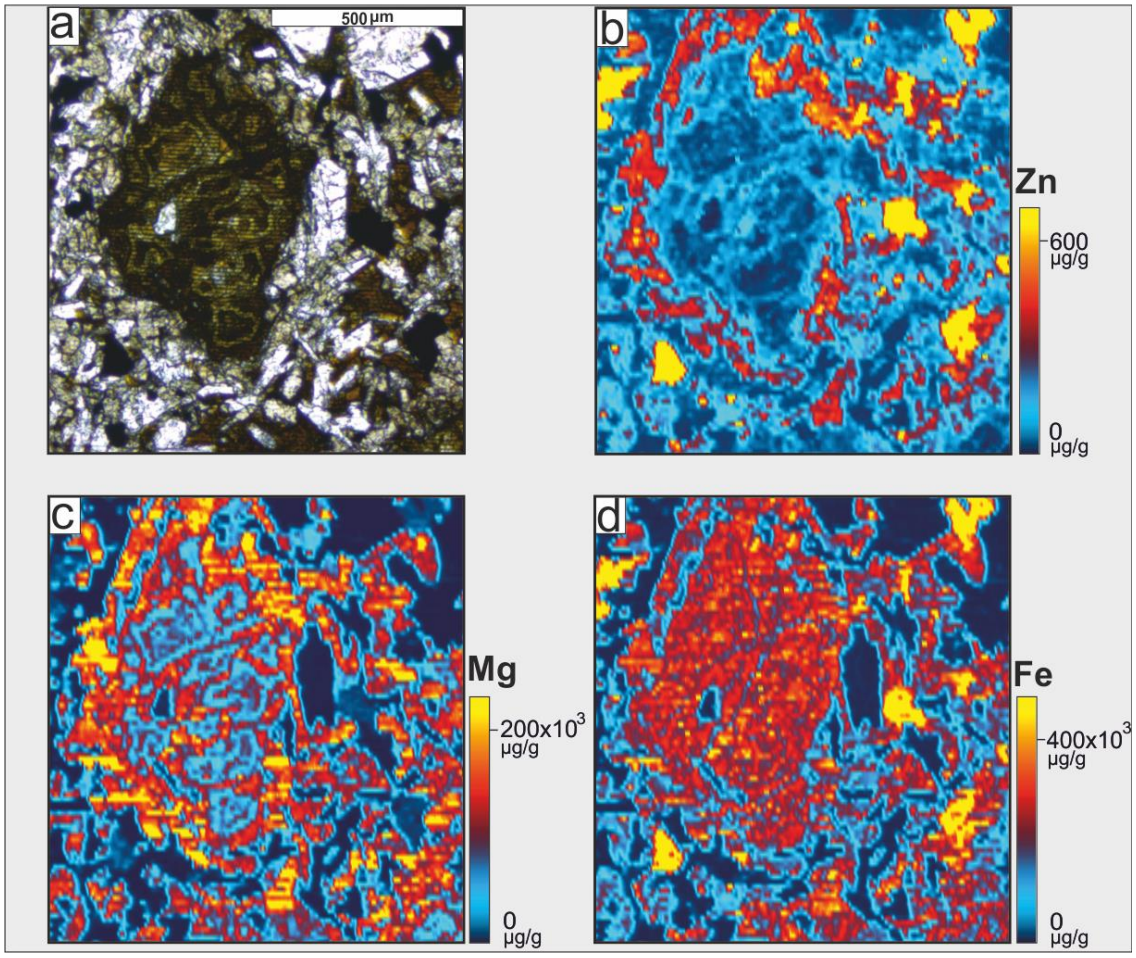

Supplemental Figure 7. (a) Photomicrograph under ppl of altered Mg-Fe silicate and volcanic glass from the bedrock of the lower volcanic flow of the Chhindwara profile. Semi-quantitative LA-ICP-MS compositional maps of Zn **(b)**, Mg **(c)**, and Fe **(d)**. The trace element maps indicate that Zn substituted for Mg and Fe. Magnesium and Zn were already released in parts, whereas oxidative weathering resulted in the immobilisation of Fe.

7.3.3. Bidar bedrock, palaeo-water table, nodular cap

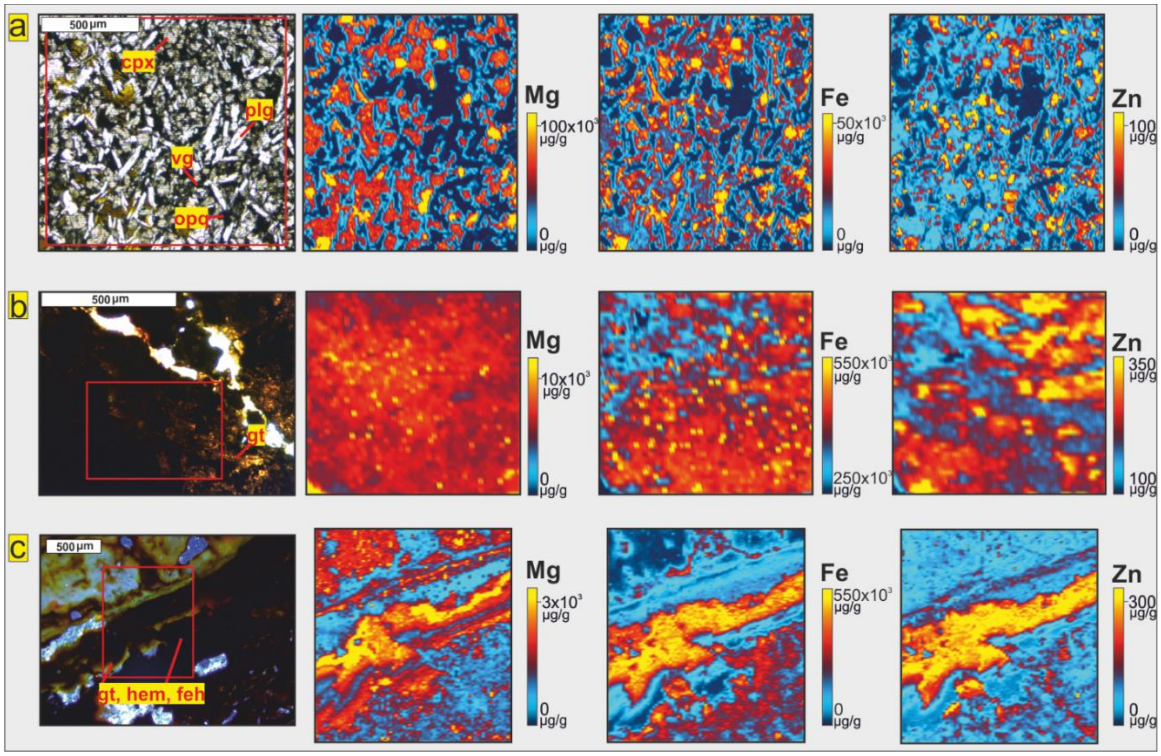

Supplemental Figure 8. Photomicrograph under ppl of the **(a)** bedrock (clinopyroxene (cpx), volcanic glass (vg), plagioclase (plg), primary Fe-Ti oxide (opq = opaque)) **(b)** palaeo-water table, (gt = goethite) and **(c)** nodular cap of the Bidar laterite profile (hem = hematite; feh = Fe-hydroxide) with semi-quantitative LA-ICP-MS compositional maps of Mg, Fe, and Zn. The red frame in each photomicrograph delineates the area that has been laser ablated. **(a)** The trace element maps indicate that Zn substituted for Mg and Fe. Clinopyroxene and primary Fe-Ti oxides host Zn. **(b)** In the photomicrograph, mainly goethite is visible and enriched in Fe and Zn and both concentrations derived from an extraneous source. **(c)** In the centre, a vein composed of Fe-hydroxide, goethite and hematite is visible that is enriched in Fe and Zn. Particularly, below the vein lower but still high concentrations of Fe are visible, whereas only in places moderately to high concentrations of Zn are evident. This indicates that Zn in the primary Fe-oxides remained immobile and is inherent, whereas in newly formed Fe-oxides very low concentrations of Zn occur.

Supplemental Table. Results of replicate BCR-2 and BHVO-2 analyses.

	BHVO-2	*2σ*	*BCR-2*	*2σ*
1	0.351	0.028	0.297	0.028
2	0.298	0.040	0.278	0.040
3	0.297	0.041	0.265	0.041
average	*0.315*	*0.036*	*0.280*	*0.036*

Chapter 4: Silicon and chromium stable isotopic systematics during basalt weathering and lateritisation: A comparison of variably weathered basalt profiles in the Deccan Traps, India

Published in Geoderma (2018, Vol. 314, 190-204)

Authors: Martin Wille, Michael G. Babechuk, Ilka C. Kleinhanns, Jonas Stegmaier, Nils Suhr, Mike Widdowson, Balz S. Kamber, Ronny Schoenberg

Abstract

Global biomass production is fundamentally affected by the hydrological cycling of elements at the Earth's surface. Continental weathering processes are the major source for most bioessential elements in marine environments and therefore affect primary productivity. In addition, critical zone biomass depends on energy and chemical exchange reactions in weathering profiles. The latter reservoirs are in turn influenced by different climatic conditions that control weathering and pore water parameters like pH and Eh, these then regulate mineral break down rates that dictate the mobility and mass flux of elements.

Two Deccan Trap basalt-weathering profiles of contrasting age and alteration intensity provide a natural laboratory for investigating the effects of rock alteration on Si and Cr and their isotopic systematics. The sub-recent Chhindwara profile has progressed to a moderate degree of alteration (saprolite), whilst the Paleogene Bidar example displays an extremely altered laterite. The Chhindwara profile shows a near uniform chromium (Cr) and silicon (Si) concentration and isotopic composition, whereas the Bidar profile is characterised by an intense loss of Si, a large enrichment of Cr within the most altered uppermost levels, and a wide range of Cr stable isotope ratios (-0.85 to 0.36 ‰ $\delta^{53/52}$Cr). A co-variation between Si and Cr isotopes, as well as their co-variation with iron (Fe) content, provides empirical evidence that iron redistribution within the profile has a large effect on Cr mobility. Therefore, it is concluded that iron oxides exert a primary control over the isotopic composition of both Cr and Si in pore waters of laterites.

Because laterite formation is promoted by tropical climates, the results of this study provide new evidence to suggest that the hydrological Cr and Si fluxes originating from continental weathering have changed in accordance with large-scale, deep time climate variation and continental plate configuration. An increased flux of Si and greater magnitude of Cr mobility and isotopic fractionation are possibly amplified under carbon dioxide (CO_2)-rich, greenhouse episodes and/or when large landmasses were tectonically arranged at near-equatorial latitudes.

1. Introduction

Dissolved Si and Cr of the modern oceans are supplied primarily by the release during continental weathering of silicate rocks (Reinhard et al., 2013; Tréguer and Rocha, 2013). The initial isotopic composition of soluble Cr supplied to the oceans is thought to be dominated by Cr(VI), which itself is released from soils as a result of Cr(III) oxidation reactions catalysed on manganese (Mn) oxide surfaces (Cranston and Murray, 1980; Ellis et al., 2002; Zink et al., 2010). Oxidative weathering reactions are therefore necessary to transform particle reactive Cr(III) within crustal rocks to more soluble Cr(VI). Furthermore, oxidation processes coupled with partial back reduction of aqueous Cr(VI) to Cr(III) by ferrous iron or organic matter (Døssing et al., 2011) are likely to leave an isotopic fingerprint in weathering profiles (D'Arcy et al., 2016; Frei and Polat, 2013). The dissolved Cr isotope and speciation signatures in the hydrosphere are therefore interpreted to be controlled initially by the redox state and biogeochemical conditions of the weathered rocks (D'Arcy et al., 2016). The weathering of primary minerals containing Cr(III) (silicates, oxides; e.g., pyroxene, magnetite) and the oxidative transformation of liberated Fe results in pedogenic Fe(III)-(oxyhydr)oxides. These pedogenic Fe(III) minerals become influential as scavengers for numerous particle reactive aqueous metals/metal complexes, including those of Cr(III) and Cr(VI), such that the Cr budget and isotope systematics could be predicted to be coupled to iron behaviour within weathering profiles (Zhong et al., 2015; Schwertmann, 1996). Thus, in addition to the direct redox influence of Mn-oxides in forming Cr(VI), Fe-oxides are an integral part of the Cr weathering cycle. On a global scale, climatic conditions are likely to have exerted a large influence on the dissolved Cr isotopic composition over geological time when enhanced silicate weathering overlapped with highly oxidative conditions. To date, several studies have started to shape the basis of Cr isotopic systematics in ancient marine and continental deposits serving as a paleo-environmental redox proxy (e.g., Crowe et al., 2013; Frei et al., 2016; Frei et al., 2009; Scheiderich et al., 2015; Holmden et al., 2016).

Unlike Cr, aqueous Si mobility is not a direct function of redox state, but released, predominantly as silicic acid, during the dissolution of silicate minerals. Chemical weathering releases isotopically heavy Si into solution due to preferential adsorption of isotopically light Si into neo-formed secondary phases such as aluminium (Al) and Fe

oxides (Delstanche et al., 2009; Oelze et al., 2015; Oelze et al., 2014). Both the kinetic sorption and incorporation of the lighter Si isotopes into secondary formed oxides, as well as biological utilisation of isotopically lighter Si, drive aqueous Si towards heavier isotope compositions (Qin et al., 2017; Oelze et al., 2014). Thus, apart from biological Si utilisation, the Si isotopic variability of surface waters is controlled by mineralogy, weathering kinetics, and pore water variables like pH and Eh (Cardinal et al., 2010; Ding et al., 2004; Ding et al., 2011; Georg et al., 2006; Georg et al., 2007). Accordingly, like Cr, the mobility of mineralogy of Fe within a weathering profile might also exert an influence on the isotopic composition of the dissolved Si pool. Here, the effects of Fe mobility and oxidation might be of particular interest since experiments conducted upon natural soil samples have demonstrated the adsorption of isotopically light Si on Fe-oxides (Opfergelt et al. 2009). Importantly, an unusually light Si isotopic composition of +0.02 ± 0.15% $\delta^{30/28}Si_{NBS28}$ was found in organic-rich river waters of the Congo Basin draining a lateritic catchment that has developed under prevailing tropical climate conditions (Cardinal et al., 2010). These examples highlight a need to further examine Si isotopic fractionation in lateritic profiles, since documentation of the Si isotope distribution within these environments and its influence on the Si isotopic composition of the riverine flux remains sparse.

To date, no studies exist that document coupled isotopic fractionation and cycling of Si and Cr within the terrestrial realm. Although Si and Cr do have different physical and chemical properties, both elements share isotopic reservoir characteristics (Poitrasson, 2017; Qin and Wang, 2017) in terms of their limited isotopic variation within magmatic rocks and heavy average river and seawater isotopic compositions (Poitrasson, 2017; Savage et al., 2010; Savage et al., 2013; Scheiderich et al., 2015; Schoenberg et al., 2008). Further, the mobility, concentration, and isotopic composition of both elements in meteoric waters appear to respond to adsorption onto mineral surfaces and pore water Eh-pH conditions (Babechuk et al., 2017; Bern et al., 2010; Cardinal et al., 2010; Chemtob et al., 2015; D'Arcy et al., 2016; Delstanche et al., 2009; Farkaš et al., 2013; Frei et al., 2014; Opfergelt et al., 2009; Paulukat et al., 2015; Ziegler et al., 2005a; Ziegler et al., 2005b). The relative impact of each of these processes on Si and Cr isotopic signatures are likely to vary within different weathering regimes (e.g., desilication favoured under acidic conditions, and Cr being both acid soluble and redox-sensitive). Accordingly, it may

potentially become possible to distinguish reactions and transportation processes using combined data from the two isotopic systems.

Our study investigates the Si and Cr isotope composition of two well-documented basaltic weathering profiles in the Deccan Traps (India); these being the Paleogene Bidar laterite and the sub-Recent Chhindwara saprolite (Babechuk et al 2014). Both profiles have developed at different times, under different climatic conditions and exposure times, and thus represent a range of alteration intensities. The Si and Cr isotopic signatures of both profiles are compared to investigate conditions within the profiles that led to the greatest Cr and Si release and accompanying isotopic fractionation. Notably, the Paleogene lateritic profile represents an end- member of chemical weathering where the coupled loss of Si and enrichment of Fe becomes extreme.

The element and isotopic geochemistry of samples from both profiles have been investigated in previous studies in great detail (Babechuk et al., 2014; Babechuk et al., 2015; Kısakürek et al., 2004; Widdowson, 2008; Wimpenny et al., 2007) and thus provide a foundation to understand the chemical weathering evolution that can be linked to changing Si and Cr isotopic signatures. The Cr isotope geochemistry of the Bidar profile are the first reported values from a deeply weathered Paleogene laterite profile.

2. Geological setting and sample material

The Deccan Volcanic Province (DVP), located in western to central India (Figure 1), is one of the largest flood-basalt provinces on Earth. Emplacement of basaltic lava flows took place between ~67 and 63 Ma (Jay et al., 2009; Venkatesan et al., 1993; Widdowson et al., 2000), and thus volcanism occurred before, during, and after the Cretaceous-Paleocene (K-Pg) mass extinction event (Chenet et al., 2007; Courtillot et al., 1986; Duncan and Pyle, 1988; Kelley, 2007) with the majority of flows and the largest volume being erupted during a very brief period c. 65 - 66 Ma (Chenet et al., 2009; Chenet et al., 2007; Renne et al., 2013 and references therein).

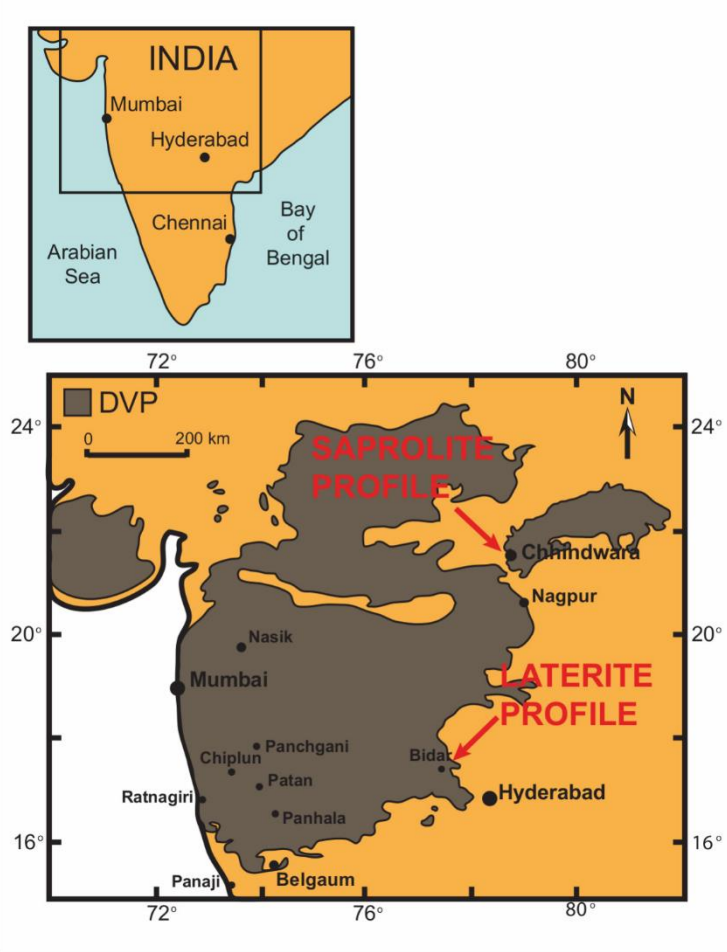

Figure 1. Simplified geological map, adapted from Babechuk et al. (2014) after Kisakurek et al. (2004), showing the extent of the Deccan Volcanic Province (DVP) within peninsular India and the location of the two studied weathering profiles.

The basaltic units presently cover c. 500,000 km^2 of peninsular India (Figure 1), and represent the eroded remnants of an original area of > 10^6 km^2, including parts that rifted away and now under the Indian Ocean, thus yielding a total original volume of ~ 1.3 million km^3 (Jay and Widdowson, 2008).

Since eruption, a long history of equatorial to sub-equatorial weathering conditions and development of the monsoonal climate led to the development of deep weathering profiles characterised by extreme alteration and the development of a widespread regional laterite between 65 and 40 Ma (Bonnet et al., 2016; Kısakürek et al., 2004). Continued, northward movement of the Indian plate and uplift of the Deccan province caused rejuvenation of fluvial erosion of the deeply weathered lava surface, and widespread abandonment of the established paleo water-table. This led to a decrease in chemical

weathering intensities and physical erosion (Widdowson and Cox, 1996). During the Neogene further increase of physical erosion due to the monsoon-influence extensively eroded the old lateritic profiles and excavated unweathered basalt surfaces which, themselves, then provided a substrate for the formation of Quaternary weathering profiles. These neo-formed profiles display considerably less intense chemical weathering alteration (Babechuk et al., 2014).

Therefore, the two DVP weathering profiles chosen for investigation of Cr and Si fractionation in this study are chronologically separate, represent differing climatic weathering regimes and associated degree of alteration.

2.1. Chhindwara profile

The Chhindwara samples were taken from a 6 m deep, saprolite-dominated profile exposed in a quarry (22°04.213’ N, 79°01.393’ E) situated on a basaltic plateau (600-750 m elevation) in the Chhindwara District of the Madhya Pradesh state (Babechuk et al., 2014). The weathering profile spans across two separate lava flows clearly identifiable by a sharp colour (rust red/brown to greenish grey) and textural boundary where relict volcanic textures, such as flow banding and flow-top breccia, are still recognisable (Figure 2a,b). The uppermost, rust red/brown flow is fully exposed and capped by a thin, modern, soil veneer. By contrast, the lower greenish-grey flow was incompletely exposed at the time of sampling and offering samples from only the upper 2.2 m of this flow; thus this profile does not reach unaltered bedrock. It is unclear whether the colour difference between both flows reflects an earlier weathering episode during volcanic quiescence prior to the eruption of the upper flow. The drab colour of the lower flow is presumably the result of higher abundance of pedogenic clays and zeolite minerals and the volcanic textures of the flow; vesicularity, represented by amygdules partly filled by zeolite minerals, increases upwards in the exposed section of the lower flow towards the highly brecciated and vesicular flow-top. By contrast, the upper flow protolith was a more massive and homogeneous basalt flow, and the saprolite is instead dominated by spheroidal weathering textures bearing a wide range in corestone size and alteration intensity. The lower 80 cm of this flow was weakly banded and finer-grained upon emplacement and is more weathered than the overlying saprolite in the centre of the flow. The upper 20 cm of the flow consists

of a thin, highly altered soil horizon. The clay mineralogy is relatively consistent throughout the lower flow with a greater alteration of primary basalt textures, indicative of a higher weathering intensity compared to the upper flow. The protolith composition of both flows is represented by the centre area of a large corestone extracted from the upper flow, displaying essentially pristine volcanic mineralogy and texture (sample ChQB12). The detailed major and trace element composition of 27 samples, covering a depth of 6 m across the weathering progression in both flows, are described in detail elsewhere (Babechuk et al., 2014; Babechuk et al., 2015).

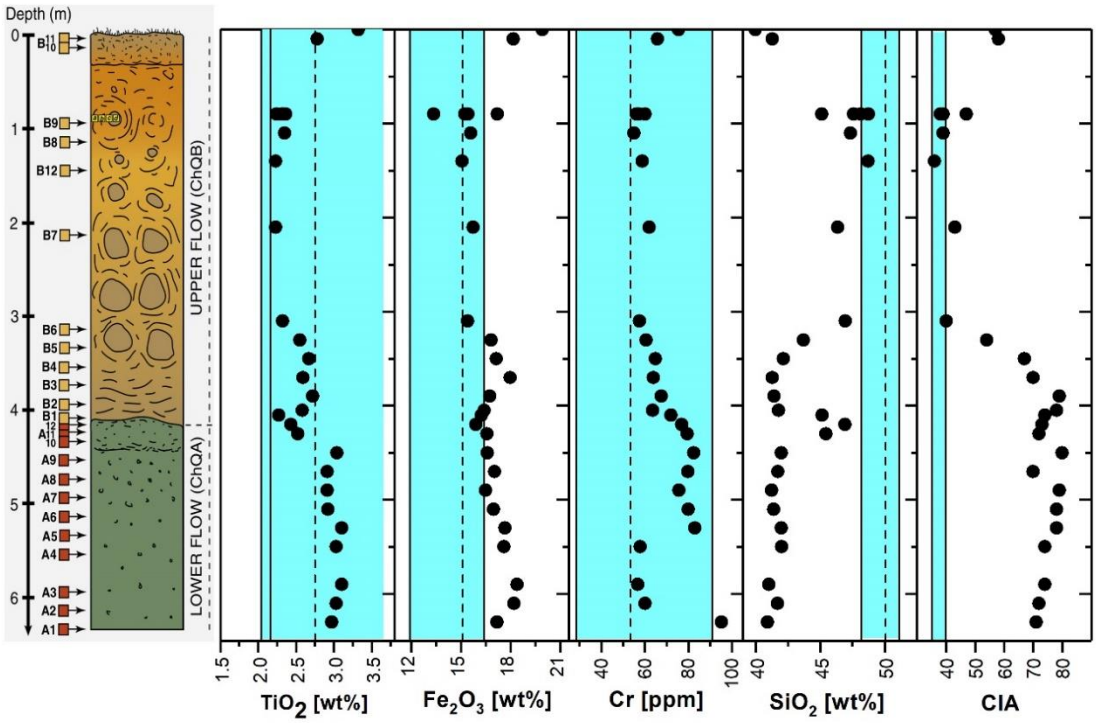

Figure 2. (a) Element, oxide concentration and chemical index of alteration (CIA) values for the Chhindwara profile (Babechuk et al., 2014); dashed line and grey shaded areas indicate average and range of element concentration data of unweathered basalts from different flows of the Chhindwara area (Ganguly et al., 2014).

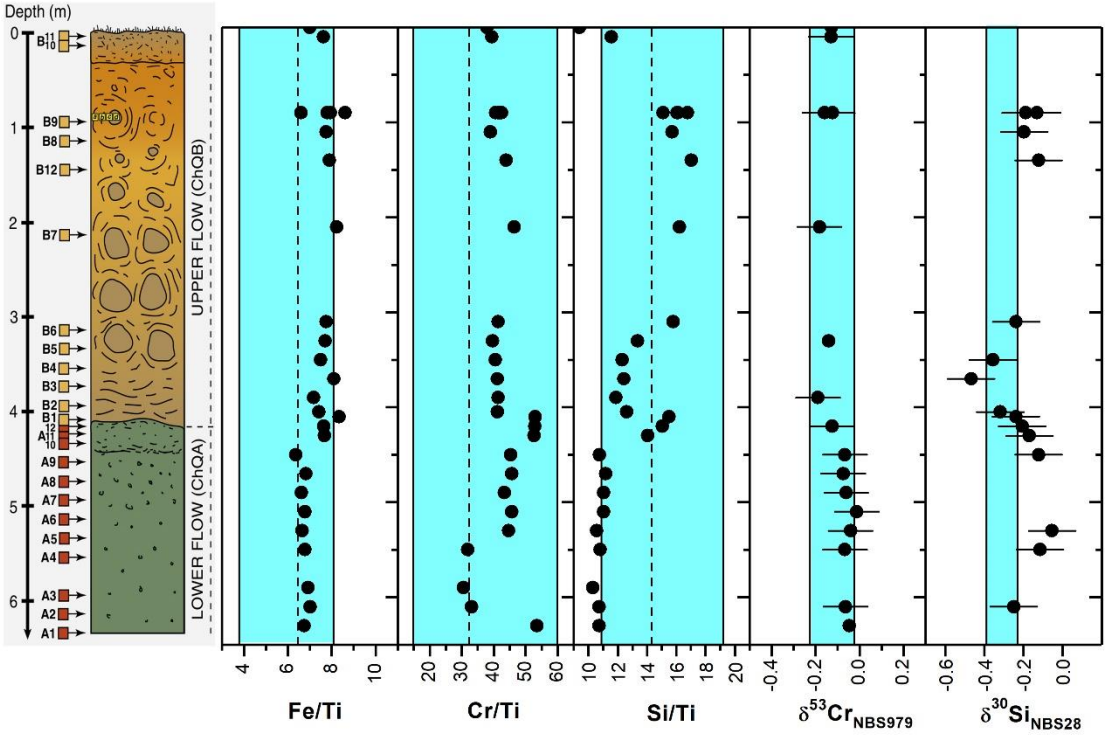

(b) Titanium (Ti) normalised element ratios and Si and Cr isotopic data; dashed line and grey shaded areas either indicate average and range of unweathered basalts from different flows at the Chhindwara area for Ti normalised concentration data (Ganguly et al., 2014) or Si and Cr isotopic range of unaltered mafic rocks (Savage et al., 2010; Schoenberg et al., 2008).

2.2. Bidar lateritic profile

The Bidar samples (BB 1–9) were taken from a deep, lateritic weathering profile (ca. 50 m depth) located in central India near the hilltop city of Bidar (17°54.87’ N, 77°32.39’ E), in the north-eastern part of Karnataka state in south-central India. This locality has historic precedent since it was here that studies of laterite-capped plateaux prompted Newbold (1846) to suggest that laterite developed as an in situ weathering product through the segregation and subsequent rearrangement of minerals and elements that originally comprised the parent rock. The nine samples of the profile have provided the focus for several key studies; the detail of their elemental and isotopic characteristics may be found elsewhere (Babechuk et al., 2014; Babechuk et al., 2015; Kısakürek et al., 2004; Widdowson, 2008; Wimpenny et al., 2007)

This profile developed on the last major DVP basalt package (i.e., Ambenali formation) to be emplaced in the eastern Deccan region (Jay and Widdowson, 2008), and thus marks the most topographically elevated lava sequence. The profile displays an upwardly increasing alteration progression, whereby unweathered basalt gradationally transitions into corestone-rich saprolite and further through individual lateritised horizons that are capped with an indurated Fe-crust. The indurated laterite cap is characterised by a 'tubular' (vermiform) fabric (Babechuk et al., 2014; Widdowson, 2008) (Figure 3 a,b). Along this weathering progression, primary silicates are progressively replaced by pedogenic sesquioxides, initially as pseudomorphs, and with a mineralogy dominated by kaolinite and goethite. Beyond this stage in the upward alteration progression the primary igneous texture is lost, and sesquioxides of Fe and Al begin to predominate with Fe-mottling and micro-aggregation textures that finally gives way to the capping Fe crust that is dominated by interlocking Fe and Al sesquioxides with no remaining phyllosilicates. The corresponding major element chemistry of this alteration progression is characterised by an upward loss of Si and Al relative to Fe, which is typical for in situ lateritisation (Schellmann, 1986). Departure from this progression is only observed at the location of a paleo-water table at a depth in the profile between ~ 15 and 10m, where Fe abundances are stratigraphically higher than above and below as a result of enhanced, laterally driven Fe (and other metal) deposition (Widdowson, 2008).

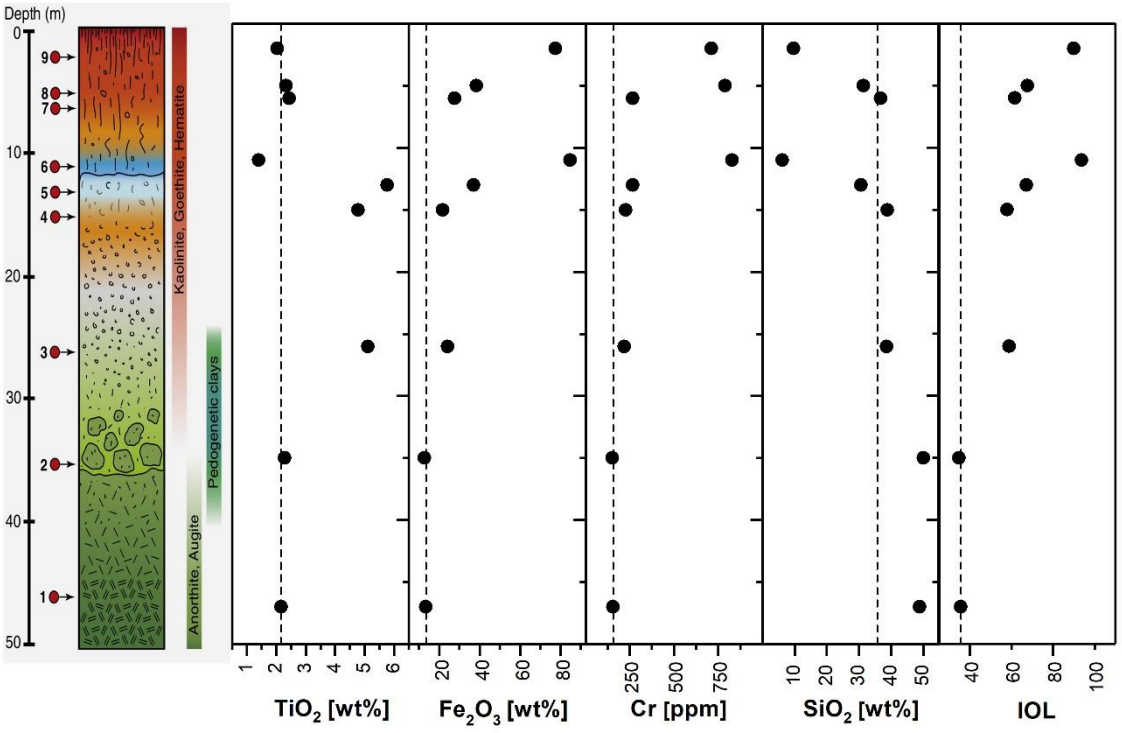

Figure 3. (a) Element, oxide concentration and index of lateritisation (IOL) values for the Bidar profile (Babechuk et al., 2014); dashed line represents the element, oxide concentration and IOL index of protolith BB-1.

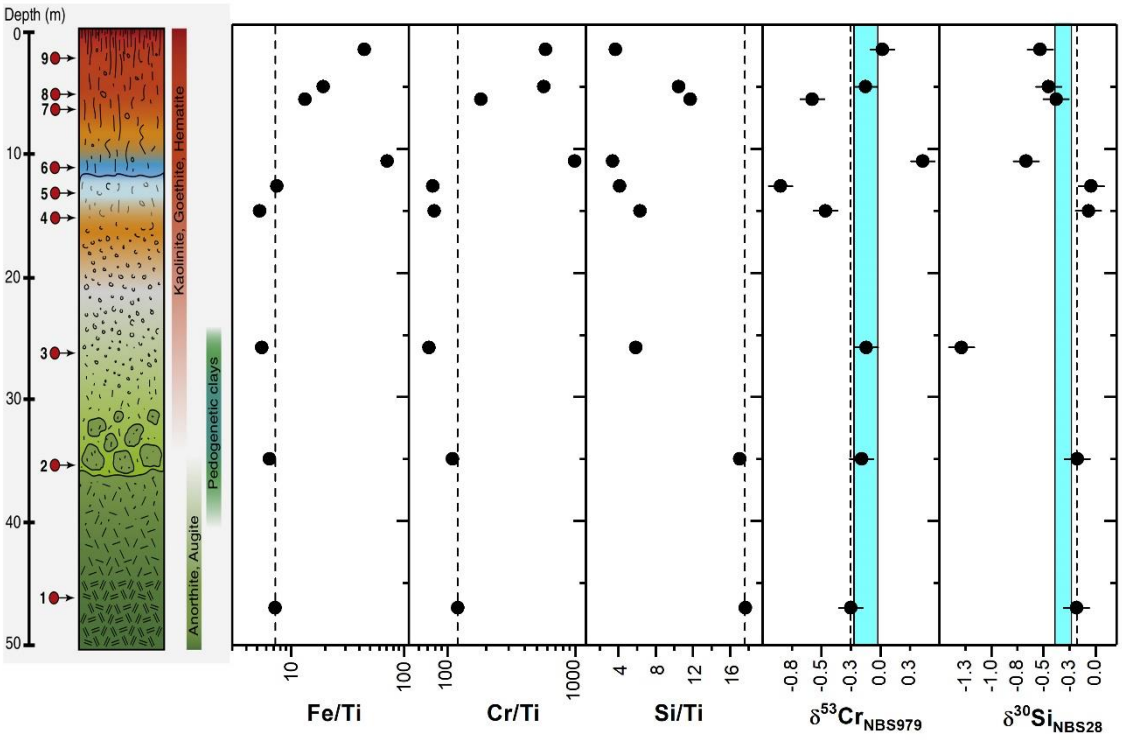

Figure 3. (b) Titanium (Ti) normalised element ratios and Si and Cr isotopic data; dashed line of unweathered basalt BB-1 and Si and Cr isotopic range of unaltered mafic rocks; dashed line and grey shaded areas either indicate average and range of unweathered basalt BB-1 or Si and Cr isotopic range of unaltered mafic rocks (Savage et al., 2010; Schoenberg et al., 2008).

3. Analytical Methods

3.1. Silicon isotope analysis

The bulk rock sample powders of the Bidar profile were prepared using a tungsten carbide mill, whereas the Chhindwara powders were prepared in an agate mill. Previous studies have demonstrated that the employment of an agate mill causes no resolvable Si isotopic contamination (Savage et al., 2011; Zambardi and Poitrasson, 2011). Splits of all 9 Bidar profile and 15 Chhindwara profile sample powders were selected for Si isotope composition.

Sample decomposition and Si purification procedures followed the general method described in van den Boorn et al. (2006) and Wille et al. (2010). Briefly, 1-2 mg of homogenised sample powder was digested using 2 M sodium hydroxide (NaOH) produced from sodium hydroxide monohydrate ($NaOH \cdot H_2O$) (Fluka, TraceSelect) in Berghof DAB-3 high-pressure digestion vessels. The solid residue was separated from the NaOH supernatant and decomposed with concentrated aqua regia (HNO_3 + 3 HCl). After complete sample digestion, supernatant was evaporated and re-dissolved in 0.25 ml of 0.25 M nitric acid (HNO_3). To purify Si from major cations, HNO_3 and NaOH supernatant was passed through 0.5 ml of cation exchange resin (Dowex AG-X8, 100-200 mesh, Bio-Rad). Subsequently, HNO_3 was added to the eluted Si-bearing solution in order to attain ~2 ppm Si in a 1% (v/v) HNO_3 solution. Silicon isotopes were determined by multiple collector inductively coupled plasma mass spectrometry (MC-ICP-MS) (Neptune Plus, ThermoFisher Scientific) at the Isotope Geochemistry Lab, Department of Geosciences, University of Tübingen. Measurements were performed in medium resolution and dry plasma mode using the ESI Apex Q desolvating system. A sapphire injector was used to direct sample aerosol into the argon (Ar)-plasma. Data acquisition and reduction were carried out using a standard bracketing technique (Albarede et al., 2004). All values are

reported relative to the silicon isotope reference standard NBS-28 reported in delta (δ) notation in ‰ units: $\delta^{30/28}Si = [(^{30}Si/^{28}Si_{sample})/(^{30}Si/^{28}SI_{NBS-28}) - 1] \times 1000$. The isotopic difference between two Si reservoirs A and B are expressed as $\Delta^{30/28}Si_{A-B} = \delta^{30/28}Si_A - \delta^{30/28}Si_A$. Repeated decomposition and measurement of an in-house homogenised sponge material SP150 (n = 10) (Wille et al., 2010) and Herkimer "diamond" quartz (n = 13) (Douthitt, 1982) yielded a 2SD reproducibility of $\delta^{30/28}Si_{NBS28}$ of ± 0.12 ‰ which is used for error bars in illustrated figures. Further details of the Si isotopic methods can be found in the supporting information.

3.2. Chromium isotope analysis

Splits of all 9 Bidar profile and 16 Chhindwara profile sample powders were selected for stable Cr isotope analysis. Based on the previously determined Cr concentration (Babechuk et al., 2015), a mass of powder sufficient to yield at least 500 ng of Cr for isotopic measurement was weighed and transferred into a Savillex PFA Teflon beaker. The sample powder was then tagged with a Cr double spike enriched in isotopes ^{50}Cr and ^{54}Cr to yield a 1:1 sample:spike Cr abundance ratio. Sample digestion and spike-sample homogenisation was achieved by the successive addition of a concentrated hydrofluoric/nitric (HF/HNO_3) acid and 6 M hydrochloric acid (HCl). Decomposed sample matrix was re-dissolved in 1 ml 6 M HCl in preparation for chromatographic Cr separation. The purification of Cr from matrix elements was achieved with one of two protocols. The first protocol is described in detail by Schoenberg et al. (2008) and involves a liquid-liquid extraction followed by an anion resin (Biorad Dowex© AG1-X8, 100-200 mesh) exchange chemistry. The second recipe is described in detail by Schoenberg et al. (2016) and involves a three-step chromatography using an anion resin (Biorad Dowex© AG1-X8, 100-200 mesh) and two cation resin (Biorad Dowex© AG50W-X8, 200-400 mesh) steps. Samples processed using both chemistries have been shown to produce matching Cr isotope ratios (Babechuk et al., 2017; Schoenberg et al., 2016). In preparation for Cr isotope analysis, all purified samples were dissolved in 0.15 M HNO_3 to produce a matched measurement concentration of ~150 ng g^{-1}

The Cr isotope analyses were performed over three analytical sessions on a ThermoFisher Scientific NeptunePlus MC-ICP-MS in the Isotope Geochemistry Lab,

Department of Geosciences, University of Tübingen. The MC-ICP-MS was operated in medium resolution mode using an Aridus II desolvating system to generate dry plasma conditions. The double spike-deconvoluted $^{53}Cr/^{52}Cr$ ratios of the experiment session were normalised to the mean of this ratio measured for the SRM979 standard and reported in delta (δ) notation ‰ units, consistent with other studies, as: $\delta^{53/52}Cr = [(^{53}Cr/^{52}Crsample)/(^{53}Cr/^{52}Cr_{SRM979}) - 1] \times 1000$. The reproducibility of $\delta^{53}/^{52}Cr$ in natural samples is conservatively estimated at 0.05 ‰ (Schoenberg et al., 2008), which is the error value used in all data plots unless the internal standard error of an individual sample measurement exceeded this value. Further details of the Cr isotopic methods can be found in the supporting information.

3.3. Weathering progression and elemental characteristics of the profiles

To express the magnitude of alteration of samples in each profile, relatively immobile major elements (i.e., Al and Ti) are used to track the loss of highly mobile elements (e.g., calcium (Ca), magnesium (Mg), sodium (Na), potassium (K)). Specifically, the chemical index of alteration, CIA (Fedo et al., 1995), the mafic index of alteration, MIA, and the IOL (Babechuk et al., 2014; Schellmann, 1986) are employed. Further details of these major element trends were reported for both profiles previously in Babechuk et al. (2014). Losses and gains of other elements not included in the weathering indices are calculated individually by normalising to concentrations of the immobile element Ti assuming minimal allochthonous Ti addition (see supporting information).

4. Results

4.1. Cr and Si isotope composition

The first key observation is that the difference in major and trace element behaviour of both weathering profiles are similarly expressed in their Cr and Si isotopic variability. Therefore, we next consider first the broad isotopic composition of the analysed samples and their comparison with published ranges, and secondly discuss the observed variation within each profile. Considering the data from both profiles, the overall Si isotopic range is 1.25 ‰ $\Delta^{30/28}$Si (-0.04 to -1.29 ‰ in $\delta^{30/28}Si_{NBS28}$), which is relatively small compared to the overall published Si isotopic range of soils and clay minerals formed during weathering (up to 3 ‰ $\Delta^{30/28}$Si) (Douthitt, 1982; Opfergelt and Delmelle, 2012; Ziegler et al., 2005b). However, this measured isotopic range exceeds that reported for unweathered mafic rocks (Savage et al., 2010). In addition, the Si isotopic variability within the sample set of both weathering profiles is significantly larger than that of the Si isotopic range defined by the two protolith Deccan Traps basalt samples (BB-1 -0.18 ‰ $\delta^{30/28}Si_{NBS28}$ and ChQB-12 -0.12 ‰ $\delta^{30/28}Si_{NBS28}$) even after considering Si isotopic experimental reproducibility of ±0.12 ‰ in $\delta^{30/28}$Si (Figure 2b, 3b, Table 1). The Cr isotopic variability of 1.21 ‰ $\Delta^{53/52}$Cr (0.36 to -0.85 ‰ $\delta^{53/52}Cr_{NBS97}$) of both profiles is larger than that reported for magmatic rocks (Schoenberg et al., 2008), $\delta^{53/52}Cr_{NBS979}$ of -0.12 ± 0.10 (2 SD), and in the range of previously reported weathering profiles and paleosols ($\delta^{53/52}Cr_{NBS979}$ of -1.29 to +2.38 ‰) (Babechuk et al., 2017; Berger and Frei, 2014; Crowe et al., 2013; D'Arcy et al., 2016; Frei et al., 2014; Frei and Polat, 2013; Paulukat et al., 2015).

Table 1. Major, trace element concentration; * (Babechuk et al., 2014); # (Babechuk et al., 2015) and Si and Cr isotopic data of the Chhindwara and Bidar weathering profile. Different Digest # represent Si isotope replicates of different sample powder aliquots.

												Digest #1		Digest #2		average	
Sample	**Depth**	**SiO_2**	**TiO_2**	**Fe_2O_3**	**S**	**Cr**	**Fe^{2+}/Fe_T**	**Si/Ti**	**Fe/Ti**	**Cr/Ti**	**$\delta^{53/52}Cr_{NBS979}$ 2 SE**		**$\delta^{29/28}Si_{NBS28}$**	**$\delta^{30/28}Si_{NBS28}$**	**$\delta^{29/28}Si_{NBS28}$**	**$\delta^{30/28}Si_{NBS28}$**	**$\delta^{29/28}Si_{NBS28}$**	**$\delta^{30/28}Si_{NBS28}$**
	[cm]	**[wt%]**	**[wt%]**	**[wt%]**	**[wt%]**	**[ppm]**					**[‰]**	**[‰]**	**[‰]**	**[‰]**	**[‰]**	**[‰]**	**[‰]**	**[‰]**
ChQA1	630	40.91	2.97	17.18		95.2	0.111	10.7	6.7	53.5	-0.05	0.02						
ChQA2	610	41.7	3.03	18.21	< 0.01	60.1	0.092	10.7	7	33.1	-0.06	0.02	-0.16	-0.25			-0.16	-0.25
ChQA3	590	41.02	3.1	18.39		56.8	0.109	10.3	6.9	30.6								
ChQA4	550	42.0	3.03	17.59		57.8	0.108	10.8	6.8	31.8	-0.07	0.02	-0.07	-0.12			-0.07	-0.12
ChQA5	530	41.99	3.1	17.65	< 0.01	83	0.103	10.6	6.6	44.7	-0.04	0.02	-0.03	-0.05	-0.03	-0.06	-0.03	-0.05
ChQA6	510	41.38	2.92	16.97		79.9	0.096	11	6.8	45.7	-0.01	0.02						
ChQA7	490	41.23	2.91	16.5		75.6	0.084	11	6.6	43.4	-0.06	0.01						
ChQA8	470	41.72	2.91	17.04		79.7	0.089	11.2	6.8	45.7	-0.07	0.02						
ChQA9	450	41.98	3.04	16.59	< 0.01	82.5	0.092	10.8	6.4	45.3	-0.07	0.02	-0.08	-0.14	-0.06	-0.1	-0.07	-0.12
ChQA10	430	45.44	2.52	16.57	< 0.01	79.5	0.062	14.1	7.7	52.6			-0.09	-0.13	-0.09	-0.21	-0.09	-0.17
ChQA11	420	46.92	2.43	15.91	< 0.01	77	0.059	15.1	7.6	52.8	-0.13	0.01	-0.11	-0.21	-0.1	-0.2	-0.11	-0.21
ChQA12	410	45.14	2.27	16.23	< 0.01	72	0.056	15.5	8.3	52.9			-0.16	-0.29	-0.12	-0.19	-0.14	-0.24
ChQB1	405	41.76	2.58	16.4		63.6	0.032	12.6	7.4	41.1			-0.16	-0.36	-0.15	-0.28	-0.15	-0.32
ChQB2	390	41.43	2.72	16.74		67.5	0.04	11.9	7.2	41.4	-0.19	0.03						
ChQB3	370	41.29	2.59	17.97	< 0.01	63.9	0.073	12.4	8.1	41.1			-0.24	-0.47	-0.23	-0.47	-0.23	-0.47
ChQB4	350	42.14	2.67	17.14	< 0.01	64.8	0.071	12.3	7.5	40.5			-0.19	-0.34	-0.21	-0.37	-0.2	-0.36
ChQB5	330	43.69	2.55	16.82		60.5	0.16	13.4	7.7	39.6	-0.14	0.02						
ChQB6	310	46.95	2.32	15.4		57.6	0.445	15.8	7.7	41.4			-0.09	-0.15	-0.17	-0.32	-0.13	-0.24
ChQB7	210	46.35	2.23	15.73	< 0.01	62	0.437	16.2	8.2	46.4	-0.18	0.03						
ChQB8	110	47.34	2.35	15.6		55	0.499	15.7	7.7	39			-0.08	-0.17	-0.13	-0.22	-0.11	-0.2
ChQB9a	90	45.12	2.33	17.2	< 0.01	56.7	0.304	15.1	8.6	40.6	-0.16	0.03						
ChQB9b	90	47.58	2.31	15.42		57.1	0.474	16.1	7.8	41.3			-0.07	-0.13	-0.06	-0.14	-0.07	-0.13
ChQB9c	90	48.16	2.24	15.23	< 0.01	56.2	0.525	16.8	7.9	41.8			-0.06	-0.12	-0.16	-0.26	-0.11	-0.19
ChQB9d	90	48.75	2.36	13.36	< 0.01	60	0.545	16.1	6.6	42.4	-0.12	0.03						
ChQB10	10	41.28	2.78	18.16		65.7	0.304	11.6	7.6	39.4	-0.13	0.03						
ChQB11	0	39.98	3.32	19.92		75.4	0.29	9.4	7	37.9	-0.13	0.03						
ChQB12	140	48.72	2.23	15.07		58.7	0.719	17	7.9	43.9			-0.04	-0.05	-0.11	-0.2	-0.07	-0.12

Sample	**Depth**	*****	*****	*****	**S**	**Cr**	**Si/Ti**	**Fe/Ti**	**Cr/Ti**	**$\delta^{53/52}Cr_{NBS979}$**	**2 SE**	**$\delta^{29/28}Si_{NBS28}$**	**$\delta^{30/28}Si_{NBS28}$**	**$\delta^{29/28}Si_{NBS28}$**	**$\delta^{30/28}Si_{NBS28}$**	**$\delta^{29/28}Si_{NBS28}$**	**$\delta^{30/28}Si_{NBS28}$**
		SiO_2	**TiO_2**	**Fe_2O_3**													
	[cm]	**[wt]**	**[wt%]**	**[wt%]**	**[wt%]**	**[ppm]**				**[‰]**	**[‰]**	**[‰]**	**[‰]**	**[‰]**	**[‰]**	**[‰]**	**[‰]**
BB-1	4700	48.9	2.16	13.4	< 0.01	156.28	17.7	7.2	120.7	-0.25	0.02	-0.09	-0.16	-0.12	-0.21	-0.11	-0.18
BB-2	3500	50.06	2.29	12.63	< 0.01	150.56	17	6.4	109.7	-0.16	0.02	-0.08	-0.13	-0.11	-0.22	-0.09	-0.18
BB-3	2600	38.59	5.11	24.1	< 0.01	219.28	5.9	5.5	71.6	-0.12	0.02	-0.67	-1.27	-0.65	-1.3	-0.66	-1.29
BB-4	1500	38.78	4.78	21.64	< 0.01	226.23	6.3	5.3	78.9	-0.46	0.02	-0.02	-0.09	-0.02	-0.05	-0.02	-0.07
BB-5	1300	30.61	5.76	36.95	< 0.01	266.42	4.1	7.5	77.2	-0.85	0.01	-0.03	-0.04	-0.01	-0.04	-0.02	-0.04
BB-6	1100	6.12	1.4	84.81	0.02	828.75	3.4	70.7	987.4	0.36	0.03	-0.3	-0.64	-0.29	-0.7	-0.3	-0.67
BB-7	600	36.68	2.44	27.7	<0.01	266.99	11.7	13.2	182.5	-0.58	0.02	-0.21	-0.39	-0.17	-0.36	-0.19	-0.38
BB-8	500	31.35	2.33	38.37	<0.01	787.34	10.5	19.2	563.7	-0.13	0.02	-0.22	-0.43	-0.25	-0.47	-0.23	-0.45
BB-9	200	9.59	2.03	77.53	0.03	710.05	3.7	44.6	583.4	0.02	0.02	-0.28	-0.53	-0.25	-0.54	-0.26	-0.53

In the Chhindwara profile, the Si (-0.12 to -0.47 ‰ $\delta^{30/28}Si_{NBS28}$) and Cr (-0.01 to -0.19 ‰ $\delta^{53/52}Cr_{NBS979}$) isotopic variability is small, and for Si only slightly beyond that of unweathered mafic rocks (Savage et al., 2010). Low variability of $\delta^{30/28}Si_{NBS28}$ accord with Si/Ti which do not depart significantly from the that of the protolith, and indicate that weathering reactions and any concomitant clay mineral formation within the profile have let to only moderate amounts of Si mobilisation within the Chhindwara profile (Figure 2b). The low variability in $\delta^{53/52}Cr_{NBS979}$ and Cr/Ti ratios is evidence for a conservative weathering behaviour of Cr within the Chhindwara Profile and demonstrate that even during weathering of pyroxenes, the primary host for Cr (Figure 4), an insufficient amount of Cr is mobilised to imprint an isotopic shift within the weathered rock. However, a slight offset in $\delta^{53/52}Cr_{NBS979}$ between upper (-0.15 ± 0.05 ‰ (2SD)) and lower (-0.06 ± 0.06 ‰ (2SD)) is visible.

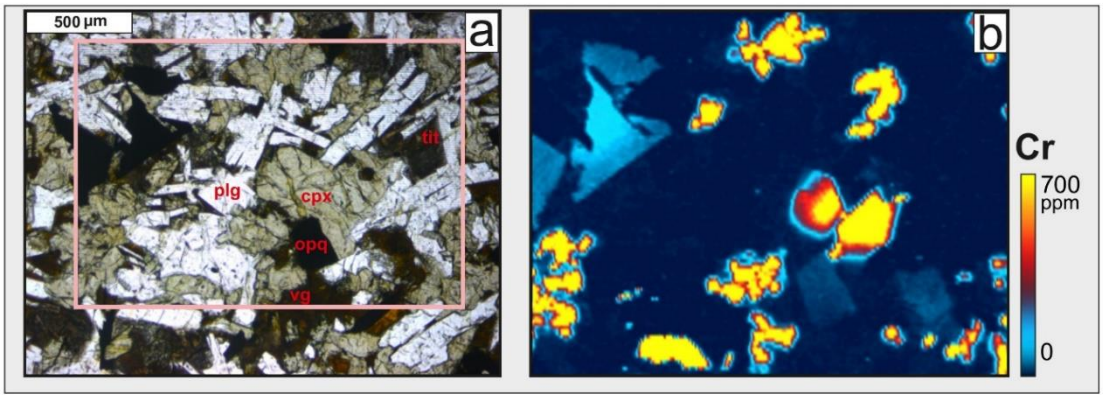

Figure 4. Trace element maps of the Chhindwara profile samples **a)** Photomicrograph under plane polarised light (ppl) of Fe-Mg rich clinopyroxene (cpx), volcanic glass (vg), plagioclase (plg), primary Fe-Ti oxide (opq = opaque) and titanite (tit). Volcanic glass occurs as inclusions in all silicate minerals and the matrix. The pink frame delineates the area that was laser ablated. **b)** Semi-quantitative LA-ICP-MS compositional maps of Cr.

The magnitude of the overall Cr and Si isotopic variability observed is much greater in the extensively weathered, Fe-oxide rich samples of the Bidar profile. This observation is accompanied by the fact that Cr within the Bidar profile is enriched in areas where Fe concentrations are particularly high (e.g. within the nodular cap, Figure 5a; or within the paleo- water table, Figure 5b). This observation differs from the element distribution map of the unweathered basalt where regions of highest Fe concentrations do not contain the highest amount of Cr (Figure 5c). By contrast to Chhindwara, the Bidar profile shows a larger variability of Cr isotope ratios, with $\delta^{53/52}Cr_{NBS979}$ ranging from +0.36 to -0.85 ‰,

with increasing variability towards the top of the lateritic profile where higher Fe concentration and Si depletion is evident (Figure 3a,b, Table 1). In the saprolitic zone of the Bidar profile, samples BB-2 and BB-3 show an alteration intensity that is comparable to samples from the Chhindwara profile, with a limited range in $\delta^{53/52}Cr_{NBS979}$ and slightly heavier isotopic composition compared to the protolith BB-1. These values still lie within the range of unaltered igneous rocks (Schoenberg et al., 2008).

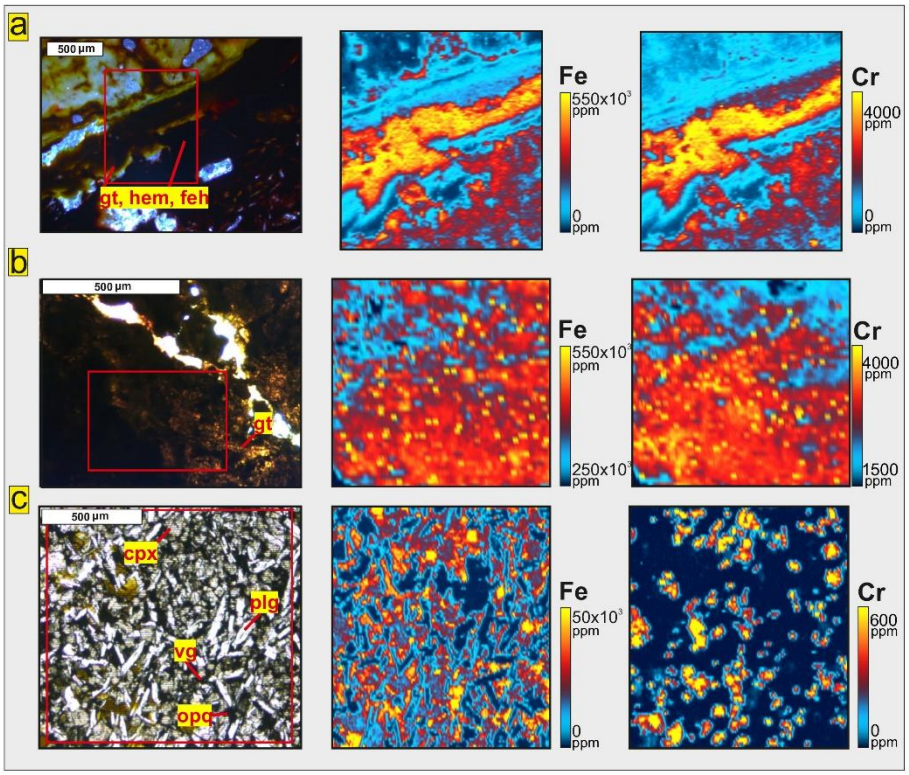

Figure 5. Photomicrograph under ppl of the **(a)** nodular cap (hem = hematite; feh = Fe-hydroxide), **(b)** paleo water-table (gt = goethite), **(c)** bedrock (cpx = clinopyroxene; vg = volcanic glass; plg = plagioclase; opq = opaque primary Fe-Ti oxide) of the Bidar laterite profile with semi-quantitative laser ablation inductively coupled plasma mass spectrometry (LA-ICP-MS) compositional maps of Fe, and Cr. The red frame in each photomicrograph delineates the area that has been laser ablated. **(a)** In the centre, a vein composed of iron hydroxide, goethite and hematite is visible that is enriched in Fe and Cr. Particularly, below the vein lower but still high concentrations of Fe are visible, whereas only in places moderately to high concentrations of Cr are evident. This indicates the relationship between iron oxides and Cr. **(b)** In the photomicrograph, mainly goethite is visible and enriched.

By contrast, samples BB-4 and BB-5 show lighter $\delta^{53/52}Cr_{NBS979}$ down to -0.85 ‰ accompanied by increasing Fe concentration and Si loss, whereas at the paleo-water table,

a shift to the highest Fe concentrations is accompanied by the heaviest $\delta^{53/52}Cr_{NBS979}$ composition of +0.36 ‰. Above the paleo-water table the isotopic composition returns to ^{53}Cr-depletion (BB-7) and, in the uppermost and most Cr-enriched samples (BB-8 and BB-9), to values closer to the range of unaltered igneous rocks (Figure 3b).

5. Discussion

The major and trace element systematics of both profiles, and their relationship to the different weathering intensities and critical zone processes, have been described in earlier studies (Babechuk et al., 2014; Kısakürek et al., 2004; Wimpenny et al., 2007). Therefore, only those data pertinent to understand the new Si and Cr isotopic systematics are considered here. These together with the new Si and Cr isotope data are presented in Table 1, Figure 2 a,b, Figure 3 a,b for the Chhindwara and Bidar profiles, respectively.

5.1. Weathering progression and elemental characteristics of the profiles

The Chhindwara profile displays considerable variation in CIA values from 36 to 80, with the lowest values preserved in the centre of the upper flow between a depth of 90 to 310 cm. A gradual increase in CIA values to about ~70-80 occurs below a depth of 310 cm towards the contact zone between upper and lower flow. The two samples within and immediately below the soil surface of the upper flow also exhibit higher CIA values (57-58). Compared to these significant changes in the CIA, near-constant Fe/Ti ratios of 7.3 ± 1.2 (2SD) characterise the upper flow, with only a small change towards lower Fe/Ti ratios at the transition between the two flows (~16 % variability within 2SD range). This clearly demonstrates low mobility of Fe throughout much of this profile (Figure 2 a,b) that is related to its progressive oxidation with increasing weathering intensity, which crosses the contact zone of both flows. The progression in oxidation, expressed as the Fe^{2+}/Fe_T ratio (where $FeT = Fe^{2+}+Fe^{3+}$) is discussed in detail in Babechuk et al. (2014). Accompanying this change in Fe oxidation and CIA, is also a loss of Si, with SiO_2 and Si/Ti ratios ranging

from 48.7 wt % to 40.9 wt % and 17.0 to 9.4 (Figure 2 a,b). For most of the samples, and especially those of the lower flow, the SiO_2 abundances are lower than in the protolith basalt, as well as other basalts from the Chhindwara area (Ganguly et al., 2014). These trends are comparable to those documented in other kaolinised basalt weathering profiles elsewhere (Nesbitt et al., 1980). Nevertheless, since the Si/Ti ratios do not depart substantially from that of the protolith, weathering reactions within this profile (and concomitant clay mineral formation) can only be supplying low to moderate amounts of Si to rivers and oceans (Figure 2b). The variability in Cr/Ti ratios of the Chhindwara profile, encompassing the data from both flows is limited, ranging from 30.6 to 53.5, with a mean of 42.6 ± 11.5 (2SD) amounting to 27 % variability. However, unlike the Si/Ti and Fe/Ti ratios, there is no distinct offset in Cr/Ti ratio between the upper and lower flow, although the latter flow exhibits a larger degree of internal Cr/Ti variability.

The Bidar laterite profile is thicker and its upper levels significantly more altered. Here, the lowermost and least weathered samples, BB-2 and BB-3, are comparable in alteration intensity to that of the entire variation observed in the Chhindwara saprolite. Above these samples, alteration of much greater intensity is encountered. The mobile major cations are so heavily depleted and the CIA become insensitive for accurately tracking the further stages of weathering intensity (Babechuk et al., 2014). Instead, the chemical changes are dominated by the loss of Al and Si relative to Fe and the weathering intensity is better represented with the IOL, which ranges from 34.9 to 93.7 (Babechuk et al., 2014) (Figure 3a). Compared to the Chhindwara profile, much larger variability of 200 % and 217 % (2SD) in Cr/Ti and Fe/Ti ratios are found, which is expressed through an upward increase from 72 to 987 and from 5.3 to 71, respectively (Table 1, Figure 3b). Furthermore, increasing Cr/Ti ratios show a systematic coupling to increasing Fe/Ti ratios upwards in the profile (Figure 3b, Figure 6a) with the exception of the saprolitic section of the Bidar profile (between 13 to 35 m depth), where Cr/Ti and Fe/Ti ratios are lower than the protolith BB-1. While Cr/Ti and Fe/Ti ratios show a positive covariation, Si/Ti ratios steadily decreasing along the Bidar profile opposing the trend defined by Cr and Fe. SiO_2 concentrations and Si/Ti ratios range from 6.1 to 50.1 wt% and 17.7 to 3.4, respectively, with a Si/Ti variability of 118 % based on 2SD variability around the mean (Figure 3a,b).

5.2. Silicon isotopes

Quaternary age weathered volcanic ash displays isotopically light Si due to preferential adsorption on Fe-oxides (Opfergelt et al., 2009). The degree of weathering, as well as the abundance and mineralogy of the Fe-oxides, apparently exert control on the magnitude of isotopic fractionation (Opfergelt et al., 2009). Isotopically light Si compared to primary magmatic host rock is a typical signature of secondary aluminous clay minerals (Bern et al., 2010; Georg et al., 2006; Georg et al., 2007; Opfergelt and Delmelle, 2012; Ziegler et al., 2005b). The adsorption of Si from solution onto precipitated Al-hydroxides is associated with a large kinetic isotopic fractionation favouring the adsorption of isotopically light Si (Oelze et al., 2014; Ziegler et al., 2005a; Ziegler et al., 2005b). However, re-equilibration between adsorbed and dissolved Si occurs if the transformation from Al-hydroxides into minerals with higher degree of order does not proceed fast enough. In such a case, no significant $\Delta^{30/28}$Si difference is expected between both Si reservoirs (Oelze et al., 2014). Therefore, re-equilibration conditions may thus explain the relatively homogeneous Si isotopic composition of the Chhindwara profile where the Si isotopic composition broadly matches the range of unweathered basalts (Savage et al., 2010), although changing Si/Ti ratios indicate significant Si mobility and loss of primary Si especially from the lower flow that appears to be accompanied with the formation of kaolinite. However, the use of whole rock powders, rather than mineral separates, might add to the limited variance in Si isotopic values due to the superposition of primary and secondary Si isotopic signatures. A localised signature of isotopically light Si was measured near the transition between the upper and lower flows, coinciding with the higher abundance of pedogenic clays, zeolite minerals, and Fe-oxides. This shift towards lighter Si isotopic values at the contact zone might therefore record increased incorporation of isotopically light Si within secondary clay minerals caused by higher weathering kinetics at this contact zone and/or adsorption of dissolved isotopically light Si onto secondary Fe-oxides. Qualitatively, it is difficult to untangle which, if any, of the known Si isotopic fractionation mechanisms is exerting the dominant control on the storage of isotopically light Si in this zone. A weak negative co-variation between Si isotopes and Al_2O_3 content (as indicator for clay fraction), Mn/Ti and Fe^{2+}/Fe_T ratios (as indicators for pedogenic oxide formation) within the profile is insufficient to permit a clear distinction of mechanisms.

By contrast, the Bidar profile samples record a higher magnitude of Si isotope fractionation and there is strong evidence that the formation of Fe-oxides exerted the primary control on the Si isotopic composition, especially in the most aggressively altered laterite horizons. The increase of Fe coincides with a decrease in Si concentration leading to co-variation between Fe/Ti and Si/Ti ratios (Figure 6b). Therefore, the extreme decrease in SiO_2 content down to 6 wt. % in samples BB-6 to BB-9 was caused by a combination of Si loss and Fe-oxide precipitation, whereas Si concentration and Si/Ti ratios within samples BB-3 to BB-5 are controlled by Si loss (Figure 6b) without accompanying precipitation of Fe-oxides. Although the formation of abundant Fe-oxyhydroxides within samples BB-6 to BB-9 is not accompanied by an observable Si gain, the adsorption of isotopically light Si on the Fe-oxyhydroxides likely overwhelmed the Si signatures of secondary clay minerals and remnant primary silicates. This is shown by a significant co-variation between Fe/Ti and $\delta^{30/28}Si_{NBS28}$ in these sections (Figure 6c). In the less altered horizons of the profile (between 35 and 15 m in depth; BB-2 to BB-5), phyllosilicates dominate the neo-formed pedogenic mineralogy, but only BB-3 shows a distinct light Si isotopic composition relative to the unweathered basalt, whereas BB-2 and BB-4 are, within error, identical to BB-1. Similar to the low Si isotopic variability of the Chhindwara profile, $\delta^{30/28}Si_{NBS28}$ signatures of samples BB-4 and BB-5 are not very different from the unweathered protolith BB-1, despite showing a high loss of Si and high degree of kaolinisation. Similar to the Chhindwara profile, equilibrium conditions between the Si dissolved in pore water and Si adsorbed on Al-hydroxides (Oelze et al., 2014) might explain these unfractionated Si signatures. Superimposed on this, the contribution of primary, unweathered silicates could have also shifted Si isotopic values of BB-4 and BB-5 closer to BB-1.

Previous studies identified significant element redeposition in the horizon represented by BB-3 that must have been derived from leaching of minerals higher in the profile, as indicated by heavy rare-earth elements (HREE) enriched patterns, superchondritic yttrium/holmium (Y/Ho) ratios and significantly less radiogenic neodymium (Nd) isotope ratios than the BB-1 protolith (Babechuk et al., 2014; Babechuk et al., 2015). Such element redistributions into depth are common in laterite profiles (Patino et al., 2003; Viers and Wasserburg, 2004) and presumably triggered by pore-waters meeting a sharp permeability and/or pH boundary that drives element deposition into neo-formed minerals (e.g., phosphates). Although low Si/Ti ratios indicate an overall loss of Si from sample BB-3, the

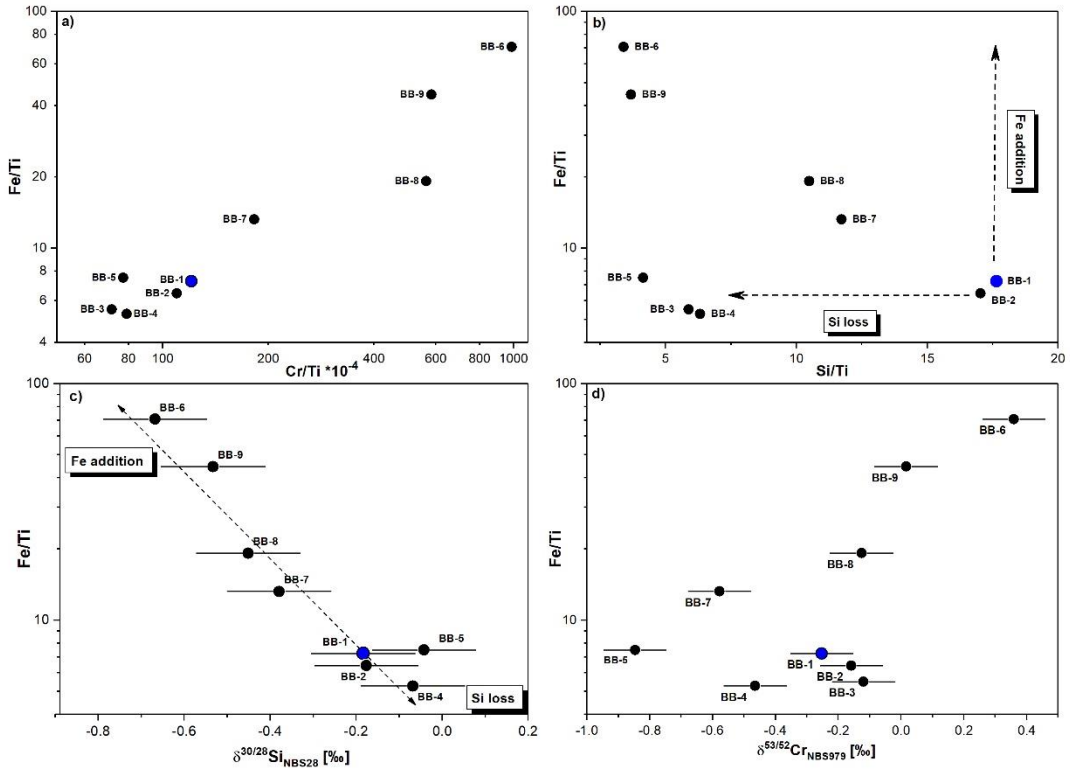

Figure 6. (a) Titanium normalised Fe concentrations (Fe/Ti) vs. Ti normalised Cr concentrations (Cr/Ti) **(b)** Ti normalised Fe concentrations (Fe/Ti) vs. Ti normalised Si concentrations Si/Ti **(c)** Ti normalised Fe concentrations (Fe/Ti) vs. Si isotopic composition (δ^{30}Si) **(d)** Ti normalised Fe concentrations (Fe/Ti) vs. Cr isotopic compostion (δ^{53}Cr) of Bidar profile samples.

formation of secondary Si minerals capturing remobilised Si simultaneously with the REE cannot be discounted.

The precipitation of small amounts of secondary Si phases in the form of siliceous cements or opaline silica from pore water favour the lighter isotopes of Si (André et al., 2006; Basile-Doelsch et al., 2005) and could explain the shift in Si isotopic composition of sample BB-3 to lighter values relative to BB-4 and BB-2.

5.3. Chromium isotopes

The Cr isotope composition of several weathering profiles has been investigated previously, including two highly ferruginous modern profiles developed on tonalite in a tropical region and basalt in a sub-tropical region (Berger and Frei, 2014; D'Arcy et al., 2016; Frei et al., 2014; Paulukat et al., 2015). Consequently, two models have been

proposed for the within profiles Cr variations. In the first scenario, Cr loss may reflect leaching and small-scale redistribution of Cr(III) under low Eh and pH conditions with no evidence of isotopic fractionation. In the second scenario, partial oxidation of Cr(III) to Cr(VI) at comparatively higher Eh and pH conditions led to loss of soluble and isotopically heavy Cr(VI) species (Berger and Frei, 2014). This implies that the elemental mobility of Cr as Cr(III) is promoted by acidic conditions without isotopic fractionation, while the partial oxidation of Cr(III) to Cr(VI) subsequently triggers isotopic fractionation that can be stored within the weathering profile. The presence of Mn(III)/(IV)-oxides as a catalyst is likely required to induce redox reactions (Ball, 2004; Landrot et al., 2010; Tang et al., 2014) and isotopic fractionation between Cr(III) and Cr(VI), which is 6-7 ‰ at equilibrium at 24.85 °C obtained by theoretical calculations (Schauble et al., 2004). The separation of isotopically heavy Cr(VI) as a soluble anionic species to be transported within a profile with subsequent reduction or escape to the hydrosphere is then viewed as the means of preserving variable but often isotopically light Cr isotope signatures in weathering profiles. Accordingly, the overall behaviour of Cr is driven by the complex interplay between Eh and pH conditions. Given that deep, lateritic weathering profiles reach pH and Eh extremes beyond those found in stratigraphically thinner and less altered weathering profiles, new constraints can be placed on the Cr isotope systematics under oxidative weathering conditions by comparing the geochemistry of the contrasting Chhindwara saprolite and Bidar laterite.

Limited Cr mobility is indicated by the relatively homogeneous Cr/Ti ratios and the absence of stable Cr isotope fractionation of the Chhindwara profile (Figure 2b). Thus, despite the weathering intensity and magnitude of Fe oxidation, any Cr isotope signatures generated through pedogenic processes are likely masked by the comparatively larger isotopic pool of unfractionated igneous Cr(III) in the bulk rock measurements. If correct, neither the Quaternary weathering nor the vegetative conditions triggered a sufficient aqueous mobility of Cr within the soil profile to imprint Cr isotopic differences caused by isotopic fractionation through interaction with neoformed pedogenic oxides (D'Arcy et al., 2016). This exemplifies that oxidative weathering under modern atmospheric conditions does not necessarily imprint changing Cr isotopic signatures within soils and that soil Cr isotopic signatures are not necessarily indicative of oxidative atmospheric conditions. Interestingly, the coupled offset in Cr/Ti ratios and $\delta^{53/52}Cr_{NBS979}$ at the flow boundary matches that of other immobile element ratios (Babechuk et al., 2015) and may instead

record a very subtle primary isotopic difference between the lava flows. In a recent study by Schoenberg et al. (2016), small isotopic heterogeneities within (ultra-)mafic magmatic rocks have been shown that are correlated with geochemical indices like Mg# that possibly could explain the observed difference in $\delta^{53/52}Cr_{NBS979}$.

The behaviour of Cr is significantly different in the deep and highly altered Bidar laterite. Lateritic weathering can occur under variable but very low pH conditions (Widdowson, 2008). For instance, the solubility of Al only rises significantly below a pH of 4, and pH conditions are modelled to reach as low as 2 in order to induce the ligand-mediated mobilisation of platinum group elements (PGE) and gold (Au) and silver (Ag) (Bowles, 1986; Mann, 1984; Wimpenny et al., 2007). Low pH conditions develop through oxidation of Fe^{2+} that produces excess H^+ (Mann, 1984). Therefore, the lowest pH values were likely present around the paleo-water table where dissolved Fe^{2+} was oxidised and removed as Fe-oxyhydroxides from pore water under increasingly oxidising conditions. Weathering under acidic conditions can lead to large Cr depletion within the weathered rock due to increased Cr(III) mobilisation. Such a scenario has been proposed for extreme Cr depletion of up to 90% reported from a lateritic profile developed on tonalitic bedrock (Berger and Frei, 2014). Such an extreme Cr depletion is not seen within the Bidar lateritic profile. Rather, samples from near and above the paleo-water table which have been exposed to low pH pore waters show a significant increase in Cr concentration and Cr/Ti ratios associated with a highly variable $\delta^{53/52}Cr_{NBS979}$ isotopic signature (Figure 3a,b, 6d). The positive covariation between Cr and Fe concentrations show that these Cr enrichments were likely caused by Fe oxidation and precipitation from pore waters.

Although it is difficult to attribute a single mode of weathering to be responsible for the Cr isotopic signature within the Bidar profile, dissolution of sulphides and silicate minerals deep within the profile under variable pH, Eh conditions might have liberated Fe(II) and Cr(III) into pore solution without significant isotopic fractionation. The mobility of Cr(III) across different pH ranges in association with ligands (organic or inorganic) is scientifically recognised (Cao et al., 2011; Duckworth et al., 2014; McClain and Maher, 2016), yet not widely regarded to induce an isotopic effect in the stable Cr isotope distribution in weathering profiles. An important observation is that the Fe and Cr concentrations are highly correlated, which concludes that Fe oxides and hydroxides incorporated Cr after its mobilisation. Chromium is structurally incorporated into many pedogenic Fe minerals as Cr(III) (Schwertmann et al., 1989; Schwertmann and Pfab,

1996). Lower Cr/Ti ratios in samples BB-2 to BB-5 compared to the protolith BB-1 indicate that Cr was mobilised in the lower parts of the profile (Figure 3b). As a result, Cr enriched pore fluids may have migrated upwards in the weathering profile to the paleo-water table where increasing Eh conditions in combination with the oxidation of Fe(II) led to the precipitation of ferric iron and co-precipitation in Fe(III)-oxides. Although isotopic fractionation during co-precipitation of Cr(III) with Fe-oxides or -hydroxides has not been investigated so far, preferential adsorption of isotopically light Cr might have shifted the isotopic composition of the remaining dissolved Cr reservoir to heavier values. Such a local transport of mobilised Cr from deeper parts of the profile and Cr accumulation by reduction and adsorption has been interpreted to be the reason for light $\delta^{53/52}Cr_{NBS979}$ of top soils from a Central Madagascar lateritic profile (Berger and Frei, 2014). Therefore, migration of dissolved Cr upwards the profile coupled with precipitation of Fe-hydroxides could have caused open system Rayleigh type characteristics in $\delta^{53/52}Cr_{NBS979}$ of the evolving dissolved Cr reservoir. This might explain the isotopic pattern from light to heavy $\delta^{53/52}Cr$ seen in samples BB-4 to BB-6 and again BB-7 to BB-9 (Figure 3b, 6d). It must be noted that the oxidation of Cr(III) to Cr(VI) may also be triggered by the formation of Mn-oxides and the partial removal and adsorption of Cr(VI) could also have led to some isotopic variability. This may also have contributed to the dissolved Cr pore water pool, especially in the upper part of the profile with increasing Eh conditions. The reduction and co-precipitation of Cr(VI) with Fe-oxides is known to favour the light Cr isotope and might have led to similar isotopic pattern as described above (Døssing et al., 2011; Ellis et al., 2002; Izbicki et al., 2008; Zink et al., 2010).

At present, a more conclusive evaluation of fractionation factors is not possible since whole rock Cr signatures are a combination of re-absorbed Cr(III) on Fe-hydroxides superimposed by primary Cr(III) within the soil. The modal abundances of both phases are not known. However, the good correlation between $\delta^{53/52}Cr_{NBS979}$ and $\delta^{30/28}Si_{NBS28}$ (Figure 7) (except for sample BB-3, see discussion above) indicates that the cycling and redistribution of iron within the profile had a strong influence on the isotopic composition of Cr and Si. The preferred model to explain the Cr distribution and isotopic characteristics involves mobilisation and sequestration of Cr predominantly in its Cr(III) state with a subordinate, but non-negligible role of Cr(VI). However, more robust Cr reconstruction is hindered by a lack of Cr(III)/Cr(VI) speciation and an unconfirmed role of Cr(III) processes (dissolution, complexation, and adsorption) in stable isotopic fractionation. The

latter has been suspected to cause significant isotopic fractionation in other studied paleosols (Babechuk et al. 2017).

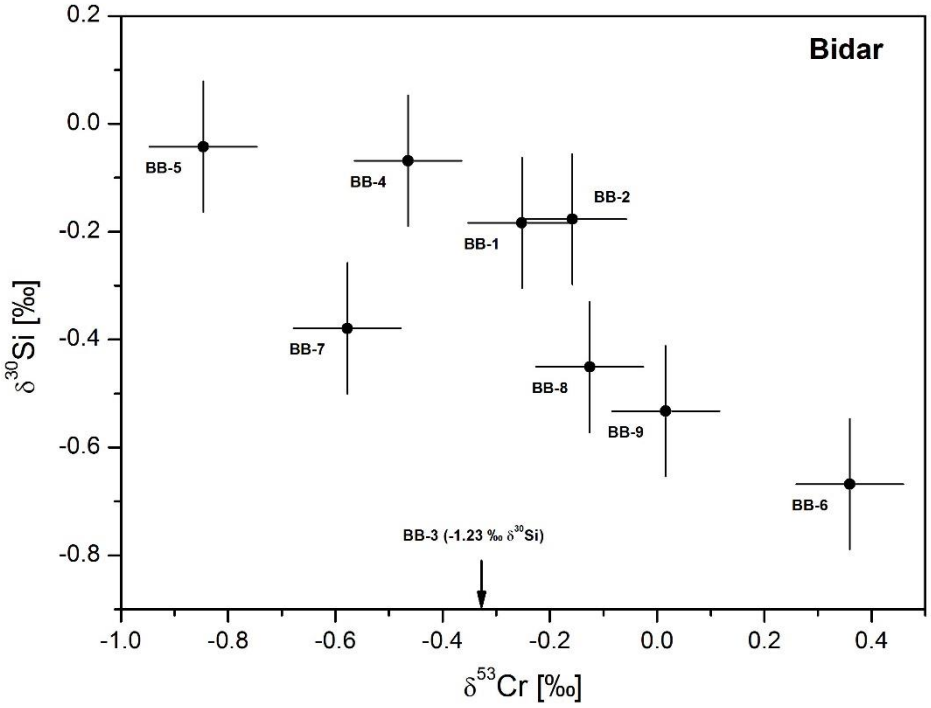

Figure 7. $\delta^{30}Si$ vs. $\delta^{53}Cr$ of Bidar profile samples.

5.4. Sources of allochthonous chromium, iron and silicon

Previous studies of the Bidar laterite profile have used a mass balance calculation and isotopic constraints to investigate the role of allochthonous input. Although the low sampling density throughout the Bidar profile hinders an accurate mass balance determination, previous studies demonstrate that changing ratios of immobile element ratios and radiogenic isotope patterns cannot be explained without dust input (Babechuk et al., 2015; Kısakürek et al., 2004; Wimpenny et al., 2007). However, dust input alone is insufficient to explain the excess of the elemental budgets in certain horizons, notably that of the paleo-water table. Therefore, lateral and open-system addition of elements from groundwater have been invoked to explain particularly elevated concentrations at a postulated paleo-water table level within the profiles. Groundwater transport was likely to have been active concurrently with dust accretion to the profile.

Given these documented complexities and their detailed treatment in previous studies, similar mass balance calculations are attempted here for Cr and Fe to investigate the influence of dust on excess Fe and Cr within the upper Bidar profile. For this reason, an absolute mass change of an element per unit volume of material is determined to test whether a vertical redistribution can account for Cr and Fe enrichment within the profile (see supporting information for the model details). This model illustrates that lateral redistribution of Cr and Fe from bottom upwards can only account for their enrichments up to the position of the paleo-water table. For instance, nearly twice to three times more Cr and Fe is deposited within the top of the profile than released from the lower parts (Figure 8). Therefore, it seems likely that Cr and Fe enrichment in the top samples of the Bidar profile is partly derived from lateral groundwater transport of dissolved Cr and, in the upper parts of the profile, by atmospheric deposition as indicated by strong enrichments of thorium/niobium (Th/Nb) ratios coupled with less radiogenic $^{143}Nd/^{144}Nd$ ratios (Babechuk et al., 2015). However, the fact that the concentration weighted average $\delta^{53/52}Cr_{NBS979}$ of all measured Bidar samples is -0.1 ‰ and therefore close to the protolith BB-1 shows that any possible source for excess Cr, and possibly also Fe, was likely unfractionated compared to the average isotopic composition of the continental crust. The most probable sources for such dust input would likely be either the surrounding exposed basaltic terrain, the cratonic basement or sources of loose, fine-grained sediment that surrounds it.

Although an addition of Fe and Cr via dust or groundwater transport to the upper part of the Bidar profile is likely, only ~2% Cr would need to be incorporated in order to account for the overall Cr content of the unweathered profile. Further, this modest input seems to have not affected: a) the isotopic covariation between Cr and Si; b) the Si isotopic covariation with Fe within these samples; c) the overall, concentration weighted Cr isotopic composition of all Bidar samples (the latter remains close to the unweathered sample BB-1). Importantly, dust input to the top of the profile must have occurred concurrently with the process of lateritisation to explain our isotopic observations. If this interpretation is correct, then the dust input itself will also have been affected by the internal chemical weathering reactions and element remobilisation. Therefore, we conclude that the Cr isotopic signatures of the Bidar profile developed through the vertical redistribution of autochthonous and allochthonous Cr and Fe and changing Eh and pH conditions.

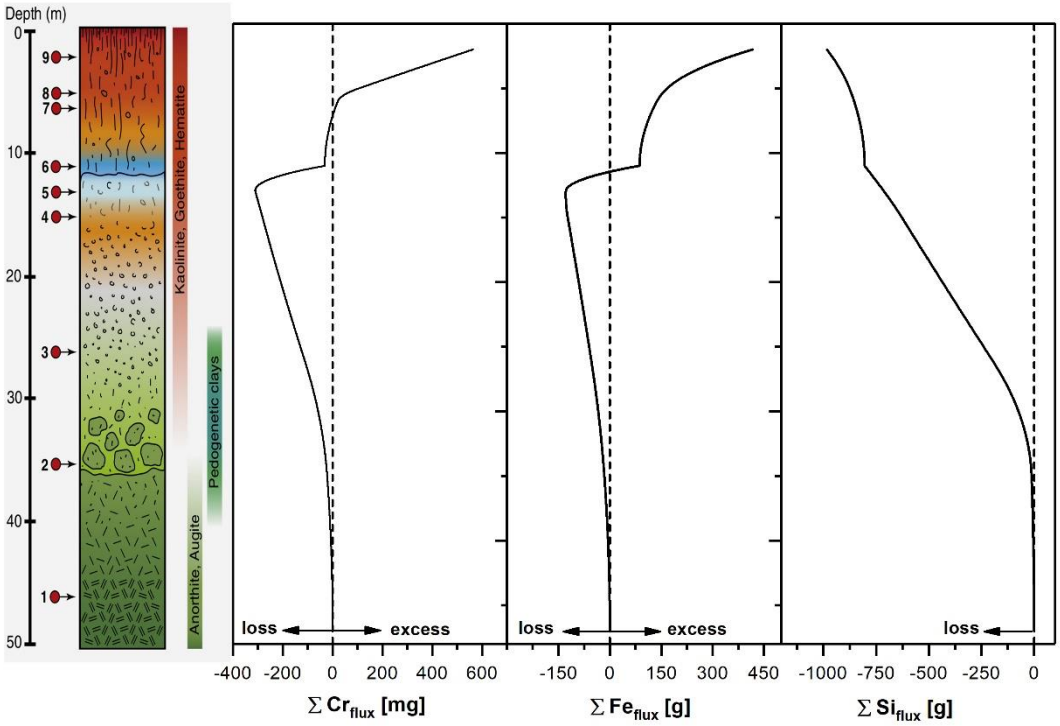

Figure 8. Depth integrated fluxes of Cr and Fe per cm^2 based on mass balance reference to the unweathered basalt protolith (sample BB-1). Negative values indicate loss from the profile, positive values indicate excess allochthonous Cr and Fe input to the profile.

The Si elemental mass balance and isotopic systematics of the Bidar profile samples also provide evidence that dust input to the Bidar site must have been contemporaneous with laterite formation. Up to 50% dust input with average UCC element concentrations (Rudnick and Gao, 2003) to the top samples BB-8 and BB-9 have been calculated using Nb/Th ratios (Babechuk et al., 2015). For sample BB-9, such a contribution of dust after lateritisation would have raised its SiO_2 concentration far beyond 9.6 wt%. Again, this simple mass balance calculation shows that although the Si input by dust cannot be neglected, the $\delta^{30/28}Si_{NBS28}$ vs. Fe/Ti and $\delta^{30/28}Si_{NBS28}$ vs. $\delta^{53/52}Cr_{NBS979}$ co-variations of the Bidar profile samples BB-8 and BB-9 follow the same trend as the deeper samples that experienced minor dust input. This indicates that the Si isotopic composition is not significantly altered by dust. Possibly, the dust input in the topmost levels was similarly exposed to intense weathering and consequently changed the elemental composition. This might explain why the dust input is not imprinted within the Si and Cr isotopic composition of the weathering profiles.

We acknowledge that the topmost samples in both profiles could also be influenced by biotic fractionation processes (Opfergelt and Delmelle, 2012). However, given the behaviour of $\delta^{30/28}Si_{NBS28}$ vs. Fe/Ti and $\delta^{30/28}Si_{NBS28}$ vs. $\delta^{53/52}Cr_{NBS979}$ throughout the samples of the Bidar profile, it appears unlikely that plant uptake or biogenic silicia (phytoliths) (Opfergelt and Delmelle, 2012) have significantly altered the Si isotopic signature defined by Fe-oxide adsorption processes.

The Si and Cr isotopic information of the profile to the total loss and gain of the respective elements may be summarised as follows:

1) Chromium shows a largest isotopic variability within the Bidar lateritic soil profile, and is mainly attributable to fractionation and redistribution processes operating within the weathering profile. However, regardless of its strong fractionation in such lateritic profiles, the primary impact of this behaviour upon the dissolved Cr flux to the oceans is likely to be small. This is because most of the liberated Cr rapidly becomes incorporated into neo-formed Fe-oxides and because the overall weighted isotopic composition of the entire profile remains close to that of unweathered basalt. However, the aeolian transportation of Fe-oxides in mineral dust particles might supply isotopically fractionated Cr into the ocean.

2) With considering the calculated Si loss of ca. 60% from the Bidar laterite profile, and by using the concentration, the overall weighted average $\delta^{30/28}Si_{NBS28}$ of −3.74‰, the isotopic composition of mobilised Si would be −0.05‰ $\delta^{30/28}Si_{NBS28}$. Although this weighted average is consistent with the Si isotopic range of river waters (−0.70 to 4.66‰ $\delta^{30/28}Si_{NBS28}$), the predicted light isotopic composition is somewhat lighter to predominantly heavy $\delta^{30/28}Si_{NBS28}$ values of dissolved Si in rivers (Poitrasson, 2017), but perhaps more comparable to $\delta^{30/28}Si_{NBS28}$ values of +0.02 ± 0.15‰ in the Congo and Amazon Basin rivers which are known to drain large areas affected by lateritisation (Cardinal et al., 2010; Hughes et al., 2013). Hence, the isotopically light Si fingerprint in rivers is likely to indicate that they are, in part, sourced from areas where lateritic profiles are forming, or are being actively eroded, and not simply from currently active weathering zones which are only progressing to the saprolitic stage (i.e., where primary minerals are broken down).

6. Conclusions and broader implications

We report Si and Cr isotopic data of two weathering profiles of different ages and degrees of alteration. These data are compared to compositional changes in major and trace element abundances relative to the unweathered protolith in order to investigate the mobility and adsorption processes of Si and Cr within different weathering regimes and intensities.

The Si isotopic compositions within the moderately weathered, Quaternary Chhindwara profile show a modest shift towards lighter $\delta^{30/28}Si_{NBS28}$ in those levels which contain higher abundances of pedogenic clays, zeolite minerals, and Fe-oxides. Accordingly, we conclude that this Si isotopic signature is related to the incorporation of isotopically light Si into secondary clays, or else to adsorption of isotopically light Si onto secondary Fe-oxides. The absence of any Cr isotopic shift beyond that of the parent substrate, together with the homogeneous Cr/Ti ratios, indicates that oxic alteration in this profile was insufficient to allow the degree of aqueous mobility of Cr required to deliver Cr isotopic fractionation to the neo-formed pedogenic oxides.

By contrast, the more extreme weathering regime, displayed by the lateritic Bidar weathering profile, results in much greater variation in Si and Cr abundances, and a larger variability of Si and Cr isotopic values relative to unweathered parent basalt. This indicates a much greater mobility of both elements within this weathering regime. Further, the strong co-variation of Fe with enrichment as well as the Si and Cr isotopic composition, strongly indicates that within profile Fe mobility and oxidation of Fe is a dominant factor for isotopic variability.

Although mass balance calculations reveal autochthonous or allochthonous Cr and Fe inputs to the profile, the vertical redistribution of Fe, Cr and Si during chemical weathering under changing pH-Eh conditions remain the most plausible explanation for the observed isotopic behaviour. The importance of Fe-oxide formation upon both Si and Cr isotopes illustrates that redox-dependent transformation and the redistribution of Fe during weathering have a significant influence on the overall aqueous mobility of Cr and the isotopic signatures of Si and Cr in meteoric waters.

Intense chemical weathering during lateritisation favours significant removal of Si. The formation of Fe-oxides during lateritisation is accompanied by Si isotopic fractionation in response to Si adsorption. However, its effect on the net Si isotopic removal is likely to be relatively small. Therefore, rivers draining areas of dominantly lateritic terrains are likely to display slightly lighter Si isotopic values, but will remain close to that of the initial parent lithology, (e.g., as observed in rivers of the Congo Basin by Cardinal et al., 2010).

It has been reported that Cr can be mobilised in pore waters under low pH and Eh conditions during lateritisation (Berger and Frei, 2014). Here, reductive loss of Fe and Cr from the profile is likely associated with a limited isotopic fractionation such that the overall Cr removal has an isotopic composition close to that of the magmatic range. This is consistent with Fe isotope investigations in modern lateritic profiles which display little or no Fe isotopic variation within laterites (Li et al., 2017; Poitrasson et al., 2008). However, by contrast to Fe, significant Cr isotopic fractionation is observed in those horizons where liberated Cr is effectively scavenged by the formation of Fe-oxides. Such a process will decrease the dissolved Cr output from the soil horizon and, accordingly, its overall influence upon the global budget. However, on a local scale the input of lateritic dust by aeolian transportation into marine basins or the open ocean might have a strong influence on dissolved Cr isotopic composition in marine surface waters.

Lateritisation processes affect large areas of continents located at low latitudes, where precipitation rates are high. Chemical reactions and element mobilities during laterite formation have considerable influence on the ocean element budgets. Long-term increase in laterite formation and associated elemental fluxes and isotopic fractionation processes would coincide with those periods when tectonic processes have preferentially assembled landmasses at low, tropical latitudes. Short-term increases would be coeval with times of climatic global warming and high precipitation rates coupled with elevated atmospheric CO_2, ocean anoxia and mass extinction events (Retallack, 2010). An increased Si flux to the oceans coupled with a lighter, continental isotopic signature in the marine sedimentary record should, therefore, reflect those times when extensive continental areas, and/or ‘greenhouse’ climate conditions became prevalent.

Acknowledgements

We thank Dr David Chew for assistance with the LA-ICP-MS mapping work. NS acknowledges the ISONOSE Marie Curie Research training network funded from the People Programme (Marie Curie Actions) of the European Union's Seventh Framework Programme FP7/2007- 2013/ under REA grant agreement n° [608069]. Financial support for this study was provided by Deutsche Forschungsgemeinschaft (DFG) project SCHO 1071/7-1 to R.S under the DFG- Priority Programme SPP-1833 “Building a Habitable Earth”. We thank Damien Cardinal, one anonymous reviewer and Editor Alexander McBratney for their time and effort that helped to improve this contribution.

7. Supporting Information

7.1. Analytical Methods

7.1.1. Chemical Index of Alteration (CIA)

The CIA is calculated from the major element geochemistry of bulk sediment samples to determine to which extent sediments have experienced chemical weathering. During chemical weathering, the values of the CIA weathering indices increase due to the loss of mobile elements of Ca, Na and K that are commonly hosted in feldspars, relative to an element assumed to be immobile like aluminium (Nesbitt and Young, 1982). The CIA is defined by the formula:

$$CIA = Al_2O_3/[Al_2O_3+CaO^*+Na_2O+K_2O]*100$$

where the elemental abundances are expressed as molar proportions, and CaO* represents the CaO contained only in the silicate fraction (i.e., corrected for Ca in apatite; Fedo et al., 1995).

7.1.2. Mafic Index of Alteration (MIA)

The mafic index of alteration (MIA) extends the equation of the CIA to include the elements Mg and Fe which are a major constituent of mafic minerals like pyroxene and olivine which are susceptible to chemical weathering. However, the mobility and loss of Fe during weathering is determined by redox conditions. While mobile under reducing conditions as Fe^{2+}, Fe is typically regarded as immobile under oxidising weathering conditions when Fe^{2+} can oxidise to Fe^{3+}. Therefore, two versions of the MIA are proposed (Babechuk et al., 2014):

$$MIA_{(oxidising)} = [Al_2O_3+Fe_2O_{3(T)}]/[Al_2O_3+ Fe_2O_{3(T)}+MgO+CaO^*+Na_2O+K_2O]*100$$

$$MIA_{(reducing)} = Al_2O_3/[Al_2O_3+ Fe_2O_{3(T)}+MgO+CaO^*+Na_2O+K_2O]*100$$

where the elemental abundances are expressed as molar proportions, and CaO* represents the CaO contained only in the silicate fraction. The $MIA_{(oxidisting)}$ formula has been used for calculating extent of alteration for both weathering profiles.

7.1.3. Index of Laterisation (IOL)

In the process of lateritisation, dissolution of quartz and kaolinite and the enrichment of Fe oxides are the dominant processes, resulting in a loss of Si relative to Al and Fe in the weathered residue. Therefore chemical characterisation of laterisation based on major elements is based on the $SiO_2/[Al_2O_3/Al_2O_3+ Fe_2O_{3(T)}]$ ratio (Schellmann, 1986) and calculated :

$IOL = [Al_2O_3+Fe_2O_{3(T)}]/[SiO_2+Al_2O_3+Fe_2O_{3(T)}]$

using the mass (wt.%) ratio of SiO_2, $Fe_2O_{3(T)}$, and Al_2O_3 (Babechuk et al., 2014)

7.2. Silicon isotope analysis

Sample decomposition and Si purification procedures followed the general method described in (van den Boorn et al., 2006; Wille et al., 2010). Briefly, 1-2 mg of homogenised sample powder was transferred into 2 ml Teflon vials with the addition of 0.5 ml 2 M NaOH produced from $NaOH·H_2O$ (Fluka, TraceSelect). Eight of these Teflon vials, closed with a loose lid, were placed in a Teflon liner with the addition of 10 ml 2 M NaOH and then clamped into a Berghof DAB-3 High pressure digestion vessel. The process of silicate depolymerisation was then accelerated by placing digestion vessels in a furnace at 200 °C for 3 days. After cooling the sample vials, the sample-NaOH mixture was transferred into pre-cleaned 2 ml centrifuge tubes and centrifuged at 12000 rpm for 10 min to separate solid residue from NaOH. The NaOH supernatant was pipetted to a separate vial. The residue was washed with 0.5 ml of Milli-Q, centrifuged again, and the Milli-Q was combined with the NaOH supernatant. A 0.5 mL aliquot of concentrated HNO_3 + 3 HCl was added to the solid residue and the sample+acid mixture was transferred to the previously used Teflon vials, capped, and placed on a hot plate at 100 °C for several

hours to decompose the solid residue. The HNO_3 + 3 HCl was then evaporated and samples were dissolved in 0.25 ml of 0.25 M HNO_3. In contrast to pure silica samples, which completely dissolved after this decomposition procedure, most of the whole rock samples contained a whitish, lactic residue. In these cases, the residue was decomposed by repeating the HNO_3 + 3 HCl dissolution treatment described above. After complete decomposition, 1 ml LDPE pasture pipettes with a stem diameter of 5 mm, filled with 0.5 ml of cation exchange resin (Dowex AG-X8, 100-200 mesh, Bio-Rad) were used in order to separate silicon from major sample matrix elements. At this stage, both the NaOH and HNO_3 sample aliquots were loaded onto the column and Si was eluted from the resin by adding 1.75 ml of Milli-Q water. Subsequently, HNO_3 was added to the eluted Si-bearing solution in order to attain ~2 ppm Si in a 1% (v/v) HNO_3 solution. Silicon isotopes were determined by multiple collector inductively coupled plasma mass spectrometry (MC-ICP-MS) (Neptune Plus, ThermoFisher Scientific). Measurements were performed in medium resolution and dry plasma modes using the ESI Apex Q desolvating system to resolve polyatomic interference on all three stable isotopes (^{28}Si, ^{29}Si, ^{30}Si). Sample introduction into the desolvating system were performed with an ESI PFA self-aspirating nebulizer generating a dry aerosol, which was transferred via Teflon tubing and a sapphire injector into the Ar-plasma. Although signal intensities varied on a session to session basis, typical signal intensity of around 20 V (10^{11} Ω amplifier resistor) on mass ^{28}Si was achieved with an uptake of ~100 µl/min of the 2 ppm sample solution. A background ^{28}Si signal <0.04 V was achieved within a few minutes with a washout of blank 1% HNO_3 solution despite using a quartz instead of Teflon ESI Apex Q. Data acquisition and reduction were carried out using a standard bracketing technique (Albarede et al., 2004). All values are reported relative to the Si isotope reference standard NBS-28 reported in delta (δ) notation in ‰ units: $\delta^{30/28}Si = [(^{30}Si/^{28}Si_{sample})/(^{30}Si/^{28}SI_{NBS-28}) - 1] \times 1000$. The isotopic difference between two Si reservoirs A and B are expressed as $\Delta^{30/28}Si_{A-B} = \delta^{30/28}Si_A - \delta^{30/28}Si_A$. Repeated decomposition and measurement of an in-house homogenised demosponge SP150 (n=10) from the Antarctic shelf at a depth of 457 m (Wille et al., 2010) and Herkimer “diamond” quartz (n=13) (Douthitt, 1982) yielded an average value and 2SD of $\delta^{30/28}Si_{NBS28}$ = -3.24 ± 0.12 ‰ and $\delta^{29/28}Si_{NBS28}$ = -1.65 ± 0.07, and $\delta^{30/28}Si_{NBS28}$ = +1,47 ± 0.11 ‰ and $\delta^{29/28}Si_{NBS28}$ = +0.76 ± 0.05, respectively which are in line with published values for these materials $\delta^{30/28}Si_{NBS28}$ = - 3.13 ‰ and $\delta^{29/28}Si_{NBS28}$ = - 1.63 ‰ for SP150 (Wille et al., 2010) and $\delta^{30/28}Si_{NBS28}$ = + 1.4 ‰ for Herkimer “diamond” quartz (Douthitt, 1982). Furthermore, 5 measurements from replicate processes of the Diatomite standard

(Reynolds et al., 2007) yielded mean and 2SD $\delta^{30/28}Si_{NBS28}$ and $\delta^{29/28}Si_{NBS28}$ values of +1.21 ± 0.07 ‰ and +0.66 ± 0.07 ‰, respectively which is within analytic errors identical to published, compiled values of $\delta^{30/28}Si_{NBS28}$ = + 1.25 ‰ and $\delta^{29/28}Si_{NBS28}$.= + 0.65‰ (Reynolds et al., 2007). Silicon isotopic values of two geological reference materials, the basalt BHVO-2 and iron formation IF-G, were measured in the same experiment as the samples for this study. The BHVO-2 standard gave an average value of $\delta^{30/28}Si_{NBS28}$ = -0.23 ± 0.02 ‰ and $\delta^{29/28}Si_{NBS28}$ = -0.11 ± 0.01 ‰ (2SD, n=2). While the $\delta^{29/28}Si_{NBS28}$ isotopic difference in close agreement with the compiled $\delta^{29/28}Si_{NBS28}$ value of -0.15 ± 0.02 ‰ the $\delta^{30/28}Si_{NBS28}$ value is slightly heavier compared to average compiled values other research groups of $\delta^{30/28}Si_{NBS28}$ = - 0.28 ± 0.05 ‰ (Savage et al., 2014). Although this offset is near the external reproducibility, it likely represents a minor and uncorrected interference from sulphur (S) (van den Boorn et al., 2009). To evaluate the influence of this interference on sample unknowns, the total S was measured with a carbon nitrogen sulphur (CNS) analyser Vario EL III from Elementar at the at the Soil Science and Geomorphology Group, University of Tubingen and the SO_4/Si ratio compared to that of BHVO-2. In all samples except BB-6 (SO_4/Si = 0.021) and BB-9 (SO_4/Si = 0.020) the SO_4/Si ratios are lower than that of BHVO-2 (SO_4/Si = 0.002). Thus, the maximum potential offset from S interference in the samples could not exceed a $\Delta^{30/28}Si$ of 0.05 ‰ (except samples BB-6 and BB-9) and is indistinguishable within the overall method reproducibility. In samples BB-6 and BB-9 the S interference should not have influenced the final Si isotope value significantly beyond the method reproducibility and thus does not influence the interpretations of the study. The IF-G standard, from a large Fe ore deposit in the 3.8 Ga old Isua Supergroup, West Greenland, yielded an average value of $\delta^{30/28}Si_{NBS28}$ = -2.66 ± 0.03 ‰ and $\delta^{29/28}Si_{NBS28}$ = -1.36 ± 0.01 ‰ (2SD, n=2). To our knowledge, no Si isotopic value for IF-G has been published elsewhere to permit comparison. However, the isotopic composition measured here matches well with published values for quartz sampled from banded iron formation in the same locality (André et al., 2006). Error bars within figures indicate 2SD external reproducibility of the Herkimer “diamond” quartz of $\delta^{30/28}Si$ = 0.12 ‰

7.3. Chromium isotope analysis

The sample powders were combined with a mass of a ~22 ug g^{-1} ^{50}Cr-^{54}Cr 2 M HNO_3 double spike solution within the beakers to yield a 1:1 sample:spike Cr abundance ratio. Sample digestion and spike-sample homogenisation was achieved by the addition of a concentrated HF and HNO_3 mixture. Samples were placed on a hotplate at 110 °C for 3 days. The mixture was then evaporated and the residue was reacted in the sealed beakers with 6 M HCl at 130 °C for 1 day to breakdown any fluorides formed during the preceding step. The HCl was then evaporated and the residue was dissolved again in 6 M HCl and evaporated once more to form a chloride residue. This residue was dissolved in a 1ml 6 M HCl solution in preparation for chromatographic Cr separation.

The purification of Cr from matrix elements and notably those with isobaric interferences on the Cr isotopes (^{54}Fe, ^{50}Ti and vanadium-50 (^{50}V)) was achieved with one of two protocols. The first protocol is described in detail by Schoenberg et al. (2008) and involves a liquid-liquid extraction with Cyanex® 923 followed by an anion resin (Biorad Dowex© AG1-X8, 100-200 mesh) exchange chemistry that separates Cr as Cr(VI) from remaining matrix elements. The second recipe is described in detail by Schoenberg et al. (2016) and involves a three-step chromatography initially separating Fe from the matrix including Cr using an anion resin (Biorad Dowex© AG1-X8, 100-200 mesh) with the remaining matrix elements separated from Cr using two cation resin (Biorad Dowex© AG50W-X8, 200-400 mesh) steps. The recovery of the total dissolved Cr following either protocol was typically > 70% and any mass-dependent isotopic fractionation occurring from partial loss of Cr is accurately corrected for by the fully homogenised Cr double spike as part of the correction procedures outlined below (Trinquier et al., 2008; Larsen et al., 2016). Samples processed using both chemistries have been shown to produce matching Cr isotope ratios (Schoenberg et al., 2016; Babechuk et al., 2017). Following both of the aforementioned purification protocols, the final aliquot of recovered Cr was converted to a nitrate form using addition of concentrated HNO_3 in preparation for isotopic analysis.

In preparation for Cr isotope analysis, all purified samples were dissolved in 0.15 M HNO_3 along with aliquots of an in-house Merck Cr(III) and NBS SRM979 standards, combined and homogenised with the Cr double spike on the day of analysis, to produce for all a matched measurement concentration of ~150 ng g^{-1}. The Cr isotope analyses were

performed over three analytical sessions on a ThermoFisher Scientific NeptunePlus MC-ICP-MS operated in medium resolution mode to resolve and avoid Ar-carbide, -oxide, and –nitride interferences on the monitored Cr and Fe masses. Sample and standard solutions were aspirated using a ESI µFlow nebulizer at an uptake rate of 100-150 µl min^{-1} into an Aridus II desolvating system to generate dry plasma conditions. Data were acquired in static mode with simultaneous measurement of all Cr (50, 52, 53, 54) and isobaric monitor (^{49}Ti, ^{51}V, and ^{56}Fe) masses bracketed with pure 0.15 M HNO_3 blank solutions for online on-peak-zero baseline corrections. Sample and blank measurements consisted of 120 and 45 cycles, respectively, and each with 4.1 s integration time. Chromium signal intensities ranged from ~9 to 12 V on ^{52}Cr using a 10^{11} Ω resistor. Experiment sequences were started and finished with measurements of standards, which were also interleaved every three sample unknowns throughout. The baseline corrected Cr isotope ratios were processed offline to correct for signal interference by the relevant isobars, mass-dependent instrument fractionation, and any of the mass-dependent isotopic fractionation inherited from the chromatography, assuming an exponential law (Schoenberg et al., 2008). The double spike-deconvoluted ^{53}Cr/^{52}Cr ratios of the experiment session were normalised to the mean of this ratio measured for the SRM979 standard and reported in delta (δ) notation ‰ units, consistent with other studies, as: $\delta^{53/52}Cr = [(^{53}Cr/^{52}Cr_{sample})/(^{53}Cr/^{52}Cr_{SRM979}) - 1] \times 1000$. The procedural blank Cr levels ranged from 24 to 28 ng for the first and 0.6 to 2.5 ng for the second purification procedures, respectively. All procedural blank levels were insignificant relative to the amount of processed sample Cr and did not require further blank correction.

The repeated measurement of the in-house Merck Cr(III) standard solution in the combined analytical sessions returned an average $\delta^{53/52}Cr_{NBS979}$ value of -0.431 ± 0.042 ‰ (2 SD, n = 19) relative to SRM979, in agreement with previous studies (Babechuk et al., 2017; Schoenberg et al., 2016; Schoenberg et al., 2008; Zink et al., 2010) which report average $\delta^{53/52}Cr_{NBS979}$ values of between -0.433 and -0.443 ‰ for the in-house Merck Cr(III) standard solution. The reproducibility of $\delta^{53/52}$Cr in natural samples is conservatively estimated at 0.05 ‰ (Schoenberg et al., 2008), which is the error value used in all data plots unless the internal standard error of an individual sample measurement exceeded this value.

7.4. LA-ICP-MS element mapping

New hand samples from the same localities described in Babechuk et al. (2014) were collected in 2016 for LA-ICP-MS trace element mapping of the Chhindwara basaltic bedrock and selected areas of the Bidar laterite profile. The LA-ICP-MS data were acquired using a Photon Machines Analyte Exite 193 nm ArF Excimer laser-ablation system with a Helex 2-volume ablation cell coupled to an Agilent 7900 ICPMS at the Department of Geology, TCD. The ICP-MS was tuned on NIST 612 glass as described by Ubide et al. (2015), with ThO+/Th+ ratios < 0.15% and Th/U ratios close to unity. Ten isotopes (lithium-7 (^{7}Li), ^{24}Mg, ^{29}Si, ^{52}Cr, ^{57}Fe, Ni-60 (^{60}Ni), copper-63 (^{63}Cu), Zn-66 (^{66}Zn), ^{232}Th and uranium-238 (^{238}U)) were measured using a total duty cycle of 135 ms. A laser fluence of 3.3 J/cm^2, a repetition rate of 31 Hz, a 12 μm spot size and a scan speed of 20 μm/s were employed. The NIST612 glass reference material was used as the calibration standard and data reduction and production of trace element distribution maps was undertaken with the Iolite software (Paton et al., 2011) using the "Trace Elements" data reduction scheme in "Semi-Quantitative" mode. The final ablated area was rectangle-shaped and the map was generated by "rastering" the sample under the ablation site for processing with the "Image from Integrations" module in Iolite, similar to in (Ubide et al., 2015).

7.5. Model calculation

The loss or gain of an element j from a weathering profile, defined as τ, is calculated relative to an immobile element i, where p and s refers to the parental basalt and weathered material respectively.

$$\tau_{j,s} = \frac{\left(C_{j,s} / C_{i,s}\right)}{\left(C_{j,p} / C_{i,p}\right)} - 1$$

For the Bidar profile we regard the elements Cr, Fe and Si as mobile elements j and we use Ti as immobile element i. Using element concentration of the parental basalt BB-1,

indexed p, the loss and gain of Cr, Fe and Si for all 9 Bidar samples, indexed s, can be calculated. Knowing the density of the parental basalt BB-1 ρ_p=2.6 g/cm^3 (Babechuk et al., 2015) the absolute mass flux θ of an mobile element j from and sample volume can be calculated:

$$\theta_{j,s} = \frac{\tau_{j,s} * C_{j,p} * \rho_p}{100}$$

We assumed a linear change in τ with depth between the unweathered basalt BB-1 and the paleo-water table at BB-6 and between BB-7 and BB-9. With that assumption the θj can be calculated for any depth interval between BB-1 at 4700 cm and BB-9 at 200 cm profile depth. For Figure 8 in the main text we calculated θj in a depth interval of 1 cm and integrated the total element loss or gain by summation of single θj, expressed as $\sum j_{flux}$, between samples BB-1 and BB-9.

Supplemental Table. Model calculations of loss and gain and mass fluxes of Cr, Fe and Si in the Bidar laterite.

Sample	Depth [cm]	Density [g/cm^3]	τ_{Cr}	τ_{Fe}	τ_{Si}	θ_{Cr} [mg/cm^3]	θ_{Fe} [g/cm^3]	θ_{Si} [g/cm^3]
BB-9	200	3.2	3.83	5.16	-0.79	1.56	1.26	-0.47
BB-8	500	2.6	3.67	1.65	-0.41	1.49	0.4	-0.24
BB-7	600	1.7	0.51	0.83	-0.34	0.21	0.2	-0.2
BB-6	1100	2	7.18	8.76	-0.81	2.92	2.14	-0.48
BB-5	1300	1.5	-0.36	0.03	-0.77	-0.15	0.01	-0.45
BB-4	1500	1.5	-0.35	-0.27	-0.64	-0.14	-0.07	-0.38
BB-3	2600	1.2	-0.41	-0.24	-0.67	-0.17	-0.06	-0.4
BB-2	3500	2.6	-0.09	-0.11	-0.03	-0.04	-0.03	-0.02
BB-1	4700	2.6	0	0	0	0	0	0

Chapter 5: The role of pedogenic impacts and cow dung for available essential metal contents in agricultural topsoils of Central India

To be submitted to an agricultural journal after the submission of this PhD thesis

Authors: Nils Suhr, Mike Widdowson, Balz S. Kamber

Abstract

Essential metals are micronutrients for plants, livestock and humans at trace concentrations and consequently involved in complex bio-geochemical cycles in the environment. In Central India, people strongly depend on local agriculture and crops grown in most soils suffer from deficiencies of essential metals (iron (Fe), zinc (Zn), molybdenum (Mo)) through soil over-cropping although the soils often contain adequate total amounts of these elements. Additionally, new types of metal deficiencies in soils are likely to emerge until 2050 as a result of population growth and higher demands on crop production. Here we present major element, organic carbon (C_{org}) and total as well as diethylenetriamine pentaacetic acid (DTPA)-extractable (i.e. plant available) essential trace metal data (Zn, copper (Cu), chromium (Cr), nickel (Ni), cobalt (Co), Mo) of agricultural topsoils from Central India to determine the role of the (in)organic constituents regarding metal deficiencies. The same elements were measured in cow dung to find out if trace metal cycles are affected by a soil-plant-cattle relation on Indian farmland. Our results demonstrate that oxide minerals contain high concentrations of essential trace metals (Fe, Zn, Cu, Cr, Ni, Co) in the soils in bio-unavailable forms, whereas complex clay minerals and residual primary silicates have modest quantities of plant available essential metals (Zn, Cu, Ni, Co). By contrast, concentrations of Mo are extremely low or non-existent in soil minerals. Organic C in soils is crucial for bio-available Zn, Cu and Fe. Our calculations demonstrate that cattle ingest soil matrix in Central India and that Fe, Cr, Co and Ni concentrations are contaminated by oxide minerals, whereas Zn, Cu and Mo concentrations are stronger linked to traditional fodder and food additives. However,

except for Fe, the bio-available quantities of essential metals in cow dung are likely insufficient to correct multi-metal deficiencies in soils that are caused by over-cropping. Regardless, the importance of C_{org} for the bio-availability of essential metals and physicochemical health of soils suggest that the combination of farmyard manure with cheap metal fertilisers might represent a useful approach to combat multi-metal-deficiency in soils in the future.

1. Introduction

Malnutrition from a lack of micronutrients in diet, also known as *hidden hunger* (e.g., Andersen, 2007), is a threat to human health in developing countries. Micronutrients are only required at trace concentrations but are essential for a healthy life and therefore they are considered to be a fundamental aspect of food security. Presently, the World Health Organisation (WHO) recognises iodine (I), vitamin A and Fe as the most important micronutrients in global public health terms. However, Fe is not the only essential metal and many studies have provided evidence that Zn deficiency in soils has knock-on effects for plants and ultimately humans that over-depend on crops local for diet (e.g., WHO 1996; Bhan et al., 2001; Andersen, 2007). Through advances in analytical chemistry and instrumentation there is increasing awareness that apart from Fe and Zn, other metals are bio-essential at trace levels (Maret, 2016). For instance, Cu, Mo and Co are essential to the growth and health of plants, animals and humans (He et al., 2005). Furthermore, Ni is essential for plant growth (e.g., Brown et al., 1987) and bacteria, whereas researchers are still disputing the vital role of Cr (III) (e.g., Maret, 2016). Possibly, Cr (III) functions as co-factor for insulin in the human body (e.g., Deckers and Steinnes, 2004).

Despite the importance of essential trace metals for life, there is a lack of knowledge about the origin of deficiency of most of these metals. Little is known about their deficiency in soils and even less about the relationship of deficiency to the mineralogical makeup of the soil. Therefore, the potential risks for plant and human health due to multi-essential trace metal deficiency in soils are relatively unknown.

Metal deficiency in soils occurs most commonly in (sub)-topical regions, where aggressive chemical weathering of the rock substrate leads to strong elemental depletion in the residue. During soil formation in (sub)-tropical regions, essential metals are often completely lost from newly formed soil minerals (Fyfe et al., 1983). Furthermore, it is possible that a fraction of the essential metals redistributes into inert pedogenic oxides (e.g., Cr; Zn; Wille et al., 2018; Suhr et al., 2018a), or that high concentrations remain entirely immobile in weathering resistant primary oxides (Nesbitt and Wilson, 1992). An important factor is that in topographically static regions (geologically speaking cratons) in the tropics, physical erosion rates are low, and soil profiles become very thick, old and depleted (Fyfe et al., 1983). The release of elements (e.g., Buss et al., 2013), including

metals (e.g., Suhr et al. 2018a,b), from the inorganic constituents of subsoils to soil solutions usually occurs at the bedrock saprolite interface, whereas the strongly weathered, often oxide-rich upper levels of soil profiles are incapable to supply metals to plants. Consequently, bio-available pools of elements and metals in the soil reservoir are often concentrated in the deep subsurface in tropical cratonic regions, whereas the natural supply of plants in top horizons through leaching of primary (silicates) and secondary minerals (clays) is very limited (Kronberg et al., 1979; Fyfe et al., 1983).

The Indian subcontinent is one of the most densely populated and heavily farmed regions on Earth. It is anticipated that by the year 2050, 1.5 billion people will live in India and that a high proportion of this population will rely on local food sources. As a result, food production must increase to 5 Mt as compared to 3.1 Mt $year^{-1}$ in 2000, with little scope for expanding the area under cultivation (Singh, 2008). The increase in food production will rely on a modernisation of agricultural practices, i.e. the "Green Revolution" which started in the second half of the 20^{th} century. To increase yield, farmers are replacing traditional grain crops with new high yielding varieties (HYV) to meet the exploding food demand (e.g., Hazell, 2009). The resulting increase in grain production results in additional removal of micronutrients from soils. On Indian farmland, essential metal deficiency problems with knock-on effects for crops have already developed (e.g., Zn, Fe, Mo; Singh, 2008). These new farming practices have the most severe consequences for the health of those humans that rely on local crops as their main diet (Welch and Graham, 1999). Amongst others, essential metal depletion in soil is triggered by the use of nitrogen (N) and phosphor (P) fertilisers and associated high cropping intensity, and the soil-crop-human micronutrient deficiency chain has been documented for Zn, Fe and Mo. Through the continuous and increasing application of such modern farming practices, it is anticipated that further essential metals (e.g., Ni, Cu, Co) will become deficient in Indian soils by 2050 (Figure 1).

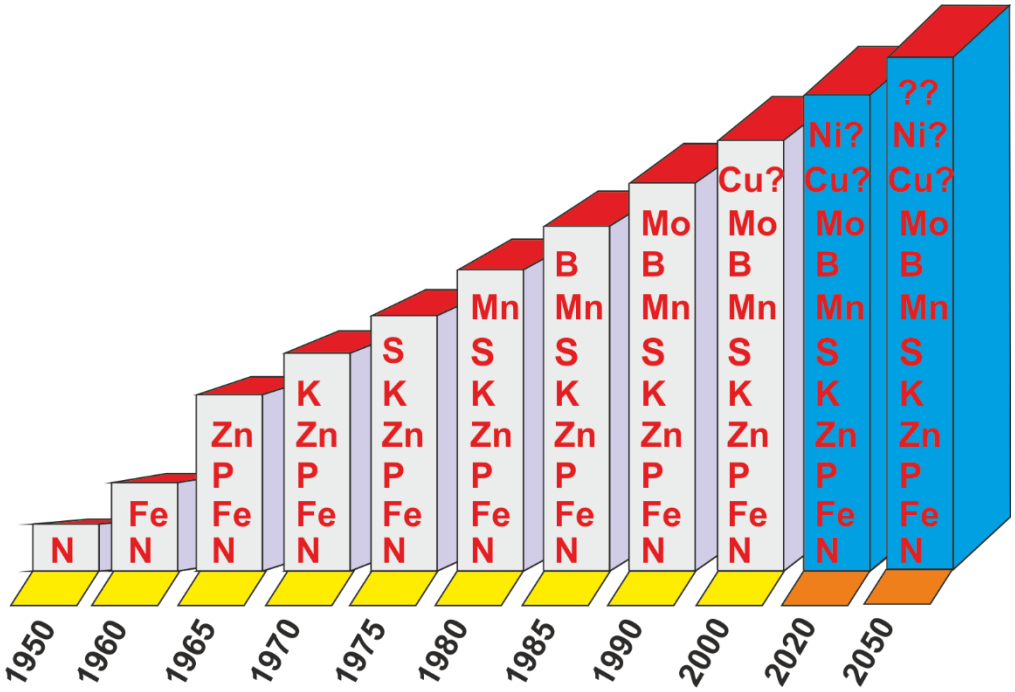

Figure 1. Impact of "The Green Revolution" in the past, present and future (illustrated as blue beams) on the emergence of micronutrient deficiencies (including essential metals) in crops in India (modified after Singh, 2008).

The details of this relatively recent phenomenon are not well understood and the latest developments in biofortification, such as the ability of rice to uptake high concentrations of Fe and Zn (Singh et al., 2017), will further cause stress on the essential metal status of agricultural soils in India.

There is the awareness that strategies are needed to combat essential metal deficiencies in Indian soils through the development of balanced fertilisation practices that involve customised fertiliser products, complex fertiliser formulations and organic matter enrichment (Singh, 2008). An important geological factor is that much of the Indian subcontinent is underlain by ancient, cratonic crust and large areas are covered with old and deeply weathered soils under agricultural cultivation (Figure 2). It is, therefore, possible and probable that the soil reservoirs of Indian farmland contain minerals depleted in many essential trace metals. Better information on the status quo and mineralogical distribution of essential trace metals in soils is needed for the design and development of sustainable land use in India.

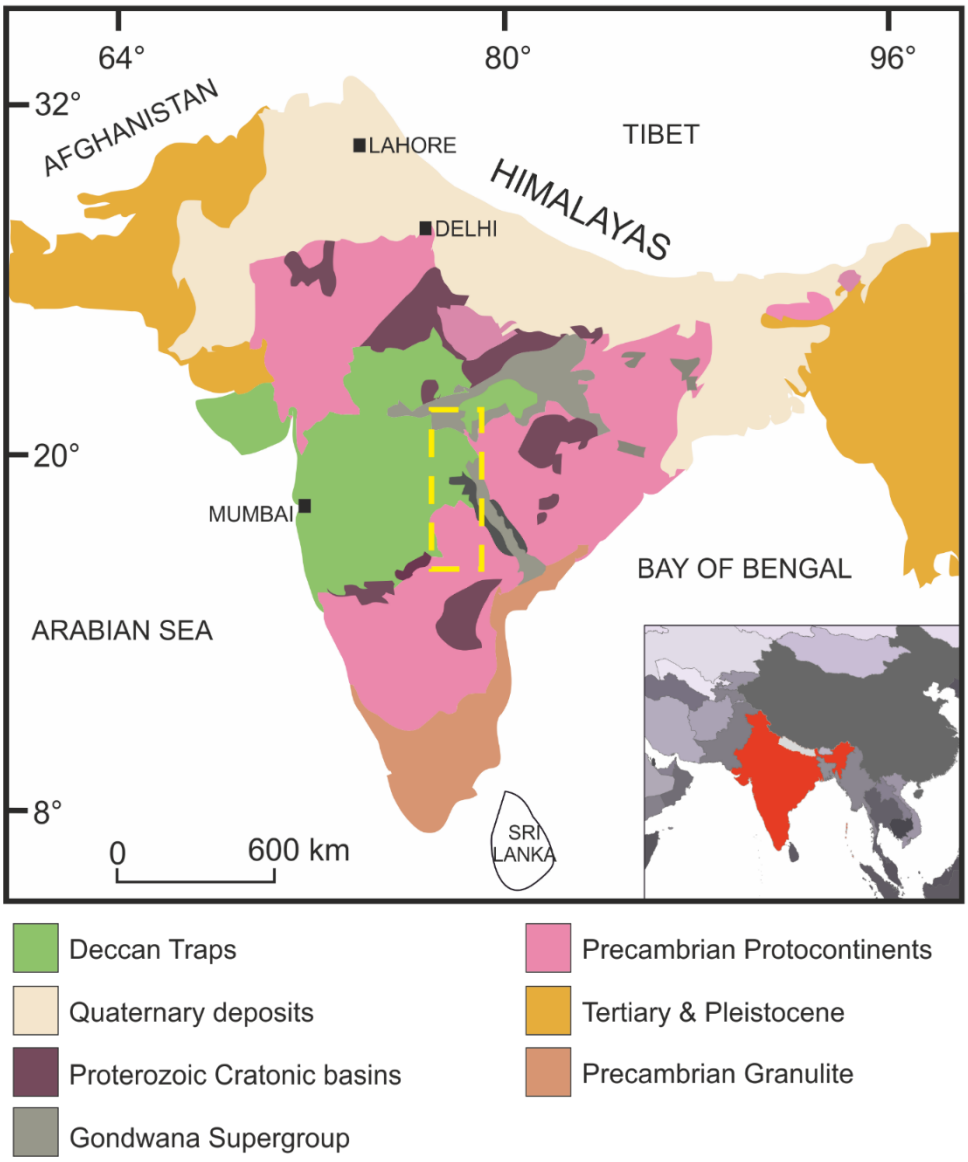

Figure 2. Geological map of the Indian Subcontinent (based on the Geological Survey of India map, 1993), modified after Roy (2012). The dashed yellow rectangle illustrates the area of Central India that we investigated for this study. The overview map in the lower, right corner of the figure shows the Indian state territory in red colour.

Most farmers in India still use traditional farming practices, relying on farmyard manure (FYM) as a fertiliser. Within the scientific community, there is an awareness that FYM ameliorates the bio-availability of micronutrients in soils (e.g., Singh, 2008) and that moderate manure application can lead to a bioavailable Zn-deficit in soils and consequently in crops (Figure 3; Alloway, 2008). Due to the importance of FYM, the uptake and release of Zn and other essential metals by cattle and other grazing livestock in India is clearly of interest but little knowledge exists about the cycling of soil nutrients by

grazing stock. Furthermore, at least to our knowledge, no one investigated the C_{org} or multi-essential trace metal content of cow dung in India. An important aspect of elemental cycling investigated is C_{org} (Figure 3). For instance, the application of too much C_{org} on agricultural fields via FYM may potentially immobilise Zn through complexation. As a result, Zn may become unavailable to crops. By contrast, scarce FYM application can also result in inferior bio-availability of Zn and cause Zn deficiency.

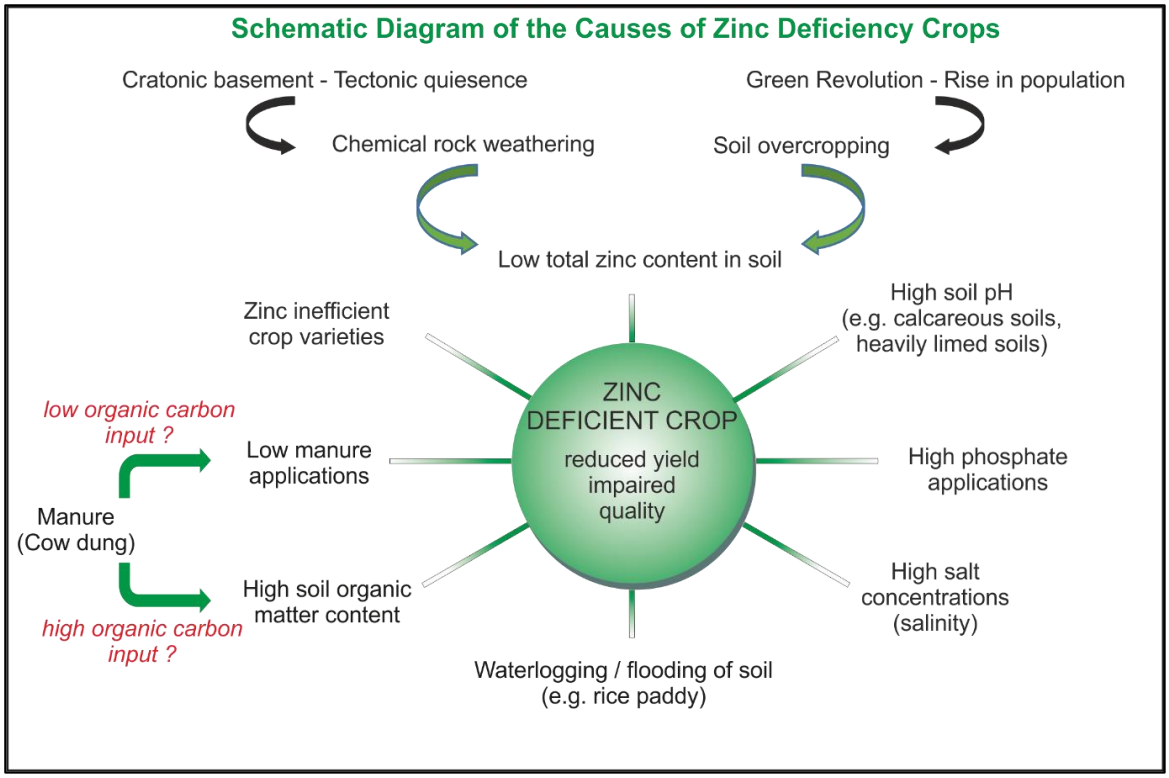

Figure 3. Schematic diagram of the causes of Zn deficiency in crops (modified after Alloway, 2008), including geological factors (Suhr et al., 2018a) and "The Green Revolution" (e.g., Singh, 2008; Andersen, 2002).

The present study aimed to contribute towards the investigation of the relationship between soil geochemistry and agriculture on the Indian subcontinent. It goals were to address whether the inorganic or organic constituents of the soil reservoir play key roles in essential metal availability for crops. To this end, we studied major oxides (calcium (CaO), sodium (Na_2O), potassium (K_2O), magnesium (MgO), aluminium (Al_2O_3), iron (Fe_2O_3), titanium (TiO_2), manganese (MnO)) (wt%) and essential metal concentrations (Zn, Cu, Co, Ni, Cr, Mo) (µg/g) on twenty soil samples from Central India. In addition, we measured

their C_{org} (wt%) and conducted a DTPA metal extraction (Fe, Zn, Cu, Ni, Cr, Co, Mo) (µg/g). Furthermore, we measured the C_{org} content as well as essential metal concentrations on eighteen FYM samples from Central India to discover whether the composition of this traditional fertiliser might help in the development of balanced fertilisation practices (Figure 1).

Geochemical study focusing on the inorganic features of soil nutrients is a relatively new approach to help assess the current fertility status of cultivated land in Central India. The ambition of such studies is to more clearly distinguish between bio-available and immobile pools of essential metals in soils in support of the development of alternative farming practices required to meet the population rise in India.

2. Sampling strategy and soil types of the study area

We collected agricultural topsoil samples (n = 20) in Central India over a distance of approximately 600 km to ensure geographic significance (Figures 2; 4). The soils lie over bedrocks of Deccan basalt (n = 11), granite-gneiss (n = 5), grey shale (n = 3) as well as clay-rich basaltic alluvium (n = 1), and farmers cultivated different crop types on these soils (maize, rice, lentils, cotton, wheat, millet). Importantly, most samples were taken from soils that formed over the cratonic basement (Figure 2). This choice of sampling site aimed to expose whether geological factors contribute significantly to the development of metal depleted soils with knock-on effects for crops (Fyfe et al., 1983).

Approximately, 100-200 g of sample material from a depth of ca. 5-15 cm was taken. The samples were collected from four agro-ecological zones (Madhya-Pradesh, Maharashtra, Andhra Pradesh and Karnataka). Based on the analysis of 256,000 surface soils and 25,000 plant samples in India, Singh (2001; 2008) classified these zones to have the highest per cent contribution from soils with Zn deficiency (Figure 4). It was anticipated that this sampling focus would expose other essential metal deficiencies if they exist in these regions. Figure 4 illustrates the dominant soil types according to the Food and Agriculture Organisation (FAO) of the United Nations classification as well as the climatic conditions of these agro-ecological zones. Acrisols (also named Red soils) develop over ancient crystalline and metamorphic rocks and have limitations of soil depth

and poor water retention as well as nutrient-holding capacity. Soils which developed over Deccan basalt and grey shale can be classified as Vertisols, whereas the laterites developed over Deccan basalt are Ferralsols (n = 3 samples in this study).

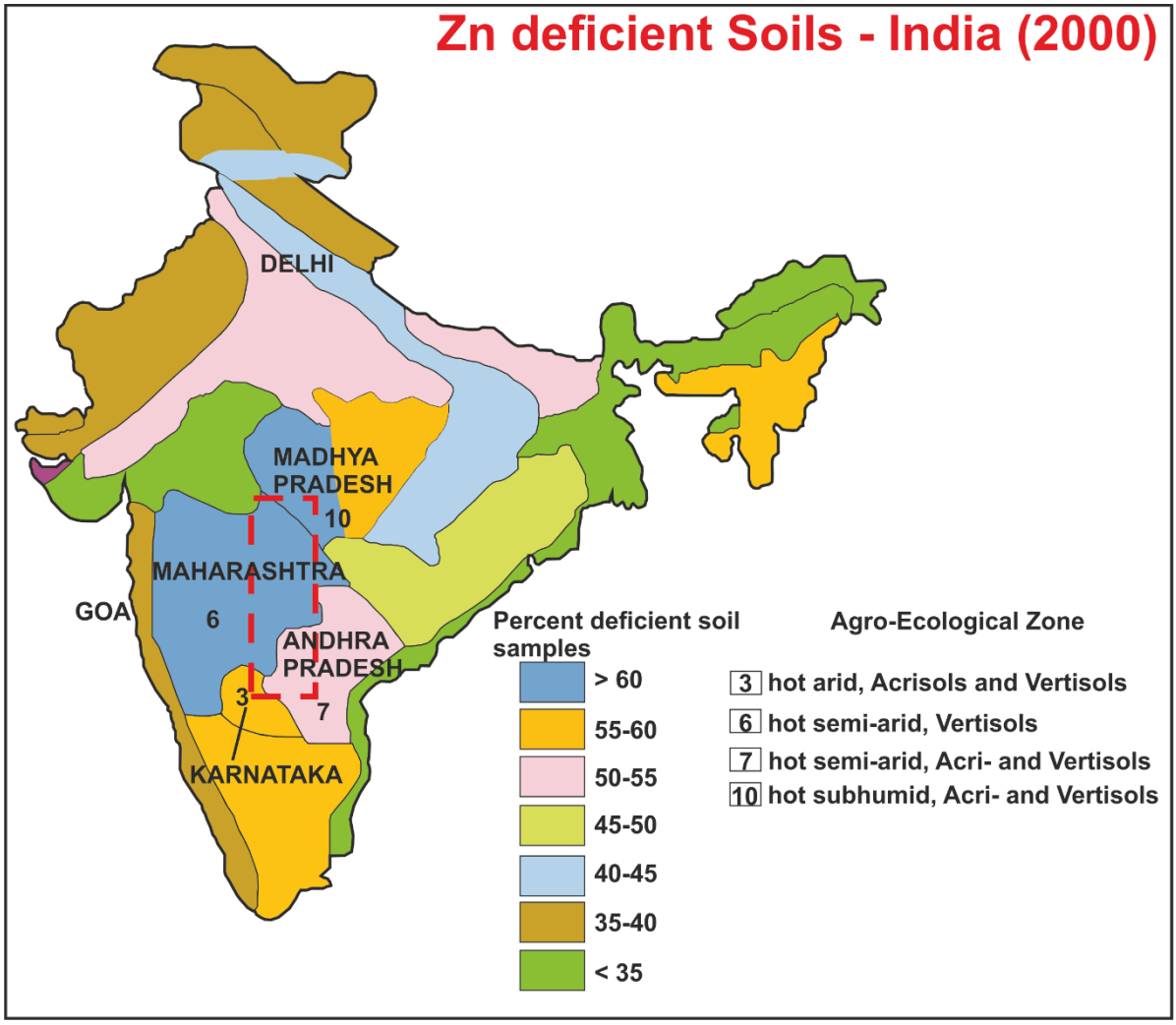

Figure 4. Percentage of Zn deficient soils in the different agro-ecological zones of India (Singh, 2001; 2008). In addition, the major soil groups in this area are illustrated according to the classification of the FAO (2005).

It should be noted that soils in Central India that derived from granite-gneiss commonly are Acrisols. However, our samples from granite-gneiss localities classify as Vertisols, regardless of the fact that weathered granite-gneiss crops out nearby (Supplemental Figure 1). This is because, in the lower piedmont plain of Central India, the mineralogy of Vertisols is inherited primarily from alluvium derived from weathering of Deccan basalt. Furthermore, multicycle erosion since the Pliocene-Pleistocene exhumed Archean to Upper Cretaceous formations so that weathering products such as quartz and

mica together with smectites from Deccan basalt were transported downstream and deposited as alluvium (Deshmukh, 1980; Pal and Deshpande, 1987). These Vertisols of the lower lying valleys, therefore, do not directly represent autochthonous soil formation (Supplemental Figure 1) and break the geology-soil relationship.

Historically, the study area is known for prolific cotton production and the Vertisols are locally known as "black cotton soils". Newbold (1843) first described this soil type to chemically consist of silica (SiO_2) together with CaO, Al_2O_3, Fe_2O_3, and minute portions of vegetable and animal debris. The region of their main occurrence is the Deccan plateau between 15° and 25° north latitude and 73° and 80° east longitude (e.g., Simonson, 1954). Smectite is the most dominant mineral in the Vertisols. Non-expanding clay minerals (kaolinite, micas, chlorites, palygorskite and vermiculites) also occur in Vertisols (e.g., Pal et al., 2012) and carbonate of pedogenic and non-pedogenic origin (relict iron-manganese (Fe-Mn) coated carbonate nodules) can also occur in this type of soil in India (Pal et al., 2000; Pal et al., 2009; Pal et al., 2012). The dark colour of Vertisols results from clay-organic complexes rather than from C_{org} content alone and Fe-Ti-Mn oxides also contribute to the dark pigmentation of this soil type (e.g., Coulombe et al., 1996).

Generally, the clay-rich (>35% (e.g., Nageswara Rao et al., 1997)) Vertisols are inherently very fertile. However, their physical conditions (swelling clay minerals) make them very difficult to cultivate and manage (FAO, 2005). Smectite is one of the earlier breakdown products in the Fe-Mg silicate weathering chain and the total content of micronutrients (Zn, Cu, Fe and Mn) of Vertisols is therefore quite high. In view of the high smectite content of Vertisols, it is therefore surprising that the study area belongs to the most metal-deficient regions in Central India. This clearly suggests that only a small fraction of the total content of these metals is bioavailable (Katyal and Sharma, 1991).

To date, studies on Vertisols in India (Srinivasarao et al., 2014; Sharma et al., 2006) and elsewhere (Yerima et al., 2014) have demonstrated that the quantity of clays exerts control over the total contents of essential metals such as Fe, Mn, Zn, Cu, Co and Ni and plant availability of these metals. Furthermore, the C_{org} content has been found to positively correlate with extractable forms of essential metals (Zn, Cu, Mn, Fe) (Sharma et al., 2006; Katyal and Sharma, 1991), whereas soil pH and higher $CaCO_3$ contents resulted in lower concentrations of Fe, Mn and Zn (Yerima et al., 2014; Katyal and Sharma, 1991).

By contrast, the role of other mineral constituents, such as primary silicates or oxides is unknown.

In addition to soil samples, we also obtained dung samples (whole cowpats) at representative locations (Figures 2; 4). One single sample (P4) contained a high amount of hay bedding whereas the rest are considered to represent FYM from grazing stock. Sampling locations are tabulated in the supporting information (Supplemental Table 1).

3. Methodology and analyses

3.1. Soil sample analyses

3.1.1. Bulk soil elemental analyses

The soil samples were stored in plastic bags and remained open to air dry them before they were sealed and sent to Ireland. At Trinity College Dublin (TCD), samples were oven dried at 60°C for 96 h to guarantee that all water evaporated. Dried samples were then sieved to collect the ≤ 2 mm soil fraction and subsamples of ca. 40 g pulverised in an agate mill for major and trace element analyses at ALS Minerals, Loughrea, Ireland. The full dataset is listed in the supporting information (Supplemental Table 2). For analysis of major oxides, 0.2 g of each sample was decomposed using a lithium metaborate/lithium tetraborate ($LiBO_2$/ $Li_2B_4O_7$) fusion and analysed by inductively coupled plasma atomic emission spectroscopy (ICP-AES) (ALS method ME-ICP06). For trace element analysis of Cr, 0.2 g of each sample was fused with $LiBO_2$ and analysed by inductively coupled plasma mass spectrometry (ICP-MS) (ALS method ME-MS81). A four-acid digestion was used to decompose samples for trace element measurements of Ni, Co, Cu, Mo and Zn by ICP-AES (ALS method ME-4A CD81). The precision of the data is 10% or better for both major elements and trace elements of interest. For the determination of the loss on ignition (LOI), 1.0 g was placed in an oven at 1000°C for one hour, cooled and then gravimetrically determined (ALS method OA-GRA05). To determine the total C_{org} (TOC, wt%) of the soil samples, between 30-50 mg of the powdered sub-samples was acidified with HCl to

remove the inorganic C (Harris et al., 2001). Analyses of the TOC were then undertaken using an Elementar Vario EL cube instrument at TCD.

3.1.2. DTPA extraction on soils for Zn, Cu, Co, Ni, Mo, Cr

We used the DTPA extraction method of Lindsay and Norvell (1978) and weighted a subsample of 10 g into flasks. To this we added 20 ml of the DTPA extracting solution and after that samples were shaken for 2h at 160 rpm on a shaker table. Next, we filtered the solution through a Whatman No. 2 filter paper and collected the filtrate in pre-cleaned flasks and decanted it into test tubes for inductively coupled plasma optical emission spectrometry (ICP-OES analysis). We measured the samples with a Varian Liberty Series II ICP-OES and tabulated the instrument method parameters and analyte settings in Supplemental Table 3. For the calibration of the instrument response a multi-element standard (Merck CertiPur ICP multi-element standard solution IV) and different dilution factors were used: 0.5, 1, 5 and 10 mg/l for Cu, Cr, Mo, Co, and Ni; and a single element standard for Fe at 50 and 100 mg/l. We also ran a quality control (QC) multi-element standard at 1 mg/l (AccuStandard ICP multi-element standard solution IV). We prepared the calibration, blank and QC solutions with the same DTPA extraction solution as the soil samples. Calibration coefficients were greater than 0.999. The internal blank levels for all elements of interest were beyond detection limit. Moreover, the mean concentration of two external blanks was ≤ 0.02 µg/g. We listed the concentration of all essential metals of the soil samples in Table 2, except for Cr and Mo that were beyond detection limit (≤ 0.01 µg/g).

3.2. Cow dung - trace element and C analyses

All cow dung samples were already air dry when we sampled and sterilised. In the laboratory, samples were then divided, recombined and mixed with a spatula to minimise heterogeneity (Peters et al., 2003). After that, the samples were oven dried at 60 °C for 72 h. Two grams of oven dried cow dung was then combusted in air at 500 °C for 8h (heating steps = 5 °C/min) to remove C, N, sulphur (S) and residual water, and then weighted to

determine the LOI for the conversion of the element concentrations. A 100 mg ash aliquot was digested in thoroughly cleaned Savillex Teflon® beakers using a hydrofluoride-nitric ($HF-HNO_3$) (4:1) acid mixture at ~ 160 °C for 72 h. After digestion, samples were dried down at 110 °C to drive off silicon tetrafluoride (SiF_4). The fluoride residue was attacked twice with concentrated hydrochloric acid (HCl) (2 mL) at 160 °C to liberate any residual metals associated with organic material. After the evaporation, 2 ml of concentrated HNO_3 were introduced to the residue for 24 h at 135 °C, and a double conversion with HNO_3 followed. The converted residue was then taken up in 10 g of 20% HNO_3 to yield a nominal 1:100 parts total dissolved solid stock solution and put on the hotplate for 96 hours to guarantee the complete dissolution of the samples. We measured the trace element composition at TCD. The method of Eggins et al. (1997) was followed, incorporating modifications described in Kamber (2009) and Babechuk et al. (2010). Approximately 4 % of this stock was gravimetrically diluted to produce a 2 % HNO_3 solution with an internal standard mixture containing ^{6}Li, rhodium (Rh), rhenium (Re), bismuth (Bi), and uranium-235 (^{235}U) for solution quadrupole ICP-MS (Q-ICP-MS) analysis on a Thermo Scientific iCap-Qs. During the analytical sessions, sample unknowns were preceded by blanks, calibration (USGS rock standard W-2a) and a quality control standard (BCR-2), and bracketed with monitor samples (one every 4-6 unknowns) for external drift correction (Eggins et al., 1997). The method reproducibility and accuracy was assessed using the long-term average of USGS and GSJ standards run as unknowns. The concentrations of the essential trace metals of interest reproduced better than 1% relative standard deviation (RSD) (1 sigma) for Cr, Co, Ni, Cu, at 2% RSD for Mo and 3% RSD for Zn. Furthermore, Fe reproduced at 0.5% and Ti at 0.8% RSD. The apparent reproducibility for Mo is poorer due to contamination of the second-generation USGS standards (e.g., Babechuk et al., 2015). The highest blank contribution was for Zn (<0.00004 µg/g). All other elements of interest had very low blank contributions, which we corrected, and did not affect the final sample concentrations. For the analysis of the C content, we needed only very low amounts of unashed cow dung. Therefore, we grounded sub-samples of the cow dung in a zirconium oxide ball mill at TCD. We weighted in 10-20 mg of the subsamples for the analysis of TOC (%) with an Elementar Vario EL cube instrument.

4. Results

4.1. Bulk soil elemental analysis and Chemical Index of Alteration (CIA)

Table 1 lists the major element (Na_2O, K_2O, CaO, MgO, Al_2O_3, Fe_2O_3, TiO_2, MnO), C_{org} (wt%) and essential trace metal concentrations (Zn, Cu, Ni, Cr, Co, Mo) (µg/g). In the soil samples, Na_2O (wt%) ranged from 0.04-1.99%, K_2O from 0.16-4.1%, CaO from 0.39-20.5%, MgO from 0.45-4.14%, Al_2O_3 from 8.95-21.00%, Fe_2O_3 from 3.04-29.60%, TiO_2 from 0.45-3.40%, MnO from 0.02-0.37%, and C_{org} from 0.67-1.83%. In terms of trace metals, Zn showed concentrations between 33-129 µg/g, Cu between 24-342 µg/g, Ni between 19-159 µg/g, Cr between 30-340 µg/g and Co between 7-82 µg/g. Except for two samples, Mo values were below the detection limit of 1 µg/g. To determine the degree of chemical weathering in the samples, we calculated the chemical index of alteration (CIA; Nesbitt and Young, 1982) (Table 1).

Table 1. Selected major elements, organic carbon content C_{org} (wt%), CIA and essential metal concentrations (µg/g) (Zn, Cu, Ni, Cr, Co, Mo) in agricultural topsoil samples from Central India (n = 20). To simulate the bedrock compositions of the topsoils, typical protolith compositions from the literature are presented (Sano et al., 2001; Nagarajan et al., 2007; Prabhakar et al., 2009; Babechuk et al., 2014).

	Na_2O	K_2O	CaO	MgO	Al_2O_3	Fe_2O_3	TiO_2	MnO	C_{org}	CIA	Zn	Cu	Ni	Cr	Co	Mo	Subcropping geology	Crop type
Sample	(wt%)	(wt%)	(wt%)	(wt%)	(wt%)	(wt%)	(wt%)	(wt%)	(wt%)		(µg/g)	(µg/g)	(µg/g)	(µg/g)	(µg/g)	(µg/g)		
S38	0.78	0.6	4.4	4.14	13.9	13.85	2.11	0.21	0.87	60	111	211	58	50	48	<1	basalt	cotton
S10	0.42	0.58	5.63	3.23	12.5	11.55	1.85	0.19	1.82	64	91	142	97	150	53	<1		wheat
S9	0.4	0.52	5.13	3.34	12.55	11.75	1.89	0.24	0.95	65	92	149	95	160	54	<1		maize
S16	0.25	0.58	3.56	2.42	14.35	13.05	2.39	0.25	1.31	67	93	166	99	140	56	<1		lentils
S29	0.11	0.91	3.1	2.29	13.45	10.4	1.8	0.22	1.02	78	84	130	89	110	44	<1		millet
S7(ChQ)	0.29	0.4	2.32	1.94	15.2	19.95	2.99	0.37	1.83	76	129	281	81	90	82	<1		wheat
S8	0.82	0.28	3.92	2.74	14.05	15.2	2.53	0.25	0.82	62	128	222	71	70	57	<1		wheat
S5	0.6	0.42	20.5	2.68	8.95	9.79	1.64	0.14	0.73	79	78	134	42	50	29	<1		cotton
S6	0.58	1.71	1.8	2.1	13.55	9.39	1.57	0.18	0.85	72	88	111	70	100	35	<1	basaltic alluvium	wheat
S25	0.06	0.87	0.39	0.55	21	17.45	2.16	0.37	1.15	96	59	127	130	290	73	2	basalt / laterite	lentils
S28	0.04	0.32	0.58	0.55	20.2	29.6	3.4	0.19	1.3	97	129	342	133	340	61	<1	basalt / laterite	lentils
S26	0.04	0.29	0.62	0.53	20.4	29.5	2.87	0.16	1.69	98	124	302	131	340	62	1	basalt / laterite	rice
Chhindwara basalt	*2.43*	*0.28*	*10.55*	*5.46*	*12.93*	*15.07*	*2.23*	*0.23*		*36*	*113*	*213*	*56*	*59*	*52*	*<1*	*protolith*	
Bidar basalt	*2.46*	*0.16*	*10.99*	*6.93*	*13.72*	*13.4*	*2.16*	*0.19*		*37*	*105*	*180*	*93*	*156*	*52*	*<1*	*protolith*	
NY1 basalt	*2.26*	*0.49*	*10.3*	*5.62*	*13.2*	*16.17*	*2.83*	*0.21*		*37*	*146*	*295*	*82*	*84*	-	-	*protolith*	
S13	0.69	1.28	3.31	2.59	12.35	8.26	1.66	0.15	1.2	66	71	73	84	170	30	<1	granite-gneiss	lentils
S14	1.04	0.96	8.28	2.8	12.35	9.65	1.79	0.16	1.27	60	79	107	63	100	35	<1		maize
S15	1.13	0.62	6.88	3.3	13.85	12.1	2.08	0.17	1.35	59	95	151	65	90	40	<1		wheat
S37	1.94	3.7	1.81	0.61	14.8	3.72	0.58	0.03	1.66	60	49	29	24	30	9	<1		rice
S36	1.99	4.1	1.74	0.45	13.9	3.04	0.45	0.02	0.98	59	39	24	19	30	7	<1		rice
*TTG gneisses (n = 11)***	*4.95*	*1.55*	*3.07*	*0.68*	*15.1*	*3.72**	*0.3*	*0.07*		*50*	*18.88*	*0.92*	*1.8*	*23.71*	*5.21*	-	*protolith*	
std dev.	*0.83*	*0.5*	*0.78*	*0.31*	*1.26*	*0.58*	*0.07*	*0.12*		-	*4.33*	*0.27*	*0.34*	*14.78*	*1.08*	-		
*Granite (n = 10)***	*4.85*	*2.74*	*3.24*	*1.37*	*15.13*	*5.12**	*0.37*	*0.12*		*48*	*25.17*	*2.31*	*2.47*	*26.94*	8.54	-	*protolith*	
std dev.	*0.76*	*0.64*	*0.87*	*0.67*	*0.88*	*1.23*	*0.11*	0.2		-	*5.93*	*1.76*	*0.56*	*8.22*	2.99	-		
Sample																		
S21	0.45	1	0.83	0.77	9.96	5.24	0.91	0.16	0.67	80	33	41	51	80	29	<1	grey shale	lentils
S19	1.92	0.57	2.19	1.02	13.8	7.08	1.38	0.12	0.89	67	53	65	64	100	28	<1		millet
S18	0.16	0.16	1.51	1.98	14.4	13.55	2.99	0.26	1.33	95	92	213	159	270	51	<1		millet
*Grey shale (n = 3)***	*0.39*	*2.11*	*0.69*	*1.12*	*10.7*	*5.13*	*0.61*	-		*75*	*57.2*	*14.64*	*25.33*	*59.8*	*60.7*	-	*protolith*	
std dev.	*0.26*	*0.66*	*0.52*	*0.83*	*2.01*	*4.76*	*0.24*	-		-	*59.29*	*8.2*	*21.12*	*11.07*	*27.3*	-		

* The Fe_2O_3 (wt%) was converted from FeO (wt%) using the equation FeO = Fe_2O_3 * 0.8998; ** n = number of samples that have been used to calculate the average concentrations in rocks

The CIA follows the equation: Al_2O_3 / (Al_2O_3 + CaO + Na_2O + K_2O) x 100, where CaO represents the molar proportion of Ca in silicate-bearing minerals only (e.g., Nesbitt and Young, 1982; Fedo et al., 1995; McLennan, 1993). The extent of chemical weathering is reflected in an increase of CIA values from 45-50 (unweathered) to 100 (complete breakdown of original silicates) and reflects the removal of the labile three cations (e.g., Ca^{2+}, Na^{+}, K^{+}) relative to stable residual silicates (Al^{3+}, Ti^{4+}) (Fedo et al., 1995). The CIA values in the samples ranged from 59-98.

4.2. Comparison of CIA and tau diagrams to the subcropping geology

In autochthonous situations, soil formation usually shows a close relationship to the underlying bedrock. Although bedrocks were not analysed in this study, compositions of relevant rock types from close to the sample locations were compiled from the literature (Table 1) (Sano et al., 2001; Nagarajan et al., 2007; Prabhakar et al., 2009; Babechuk et al., 2014). Most igneous rocks of varying composition will plot between a CIA value of 40 and 50 (e.g., Babechuk et al., 2014), whereas the CIA value in average shale is about 65-70 (McLennan, 1993). Hence, there is only one bedrock variety with the grey shale with high CIA value (75) albeit highly variable. This explains why one soil that developed over grey shale (S19) has a lower value than the average bedrock.

Regardless, the main finding is that CIA values of most Vertisol topsoils that formed over basalt, granite or tonalite-trondhjemite-granodiorite (TTG) gneisses show low to intermediate weathering degrees (52-79). This is typical for saprolite that contains substantial amounts of smectite (Babechuk et al., 2014). Except for one strongly weathered soil (S18: CIA of 95) developed over grey shale, the CIA values are similar (67-80) to the Deccan Trap basalt-hosted Vertisols. By contrast, the strongly weathered Ferralsol topsoils have very high CIA values (>95).

A robust way of quantifying element loss and gain during soil formation relative to the bedrock geology is the calculation of tau values (τ) to determine the enrichment-depletion of elements. To evaluate these quantifications, concentration (C) of an immobile element is commonly used to compare with the relative loss or gain of a more mobile

element (j) relative to the concentration of the underlying bedrock (i) on which the soil developed (Brimhall and Dietrich, 1987; Anderson et al., 2002):

$$\tau_{j,s} = \frac{\left(C_{j,s} / C_{i,s}\right)}{\left(C_{j,p} / C_{i,p}\right)} - 1$$

Positive τ values indicate the extent of enrichment of element j, whereas negative values define the fractional depletion with respect to the immobile element j (in this study niobyum (Nb)) (e.g., Babechuk et al., 2015) in the underlying bedrock. A value of zero means that element j is determined to be as immobile in the soil (s) as the immobile element in the parent rock (p).

The first order finding from these calculations (supporting information; Supplemental Table 4) is that soils which formed over basalt have often lost substantial amounts of essential trace metals. Vertisols that developed over granite-gneiss, on the other hand, are enriched in vital trace metals relative to typical bedrock compositions and only in two samples from rice fields (S36, S37) Cr, Co and Zn are depleted. Copper and Ni in particular, exhibit extreme gains in all Vertisols that developed over granite-gneiss. Similarly, an enrichment of Cu, Cr and Ni in Vertisols that formed over shales is evident. By contrast, Co and Zn show depletion in comparison to the shale bedrocks. Finally, only two Ferralsol topsoils have Mo concentrations ≥ 1 µg/g, whereas all other samples of this study have concentrations ≤ 1 µg/g (below the detection limit). For this reason, we do not illustrate the relative enrichment and depletion diagrams of Mo in comparison to underlying protoliths.

We further wanted to attest whether geological variability results in strong metal variations in the soils. To this end, we conducted Pearson's correlation analysis with τ values between metal phases that represent major elements (Al, Ti, Fe) and Co, Cu, Ni as well as Zn in the soil samples (Table 2). The most important key finding of these τ correlations is that independent of the underlying bedrock, Co, Cu, Ni and Zn exhibit moderate to strong correlations to Fe and Ti, while Al can only play a subordinate role for an association to these metal phases. Furthermore, Co, Cu, Ni and Zn are strongly correlated with each other, whereas Cr solely shows a moderate relationship with Co, Ni and Zn. The overall association to Fe and Ti phases consequently suggest that, except for

Cr, there is only a weak dependency to the bedrock geology in the studied soil samples (Table 2).

Table 2. Pearson Product Moment Correlation between τ values. Note that Cr, Co, Cu, Ni and Zn are normalised to Nb, while Ti was used for the normalistion (nrm) of Al and Fe. Additionally, Fe was normalised to Al.

	Co	Cu	Ni	Zn	Al-Ti_{nrm}	Fe-Ti_{nrm}	Fe-Al_{nrm}	
Cr	0.50		0.48	0.50				*
	0.04		0.03	0.02				**
Co		0.95	0.91	0.93	-0.55		0.83	
		6.7E-08	2.2E-07	2.8E-08	0.02		2.1E-05	
Cu			0.91	0.88	-0.73	-0.62	0.88	
			2.2E-07	1.2E-06	0.001	0.01	1.4E-06	
Ni				0.84	-0.68	-0.61	0.82	
				1.6E-06	0.001	0.004	5.3E-06	
Zn					-0.55	-0.44	0.76	
					0.01	0.04	6.4E-05	
Al-Ti_{nrm}						0.78	-0.80	
						2.6E-05	1.5E-05	
Fe-Ti_{nrm}							-0.50	
							0.02	

* First cell content = correlation coefficient ; ** Second cell content = P value

4.3. Relationship between the major elements and essential trace metals in the bulk soil samples

The most obvious finding from major element geochemistry is that regardless of the type of underlying bedrock, a strong correlation ($r^2 = 0.771$) exists between Fe_2O_3 (wt%) and TiO_2 (wt%) in all topsoil samples (Figure 5a). This is even stronger in soils that developed over silicate bedrocks, i.e. basalts and granite-gneisses ($r^2 = 0.952$; not shown). Furthermore, a moderate correlation between Fe_2O_3 (wt%) and Al_2O_3 (wt%) also exists ($r^2 = 0.556$) (Figure 5b).

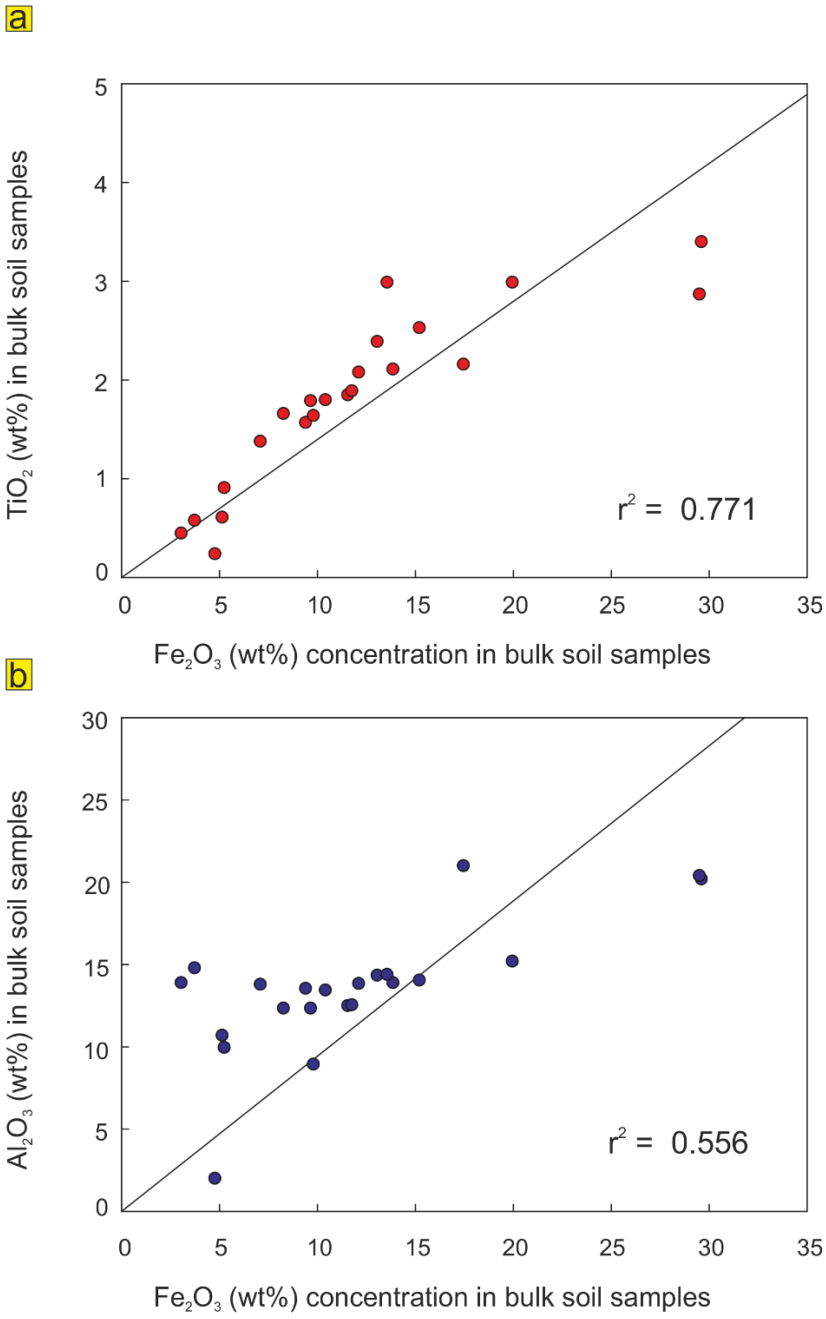

Figure 5. Relationship of bulk soil TiO_2 (wt%) **(a)** and Al_2O_3 (wt%) **(b)** to Fe_2O_3 (wt%).

TiO_2 (wt%) exhibits a strong relationship to Zn (r^2 = 0.748) and Cu (r^2 = 0.882) (Figure 6a). Fe_2O_3 (wt%) correlates strongly with Cu (r^2 = 0.882) and moderately with Zn (r^2 = 0.628) (Figure 6b). Cobalt has an almost identical relationship with TiO_2 (wt%) (r^2 = 0.736) as Zn (Figure 6a). In addition, the relationship of Co with Fe_2O_3 (wt%) is very similar (r^2 = 0.620). Chromium and Ni concentrations moderately correlate with TiO_2

(wt%) (Ni: $r^2 = 0.635$; Cr: $r^2 = 0.449$) and Fe_2O_3 (wt%) (Ni: $r^2 = 0.508$; Cr: $r^2 = 0.584$) (Figure 6a, b). Importantly, the exclusion of the Vertisols that developed over Deccan basalt leads to even stronger correlations of Cr with TiO_2 (wt%) (Cr: $r^2 = 0.774$) and Fe_2O_3 (wt%) (Cr: $r^2 = 0.803$) and suggest a somewhat different phase relation of Cr with major elements that seems to relate to the bedrock geology (Table 2). In addition, Co ($r^2 = 0.818$), Zn ($r^2 = 0.507$) and Cu ($r^2 = 0.700$) exhibit moderate-strong correlations with Cr without the basaltic Vertisols.

Moderate correlations between Al_2O_3 (wt%) and all essential trace metals exist (Figure 6c), except for Zn ($r^2 = 0.135$). Although the correlations with Al_2O_3 may simply reflect the general correlation between Al_2O_3 and Fe_2O_3 (Figure 5b), excluding the highly evolved Ferralsol topsoils and two rice field samples that developed over granite-gneiss basement (Table 1; S36, S37), yields moderate r^2 values between Al_2O_3 (wt%) and metals: 0.334 for Zn, 0.282 for Cu, 0.315 for Ni and 0.426 for Co. By contrast, Cr shows no correlation with Al_2O_3 (wt%) ($r^2 = 0.071$) (Supplemental Figure 2). Furthermore, in the clay-rich basaltic substrate Al_2O_3 (wt%) moderately correlates with Zn ($r^2 = 0.438$), Cu ($r^2 = 0.319$), Co ($r^2 = 0.501$) and Ni ($r^2 = 0.248$), whereas Cr does not correlate ($r^2 = 0.033$).

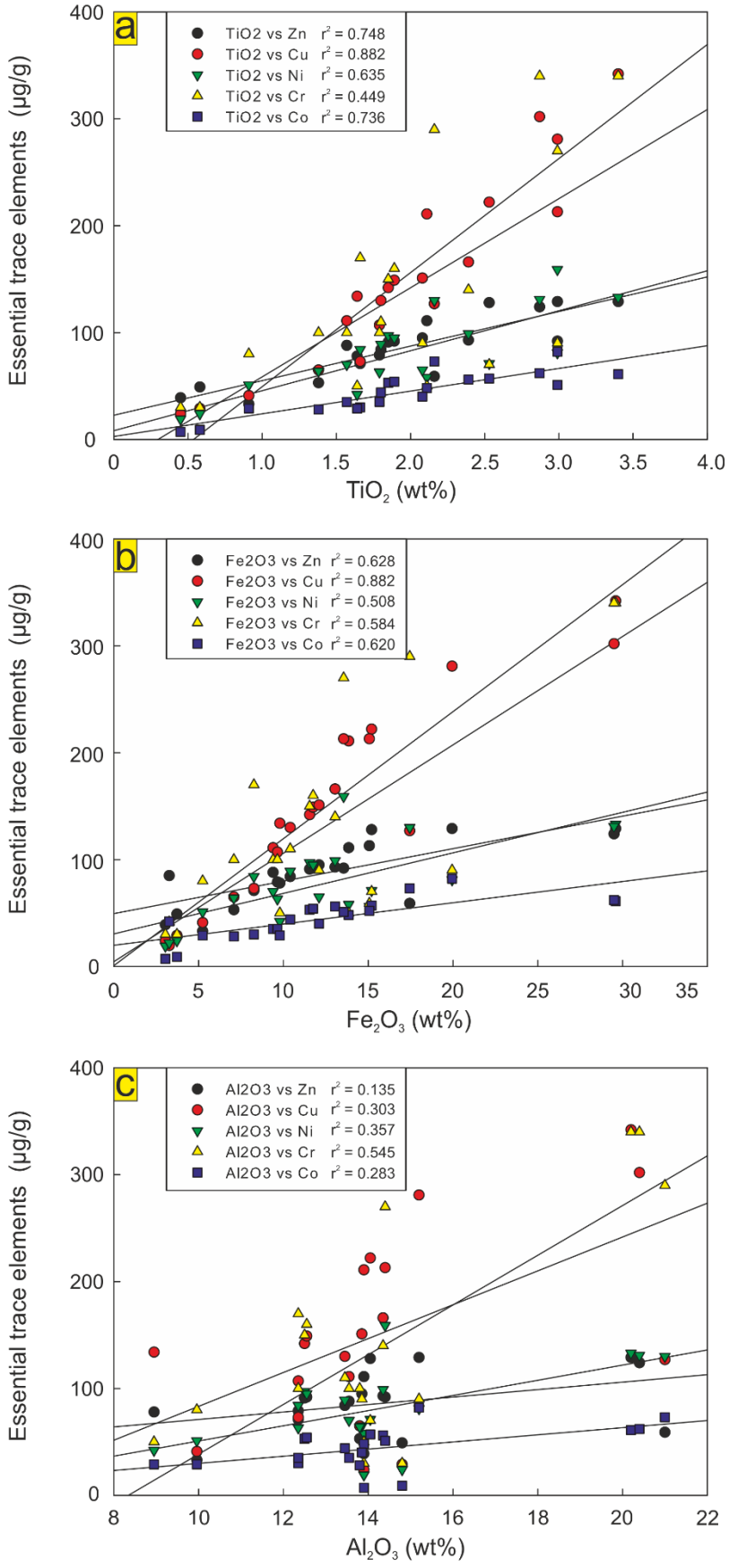

Figure 6. Relationship of bulk soil essential trace metals (Zn, Cu, Ni, Cr, Co) to TiO_2 (wt%) **(a)**, Fe_2O_3 (wt%) **(b)** and Al_2O_3 (wt%) **(c)**.

4.4. DTPA soil extractions of Zn, Cu, Ni, Cr, Co, Mo and their associations with bulk soil elements

The results of the DTPA extractions are listed in Table 3, except for Cr and Mo which were below the detection limit (≤ 0.01 µg/g). DTPA-extractable Zn ranged from 0.4-4.0 µg/g, Cu from 3.0-15.5 µg/g, Ni from 0.5-6.0 µg/g, Co from 0.2-3.2 µg/g and Fe from 18.8-91.8 µg/g. Nickel concentrations are relatively similar in the topsoil samples, except for sample S19 (2.6 µg/g) and S18 (6.0 µg/g) that developed over grey shale. Cobalt concentrations are low in the topsoils, except for the Ferralsol samples, two Vertisol samples that developed over grey shale (S18, S19) and one that developed over basalt (S7(ChQ)).

Table 3. DTPA-extractable Zn, Cu, Ni, Co and Fe of the Central Indian topsoil samples.

	Zn	Cu	Ni	Co	Fe	Crop type	Subcropping geology
Sample	**(µg/g)**	**(µg/g)**	**(µg/g)**	**(µg/g)**	**(µg/g)**		
S38	0.6	7.3	0.7	0.3	32.0	cotton	basalt
S10	0.9	12.0	1.2	0.4	39.8	wheat	
S9	0.8	8.6	0.6	0.2	33.1	maize	
S16	0.9	5.9	1.1	0.5	27.1	lentils	
S29	0.7	5.2	1.3	0.3	24.9	millet	
S7 (ChQ)	1.3	13.3	0.8	1.3	53.6	wheat	
S8	1.5	12.1	0.9	0.3	50.9	wheat	
S5	0.8	6.7	0.5	0.2	21.2	cotton	
S6	0.5	4.9	0.9	0.3	29.4	wheat	alluvium
S13	1.0	5.6	0.9	0.2	27.8	lentils	granite-gneiss
S14	0.6	11.7	0.9	0.2	42.8	maize	
S15	0.5	14.4	0.8	0.2	51.1	wheat	
S37	2.0	10.0	1.1	0.4	91.8	rice	
S36	1.4	7.2	0.6	0.2	67.5	rice	
S21	0.4	3.0	1.4	0.6	23.2	lentils	grey shale
S19	1.5	9.2	2.6	1.4	37.6	millet	
S18	0.9	15.5	6.0	1.1	36.5	millet	
S25	0.8	8.1	1.4	3.2	24.2	lentils	basalt / laterite
S28	2.5	8.3	1.1	1.0	18.8	lentils	
S26	4.0	7.9	1.3	1.3	19.6	rice	

The Pearson's correlation analysis showed that there are modest-moderate relationships between DTPA metal concentrations and bulk soil elements in the topsoils (Tables 4; 5).

Table 4. Pearson Product Moment Correlation between bulk soil concentrations of C_{org}, Al_2O_3 (wt%), CIA and DTPA-extracted essential metals (Fe, Cu, Ni, Co, Zn) (µg/g)

	Al_2O_3	**CIA**	**Fe**	**Cu**	**Ni**	**Co**	**Zn**	
C_{org}	0.42	0.121	0.32	0.53	0.08	0.20	0.44	*
	0.07	0.610	0.17	0.02	0.72	0.40	0.05	**
Al_2O_3		0.58	-0.10	0.11	0.07	0.70	0.65	
		0.01	0.67	0.63	0.78	0.001	0.002	
CIA			-0.58	-0.08	0.43	0.66	0.42	
			0.01	0.72	0.056	0.002	0.07	
Fe				0.45	-0.07	-0.23	0.05	
				0.05	0.76	0.32	0.84	
Cu					0.39	0.09	0.06	
					0.09	0.71	0.81	
Ni						0.31	0.02	
						0.19	0.93	
Co							0.25	
							0.29	

* First cell content = correlation coefficient ; ** Second cell content = P value

Table 5. Pearson Product Moment Correlation between bulk soil concentrations of C_{org}, Fe_2O_3, MnO (wt%) and DTPA-extracted essential metals (Fe, Cu, Ni, Co, Zn) (µg/g)

	Fe_2O_3	**MnO**	**Fe**	**Cu**	**Ni**	**Co**	**Zn**	
C_{org}	0.39	0.14	0.32	0.53	0.08	0.20	0.44	*
	0.09	0.56	0.17	0.02	0.72	0.40	0.05	**
Fe_2O_3		0.50	-0.44	0.19	0.03	0.43	0.61	
		0.03	0.05	0.43	0.92	0.06	0.004	
MnO			-0.40	0.24	0.16	0.54	-0.21	
			0.08	0.31	0.52	0.01	0.37	
Fe				0.45	-0.07	-0.23	0.05	
				0.05	0.76	0.32	0.84	
Cu					0.39	0.09	0.06	
					0.09	0.71	0.81	
Ni						0.31	0.02	
						0.19	0.93	
Co							0.25	
							0.29	

* First cell content = correlation coefficient ; ** Second cell content = P value

The most important finding form these comparisons is that there is no straightforward correlation between trace metal content of the soil and DTPA extractable metal concentration. The most notable correlations are between C_{org} (wt%) and extractable Zn and Cu ($p \leq 0.05$). Additionally, extractable Co and Zn correlate significantly with Al_2O_3 (wt%) ($p < 0.01$) (Table 4). Moreover, DTPA-extractable Cu and Zn correlate with Fe ($p < 0.05$), whereas an inverse relationship between extractable Fe and Fe_2O_3 (wt%) is evident ($p \leq 0.05$) (Table 5). Solely extractable Co is associated with the MnO (wt%) content in the soil samples ($p \leq 0.01$), whereas extractable Zn is the only essential metal that shows a relationship with Fe_2O_3 (wt%) ($p < 0.01$). By contrast, extractable Ni is not associated with any specific bulk soil element in the soils, even though a modest correlation with some significance ($p \approx 0.05$) with the CIA exists. Finally, extractable Fe ($p \leq 0.01$) and Co ($p < 0.01$) show a moderate relationship with the CIA.

4.5. Cow dung - element (C, Fe, Ti) and essential trace metal (Cr, Co, Ni, Cu, Zn, Mo) concentrations

Predictably, the C content is high in the cow dung samples (ca. 31-40 %), except for sample (P4) that contained hay bedding (14.0 %) (Table 6). Furthermore, the cow dung samples were found to have, on average, relatively high concentrations of Fe (21128.5 µg/g), Ti (3065.8 µg/g), Zn (202.2 µg/g) and Cu (65.4 µg/g), whereas Cr (30.9 µg/g) was present at moderate concentrations. Cobalt (11.0 µg/g) and Mo (2.2 µg/g) showed low concentrations.

Table 6. Carbon, Iron and Trace Element Concentrations (µg/g, Dry Weight Basis) in Central Indian Cow Dung (n = 18) in comparison to New York Dairy Manures (n = 20) (McBride and Spiers, 2001)*.

Sample	Bedrock	C	Cr	Co	Ni	Cu	Zn	Mo	Fe	Ti
P10b	basalt	36.7	31.2	10.3	20.6	52.8	251.5	1.9	16776.0	2257.0
P1	basalt	33.2	39.6	16.6	29.0	77.5	149.8	0.8	33908.4	4859.8
P4	alluvium	14.0	15.3	7.9	11.0	35.0	29.5	0.2	19589.1	2850.2
P13	basalt	40.8	49.3	17.5	34.8	100.0	201.1	1.8	31406.7	4554.6
P10a	basalt	38.9	9.8	7.2	10.6	62.0	226.0	0.7	13621.5	1897.5
P3	basalt	34.5	36.9	9.5	18.2	65.1	277.3	3.3	17817.7	2659.1
P2	basalt	31.0	27.9	17.3	23.3	88.3	186.2	0.9	35164.1	4947.1
P16b	basalt	40.1	50.0	12.3	28.7	109.6	306.0	4.4	29629.9	4268.5
P7	alluvium	39.4	14.3	7.6	12.6	80.2	311.7	0.8	11076.4	1813.7
P7(CHQ)	basalt	33.0	42.4	24.8	30.2	111.8	123.7	1.1	48952.2	6619.3
P16a	basalt	37.8	39.3	13.8	30.0	79.0	300.7	1.7	21819.9	3069.6
P19	basalt	38.1	15.3	7.9	11.6	47.9	199.7	1.1	14236.9	2051.5
P18	granite-gneiss	33.6	2.6	1.3	1.9	12.1	147.3	4.1	2111.9	204.8
P12	granite-gneiss	35.1	81.7	16.8	39.4	69.8	129.1	4.1	36341.0	5358.8
P17a	granite-gneiss	38.1	5.3	3.1	4.5	29.5	194.4	5.5	2595.4	260.8
P14	shale	37.7	46.3	8.3	26.6	62.7	216.2	3.2	15932.8	2608.3
P11	alluvium	35.8	28.3	10.0	19.7	63.1	228.0	1.7	19494.0	3538.5
P15	shale	36.7	21.3	5.8	13.2	31.1	160.6	2.4	9839.4	1365.6
	mean	**35.2**	**30.9**	**11.0**	**20.3**	**65.4**	**202.2**	**2.2**	**21128.5**	**3065.8**
	median	**36.7**	**29.8**	**9.8**	**20.2**	**64.1**	**200.4**	**1.8**	**18655.9**	**2754.7**
	min	**14.0**	**2.6**	**1.3**	**1.9**	**12.1**	**29.5**	**0.2**	**2111.9**	**204.8**
	max	**40.8**	**81.7**	**24.8**	**39.4**	**111.8**	**311.7**	**5.5**	**48952.2**	**6619.3**
	std dev	**6.0**	**19.7**	**5.9**	**10.6**	**27.8**	**73.2**	**1.5**	**12470.4**	**1757.5**
	*mean**	-	*4.6*	*2.5*	*8.0*	*139.0*	*191.0*	*2.5*	-	-
	*median**	-	*4.0*	*1.9*	*5.0*	*64*	*162*	*2.3*	-	-
	*min**	-	*1*	*0.8*	*2*	*18*	*87*	*0.9*	-	-
	*max**	-	*13*	*7.2*	*35*	*1100*	*488*	*4.8*	-	-
	*std dev**	-	2.6	1.7	9.5	242	115	0.95	-	-

By comparison to the mean of essential trace metal concentrations of dairy manure from New York, USA (McBride and Spiers, 2001), cow dung from Central India has higher

concentrations in Zn, Ni, Co and Cr. The concentration of Mo, on the other hand, is very similar in comparison to the dairy manure composite of McBride and Spiers (2001). Omitting one strong outlier sample, Cu concentrations in the Indian cow dung are also similar. Although not a bio-essential element (Kabata-Pendias, 2010), concentrations of Ti ranged from 205-6600 µg/g. Iron, Cu, Cr, Ni and Co concentrations are correlated to Ti, with coefficients of r^2 = 0.983, 0.664, 0.559, 0.724 and 0.924 respectively as shown in Figure 7. By contrast, Mo (r^2 = 0.084) and Zn (r^2 = 0.031) are not correlated to Ti.

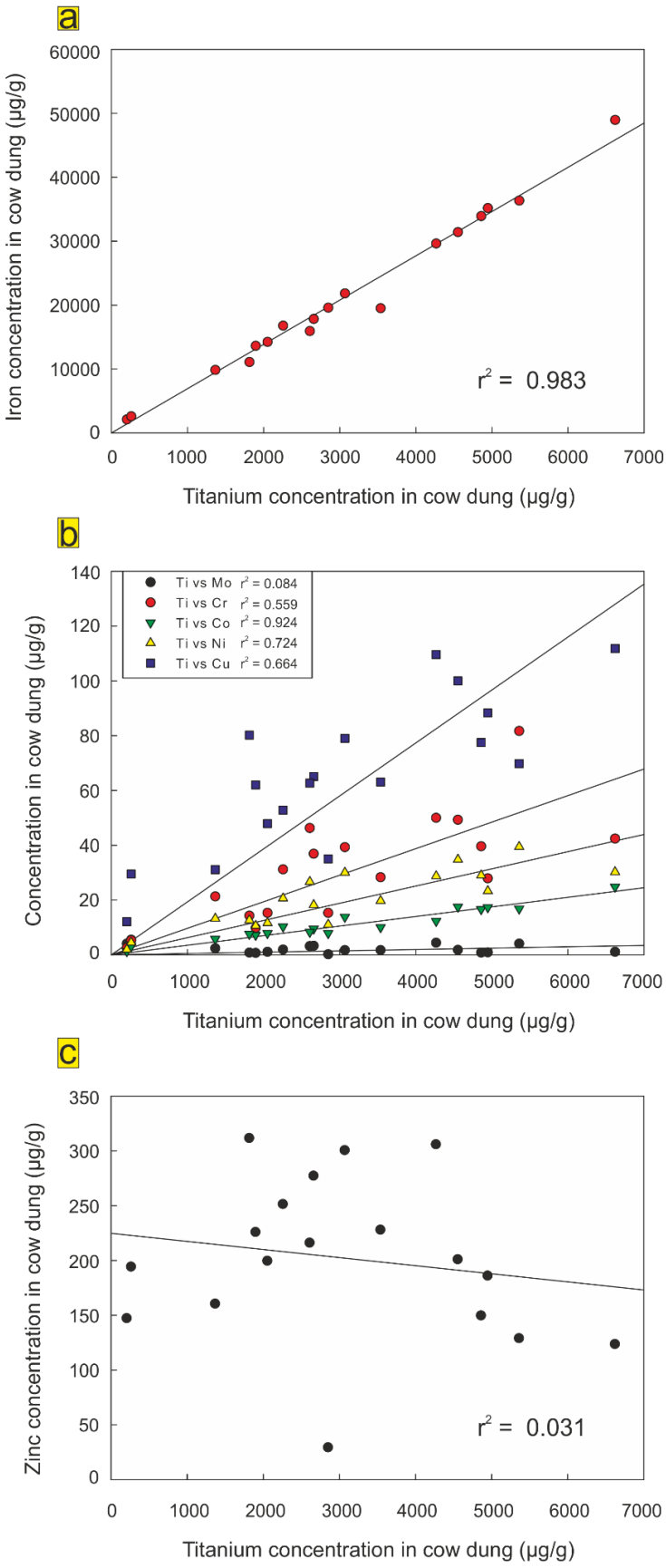

Figure 7. Relationship concentrations of Fe **(a)**, essential trace metals (Mo, Cr, Co, Ni, Cu) **(b)**, and Zn **(c)** to Ti in cow dung.

5. Discussion

5.1. Bulk soil compositions - primary silicates and clays

Aluminium remains immobile in (sub)-tropical regions under most environmental conditions. Typically, much of the Al in soils is bound in clay minerals, such as smectite, vermiculite or illite, which form through the chemical breakdown of primary silicates such as feldspar, pyroxene, olivine, biotite or chlorite (Anand, 2005; Dahlgren et al., 1997). With increasing weathering intensity (and enrichment in Al_2O_3 (wt%) relative to the underlying bedrock), these clay minerals transform into chemically less complex kaolinite and further into Al-hydroxide (gibbsite) with extremely low trace element levels, very problemeatic for agriculture (Fyfe et al., 1983). In subsoils, the CIA is widely used to distinguish the mineralogy of primary minerals (e.g., plagioclase and pyroxene: 50 and under) from those of pedogenetic minerals such as smectite, illite (70-85), and kaolinite (100) (e.g., Babechuk et al., 2014). Hence, it is possible to use the CIA to distinguish between essential metal-rich clay minerals and those clays with very low or non-existent nutrient levels.

The CIA values in the Vertisols (52-78) and Ferralsols (93-96) that developed over Deccan basalt are similar to subsoil samples of saprolite and laterite that are not in agricultural use (e.g., Babechuk et al., 2014). This suggests that Vertisols still contain fertile rock debris and nutrient-rich clay minerals, except for one soil that developed over grey shale (S18; CIA = 95). Furthermore, the Ferralsol topsoils (93-96) are kaolinite-rich, which means that the clays in these soils are poorer in essential metals (e.g., Fyfe et al., 1983). Excluding the two Vertisol rice field samples, which seem to have a different formation history (samples S36, S37; see also sections 2 and 5.2) as well as the Ferralsols, Al_2O_3 (wt%) shows modest correlations with Zn, Ni, Cu and Co concentrations (Supplemental Figure 2). This implies that fresh or partly weathered silicates and complex clay minerals are an important reservoir of Zn, Ni, Cu and Co in most Vertisol topsoils of Central India, independent of the underlying bedrock, except for Cr that must occur in other minerals (Figure 6c).

5.2. Bulk soil compositions - refractory mineral phases

In most topsoil samples from Central India, the TiO_2 (wt%) concentrations are much higher than the global average. In bedrocks, Ti forms several minerals such as ilmenite ($FeTiO_3$) or rutile (TiO_2) and is also bound in Fe-oxides such as magnetite. These phases are very resistant to weathering and often occur in soils with other heavy inert minerals; therefore, they occur practically undecomposed in soils (Kabata-Pendias, 2010). Only a small proportion of a fresh rock's Ti occurs in primary silicates such as pyroxene, amphibole, mica and garnet (Reeder et al., 2006) although biotite mica can be the main carrier of Ti. During chemical weathering of silicates, Ti and Fe are rapidly redistributed into the newly formed Fe/Ti hydrous oxides and are mainly responsible for high correlations between Fe and Ti in clay-rich fractions of soils (e.g., Taboada et al., 2006). Usually, the chemical variation of TiO_2 (wt%) in dominant clay mineral groups solely ranges between 0−0.3% (kaolinite), 0−0.5% (smectite), 0−0.6% (vermiculite), 0−0.8% (illite) and 0−0.2% (chlorite) (Blume et al., 2010). Hence, the Ti concentrations in soils are normally strongly related to oxide phases of primary and secondary origin. The global average of Ti in soils lies around 0.33%, although the concentration in organic-rich soils is often lower (e.g., Reeder et al., 2006). Accumulation of Ti in topsoil horizons indicates loss of clays due to weathering (Kabata-Pendias, 2010).

The elevated TiO_2 (wt%) contents of the studied soils are likely indicating high quantities of inert oxides. Because Ti is not a bio-essential metal, its high abundance is not of interest to the agricultural practice on these soils. However, a very relevant finding is the stronger correlation of Zn and Cu with TiO_2 (wt%), Fe_2O_3 (wt%) and $\tau_{Zn,Cu,Ni,s}$ with $\tau_{Fe,Ti,s}$ (Table 2, Figure 6a, b) because it suggests that most Zn, Cu and Ni are bound in weathering resistant oxides. This is supported by the more modest correlation with Al_2O_3 (wt%) content (Figure 6c; Supplemental Figure 2), suggesting that clays are not the main carriers of these elements. Similarly, the correlation of Co with TiO_2 (wt%), Zn, Cu, Ni, Cr and $\tau_{Co,s}$ with $\tau_{Fe,Ti,Cu,\ Ni,Zn,Cr,s}$ further illustrates the importance of oxide phases on the bulk metal concentrations in the topsoils.

The redistribution of essential metals into different oxide phases did not occur homogeneously across the study area, since the exclusion of the Vertisols, which developed on Deccan basalt results in stronger relationships of Cr with TiO_2 (wt%), Fe_2O_3

(wt%), Co, Cu as well as moderate associations with Zn. Overall, these findings suggest that substantial quantities of the residual concentrations of essential trace metals in the bulk soils exist in bio-unavailable form locked into weathering resistant oxide phases.

By contrast, Mo has no relationship to the Fe-Ti mineral phases in the topsoil samples, and the concentrations are mainly below the detection limit of 1 µg/g so that the inorganic soil constituents are not a source of Mo. Similar to the departure from the trends of Vertisols with Al_2O_3 (wt%), the two rice field samples (S36, S37) that developed over granite-gneiss deviate from the chemical trends with TiO_2 and Fe_2O_3 (wt%). With the very limited dataset it is impossible to disentangle their chemical evolution, but we note the low concentrations in Fe_2O_3 (wt%) in these samples, which could be related to reducing conditions and Fe mobilisation during flooding of the paddies. Additionally, admixture of allochthonous soil material, similar to the other soils that developed over granite-gneiss (S13-15; Supplemental Figure 1) may have further complicated the situation.

5.3. Plant available essential metal contents in topsoils

The Pearson's correlation analysis showed that there are statistical relationships between DTPA metal concentrations and bulk soil elements in the agricultural topsoils (Tables 3; 4). In particular, the bio-availability of Zn and Cu is controlled to a large extent by TOC. Additionally, the correlation of Al_2O_3 (wt%) and Fe_2O_3 (wt%) with Zn suggests that clay minerals and possibly exchange reactions on pedogenic oxides control the release of Zn to crops. In the Vertisols, minor amounts of metals may also derive from fertile rock debris such as pyroxene (Suhr et al., 2018a). This is in agreement with the observation that complex clay minerals and residual primary phases are rich in essential metals (Supplemental Figure 2; Zn, Cu, Ni, Co). Furthermore, the correlation of Co with Al_2O_3 (wt%) suggests that primary silicates and clay minerals determine the release of Co to plants, while Mn-oxides also play a role for its release to the soil solutions. Because DTPA-extractable Fe and Cu moderately correlate, it is likely that a substantial amount of bio-available Fe originates from the pool of TOC in the topsoils. The moderate inverse correlation of DTPA extracted Fe and Fe_2O_3 (wt%) corroborates this idea and implies that Fe-oxides are not the source for bio-available Fe from the soils. This finding is in agreement with studies on alluvial soils in India, which demonstrated that only a small

fraction of the total Fe reserve becomes available to growing plants (e.g., Singh, 2008). By contrast, the much larger pool of crystalline sesquioxide-bound and residual Fe fractions represent unavailable forms of Fe for plants (Sakal et al., 1996; Singh, 2008).

Chromium occurs in soils mainly (>80 %) in the immobile residual fraction (Kabata-Pendias, 2010). Chemical weathering in (sub)-tropical regions leads to further redistribution of Cr into pedogenic Fe-oxides that are weathering resistant (Wille et al., 2018). It is therefore not surprising that Cr concentrations were beyond the detection limit (< 0.01 µg/g) in the DTPA-extraction, similar to simulated plant uptake of Cr with DTPA (e.g., Penney, 2004). The very low DTPA-extraction concentrations ≤ 0.01 µg/g of Mo likely reflect the low total content of Mo in the original bulk soil samples. The concentration of Ni is possibly related to the CIA in the topsoils. Considering the previously mentioned correlations of Fe and Cu, the moderate anti-correlation of Fe and moderate correlation of Co with the CIA suggest that clay minerals seem to play a role for the bio-availability of Ni. In summary, TOC, clays or clay-organic complexes, as well as small amounts of primary silicates are the most dominant factors determining the availability of Zn, Cu, Co, Ni and Fe to crops, while pedogenic Fe-oxides might play an additional role for the supply of Zn to some extent (Tables 4, 5; Supplemental Figure 2).

5.4. Essential metal deficiency status of topsoils

An accurate assessment of critical metal deficiency limits with the DTPA method depends on the crop type and various environmental factors. As a result, various authors have proposed somewhat different DTPA values as critical deficiency limits for micronutrients (Sillanpää, 1982). For example, Lindsay and Norvell (1978) expected soils with >4.5 µg/g of Fe in the DTPA-extract solution not to show Fe deficiency. Such cut-off values are problematic because the DTPA-extraction cannot discern between forms of Fe (Horneck et al., 2011). Regardless of the fact that the Fe concentration in the DTPA-extract solution likely overestimates the total value that is available to the plant, the generally high concentrations found here (Table 3) suggest that Fe deficiency is currently not a problem in the topsoils. By contrast to Fe, the critical level for Zn seems to be relatively well established (Sillanpää, 1982) and DTPA extractable Zn values of ca. 0.5 µg/g represent the critical lower limit for several crops, even though values of up to 2 µg/g can still lead to

deficiency symptoms (Kuldeep, 2009). In previous Indian soil studies, average concentrations of DTPA-extractable Zn varied widely from 0.1-6.92 µg/g in India, with a mean of 0.87 µg/g. Soils in Central India apparently have even lower DTPA-Zn concentrations of 0.65 µg/g with the highest levels of deficiency in red loam (entisol) and black clayey soils (swell-shrink Vertisol) of the central Deccan plateau (e.g., Singh, 2008). Based on the defined critical level of Zn, two samples in this study (S6 derived from basaltic alluvium; S21 derived from grey shale) are clearly Zn deficient (<0.5 µg/g), while most other topsoils have critical levels (<2 µg/g). This result, in combination with the findings of previous studies suggests, that Vertisols are at risk of being Zn deficient in Central India.

The extractable Cu concentrations from the studied topsoil samples are above the various proposed critical limits of 0.2 µg/g (Lindsay and Norvell, 1978; Sillanpää, 1982), 0.6 µg/g (Horneck et al., 2011) and 2.5-3.0 µg/g (e.g., Sillanpää, 1982). The critical levels of Ni are as yet not established. Globally, typical Ni values in food plants range between ca. 0.2-2.0 µg/g (e.g., Kabata-Pendias, 2010). These values are comparable to the DTPA extractable Ni concentrations found in this study and suggest that Ni deficiency is presently unlikely to be a problem in the studied topsoils. Similarly, a critical deficiency level for DTPA extractable Co has not yet been defined. Regardless, Co levels in plants rarely exceed concentrations above 1-2 µg/g (Perez-Espinosa et al., 2005) so that we propose that the Co levels in the topsoil samples are above a critical level. Since the tentative critical level of Mo deficiency is <0.01−0.02 µg/g (Sillanpää, 1982), it is not possible to determine the bio-availability of Mo in the topsoil samples in this study.

5.5. Carbon content and essential metals in cow dung of Central India

The C content in the studied samples is comparable to that of other analysed solid manure (e.g., Pettygrove et al., 2010) and generally ranges between ca. 30-40 % (dry weight). Except for Fe, Zn and Cu, the cow dungs were found on average to have low concentrations of the other essential metals measured. Of all trace elements, Ti shows the second lowest index of bioaccumulation, i.e. the ratio that defines trace element

concentrations in plants relative to soils (Kabata-Pendias, 2010). This strongly suggest that the Ti concentration is a proxy for "contamination" of the cow dung by soil material, as a result of soil ingestion by the animal. Strikingly, most essential metals (Fe, Cr, Co, Ni, Cu) show a strong correlation with Ti. Hence, their concentrations are dominated by indigestible soil minerals and unrelated to the bio-available pool.

Using Ti in livestock faeces as a stable marker of soil ingestion (Green et al., 1996; Thornton and Abrahams, 1983) involves assuming a herbage digestibility factor of 72 % that is recommended for use in monthly rotational pasture grass (e.g., Green et al., 1996). It represents a typical value that can be found elsewhere in the literature (e.g., Styles et al., 2015). Moreover, we used the Ti concentration of 10 soils that were sampled at the same location as the cow dung samples (Supplemental Table 1). The resulting equation is:

$$\%\ soil\ ingestion = \frac{(1 - D_h)\ Ti_f}{Ti_s - D_h\ Ti_f} \times 100$$

Where D_h = digestibility of herbage

Ti_f = titanium in faeces

Ti_s = titanium in soil

Performing this calculation for our samples demonstrates that the amount of soil ingested by cattle ranges between 2-25 % (Supplemental Table 5). Considering the daily mineral availability from traditional foddering in India (Bhanderi et al., 2016), and a dietary intake of 10.89 kg per day for Indian cattle (Dikshit and Birthal, 2010), the contribution of soil to Zn and Cu intake is low. This implies additional feed uptake as the principal pathway (Supplemental Table 6). Because the Indian cow dung samples have concentration levels of Zn, Cu and Mo comparable to the cow manure of McBride and Spiers (2001), it appears likely that Indian farmers feed their cattle with food additives containing Zn, Mo and possibly Cu (Table 6).

By contrast, the total Co intake of cattle is much more strongly related to soil (up to 35%; Supplemental Table 6), which can explain the strong r^2 correlation between Ti and

Co (Figure 7b). Importantly, Cr, Co, Ni and Fe show positive correlation to calculated soil ingestion (%) on a statistically significant level (Cr, Fe: $p < 0.01$; Ni, Co: $p < 0.05$) (Supplemental Table 7). However, Cu is also correlated to Co and Ni ($p < 0.01$) and previously we suggested that high quantities of these metals are likely bound in weathering resistant Fe-Ti oxides in the Central Indian topsoils (Figures 5a; 6a, b). Refractory oxides could, therefore, represent a metal contamination agent in cow dung so that low concentrations in Ti and soil ingestion (%) probably give the best estimate on readily bio-available pools of essential metals in cow dung. Hence, this means that sample P18, which has the lowest concentration of Ti, Fe, Cr, Co, Ni and Cu, as well as soil ingestion (%), represents the best estimate for the potential of cow dung as essential metal fertiliser in India.

6. Challenges and opportunities in the agricultural cultivation of farmland in Central India

The results of this study confirm that the bulk soil concentrations of essential metals alone are not helpful to assess the deficiency status of Vertisols and Ferralsols in Central India. This is largely because high quantities (Zn, Cu, Ni, Co, Cr) are bound within primary and pedogenic oxides that are weathering resistant and consequently, their essential metals are unavailable to crops (Figures 5a; 6a, b). A critical observation in other studies on Indian soils is that less than 1.75 % of total soil Zn occurs as bio-available forms (e.g., Singh and Abrol, 1986; Singh, 2008), while residual mineral fractions contained ca. 95 % of Zn (Singh and Abrol, 1986). The widely studied factors controlling metal deficiency in Vertisols (Yerima et al., 2014; Katyal and Sharma, 1991) are high soil pH or $CaCO_3$ content but additionally it is important to assess in which soil minerals the essential metals occur. Deficiency levels of essential metals in Vertisols and Ferralsols are not necessarily related to the bedrock type and with an advanced weathering degree and enrichment of oxides in the soil reservoirs, initial differences in the concentrations of bio-available essential metals in different types of bedrock will diminish (see also Suhr et al., 2018a).

The correlations between Al_2O_3 (wt%) with Zn, Cu, Co and Ni in the Vertisols suggest that release reactions from metal-rich clay minerals and residual primary silicates

(pyroxene) supply essential metals to crops, while the Pearson correlation of DTPA-extractable Zn with Fe_2O_3 (wt%) (Tables 4, 5) in all samples indicates that exchange reactions on the surface sites of pedogenic oxides might also play a role in the supply of Zn to crops. In general, most of the essential metals are currently not at a deficiency level, although the low levels of Zn, Co, Cr and Mo (Table 3) in the DTPA-extract solution suggest that a continuous input of fertilisers is required to avoid essential metal-depletion of soils in India (Figure 1).

Importantly, TOC in the soils exerts control on the mobilisation of Zn, Cu and Fe to soil solutions. This observation is not surprising given the awareness that organic matter is fundamental for the improvement of the soil structure, water retention, prevention of soil erosion as well as cycling and storage of plant nutrients. It is, therefore, of concern that the climatic conditions in India accelerate organic matter decomposition in soils, which impoverishes crop productivity (e.g., Katyal et al., 2001) and possibly the bio-availability of essential metals on farmland. In particular, an adequate level of TOC is fundamental for Vertisols because their physical conditions make them very difficult to cultivate and manage (FAO, 2005). Thus, continuous application of organic fertilisers is crucial to maintaining the fertility status of agricultural soils in Central India and there is an awareness that future demands of multi-micronutrients in the soil, plant, animal and human continuum, can only be guaranteed through complex fertiliser formulations and organic matter enrichment of soils (Singh, 2008). However, chelated fertilisers are too costly and uneconomical for regular use for farmers in India. Sulphate salts of Zn, Fe and Cu are cheap and readily available (Singh, 2008) and these could be supplemented with traditional FYM to maintain the fertility of Indian soils.

Since most studies focused mainly on N in organic manure (e.g., Katyal et al., 2001) there is an insufficient database to establish whether the essential metal content of cow dung in Central India is sufficient to combat metal deficiencies in soils. The lack of information regarding the total content of essential metals in FYM is surprising because there is an awareness that the application of FYM can increase the concentrations of bio-available Zn and Cu in all fractions (exchangeable, carbonate-bound, oxide bound, organic bound and residual) in surface and sub-surface soils (Narwal et al., 2010).

Tandon (1997) estimated that in 2010, 119 million t of livestock dung would potentially be available as fertiliser in India. Based on the data of a census, approximately

37% of livestock was cattle in India in 2012 (Livestock Census, 2012). Using this data as a gross estimate for the year 2020, ca. 44 million t of cow dung are available annually for manure production, and until 2025 approximately 324,000 t Zn, 130,000 t Fe and 11,000 t Cu are needed to ameliorate essential metal deficiencies in Indian soils (Takkar et al., 1997). The metal concentrations of the least "soil contaminated" cow dung sample (P18) (Table 6; Supplemental Tables 4 and 5) of this study reveals that the amount of Fe (ca. 72 %) is high enough to counterbalance the net output of bio-available essential metals to a large extent. By contrast, the levels of Cu (ca. 5 %) and Zn (ca. 2 %) are insufficient to correct the metal deficiency in agricultural soils in India, at least from an agro-industrial perspective.

7. Summary and conclusion

Primary and secondary oxides contain high concentrations of essential trace metals in bio-unavailable forms in the studied agricultural Vertisol and Ferralsol topsoils in Central India and contribute to metal-deficiency problems in this region (Figure 4). There is a lack of a first-order relationship between the underlying bedrocks and metal-deficient soil profiles. Complex clay minerals, such as smectite, and primary silicates represent a reservoir of several essential metals (Zn, Ni, Cu, Co) in bio-available forms in low to intermediatly weathered soils (e.g., Vertisols). By contrast, Cr (enclosed in oxide phases) and Mo (very low total content) are not bio-available from the inorganic soil constituents. Importantly, the relationship between DTPA-extractable Zn and Cu with TOC and Cu with Fe provides evidence that organo-metallic complexes play an essential role in the availability of these micronutrients to plants. These findings underline the importance of traditional farming practices in India with C-rich FYM, instead of representing a risk regarding the immobilisation of essential metals such as Zn. Except for Fe, bio-available trace metal concentrations in FYM alone, are likely insufficient to balance the quantities required to sustain the anticipated productivity of this land. This is exemplified by Zn and Cu that can only contribute 2 % and 5% to the total fertiliser requirements annually. Regardless, the combination of FYM with affordable metal fertilisers could represent a successful way to combat multi-essential metal deficiencies in soils and crops and help to diminish the deficiency problems in the human diet in India until the year 2050.

Acknowledgements

This work is a contribution of the Marie Curie Initial Training Network IsoNose (www.IsoNose.eu) funded by the People Programme (Marie Curie Actions) of the European Union's Seventh Framework Programme FP7/2007-2013/ under REA grant agreement no [608069]. We thank Cora McKenna for assistance of the trace metal analysis and Mark Kavanagh for the organic carbon analysis and assistance with DTPA-extractions and analysis.

8. Supporting Information

Supplemental Table 1. Sample locations of soil samples and cow dung in Central India

Soil sample	Coordinates
S38	19°09.597'N 78°28.107'E
S37	18°06.980'N 78°28.753'E
S36	18°06.980'N 78°28.753'E
S29	17°53.974'N 77°50.826'E
S28	17°46.829'N 77°35.034'E
S26	17°46.829'N 77°35.034'E
S25	17°48.829'N 77°34.591'E
S19	16°51.43'N 77°22.43'E
S18	16°51.277'N 77°22.403'E
S21	17°08.218'N 77°36.696'E
S16	17°1.17'N 77°30.17'E
S15	19°34.612'N 78°29.709'E
S14	19°34.612'N 78°29.709'E
S13	19°34.612'N 78°29.709'E
S10	20°35.075'N 78°54.092'E
S9	20°35.075'N 78°54.092'E
S8	20°49.635'N 78°57.590'E
S7 (ChQ)	22°4.23'N 79°1.37'E
S6	21°57.23'N 78°56.55'E
S5	23°34.862'N 78°47.921'E
P19	19°09.597'N 78°28.107'E
P18	18°06.980'N 78°28.753'E
P17a	18°02.915'N 78°05.354'E
P16b	17°53.974'N 77°50.826'E
P16a	17°46.829'N 77°35.034'E
P15	17°08.218'N 77°36.696'E
P14	16°51.277'N 77°22.403'E
P13	17°1.17'N 77°30.17'E
P12	19°34.612'N 78°29.709'E
P11	19°48.615'N 78°34.563'E

Supplemental Table 1. Sample locations of soil samples and cow dung in Central India

Soil sample	Coordinates
P10b	20°12.405'N 78°41.103'E
P10a	20°35.075'N 78°54.092'E
P7(CHQ)	22°4.23'N 79°1.37'E
P7	21°57.23'N 78°56.55'E
P4	21°57.23'N 78°56.55'E
P3	21°20.987'N 78°59.955'E
P2	21°8.14'N 78°56.4'E
P1	21°8.4'N 78°39.34'E

Supplemental Table 2. Full dataset of major elements, trace elements, carbon and sulfur concentrations of the bulk soil samples from Central India.

		S14	S15	S5	S19	S37	S25	S28	S26	S13	S21	S38	S10	S16	S7 (ChQ)	S36	S18	S29	S8	S9	S6
SiO_2	(wt%)	46.2	42.5	30.7	62.4	65	41.9	29.7	28.9	56.4	71.9	43.2	44.9	45.1	36.5	67.5	45.9	48.6	43.5	45.1	53.9
Al_2O_3	(wt%)	12.35	13.85	8.95	13.8	14.8	21	20.2	20.4	12.35	9.96	13.9	12.5	14.35	15.2	13.9	14.4	13.45	14.05	12.55	13.55
Fe_2O_3	(wt%)	9.65	12.1	9.79	7.08	3.72	17.45	29.6	29.5	8.26	5.24	13.85	11.55	13.05	19.95	3.04	13.55	10.4	15.2	11.75	9.39
CaO	(wt%)	8.28	6.88	20.5	2.19	1.81	0.39	0.58	0.62	3.31	0.83	4.4	5.63	3.56	2.32	1.74	1.51	3.1	3.92	5.13	1.8
MgO	(wt%)	2.8	3.3	2.68	1.02	0.61	0.55	0.55	0.53	2.59	0.77	4.14	3.23	2.42	1.94	0.45	1.98	2.29	2.74	3.34	2.1
Na_2O	(wt%)	1.04	1.13	0.6	1.92	1.94	0.06	0.04	0.04	0.69	0.45	0.78	0.42	0.25	0.29	1.99	0.16	0.11	0.82	0.4	0.58
K_2O	(wt%)	0.96	0.62	0.42	0.57	3.7	0.87	0.32	0.29	1.28	1	0.6	0.58	0.58	0.4	4.1	0.16	0.91	0.28	0.52	1.71
Cr_2O_3	(wt%)	0.02	0.02	0.01	0.02	0.01	0.05	0.05	0.05	0.03	0.02	0.01	0.03	0.02	0.02	0.01	0.04	0.02	0.01	0.03	0.02
TiO_2	(wt%)	1.79	2.08	1.64	1.38	0.58	2.16	3.4	2.87	1.66	0.91	2.11	1.85	2.39	2.99	0.45	2.99	1.8	2.53	1.89	1.57
MnO	(wt%)	0.16	0.17	0.14	0.12	0.03	0.37	0.19	0.16	0.15	0.16	0.21	0.19	0.25	0.37	0.02	0.26	0.22	0.25	0.24	0.18
P_2O_5	(wt%)	0.12	0.14	0.19	0.07	0.13	0.12	0.22	0.23	0.1	0.01	0.13	0.09	0.06	0.11	0.08	0.04	0.1	0.13	0.1	0.12
SrO	(wt%)	0.01	0.01	0.01	0.04	0.01	<0.01	<0.01	<0.01	<0.01	<0.01	0.01	<0.01	0.01	<0.01	0.01	<0.01	0.01	<0.01	<0.01	<0.01
BaO	(wt%)	0.04	0.03	0.02	0.03	0.1	0.06	0.02	0.02	0.05	0.08	0.02	0.03	0.04	0.03	0.09	0.03	0.04	0.02	0.03	0.05
LOI	(wt%)	16.45	16.3	25.2	9.44	9.32	13.9	15.1	16.35	14.15	9.49	15.5	18.65	17.5	18	7.2	18.15	17.85	15.75	17.25	15.2
Total	(wt%)	99.87	99.13	100.9	100.1	101.8	98.88	99.97	99.96	101.02	100.82	98.86	99.65	99.58	98.12	100.58	99.17	98.9	99.2	98.33	100.2
C	(wt%)	2.35	1.96	4.64	1.03	1.71	1.21	1.34	1.74	1.43	0.74	0.89	2.33	1.36	1.79	1.12	1.26	1.35	0.79	1.38	0.91
S	(wt%)	0.03	0.03	0.02	0.02	0.06	0.03	0.02	0.02	0.02	0.01	0.01	0.03	0.01	0.02	0.02	0.01	0.01	<0.01	0.03	0.01
Ba	(µg/g)	349	273	193	310	828	515	213	148.5	398	664	189	236	362	250	888	285	365	211	249	364
Ce	(µg/g)	44	47.4	31.2	61.2	143.5	119.5	90.4	78.1	58	55.3	33.9	51.9	61.5	57.2	113.5	54.7	64.7	48.1	51.7	78.1
Cr	(µg/g)	100	90	50	100	30	290	340	340	170	80	50	150	140	90	30	270	110	70	160	100
Cs	(µg/g)	1.24	0.82	0.94	1.72	1.46	6.77	1.78	1.77	2.42	3.5	0.41	1.87	3.08	1	1.14	1.36	4.41	0.98	1.74	5.16
Dy	(µg/g)	4.36	4.97	4.58	3.29	4.79	7.13	12.3	13.25	4.59	3.7	5.11	5.33	6.36	6.7	3.86	5.91	5.47	6.08	5.82	6.62
Er	(µg/g)	2.28	2.65	2.39	1.62	2.52	4.07	7.22	7.57	2.5	2.46	2.97	3.06	3.41	3.84	2.04	3.12	3.24	3.65	3.15	3.17
Eu	(µg/g)	1.41	1.68	1.26	1.28	1.56	1.94	3.37	4.07	1.4	1.06	1.65	1.76	1.86	2.04	1.27	1.88	1.62	1.98	1.67	1.7
Ga	(µg/g)	18.4	23.1	15.4	19.2	18.8	30.8	33.5	33.8	17.9	13.3	22.5	19.7	23.5	27.5	18.6	26.3	21.5	24.2	21.3	20.9
Gd	(µg/g)	4.59	5.79	4.84	4.46	6.4	7.31	13.65	14.95	5.43	4.06	5.78	6.31	6.37	7.75	4.73	7.06	6.41	6.99	6.16	6.63
Ge	(µg/g)	<5	<5	<5	<5	<5	<5	<5	<5	<5	<5	<5	<5	<5	<5	<5	<5	<5	<5	<5	<5
Hf	(µg/g)	4.4	4.9	3.4	7.3	8.9	7.8	6.7	5.1	6.1	13.6	4.2	4.8	5.1	5.7	8.8	5.8	6.3	5	5.4	7.4
Ho	(µg/g)	0.94	1.09	0.92	0.69	1.01	1.49	2.6	2.84	0.99	0.92	1.12	1.17	1.36	1.48	0.79	1.17	1.21	1.43	1.22	1.23
La	(µg/g)	21.4	22.1	13.8	26.1	72.2	43.2	33.5	34.6	27.9	22.1	14.6	21.9	24.5	19	55.1	20.6	28	19.6	21.2	36.3
Lu	(µg/g)	0.28	0.38	0.26	0.23	0.4	0.59	0.93	1	0.37	0.37	0.35	0.39	0.5	0.48	0.32	0.44	0.4	0.47	0.41	0.51
Nb	(µg/g)	10.2	11.8	8.9	9.4	18.7	21.1	18.3	15.8	11.6	10.4	8.9	11.1	14.7	13.9	14.9	16.1	15.1	12	10.7	17.6
Nd	(µg/g)	20.4	23.7	16.2	24	46.2	37.4	43	48	23.3	19.8	18.3	23.2	26.1	23.9	37.2	25.7	27.2	24	23.8	32
Pr	(µg/g)	4.97	5.5	3.86	6.08	13.5	9.79	10.05	11.1	6.27	5.16	4.45	5.69	6.25	5.64	10.7	5.97	6.84	5.45	5.38	7.97
Rb	(µg/g)	32.8	25	14.1	34.2	120.5	75.1	22.2	20.3	51.6	68.8	21.8	36.9	48.5	23.9	133	12.6	71.4	17	35.2	87.7
Sm	(µg/g)	4.64	5.51	4.19	4.96	8.45	7.99	11.65	12.3	5.12	3.87	5.01	5.04	5.73	6.69	6.79	5.79	6.1	6.03	6.04	7.09
Sn	(µg/g)	2	2	2	2	3	3	3	3	2	2	2	2	2	2	2	2	4	2	2	3
Sr	(µg/g)	177	211	207	383	217	38.7	32.4	29.6	105.5	61	146.5	132	102	90.5	224	87.7	96.3	116	154	80.4
Ta	(µg/g)	0.8	0.7	0.6	0.7	1.9	1.3	1.2	1.2	1	0.9	0.5	0.7	1	1	1.4	1	1.1	0.8	0.8	1.5
Tb	(µg/g)	0.8	0.86	0.8	0.61	0.92	1.26	2.12	2.49	0.91	0.7	1.04	1.04	1.09	1.28	0.74	1.08	1.05	1.14	1.06	1.08
Th	(µg/g)	5.89	4.89	3.22	6	43.6	14.75	5.78	5.93	14.1	15.05	2.52	5.62	9.18	3.8	32.7	4.46	9.66	3.81	5.38	13.05
Tm	(µg/g)	0.37	0.39	0.36	0.27	0.46	0.6	1.07	1.12	0.41	0.4	0.43	0.44	0.47	0.59	0.35	0.45	0.46	0.56	0.41	0.5
U	(µg/g)	1.17	0.99	0.85	1.32	4.71	3.33	2.17	2.17	1.63	2.48	0.49	1.2	1.49	0.94	3.19	1.07	1.93	1.02	1.08	2.66
V	(µg/g)	275	350	281	252	68	492	1070	1200	216	119	353	308	364	534	65	888	281	395	317	205
W	(µg/g)	1	1	1	1	<1	3	1	1	1	1	1	1	1	1	1	1	2	<1	1	2
Y	(µg/g)	21.5	26.2	21.9	17.1	28.2	37.4	66.4	66.3	23.8	21.3	26.4	29.1	35	35.9	22.5	30.4	29.7	32.8	29.4	33.5
Yb	(µg/g)	2.17	2.18	2.03	1.58	2.65	3.62	6.11	6.26	2.24	2.56	2.34	2.49	3.03	3.43	2.26	2.92	2.86	2.93	2.46	3.82
Zr	(µg/g)	153	176	121	303	344	265	232	203	214	508	146	170	206	229	364	223	231	185	188	259
As	(µg/g)	1.9	1.6	1.5	2.5	0.9	14.6	8.3	10.8	3.5	4.1	0.5	3.4	3.1	1.6	0.4	2.8	5.6	2.1	2.9	5.7
Bi	(µg/g)	0.06	0.05	0.05	0.11	0.06	0.36	0.16	0.16	0.12	0.13	0.06	0.11	0.14	0.05	0.04	0.13	0.19	0.06	0.11	0.23
Hg	(µg/g)	0.014	0.008	0.01	0.021	0.055	0.026	0.023	0.025	0.021	0.01	0.012	0.013	0.02	0.017	0.048	0.034	0.037	0.019	0.007	0.013
In	(µg/g)	0.044	0.059	0.049	0.03	0.021	0.091	0.139	0.132	0.039	0.024	0.073	0.048	0.056	0.092	0.015	0.073	0.071	0.079	0.057	0.053
Re	(µg/g)	<0.001	0.001	<0.001	<0.001	0.001	<0.001	0.001	0.001	<0.001	<0.001	0.001	<0.001	0.001	0.001	<0.001	0.001	<0.001	0.001	<0.001	<0.001
Sb	(µg/g)	0.07	0.06	0.07	0.11	0.06	0.85	0.54	0.63	0.14	0.17	<0.05	0.2	0.18	0.07	<0.05	0.13	0.17	0.08	0.12	0.17
Se	(µg/g)	0.5	1	0.8	0.9	1	1	2.1	2.3	0.9	0.5	1	1.2	0.8	1.4	0.8	1.6	0.8	1.3	0.9	0.7
Te	(µg/g)	<0.01	0.02	<0.01	0.02	<0.01	0.11	0.07	0.1	0.01	<0.01	0.01	0.01	0.03	<0.01	<0.01	0.05	0.01	<0.01	0.01	<0.01
Tl	(µg/g)	0.07	0.06	0.04	0.04	0.08	0.24	0.08	0.09	0.08	0.09	0.05	0.06	0.08	0.06	0.05	0.1	0.14	0.05	0.06	0.17
Ag	(µg/g)	<0.5	<0.5	<0.5	<0.5	<0.5	<0.5	<0.5	<0.5	<0.5	<0.5	<0.5	<0.5	<0.5	<0.5	<0.5	<0.5	<0.5	<0.5	<0.5	<0.5
Cd	(µg/g)	<0.5	<0.5	<0.5	<0.5	<0.5	<0.5	<0.5	<0.5	<0.5	<0.5	<0.5	<0.5	<0.5	<0.5	<0.5	<0.5	<0.5	<0.5	<0.5	<0.5
Co	(µg/g)	35	40	29	28	9	73	61	62	30	29	48	53	56	82	7	51	44	57	54	35
Cu	(µg/g)	107	151	134	65	29	127	342	302	73	41	211	142	166	281	24	213	130	222	149	111
Li	(µg/g)	20	20	10	20	20	40	20	20	20	30	20	20	30	20	20	20	30	10	20	30
Mo	(µg/g)	<1	<1	<1	<1	<1	2	<1	1	<1	<1	<1	<1	<1	<1	<1	<1	<1	<1	<1	<1
Ni	(µg/g)	63	65	42	64	24	130	133	131	84	51	58	97	99	81	19	159	89	71	95	70
Pb	(µg/g)	5	2	<2	10	34	24	10	15	12	17	<2	6	9	<2	32	2	11	<2	4	10
Sc	(µg/g)	21	24	21	13	8	26	46	42	19	11	32	25	29	39	7	31	23	33	26	20
Zn	(µg/g)	79	95	78	53	49	59	129	124	71	33	111	91	93	129	39	92	84	128	92	88

Supplemental Table 3. Varian Liberty Series II ICP-OES instrument and method parameters.

Parameter	**Setting**						
Element	Cu	Fe	Mo	Zn	Cr	Co	Ni
Wavelength (nm)	324.754	259.94	202.63	213.856	267.716	228.615	231.604
Nebulizer	Glass Expansion P/N 201-0081600 Concentric High Flow						
Spray Chamber	Cyclonic						
Pump Speed	15 rpm						
Sample Pump Tubing	Grey-Grey						
Waste Pump Tubing	Blue-Blue						
RF power	1kW						
Plasma Flow	15 L/min						
Aux Flow	1.5 L/min						
Torch	Glass Expansion P/N 30-808-0478 Quartz 2.3mm injector						
Read Time	1 s						
Number of replicates	3						
Sample uptake delay	30 s						
Rinse Time	10 s						
Stabilisation time	15 s						
Background correction	Polynomial Plotted Background						

Supplemental Table 4. Tau values (τ) with relative enrichment-depletion of essential metals relative to Nb.

$\tau_{Nb\text{ - Deccan basalt}}$	Cr	Co	Cu	Ni	Zn
S38	-0.06	–	0.13	0.11	0.20
S10	1.25	–	-0.39	0.49	-0.21
S9	1.49	–	-0.34	0.52	-0.18
S16	-0.43	-0.32	-0.42	-0.33	-0.44
S29	-0.57	-0.48	-0.56	-0.41	-0.51
S25	-0.18	-0.38	-0.69	-0.38	-0.75
S28	0.11	-0.40	-0.03	-0.27	-0.38
S26	0.28	-0.30	-0.01	-0.17	-0.30
S7 (ChQ)	-0.06	-0.02	-0.18	-0.11	-0.29
S8	-0.15	-0.21	-0.25	-0.09	-0.19
S6	-0.17	-0.67	-0.75	-0.39	-0.62
S5	-0.18	-0.46	-0.39	-0.28	-0.33
$\tau_{Nb\text{ - TTG}}$	**Cr**	**Co**	**Cu**	**Ni**	**Zn**
S13	1.69	1.16	28.76	16.50	0.41
S14	0.80	1.86	48.60	13.93	0.78
S15	0.40	1.83	59.51	12.31	0.85
S37	-0.71	-0.60	6.33	2.10	-0.40
S36	-0.63	-0.61	6.62	2.08	-0.40
$\tau_{Nb\text{ - Calcaerous shale}}$	**Cr**	**Co**	**Cu**	**Ni**	**Zn**
S5	-0.31	-0.61	2.90	0.09	-0.48
$\tau_{Nb\text{ - Grey shale}}$	**Cr**	**Co**	**Cu**	**Ni**	**Zn**
S21	0.18	-0.58	–	0.77	-0.49
S19	0.63	-0.55	–	1.46	-0.10
S18	1.57	-0.52	–	2.57	-0.09

Supplemental Table 5. Essential trace metal (Cr, Co, Ni, Cu, Zn, Mo, Fe) and Ti concentrations (µg/g, dry weight basis) in Central Indian cow dung (n = 10) in comparison to the Ti conentration of the soil samples from the same locations and resultant soil ingestion (%).

Sample	Bedrock	Cr	Co	Ni	Cu	Zn	Mo	Fe	Ti	Soil sample	Ti (ug/g)	Soil ingestion (%)
P10b	basalt	31.2	10.3	20.6	52.8	251.5	1.9	16776.0	2257.0	S10	11090.9	6.7
P13	basalt	49.3	17.5	34.8	100.0	201.1	1.8	31406.7	4554.6	S16	14328.3	11.5
P10a	basalt	9.8	7.2	10.6	62.0	226.0	0.7	13621.5	1897.5	S10	11090.9	5.5
P7(CHQ)	basalt	42.4	24.8	30.2	111.8	123.7	1.1	48952.2	6619.3	S7(ChQ)	17925.3	14.1
P16a	basalt	39.3	13.8	30.0	79.0	300.7	1.7	21819.9	3069.6	S28	20383.3	4.7
P19	basalt	15.3	7.9	11.6	47.9	199.7	1.1	14236.9	2051.5	S38	12649.7	5.1
P18	granite-gneiss	2.6	1.3	1.9	12.1	147.3	4.1	2111.9	204.8	S36	2697.8	2.2
P12	granite-gneiss	81.7	16.8	39.4	69.8	129.1	4.1	36341.0	5358.8	S13	9951.9	24.6
P14	shale	46.3	8.3	26.6	62.7	216.2	3.2	15932.8	2608.3	S18	17925.3	4.6
P15	shale	21.3	5.8	13.2	31.1	160.6	2.4	9839.4	1365.6	S21	5455.5	8.5

Supplemental Table 6. Mean contribution of soil to total daily intake of Co, Zn and Cu in cattle of Central India.

Sample	% soil ingested	Soil content µg g^{-1}			Total daily intake mg			% element ingested as soil		
		Co	Zn	Cu	Co	Zn	Cu	Co	Zn	Cu
P10b	6.7	53	91	142	3.6	337.6	63.5	10.9	1.6	0.2
P13	11.5	56	93	166				19.7	3.3	0.3
P10a	5.5	53	91	142				8.9	1.3	0.2
P7(CHQ)	14.1	82	129	281				35.4	6.8	0.6
P16a	4.7	61	129	342				8.8	2.8	0.2
P19	5.1	48	111	211				7.5	1.8	0.2
P18	2.2	7	39	24				0.5	0.1	0.0
P12	24.6	30	71	73				22.6	3.1	0.6
P14	4.6	51	92	213				7.2	1.7	0.1
P15	8.5	29	33	41				7.5	0.6	0.1

Supplemental Table 7. Pearson Product Moment Correlation between soil ingestion (%) and essential trace metal concentrations (Cr, Co, Ni, Cu, Zn, Mo, Fe) (µg/g) in cow dung.

	Cr	Co	Ni	Cu	Zn	Mo	Fe
Soil ingestion (%)	0.81	0.72	0.73	0.53	-0.53	0.16	0.79
	<0.01	<0.05	<0.05	0.11	0.11	0.67	<0.01
Cr		0.69	0.95	0.60	-0.16	0.32	0.73
		<0.05	<0.01	0.07	0.66	0.38	<0.05
Co			0.83	0.93	-0.18	-0.28	0.99
			<0.01	<0.01	0.62	0.44	<0.01
Ni				0.80	0.01	0.06	0.82
				<0.01	0.98	0.86	<0.01
Cu					0.05	-0.45	0.89
					0.88	0.20	<0.01
Zn						-0.40	-0.31
						0.26	0.39
Mo							-0.19
							0.59

* First cell content = correlation coefficient ; ** Second cell content = P value

Supplemental Figure 1. Location of the granite-gneiss samples (S13−15). **(a)** Strongly weathered gneiss outcrop. Gneiss layering is still visible, and in the lower section of the top horizon, a Fe-oxide enriched layer has formed. **(b)** The agricultural topsoils next to the outcrop in **(a)** consist of dark and clay-rich material, which is typical for vertisols. **(c)** The photo illustrates Deccan basalt mesas in the background. It is likely that clay-rich material was deposited on the lower situated granite-gneiss basement so that the in-situ soil mixed with the clays.

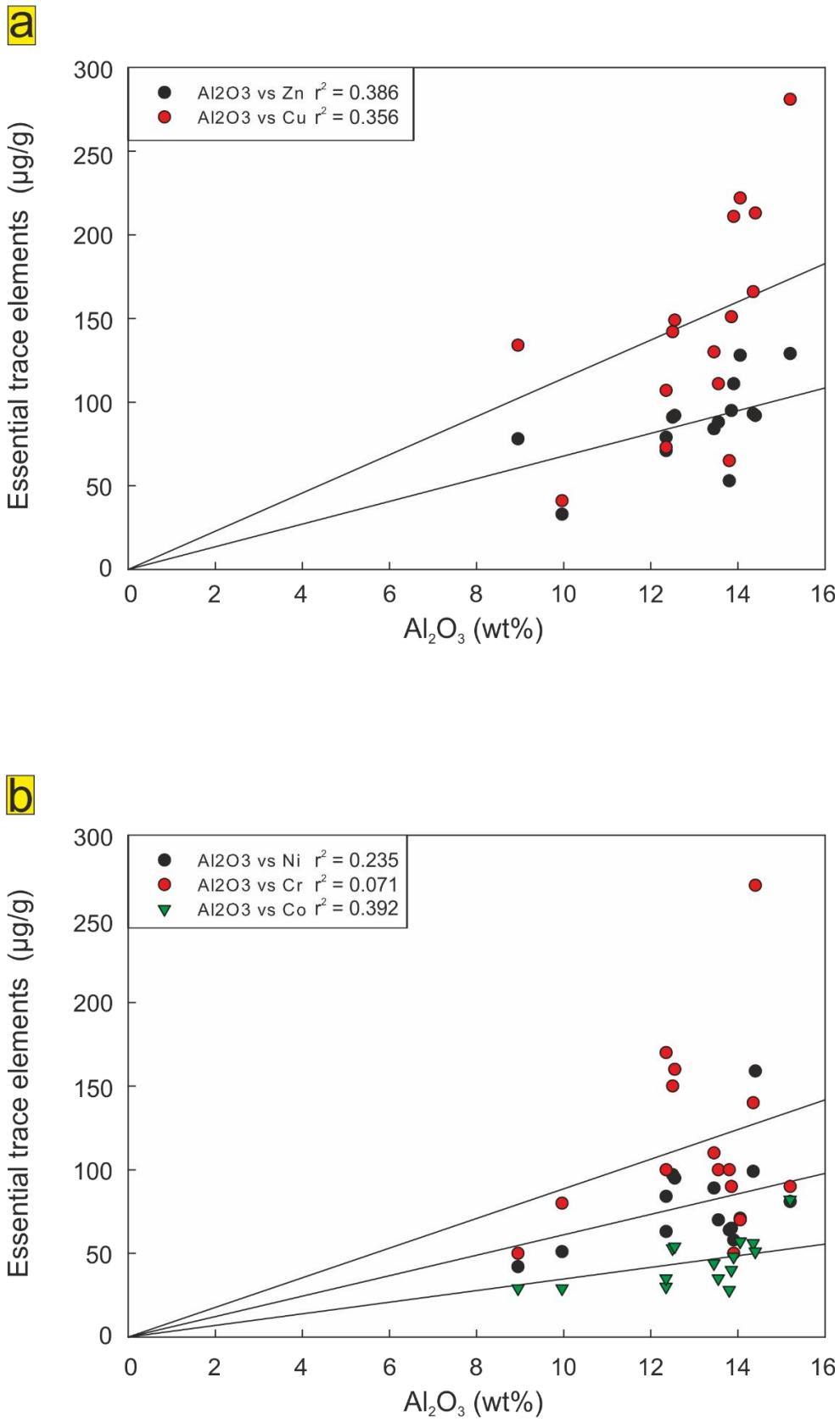

Supplemental Figure 2. Modest correlations in clay-rich soil samples between Al_2O_3 (wt%) with Zn, Cu **(a)** and Ni, Co **(b)**, which suggests that these essential metals have an association with clay minerals. By contrast, Cr shows no relationship with Al_2O_3 (wt%).

Chapter 6: Synthesis

Chemical weathering is one of the principal processes which modifies land surfaces (e.g., Kronberg et al., 1979; Kronberg and Nesbitt, 1981) and one of the most critical factors in the modification of the Critical Zone (CZ) resulting in the formation of soils. Throughout the CZ, chemical reactions proceed both abiotically and through catalysis by organisms and provide energy and nutrients for the sustenance of terrestrial ecosystems (Brantley et al., 2007). Importantly, the biogeochemical cycles of metals are affected by these reactions within the CZ, and at trace concentrations, several metals (zinc (Zn), copper (Cu), iron (Fe), manganese (Mn), cobalt (Co), nickel (Ni), chromium (Cr), molybdenum (Mo)) are essential for the health of plants (Maret et al., 2016; He et al., 2005; Brown et al., 1987) and humans (e.g., Prashanth et al., 2015). Critical Zone processes consequently impact on the health of living organisms, particularly in tropical regions where the soils are often characterised by severe depletion and enrichment of metals (e.g., Dissanayake and Chandrajith, 1999).

Zinc deficiency in soils represents a prominent example of this phenomenon, and soil-crop relations affect the health of people that depend on local crops as their principal diet (Alloway, 2009; Cakmak, 2008). However, natural depletion processes alone are not the sole cause for deficiency of essential metals within soils and since the 20th-century, intensive agricultural cultivation has impacted on the CZ and caused further stress on the micronutrient status of soils (Andersen, 2007; Gregorio et al., 1999). Primarily in developing countries such as India, the anticipated rise in population until 2050 will lead to new types of metal-deficiencies in soils due to higher crop production (Singh, 2008). This will require development of new strategies for sustainable agriculture in affected areas.

Even though historically soil science was a classical discipline of geology (Wilding and Lin, 2006) that investigated the fertility status of agricultural soils with geochemical and mineralogical principles (Jackson and Sherman, 1953), academic discipline barriers are likely to blame for the limited contributions geology made to this research field in later decades (e.g., Fyfe et al., 1983). As a result, neither the potential of the inorganic components to supply essential metals to plants nor the origin of inherently low metal contents in soils received much attention in geochemistry. The

integration of soil studies with Earth's CZ investigations and the emergence of frontier disciplines such as geobiochemistry (Wildling and Lin, 2006) are changing this situation. The research conducted in this thesis is one approach to understand how chemical weathering and farming practices in a densely populated part of the world affect Zn and other essential metal contents in soils. The resulting data and analysis have revealed new and important insights to explain how metal deficiency in soils develops with broader implications for the agricultural cultivation of (sub)-tropical regions that are affected by metal deficiencies in the context of soil-crop relations. The most important contributions and conclusions of the thesis relevant to metal deficiencies in soils can be summarised as five main findings:

- Finding 1: *Importance of active weathering reactions in saprolite*
  Active weathering reactions occur in the deeper CZ where rock transforms into saprolite. There, the chemical breakdown of metal-rich silicate and clay minerals results in the mobilisation of substantial amounts of metals to aqueous solutions. The early stages of chemical weathering, in the volumetrically minor deep actively weathering CZ are disproportionally important for the release of metals during soil formation. This is exemplified by the strong isotopic depletion of uranium-234 (^{234}U) in the Chhindwara profile and predicted from experimental findings, showing that ^{234}U resides in labile sites in minerals so that chemical weathering reactions lead to its preferential release over lattice bound ^{238}U during clay-mineral formation (e.g., Kigoshi et al., 1971). The empirical data of the Chhindwara profile, therefore, reconcile experimental findings of preferential ^{234}U loss during clay-mineral formation with weathering profiles. Moreover, mass balance calculations and the excess of ^{234}U in seawater suggest that saprolites contribute at least half the U to the dissolved river load and oceans. Thus, these global observations underline that low to intermediate weathered soils are not only locally important but that they are able to supply very high quantities of redox-sensitive (essential) metals to aqueous solutions and consequently to plants. Furthermore, these findings confirm that primary mafic silicates and clay minerals represent a reservoir of metals in bio-available forms that can be released through chemical weathering reactions (Fyfe et al., 1983).

- Finding 2: *The development of inherently low Zn content in tropical soils and its isotope fingerprint*

  The development of Zn deficiency in soils is linked to the mineralogical transformations in the weathering process from bedrock to the soil endmember. Studies on the full extent of the CZ are therefore helpful to pinpoint which mineralogical transformation cause Zn deficiency in soils. As finding one already suggested, actively weathering profiles (i.e. saprolites) still contain sufficient quantities of bio-available Zn in primary silicates and smectite (Fyfe et al., 1983). It is only the progressive breakdown of the primary minerals and phyllosilicates that leads to strong depletion of Zn and the formation of Fe-oxides that occasionally contain residual amounts of Zn in strongly weathered soils. However, the residual quantities of Zn locked in such oxides are bio-unavailable due to the weathering resistance and refractory nature of these minerals (Nesbitt and Wilson, 1992).

  The extent of isotopic fractionation of Zn revealed that a combination of biotically- and kinetically-controlled sorption reactions on Fe-oxyhydroxides causes the isotope fractionation observed in the more strongly weathered samples of the Bidar laterite profile. The isotopic composition in the Fe-oxide rich soil endmembers ($\Delta^{66}Zn_{sample-protolith}$ up to ca. -0.65‰) clearly differs from the saprolite horizons that lie within the "crustal average" of +0.27 ± 0.07‰ $\delta^{66}Zn_{JMC-Lyon}$ (Little et al., 2016). Importantly, a comparison of the global distribution of Zn deficient soils (Alloway, 2009), highly depleted weathering residues (i.e. lateritic soils) (Gidigasu, 2012) and cratons that are characterised by low denudation rates (e.g., Hewawasam et al., 2013) suggests that geology and weathering history evidently contribute to human Zn deficiency in areas where the population relies on local crops. Since the Zn isotope ratios in the Chhindwara saprolite and strongly weathered upper sections of the Bidar laterite differ, Zn isotopes could eventually serve as a new tool to evaluate the overall loss of Zn and storage of bio-unavailable Zn in oxides. The investigation of Zn isotopes in subsoils and rivers that drain these areas might, therefore, help to inform sustainable farming practices in subtropical-tropical cratonic regions where vast areas are covered by challenging soils. This emphasises the need for more scientific contributions from geologists to the research field of agricultural soil science.

- Finding 3: *Elemental and isotopic behaviour of Cr in metal-deficient soils*
  By contrast to Zn, a significant net loss of Cr from weathering profiles does not occur. Instead, Cr redistributes into newly formed Fe-oxides through chemical weathering according to pore-water parameters such as pH and Eh. These processes also control the isotopic fractionation of Cr. The strong association of Cr and Fe-oxides confirms that essential metals redistribute into newly formed, weathering resistant oxide phases during soil formation and that high concentrations in the bulk soil do not necessarily reflect the amount that will be bio-available for plants.

- Finding 4: *Pedogenic impacts on essential metal deficiencies in agricultural topsoils in Central India*
  Because Central India has one of the highest percentages of Zn deficient soils, it is likely that new types of metal deficiencies will develop through soil over-cropping in the future (Singh, 2008). Overall, the investigation of the bulk soil chemistry of 20 agricultural topsoils from a significant area of Central India revealed a strong relationship between essential metals (Zn, Cu, Ni, Cr, Co) and primary and secondary oxides in the soil reservoir and a modest correlation with clays and residual primary silicates (Zn, Cu, Ni, Co). These findings are in agreement with the previous two main findings and confirm the necessity of geochemical studies on the CZ with elemental and isotopic methods to contribute to a broader understanding of metal deficiencies in soils. Importantly, the investigation of the inorganic components in agricultural soils with geochemical data provides insights into why only a minor amount of the essential metals occurs as bio-available forms in Indian soils (Singh and Abrol, 1986; Singh, 2008). Namely, whereas clays and residual primary minerals host modest quantities of metals in these soils, much higher quantities are locked away in primary and secondary oxides that are weathering resistant (Nesbitt and Wilson, 1992; Fyfe et al., 1983) and thus incapable of releasing metals to soil solutions.

- Finding 5: *Chemical recycling of essential metals in the context of the soil-plant-cattle -relation*
  Many subsistence farmers strongly depend on farmyard manure as fertiliser in India. To date, most studies into this material have mainly focused on its benefits for soil structure

improvement and as nitrogen, phosphor, potassium (NPK) fertiliser (e.g., Hati et al., 2006; Reddy et al., 2010), whereas the essential metal concentrations are largely unknown. Building on the knowledge of the distribution of metals in soil minerals from the previous three findings, it was possible to work out that refractory oxides from the agricultural topsoils likely represent a passive metal 'contaminant' of farmyard manure. Hence, manure samples with low ingested soil contamination represent the best approximation for manure's potential as an essential metal fertiliser. It was found that the bio-available quantities of essential metals are too low to counterbalance multi-metal deficiencies in Indian soils (Takkar et al., 1997). Regardless, the association of organic carbon (C_{org}) with plant-available pools of Zn, Cu and Fe and its general importance for the physicochemical health of the agricultural topsoils suggest that C-rich farmyard manure is an indispensable fertiliser in India.

In light of the new findings from the full extent of the CZ reported in this thesis, it can be concluded that geochemical studies are able to explain how inherently low contents of essential metals develop in certain soil types. Moreover, elemental data of soils are helpful to identify minerals with bio-available forms of metals and to distinguish them from inert species of metals that are locked in heavy minerals, while isotope data of metals are powerful tools to identify the environmental factors (Wiederhold, 2015) that accompany the development of metal deficiency in soils. Another strength of the isotope data is their clear distinction in clay-rich saprolites and more strongly weathered, Fe-oxyhydroxide-rich laterites that correspond to different isotope signals in rivers. The findings of this thesis for Zn suggest that metal isotope fingerprints in entire catchments of (sub)-tropical regions might help to identify areas with favourable conditions for agriculture and help to improve sustainable farming practices.

Importantly, the identification of similar geochemical patterns in the agricultural topsoils from Central India suggests that geology and geochemistry are research disciplines with high potential to contribute to the development of more sustainable agricultural and soil science strategies. Such contributions are urgently needed since the anticipated rise in world population (Ray et al., 2013) will put additional demands on crop production with knock-on effects for essential metal depletion in soil (e.g., Singh, 2001; Singh, 2008). It is therefore unfortunate that the number of studies from the geosciences that contribute to agricultural questions is still quite limited, particularly

considering that the pioneering studies by Jackson and Sherman (1953) and Fyfe et al. (1983) demonstrated that geology and geochemistry provide a deeper understanding on the fertility status of soils. Regardless, the awareness by scientists that the CZ provides nutrients to ecosystems and human society (e.g., Brantley et al., 2005; Brantley et al., 2007; Wilding and Lin, 2006; National Research Council, 2001; Lin et al., 2005) and the integration of soil studies with new frontier disciplines such as geobiochemistry in recent years (Wildling and Lin, 2006) suggest that geochemical studies can advance scientific progress in the interface of agricultural sciences, which is also confirmed by the findings in this thesis.

For deeper Earth time studies, the relevance of findings one to three in terms of metal cycling and associated metal stable isotope fractionation is not less interesting. Many of the major global change events in the past ~250 Myr have been studied for changes in metal global geochemical cycling (e.g., Mo, U, Zn, cadmium (Cd), Fe, sulphur (S)), measuring changes in stable metal isotope ratios. The assumption often is that the residence time of these metals remains relatively constant, while isotopic fractionation results from various environmental factors. For example, an elevated level of low-oxygen marine environment and associated sulphide speciation is assumed to trigger isotope fractionation of Mo (Dickson et al., 2012; 2017), whereas fractionation of $\delta^{238}U$ can result from the reduction of $^{238}U(VI)$ relative to $^{235}U(VI)$ in anoxic marine sediments (Jost et al., 2017). By contrast, lighter compositions of thallium (Tl) (Them et al., 2018) and heavier compositions of osmium (Os) isotopes (Them et al., 2017) in marine sediments were linked to enhanced continental weathering rates and nutrient input to the oceans as a result of the formation of large igneous provinces and associated rising carbon dioxide (CO_2) and temperature levels. This observation is in agreement with the departure of Tl isotopes towards heavier values in residual soils of the Bidar laterite profile and a greywacke lateritic profile (Howarth et al., 2018) and lighter values of Os isotopes in the same profiles (Wimpenny et al., 2007). In conclusion, this means that metal stable isotope systems are likely to correspond individually to climate change and associated changes in chemical weathering rates. However, heavier Zn isotopes in marine sediments might only relate to such climate conditions on a regional scale or possibly to times in Earth history that were characterised by tectonic quiescence that

favoured the development of laterites with a subordinate influence of rock and saprolite weathering.

Regardless, the significant fractionation of Zn and Cr isotopes that relates to oxide phases in lateritic soils suggest that marine or lacustrine sediments that are dominated by the suspended load of rivers may carry a climate signal that corresponds to a time window in Earth history when chemical weathering rates were replaced by stronger physical erosion in sub-tropical latitudes, for instance, due to increased mountain building.

References

Albarède, F. & Beard, B., (2004). Analytical methods for non-traditional isotopes. *Reviews in mineralogy and geochemistry,* 55(1), 113-152.

Albarède, F., Telouk, P., Blichert-Toft, J., Boyet, M., Agranier, A., Nelson, B., (2004). Precise and accurate isotopic measurements using multiple-collector ICPMS. *Geochimica et Cosmochimica Acta*, 68(12), 2725-2744.

Allègre, C.J., Dupré, B., Négrel, P., Gaillardet, J., (1996). Sr-Nd-Pb isotope systematics in Amazon and Congo River systems: constraints about erosion processes. *Chemical Geology* 131, 93-112

Alloway, B. J., (2009). Soil factors associated with zinc deficiency in crops and humans. *Environmental Geochemistry and Health,* 31(5), 537-548.

Alloway, B. J., (2008). *Zinc in soils and crop nutrition*: International Zinc Association Brussels, Belgium.

Anand, R., (2005). Weathering history, landscape evolution and implications for exploration. *Regolith landscape evolution across Australia: A compilation of regolith landscape case studies with regolith landscape evolution models. CRC LEME Monograph,* 2-40.

Andersen, P. A., (2007). Review of Micronutrient Problems in the Cultivated Soil of Nepal: An Issue with Implications for Agriculture and Human Health. *Mountain Research and Development*, 27(4), 331-335.

Andersen, P. (2002). Geographical approaches to micronutrient deficiencies in Himalaya. *I: Vegetation and society. Their interaction in the Himalayas.* Kathmandu: Tribhuvan University, Nepal / University of Bergen, Norway, 149-156.

Anderson, S.P., Dietrich, W.E., Brimhall, G.H. (2002). Weathering profiles, mass-balance analysis, and rates of solute loss: Linkages between weathering and erosion in a small, steep catchment. *GSA Bulletin* ; 114 (9): 1143–1158.

André, L., Cardinal, D., Alleman, L.Y., Moorbath, S., (2006). Silicon isotopes in ∼3.8 Ga West Greenland rocks as clues to the Eoarchaean supracrustal Si cycle. *Earth and Planetary Science Letters*, 245(1–2), 162-173.

Babechuk, M.G., Kleinhanns, I.C., Schoenberg, R., (2017). Chromium geochemistry of the ca. 1.85 Ga Flin Flon paleosol. *Geobiology*, 15(1), 30-50.

Babechuk, M. G., Widdowson, M. & Kamber, B. S., (2014). Quantifying chemical weathering intensity and trace element release from two contrasting basalt profiles, Deccan Traps, India. *Chemical Geology*, 363, 56-75.

Babechuk, M. G., Widdowson, M., Murphy, M. & Kamber, B. S., (2015). A combined Y/Ho, high field strength element (HFSE) and Nd isotope perspective on basalt weathering, Deccan Traps, India. *Chemical Geology*, 396, 25-41.

Babechuk, M.G., Kamber, B.S., Greig, A., Canil, D., Kodolányi, J., (2010). The behaviour of tungsten during mantle melting revisited with implications for planetary differentiation time scales. *Geochimica et Cosmochimica Acta*, 74(4), 1448-1470.

Ball, J., (2004). Occurrence of hexavalent chromium in ground water in the western Mojave Desert, California. *Applied Geochemistry*, 19(7), 1123-1135.

Basile-Doelsch, I., Meunier, J.D., Parron, C., (2005). Another continental pool in the terrestrial silicon cycle. *Nature*, 433(7024), 399-402.

Beck, R. A., Burbank, D. W., Sercombe, W. J., Riley, G. W., Barndt, J. K., Berry, J. R., Afzal, J., Khan, A. M., Jurgen, H., Metje, J., Cheema, A., Shafique, N. A., Lawrence, R. D. & Khan, M. A., (1995). Stratigraphic evidence for an early collision between northwest India and Asia. *Nature*, 373(6509), 55-58.

Bekker, A., Holland, H.D., Wang, P.L., Rumble, D., Stein, H.J., Hannah, J.L., Coetzee, L.L., Beukes, N.J., (2004). Dating the rise of atmospheric oxygen. *Nature* 427, 117-120.

Berger, A., Frei, R., (2014). The fate of chromium during tropical weathering: A laterite profile from Central Madagascar. *Geoderma*, 213, 521-532.

Bermin, J., Vance, D., Archer, C., Statham, P. J., (2006). The determination of the isotopic composition of Cu and Zn in seawater. *Chemical Geology*, 226 (3–4), 280-297.

Bern, C.R., Brzezinski, M.A., Beucher, C., Ziegler, K., Chadwick, O.A., (2010). Weathering, dust, and biocycling effects on soil silicon isotope ratios. *Geochimica et Cosmochimica Acta*, 74(3), 876-889.

Berner, E. & Berner, R., (1996). Marginal marine environments: estuaries. *Global environment: water, air, and geochemical cycles*, Prentice Hall, Englewood Cliffs, N.J., pp 284–311.

Bhanderi, B., Goswami, A., Garg, M., Samanta, S., (2016). Study on minerals status of dairy cows and their supplementation through area specific mineral mixture in the state of Jharkhand. *Journal of animal science and technology*, 58(1), 42.

Black, R. E., Victora, C. G., Walker, S. P., Bhutta, Z. A., Christian, P., De Onis, M., Ezzati, M., Grantham-McGregor, S., Katz, J., Martorell, R., (2013). Maternal and child undernutrition and overweight in low-income and middle-income countries. *The Lancet*, 382(9890), 427-451.

Bloom, D. E., (2011). *Population dynamics in India and implications for economic growth. WDA-Forum*, University of St. Gallen St. Gallen, Switzerland.

Blume, H.P., Brümmer, G.W., Horn, R., Kandeler, E., Kögel-Knabner, I., Kretzschmar, R., Stahr, K. and Wilke, B.M., (2010). *Scheffer/Schachtschabel: Lehrbuch der Bodenkunde*. Springer-Verlag.

Bonnet, N. J., Beauvais, A., Arnaud, N., Chardon, D., Jayananda, M., (2014). First 40Ar/39Ar dating of intense Late Palaeogene lateritic weathering in Peninsular India. *Earth and Planetary Science Letters*, 386(Supplement C), 126-137.

Bonnet, N.J., Beauvais, A., Arnaud, N., Chardon, D., Jayananda, M., (2016). Cenozoic lateritic weathering and erosion history of Peninsular India from Ar-40/Ar-39 dating of supergene K-Mn oxides. *Chemical Geology*, 446, 33-53.

Bonotto, D.M. & Jiménez-Rueda, J.R., (2007). U-ages in soils and groundwater evidencing wet periods 400–600 kyr ago in southeast Brazil. *Applied Radiation and Isotopes* 65, 776-783.

Borger, H. & Widdowson, M., (2001). Indian laterites, and lateritious residues of southern Germany: A petrographic, mineralogical, and geochemical comparison. *Zeitschrift fur Geomorphologie,* 45(2), 177-200.

Bowles, J.F.W., (1986). The development of platinum-group minerals in laterites. *Economic Geology*, 81(5), 1278-1285.

Brantley S.L., Goldhaber M.B., Ragnarsdottir K.V., (2007). Crossing Disciplines and Scales to Understand the Critical Zone. *Elements,* 3, 307-314.

Brantley, S. L. & Lebedeva, M., (2011). Learning to Read the Chemistry of Regolith to Understand the Critical Zone. *In:* Jeanloz, R. & Freeman, K. H. (eds.) *Annual Review of Earth and Planetary Sciences, Vol 39.* Palo Alto: Annual Reviews.

Brantley, S.L., White, T.S., White, A.F., Sparks, D., Richter, D., Pregitzer, K., Derry, L., Chorover, J., Chadwick, O., April, R., Anderson, S., Amundson, R., (2005). *Frontiers in exploration of the critical zone*. Report of a workshop sponsored by the National Science Foundation (NSF), October 24–26, 2005. National Science Foundation, Newark.

Brimhall, G. H. & Dietrich, W. E., (1987). Constitutive mass balance relations between chemical composition, volume, density, porosity, and strain in metasomatic hydrochemical systems: Results on weathering and pedogenesis. *Geochimica et Cosmochimica Acta,* 51(3), 567-587.

Brown, P.H., Welch, R.M., Cary, E.E., (1987). Nickel: A micronutrient essential for higher plants. *Plant physiology*, 85(3), 801-803.

Bunney, L.R., Ballou, N.E., Pascual, J., Foti, S., (1959). Quantitative Radiochemical Analysis by Ion Exchange. Anion Exchange Behavior of Several Metal Ions in Hydrochloric, Nitric, and Sulfuric Acid Solutions. *Analytical chemistry* 31, 324-326.

Buss, H. L., Brantley, S. L., Scatena, F., Bazilievskaya, E., Blum, A., Schulz, M., Jiménez, R., White, A. F., Rother, G., Cole, D., (2013). Probing the deep critical zone beneath the Luquillo Experimental Forest, Puerto Rico. *Earth Surface Processes and Landforms,* 38(10), 1170-1186.

Cakmak I. (2008). Enrichment of cereal grains with zinc: agronomic or genetic biofortification? *Plant and soil*, 302, 1-17.

Cakmak, I., (2000). Tansley Review No. 111 Possible roles of zinc in protecting plant cells from damage by reactive oxygen species. *New Phytologist,* 146(2), 185-205.

Cao, X., Guo, J., Mao, J., Lan, Y., (2011). Adsorption and mobility of Cr(III)– organic acid complexes in soils. *Journal of Hazardous Materials*, 192(3), 1533-1538.

Cardinal, D., Gaillardet, J., Hughes, H.J., Opfergelt, S., André, L., (2010). Contrasting silicon isotope signatures in rivers from the Congo Basin and the specific behaviour of organic-rich waters. *Geophysical Research Letters*, 37(12).

Chabaux, F., Blaes, E., Stille, P., di Chiara Roupert, R., Pelt, E., Dosseto, A., Ma, L., Buss, H., Brantley, S., (2013). Regolith formation rate from U-series nuclides: Implications from the study of a spheroidal weathering profile in the Rio Icacos watershed (Puerto Rico). *Geochimica et Cosmochimica Acta* 100, 73-95.

Chabaux, F., Riotte, J., Clauer, N., France-Lanord, C., (2001). Isotopic tracing of the dissolved U fluxes of Himalayan rivers: implications for present and past U budgets of the Ganges-Brahmaputra system. *Geochimica et Cosmochimica Acta,* 65(19), 3201-3217.

Chairidchai, P. & Ritchie, G., (1990). Zinc adsorption by a lateritic soil in the presence of organic ligands. *Soil Science Society of America Journal*, 54(5), 1242-1248.

Chemtob, S.M., Rossmana, G.R., Edward D.Young, E.D., Ziegler, K., Moyniere, F., Eilera, J.M., Hurowitz, J.A., (2015). Silicon isotope systematics of acidic weathering of fresh basalts, Kilauea Volcano, Hawaii. *Geochimica et Cosmochimica Acta*, 169, 63-81.

Chen, H., Savage, P. S., Teng, F.-Z., Helz, R. T., Moynier, F., (2013). Zinc isotope fractionation during magmatic differentiation and the isotopic composition of the bulk Earth. *Earth and Planetary Science Letters*, 369–370, 34-42.

Chen, J., Edwards, R.L., Wasserburg, G., (1986). ^{238}U, ^{234}U and ^{232}Th in seawater. *Earth and Planetary Science Letters* 80, 241-251.

Chenet, A.L., Courtillot, V., Fluteau, F., Gérard, M., Quidelleur, X., Khadri, S.F.R., Subbarao, K.V., Thordarson, T., (2009). Determination of rapid Deccan eruptions across the Cretaceous- Tertiary boundary using paleomagnetic secular variation: 2. Constraints from analysis of eight new sections and synthesis for a 3500-m-thick composite section. *Journal of Geophysical Research-Solid Earth*, 114.

Chenet, A.-L., Quidelleur, X., Fluteau, F., Courtillot, V. & Bajpai, S., (2007). ^{40}K–^{40}Ar dating of the Main Deccan large igneous province: Further evidence of KTB age and short duration. *Earth and Planetary Science Letters*, 263(1), 1-15.

Claude, C., Meunier, J.-D., Chabaux, F., Dussouillez, P., Pelt, E., Hamelin, B., Traoré, D., Colin, F., (2016). Timescale of spheroidal weathering of a 293 kyr-old basaltic lava from Réunion Island, Indian Ocean. *Chemical Geology* 446, 110-125.

Clift, P., Gaedicke, C., Edwards, R., Il Lee, J., Hildebrand, P., Amjad, S., White, R., Schlüter, H.-U., (2002). The stratigraphic evolution of the Indus Fan and the history of sedimentation in the Arabian Sea. *Marine Geophysical Researches*, 23(3), 223-245.

Coulombe, C.E., Wilding, L.P., Dixon, J.B., (1996). Overview of Vertisols: characteristics and impacts on society. *Advances in Agronomy*, 57, 289-375.

Courtillot, V., Besse, J., Vandamme, D., Montigny, R., Jaeger, J.-J., Cappetta, H., (1986). Deccan flood basalts at the cretaceous tertiary boundary. *Earth and Planetary Science Letters*, 80(3-4), 361-374.

Courtillot, V., Feraud, G., Maluski, H., Vandamme, D., Moreau, M. G., Besse, J., (1988). Deccan flood basalts and the Cretaceous/Tertiary boundary. *Nature*, 333(6176), 843-846.

Cranston, R.E., Murray, J.W., (1980). Chromium species in the Columbia River and estuary 1. *Limnology and Oceanography*, 25(6), 1104-1112.

Crowe, S.A., Døssing, L. N., Beukes, N. J., Bau, M., Kruger, S. J., Frei, R., Canfield, D. E., (2013). Atmospheric oxygenation three billion years ago. *Nature*, 501(7468), 535-538.

Crutzen, P. J., (2002). The effects of industrial and agricultural practices on atmospheric chemistry and climate during the Anthropocene. *Journal of Environmental Science and Health, Part A*, 37(4), 423-424.

Cucciniello, C., Demonterova, E. I., Sheth, H., Pande, K., Vijayan, A., (2015). $^{40}Ar/^{39}Ar$ geochronology and geochemistry of the Central Saurashtra mafic dyke swarm: insights into magmatic evolution, magma transport, and dyke-flow relationships in the northwestern Deccan Traps. *Bulletin of Volcanology*, 77(5), 45.

D'Arcy, J., Babechuk, M. G., Døssing, L. N., Gaucher, C., Frei, R., (2016). Processes controlling the chromium isotopic composition of river water: Constraints from basaltic river catchments. *Geochimica et Cosmochimica Acta*, 186, 296-315.

Dahlgren, R.A., Boettinger, J.L., Huntington, G.L., Amundson, R.G., (1997). Soil development along an elevational transect in the western Sierra Nevada, California. *Geoderma*, 78(3), 207-236.

Deckers, J., Steinnes, E., (2004). *State of the Art on Soil- Related Geo-medical Issues in the World*, Advances in Agronomy. Academic Press, pp. 1-35.

Delstanche, S., Opfergelt, S., Cardinal, D., Elsass, F., André, L., Delvaux, B., (2009). Silicon isotopic fractionation during adsorption of aqueous monosilicic acid onto iron oxide. *Geochimica et Cosmochimica Acta*, 73(4), 923-934.

Dequincey, O., Chabaux, F., Clauer, N., Sigmarsson, O., Liewig, N., Leprun, J.C., (2002). Chemical mobilizations in laterites: evidence from trace elements and ^{238}U-^{234}U-^{230}Th disequilibria. *Geochimica et Cosmochimica Acta* 66, 1197-1210.

Deshmukh, S., (1980). *Geology, Petrography and Petrochemistry of the Deccan basalts in Parts of Maharashtra State. Regional Petrological Laboratory*, Geological Survey of India, Central Region, Nagpur, 71.

Dickson, A.J., Gill, B.C., Ruhl, M., Jenkyns, H.C., Porcelli, D., Idiz, E., Lyons, T.W. and van den Boorn, S.H., (2017). Molybdenum-isotope chemostratigraphy and paleoceanography of the Toarcian Oceanic Anoxic Event (Early Jurassic). *Paleoceanography*, *32*(8), 813-829.

Dickson, A.J., Cohen, A.S., Coe, A.L., (2012). Seawater oxygenation during the Paleocene-Eocene thermal maximum. *Geology*, 40(7), 639-642.

Dikshit, A., Birthal, P., (2010). India's Livestock Feed Demand: Estimates and Projections. *Agricultural Economics Research Review*, 23(1), 15-28.

Ding, T., Wan, D., Wang, C., Zhang, F., (2004). Silicon isotope compositions of dissolved silicon and suspended matter in the Yangtze River, China. *Geochimica et Cosmochimica Acta*, 68(2), 205-216.

Ding, T.P., Gao, J.F., Tian, S.H., Wang, H.B., Li, M., (2011). Silicon isotopic composition of dissolved silicon and suspended particulate matter in the Yellow River, China, with implications for the global silicon cycle. *Geochimica et Cosmochimica Acta*, 75(21), 6672-6689.

Dissanayake, C. B. & Chandrajith, R., (1999). Medical geochemistry of tropical environments. *Earth-Science Reviews*, 47(3–4), 219-258.

Dolling, P. & Ritchie, G., (1985). Estimates of soil solution ionic strength and the determination of pH in West Australian soils. *Soil Research*, 23(2), 309-314.

Dosseto, A., (2014). Chemical Weathering (U-Series). In: Rink, W.J., Thompson, J. (Eds.) *Encyclopedia of Scientific Dating Methods*. Springer Netherlands, Dordrecht, 1-28.

Dosseto, A., Buss, H.L., Suresh, P., (2012). Rapid regolith formation over volcanic bedrock and implications for landscape evolution. *Earth and Planetary Science Letters* 337, 47-55.

Dosseto, A., Bourdon, B., Turner, S.P., (2008a). Uranium-series isotopes in river materials: Insights into the timescales of erosion and sediment transport. *Earth and Planetary Science Letters* 265, 1-17.

Dosseto, A., Turner, S.P., Chappell, J., (2008b). The evolution of weathering profiles through time: New insights from uranium-series isotopes. *Earth and Planetary Science Letters* 274, 359-371.

Dosseto, A., Bourdon, B., Gaillardet, J., Allègre, C.J., Filizola, N., (2006). Time scale and conditions of weathering under tropical climate: Study of the Amazon basin with U-series. *Geochimica et Cosmochimica Acta* 70, 71-89.

Døssing, L.N., Dideriksen, K., Stipp, S.L.S., Frei, R., (2011). Reduction of hexavalent chromium by ferrous iron: A process of chromium isotope fractionation and its relevance to natural environments. *Chemical Geology*, 285(1-4), 157-166.

Douthitt, C.B., (1982). The geochemistry of the stable isotopes of silicon. *Geochimica et Cosmochimica Acta*, 46(8), 1449-1458.

Douville, E., Sallé, E., Frank, N., Eisele, M., Pons-Branchu, E., Ayrault, S., (2010). Rapid and accurate U–Th dating of ancient carbonates using inductively coupled plasma-quadrupole mass spectrometry. *Chemical Geology* 272, 1-11.

Duckworth, O.W., Akafia, M.M., Andrews, M.Y., Bargar, J.R., (2014). Siderophore-promoted dissolution of chromium from hydroxide minerals. *Environmental Science: Processes & Impacts*, 16(6), 1348-1359.

Duncan, R.A., Pyle, D.G., (1988). Rapid eruption of the Deccan flood basalts at the Cretaceous/Tertiary boundary. *Nature*, 333(6176), 841-843.

Dunk, R. M., Mills, R. A., Jenkins, W. J., (2002). A reevaluation of the oceanic uranium budget for the Holocene. *Chemical Geology*, 190(1–4), 45-67.

Eggins, S., Woodhead, J., Kinsley, L., Mortimer, G., Sylvester, P., McCulloch, M., Hergt, J., Handler, M., (1997). A simple method for the precise determination of ≥ 40 trace elements in geological samples by ICPMS using enriched isotope internal standardisation. *Chemical Geology* 134(4), 311-326.

Ellis, A.S., Johnson, T.M., Bullen, T.D., (2002). Chromium Isotopes and the Fate of Hexavalent Chromium in the Environment. *Science*, 295(5562), 2060-2062.

Engel, J.M., Ma, L., Sak, P.B., Gaillardet, J., Ren, M., Engle, M.A., Brantley, S.L., (2016). Quantifying chemical weathering rates along a precipitation gradient on Basse-Terre Island, French Guadeloupe: New insight from U-series isotopes in weathering rinds. *Geochimica et Cosmochimica Acta* 195, 29-67.

FAO, (2005). *Fertilizer use by crop in India*, FAO, Rome.

Farkaš, J., Chrastný, V., Novák, M., Čadkova, E., Pašava, J., Chakrabarti, R., Jacobsen, S. B., Ackerman, L. & Bullen, T. D., (2013). Chromium isotope variations ($\delta^{53/52}$Cr) in mantle-derived sources and their weathering products: Implications for environmental studies and the evolution of $\delta^{53/52}$Cr in the Earth's mantle over geologic time. *Geochimica et Cosmochimica Acta*, 123, 74-92.

Fedo, C.M., Nesbitt, H.W., Young, G.M., (1995). Unraveling the effects of potassium metasomatism in sedimentary rocks and paleosols, with implications for paleoweathering conditions and provenance. *Geology*, 23(10), 921-924.

Frei, R., Crowe, S. A., Bau, M., Polat, A., Fowle, D. A. & Døssing, L. N., (2016). Oxidative elemental cycling under the low O_2 Eoarchean atmosphere. *Scientific Reports*, 6, 21058.

Frei, R., Gaucher, C., Poulton, S.W., Canfield, D.E., (2009). Fluctuations in Precambrian atmospheric oxygenation recorded by chromium isotopes. *Nature*, 461(7261), 250-253.

Frei, R., Poiré, D., Frei, K.M., (2014). Weathering on land and transport of chromium to the ocean in a subtropical region (Misiones, NW Argentina): A chromium stable isotope perspective. *Chemical Geology*, 381, 110-124.

Frei, R., Polat, A., (2013). Chromium isotope fractionation during oxidative weathering — Implications from the study of a Paleoproterozoic (ca. 1.9 Ga) paleosol, Schreiber Beach, Ontario, Canada. *Precambrian Research*, 224, 434-453.

Fujiwara, A., Kameo, Y., Hoshi, A., Haraga, T., Nakashima, M., (2007). Application of extraction chromatography to the separation of thorium and uranium dissolved in a solution of high salt concentration. *Journal of Chromatography A*, 1140(1), 163-167.

Fyfe, W.S., Kronberg, B.I., Leonardos, O.H., Olorunfemi, N., (1983). Global tectonics and agriculture: A geochemical perspective. Agriculture, Ecosystems & Environment, 9(4), 383-399.

Gadu, A. & Kamber, B.S., (2008). Summary of calibration results for pre-concentration of U and Th in SNO materials, 4p. (not published)

Gallet, S., Jahn, B.-M., Torii, M., (1996). Geochemical characterization of the Luochuan loess-paleosol sequence, China, and paleoclimatic implications. *Chemical Geology*, 133(1–4), 67-88.

Ganerød, M., Torsvik, T. H., van Hinsbergen, D. J. J., Gaina, C., Corfu, F., Werner, S., Owen-Smith, T. M., Ashwal, L. D., Webb, S. J., Hendriks, B. W. H., (2011). Palaeoposition of the Seychelles microcontinent in relation to the Deccan Traps and the Plume Generation Zone in Late Cretaceous-Early Palaeogene time. *Geological Society, London, Special Publications*, 357(1), 229-252.

Ganguly, S., Raya J., Koeberl, C., Sahaad, A., Thönib, M., Balaramd, V., (2014). Geochemistry and petrogenesis of lava flows around Linga, Chhindwara area in the Eastern Deccan Volcanic Province (EDVP), India. *Journal of Asian Earth Sciences*, 91, 174-193.

Geological Map of India, (1993). Scale 1:5,000,000. Geological Survey of India

Georg, R.B., Reynolds, B.C., Frank, M., Halliday, A.N., (2006). Mechanisms controlling the silicon isotopic compositions of river waters. *Earth and Planetary Science Letters*, 249(3–4), 290-306.

Georg, R.B., Reynolds, B.C., West, A.J., Burton, K.W., Halliday, A.N., (2007). Silicon isotope variations accompanying basalt weathering in Iceland. *Earth and Planetary Science Letters*, 261(3–4), 476-490.

Gidigasu M., (2012). *Laterite soil engineering: pedogenesis and engineering principles.* Vol 9: Elsevier.

Green, N., Johnson, D., Wilkins, B., (1996). Factors affecting the transfer of radionuclides to sheep grazing on pastures reclaimed from the sea. *Journal of environmental radioactivity*, 30(2), 173-183.

Gregorio G., Senadhira D., Htut T., (1999). Improving iron and zinc value of rice for human nutrition. *Agriculture et development*, 77-81.

Guinoiseau, D., Gélabert, A., Allard, T., Louvat, P., Moreira-Turcq, P., Benedetti, M. F., (2017). Zinc and copper behaviour at the soil-river interface: New insights by Zn and Cu isotopes in the organic-rich Rio Negro basin. *Geochimica et Cosmochimica Acta*, 213(Supplement C)**,** 178-197.

Halliday, A. N., Lee, D.-C., Christensen, J. N., Walder, A. J., Freedman, P. A., Jones, C. E., Hall, C. M., Yi, W., Teagle, D., (1995). Recent developments in inductively coupled plasma magnetic sector multiple collector mass spectrometry. *International Journal of Mass Spectrometry and Ion Processes*, 146, 21-33.

Hansen, R.O., Stout, P.R., (1968). Isotopic distributions of uranium and thorium in soils. *Soil Science* 105, 44-50.

Hao, J., Sverjensky, D. A., Hazen, R. M., (2017). Mobility of nutrients and trace metals during weathering in the late Archean. *Earth and Planetary Science Letters*, 471, 148-159.

Harris, D., Horwáth, W.R., van Kessel, C., (2001). Acid fumigation of soils to remove carbonates prior to total organic carbon or carbon-13 isotopic analysis. *Soil Science Society of America Journal*, 65(6), 1853-1856.

Hazell, P.B., (2009). *The Asian Green Revolution*. IFPRI Discussion Paper 00911 (Paper Prepared for the Project "Millions Fed: Proven Successes in Agricultural Development"). Washington, DC.

He, Z.L., Yang, X.E., Stoffella, P.J., (2005). Trace elements in agroecosystems and impacts on the environment. *Journal of Trace elements in Medicine and Biology*, 19(2), 125-140.

Henderson, G. M., (2002). Seawater ($^{234}U/^{238}U$) during the last 800 thousand years. *Earth and Planetary Science Letters*, 199(1), 97-110.

Hewawasam T., von Blanckenburg F., Bouchez J., Dixon J.L., Schuessler J.A., Maekeler R., (2013). Slow advance of the weathering front during deep, supply-limited saprolite formation in the tropical Highlands of Sri Lanka. *Geochimica et Cosmochimica Acta*, 118, 202-230.

Hillier, S., (2002). Quantitative analysis of clay and other minerals in sandstones by X-ray powder diffraction (XRPD). In: Worden, R. and Sadoon, M. (eds) *Clay Mineral Cements in Sandstones (Special Publication 34 of the IAS)*. Wiley-Blackwell, 520 pages.

Holmden, C., Jacobson, A.D., Sageman, B.B., Hurtgen, M.T., (2016). Response of the Cr isotope proxy to Cretaceous Ocean Anoxic Event 2 in a pelagic carbonate succession from the Western Interior Seaway. *Geochimica et Cosmochimica Acta* 186, 277-295.

Hooper, P., Widdowson, M., Kelley, S., (2010). Tectonic setting and timing of the final Deccan flood basalt eruptions. *Geology*, 38(9), 839-842.

Horneck, D.A., Sullivan, D.M., Owen, J.S., Hart, J.M., (2011). *Soil test interpretation guide*, [Corvallis, Or.]: Oregon State University, Extension Service.

Hotz, C. & Brown, K. H., (2004). Assessment of the risk of zinc deficiency in populations and options for its control. *Food & Nutrition Bulletin*, 25 (2), 94-204.

Houben, D., Sonnet, P., Tricot, G., Mattielli, N., Couder, E., Opfergelt, S., (2014). Impact of Root-Induced Mobilization of Zinc on Stable Zn Isotope Variation in the Soil–Plant System. *Environmental Science & Technology*, 48(14), 7866-7873.

Howarth, S., Prytulak, J., Little, S.H., Hammond, S.J. and Widdowson, M. (2018). Thallium concentration and thallium isotope composition of lateritic terrains. *Geochimica et Cosmochimica Acta*, in press.

Huckle, D., Ma, L., McIntosh, J., Vázquez-Ortega, A., Rasmussen, C., Chorover, J., (2016). U-series isotopic signatures of soils and headwater streams in a semi-arid complex volcanic terrain. *Chemical Geology*, 445, 68-83.

Hughes, H.J., Sondag, F., Santos, R.V., André, L., Cardinal, D., (2013). The riverine silicon isotope composition of the Amazon Basin. *Geochimica et Cosmochimica Acta*, 121, 637-651.

Izbicki, J.A., Ball, J.W., Bullen, T.D., Sutley, S.J., (2008). Chromium, chromium isotopes and selected trace elements, western Mojave Desert, USA. *Applied Geochemistry*, 23(5), 1325-1352.

Jackson M.L., Sherman G.D., (1953). Chemical Weathering of Minerals in Soils. In: Norman AG, (ed). *Advances in Agronomy*. 5. Academic Press, 1953, 219-318.

Jay, A.E., Mac Niocaill, C., Widdowson, M., Self, S., Turner, W., (2009). New palaeomagnetic data from the Mahabaleshwar Plateau, Deccan Flood Basalt Province, India: implications for the volcanostratigraphic architecture of continental flood basalt provinces. *Journal of the Geological Society*, 166, 13-24.

Jay, A.E., Widdowson, M., (2008). Stratigraphy, structure and volcanology of the SE Deccan continental flood basalt province: implications for eruptive extent and volumes. *Journal of the Geological Society*, 165, 177-188.

Jin, L., Ravella, R., Ketchum, B., Bierman, P. R., Heaney, P., White, T., Brantley, S. L., (2010). Mineral weathering and elemental transport during hillslope evolution at

the Susquehanna/Shale Hills Critical Zone Observatory. *Geochimica et Cosmochimica Acta*, 74(13), 3669-3691.

Jost, A.B., Bachan, A., van de Schootbrugge, B., Brown, S.T., DePaolo, D.J., Payne, J.L., (2017). Additive effects of acidification and mineralogy on calcium isotopes in Triassic/Jurassic boundary limestones. *Geochemistry, Geophysics, Geosystems*, *18*(1), 113-124.

Jouvin, D., Louvat, P., Juillot, F., Marechal, C., Benedetti, M., (2009). Zinc isotopic fractionation : why organic matters ? *Environmental Science & Technology*, 43, 5747-5754.

Juillot, F., Maréchal, C., Ponthieu, M., Cacaly, S., Morin, G., Benedetti, M., Hazemann, J. L., Proux, O., Guyot, F., (2008). Zn isotopic fractionation caused by sorption on goethite and 2-Lines ferrihydrite. *Geochimica et Cosmochimica Acta*, 72(19), 4886-4900.

Kabata-Pendias, A., (2010). *Trace elements in soils and plants*, 4. CRC press, Boca Raton, FL

Kale, V. S., (2002). Fluvial geomorphology of Indian rivers: an overview. *Progress in Physical Geography,* 26(3), 400-433.

Kamber, B.S., (2009). Geochemical fingerprinting: 40 years of analytical development and real world applications. *Applied Geochemistry*, 24(6): 1074-1086.

Katyal, J.C., Rao, N.H., Reddy, M.N., (2001). Critical aspects of organic matter management in the Tropics: the example of India. In: Martius, C., Tiessen, H., Vlek, P.L.G. (Eds.), *Managing Organic Matter in Tropical Soils: Scope and Limitations*: Proceedings of a Workshop organized by the Center for Development Research at the University of Bonn (ZEF Bonn) — Germany, 7–10 June, 1999. Springer Netherlands, Dordrecht, pp. 77-88.

Katyal, J.C., Sharma, B.D., (1991). DTPA-extractable and total Zn, Cu, Mn, and Fe in Indian soils and their association with some soil properties. *Geoderma*, 49(1), 165-179.

Keech, A.R., West, A.J., Pett-Ridge, J.C., Henderson, G.M., (2013). Evaluating U-series tools for weathering rate and duration on a soil sequence of known ages. *Earth and Planetary Science Letters* 374, 24-35.

Kelley, S., (2007). The geochronology of large igneous provinces, terrestrial impact craters, and their relationship to mass extinctions on Earth. *Journal of the Geological Society*, 164, 923-936.

Kigoshi, K., (1971). Alpha-Recoil Thorium-234: Dissolution into Water and the Uranium-234/Uranium-238 Disequilibrium in Nature. *Science,* 173(3991), 47-48.

Kısakürek, B., Widdowson, M., James, R. H., (2004). Behaviour of Li isotopes during continental weathering: the Bidar laterite profile, India. *Chemical Geology,* 212(1–2), 27-44.

Klootwijk, C. T. & Peirce, J. W., (1979). India's and Australia's pole path since the late Mesozoic and the India-Asia collision. *Nature,* 282(5739), 605-607.

Kokfelt, T.F., Hoernle, K., Hauff, F., (2003). Upwelling and melting of the Iceland plume from radial variation of 238U–230Th disequilibria in postglacial volcanic rocks. *Earth and Planetary Science Letters* 214, 167-186.

Krauskopf, K. B. & Bird, D. K., (1967). *Introduction to geochemistry*: McGraw-Hill New York.

Kronberg B.I., Nesbitt H.W., (1981). Quantification of weathering, soil geochemistry and soil fertility. *Journal of Soil Science*, 32, 453-459.

Kronberg, B., Fyfe, W., Leonardos, O., Santos, A., (1979). The chemistry of some Brazilian soils: element mobility during intense weathering. *Chemical Geology*, 24(3-4)**,** 211-229.

Kühn P, Aguilar J. & Miedema R., (2010). *Textural pedofeatures and related horizons. Interpretation of micromorphological features of soils and regoliths*. Elsevier, Oxford, 217-250.

Kuldeep, S., (2009). *The critical zinc deficiency levels in Indian soils and cereal crops.* In: The Proceedings of the International Plant Nutrition Colloquium XVI. UC Davis.

Kurtz, A. C., Derry, L. A., Chadwick, O. A. & Alfano, M. J., (2000). Refractory element mobility in volcanic soils. *Geology*, 28(8), 683-686.

Landrot, G., Ginder-Vogel, M., Sparks, D.L., (2010). Kinetics of Chromium(III) Oxidation by Manganese(IV) Oxides Using Quick Scanning X-ray Absorption Fine Structure Spectroscopy (Q-XAFS). *Environmental Science & Technology*, 44(1), 143-149.

Li, M., He, Y.-S., Kang, J.-T., Yang, X.-Y., He, Z.-W., Yu, H.-M., Huang, F., (2017). Why was iron lost without significant isotope fractionation during the lateritic process in tropical environments? *Geoderma*, 290, 1-9.

Lin H., Bouma J., Wilding L., Richardson J., Kutilek M., Nielsen D., (2005). Advances in hydropedology. *Advances in agronomy*, 85, 1-89.

Lindsay, W.L. & Norvell, W.A., (1978). Development of a DTPA soil test for zinc, iron, manganese, and copper. Soil science society of America journal, 42(3): 421-428.

Little, S. H., Vance, D., McManus, J., Severmann, S., (2016). Key role of continental margin sediments in the oceanic mass balance of Zn and Zn isotopes. *Geology*, 44(3), 207-210.

Little, S. H., Vance, D., Walker-Brown, C., Landing, W. M., (2014). The oceanic mass balance of copper and zinc isotopes, investigated by analysis of their inputs, and outputs to ferromanganese oxide sediments. *Geochimica et Cosmochimica Acta*, 125, 673-693.

Luck, J.-M., Othman, D. B., Albarède, F., (2005). Zn and Cu isotopic variations in chondrites and iron meteorites: Early solar nebula reservoirs and parent-body processes. *Geochimica et Cosmochimica Acta*, 69(22), 5351-5363.

Ma, L., Chabaux, F., Pelt, E., Blaes, E., Jin, L., Brantley, S., (2010). Regolith production rates calculated with uranium-series isotopes at Susquehanna/Shale Hills Critical Zone Observatory. *Earth and Planetary Science Letters* 297, 211-225.

Ma, L., Chabaux, F., Pelt, E., Granet, M., Sak, P.B., Gaillardet, J., Lebedeva, M., Brantley, S.L., (2012). The effect of curvature on weathering rind formation: Evidence from Uranium-series isotopes in basaltic andesite weathering clasts in Guadeloupe. *Geochimica et Cosmochimica Acta*, 80, 92-107.

Ma, L., Chabaux, F., West, N., Kirby, E., Jin, L., Brantley, S., (2013). Regolith production and transport in the Susquehanna Shale Hills Critical Zone Observatory, Part 1: Insights from U-series isotopes. *Journal of Geophysical Research: Earth Surface*, 118, 722-740.

Mann, A.W., (1984). Mobility of gold and silver in lateritic weathering profiles; some observations from Western Australia. *Economic Geology*, 79(1), 38-49.

Maréchal, C. N., Télouk, P., Albarède, F., (1999). Precise analysis of copper and zinc isotopic compositions by plasma-source mass spectrometry. *Chemical Geology*, 156(1-4)**,** 251-273.

Maret, W., (2016). The Metals in the Biological Periodic System of the Elements: Concepts and Conjectures. *International Journal of Molecular Sciences*, 17(1), 66.

Mathieu, D., Bernat, M., Nahon, D., (1995). Short-lived U and Th isotope distribution in a tropical laterite derived from granite (Pitinga river basin, Amazonia, Brazil): Application to assessment of weathering rate. *Earth and Planetary Science Letters* 136, 703-714.

McBride, M.B. & Spiers, G., (2001). Trace element content of selected fertilizers and dairy manures as determined by ICP–MS. *Communications in Soil Science and Plant Analysis*, 32(1-2), 139-156.

McClain, C.N., Maher, K., (2016). Chromium fluxes and speciation in ultramafic catchments and global rivers. *Chemical Geology*, 426, 135-157.

McLennan, S. M., (2001). Relationships between the trace element composition of sedimentary rocks and upper continental crust. *Geochemistry, Geophysics, Geosystems,* 2(4), n/a-n/a.

McLennan, S.M., (1993). Weathering and Global Denudation. *The Journal of Geology*, 101(2), 295-303.

Meng, F., Wei, Y., Yang, X., (2005). Iron content and bioavailability in rice. *Journal of Trace Elements in Medicine and Biology,* 18(4), 333-338.

Menozzi, D., Dosseto, A., Kinsley, L.P.J., (2016). Assessing the effect of sequential extraction on the uranium-series isotopic composition of a basaltic weathering profile. *Chemical Geology,* 446, 126-137.

Ministry of Agriculture Department of Animal Husbandry Dairying and Fisheries Krishi Bhawan, (2012). *Livestock Census—2012 All India Report*. Ministry of Agriculture Department of Animal Husbandry Dairying and Fisheries Krishi Bhawan, New Delhi

Mitchell, C. & Widdowson, M., (1991). A geological map of the southern Deccan Traps, India and its structural implications. *Journal of the Geological Society,* 148(3), 495-505.

Moeller, K., Schoenberg, R., Pedersen, R., Weiss, D., Dong, S., (2012). Calibration of the new certified reference material ERM-AE633 and ERM-AE647 for copper and IRMM-3702 for zinc isotope amount ratio determinations. *Geostandards and Geoanalytical Research,* 36(2), 177-199.

Molnar, P. & Stock, J. M., (2009). Slowing of India's convergence with Eurasia since 20 Ma and its implications for Tibetan mantle dynamics. *Tectonics,* 28(3), n/a-n/a.

Moragues-Quiroga, C., Juilleret, J., Gourdol, L., Pelt, E., Perrone, T., Aubert, A., Morvan, G., Chabaux, F., Legout, A., Stille, P., Hissler, C., (2017). Genesis and evolution of regoliths: Evidence from trace and major elements and Sr-Nd-Pb-U isotopes. *Catena* 149, Part 1, 185-198.

Moreira-Nordemann, L.M., (1980). Use of $^{234}U/^{238}U$ disequilibrium in measuring chemical weathering rate of rocks. *Geochimica et Cosmochimica Acta* 44, 103-108.

Moynier, F., Vance, D., Fujii, T. & Savage, P., (2017). The Isotope Geochemistry of Zinc and Copper. *Reviews in Mineralogy and Geochemistry,* 82(1), 543-600.

Nagarajan, R., Madhavaraju, J., Nagendra, R., Armstrong Altrin, J.S., Moutte, J., (2007). Geochemistry of Neoproterozoic shales of the Rabanpalli Formation, Bhima Basin, Northern Karnataka, southern India: implications for provenance and paleoredox conditions. *Revista Mexicana de Ciencias Geológicas*, 24(2).

Nageswara Rao, V., Rego, T., Myers, R., (1997). Balanced fertiliser use in black soils. *Fertiliser news*, 42(4), 35-45.

Narwal, R., Kumar, R., Antil, R., (2010). *Long-term effect of farmyard manure and N on the distribution of zinc and copper in soil fractions under pearl millet–wheat cropping system*, 19th World Congress of Soil Science.

National Research Council, (2001). *Basic research opportunities in earth science*. Washington, DC, national academies Press.

Nesbitt, H. W. & Wilson, R. E., (1992). Recent chemical weathering of basalts. *American Journal of Science*, 292(10), 740-777.

Nesbitt, H. W. & Young, G. M., (1982). Early Proterozoic climates and plate motions inferred from major element chemistry of lutites. *Nature*, 299(5885), 715-717.

Nesbitt, H.W., Markovics, G., Price, R.C., (1980). Chemical processes affecting alkalis and alkaline earths during continental weathering. *Geochimica et Cosmochimica Acta*, 44(11), 1659-1666.

Newbold, T.J., (1843). On the régar or black cotton soil of India. Abstracts of the Papers Printed in the *Philosophical Transactions of the Royal Society of London*, 4, 53-54.

Noack, Y., Colin, F., Nahon, D., Delvigne, J., Michaux, L., (1993). Secondary-mineral formation during natural weathering of pyroxene; review and thermodynamic approach. *American Journal of Science*, 293(2), 111-134.

Oelze, M., von Blanckenburg, F., Bouchez, J., Hoellen, D., Dietzel, M., (2015). The effect of Al on Si isotope fractionation investigated by silica precipitation experiments. *Chemical Geology*, 397, 94-105.

Oelze, M., von Blanckenburg, F., Hoellen, D., Dietzel, M., Bouchez, J., (2014). Si stable isotope fractionation during adsorption and the competition between kinetic and equilibrium isotope fractionation: Implications for weathering systems. *Chemical Geology*, 380, 161-171.

Opfergelt, S., Cornélis, J. T., Houben, D., Givron, C., Burton, K. W., Mattielli, N., (2017). The influence of weathering and soil organic matter on Zn isotopes in soils. *Chemical Geology*, 466, 140-148.

Opfergelt, S., de Bournonville, G., Cardinal, D., André, L., Delstanche, S., Delvaux, B., (2009). Impact of soil weathering degree on silicon isotopic fractionation during adsorption onto iron oxides in basaltic ash soils, Cameroon. *Geochimica et Cosmochimica Acta*, 73(24), 7226-7240.

Opfergelt, S. & Delmelle, P., (2012). Silicon isotopes and continental weathering processes: Assessing controls on Si transfer to the ocean. *Comptes Rendus Geoscience*, 344(11–12), 723-738.

Pal, D.K., Wani, S.P., Sahrawat, K.L., (2012). Vertisols of tropical Indian environments: Pedology and edaphology. *Geoderma*, 189-190, 28-49.

Pal, D.K., Bhattacharyya, T., Chandran, P., Ray, S.K., Satyavathi, P.L.A., Durge, S.L., Raja, P., Maurya, U.K., (2009). Vertisols (cracking clay soils) in a climosequence of Peninsular India: evidence for Holocene climate changes. *Quaternary International*, 209(1-2), 6-21.

Pal, D., Dasog, G., Vadivelu, S., Ahuja, R., Bhattacharyya, T., (2000). Secondary calcium carbonate in soils of arid and semi-arid regions of India. *Global climate change and pedogenic carbonates*, 149-185.

Pal, D. & Deshpande, S., (1987). Characteristics and genesis of minerals in some benchmark Vertisols of India. *Pedologie*, 37(3), 259-275.

Partin, C.A., Bekker, A., Planavsky, N. J., Scott, C. T., Gill, B. C., Li, C., Podkovyrov, V., Maslov, A., Konhauser, K. O., Lalonde, S. V., Love, G. D., Poulton, S. W., Lyons, T. W., (2013). Large-scale fluctuations in Precambrian atmospheric and oceanic oxygen levels from the record of U in shales. *Earth and Planetary Science Letters* 369-370, 284-293.

Patino, L.C., Velbel, M.A., Price, J.R., Wade, J.A., (2003). Trace element mobility during spheroidal weathering of basalts and andesites in Hawaii and Guatemala. *Chemical Geology*, 202(3–4), 343-364.

Paton, C., Hellstrom, J., Paul, B., Woodhead, J., Hergt, J., (2011). Iolite: Freeware for the visualisation and processing of mass spectrometric data. *Journal of Analytical Atomic Spectrometry*, 26(12): 2508-2518.

Paulukat, C., Døssing, L.N., Mondal, S.K., Voegelin, A.R., Frei, R., (2015). Oxidative release of chromium from Archean ultramafic rocks, its transport and environmental impact – A Cr isotope perspective on the Sukinda valley ore district (Orissa, India). *Applied Geochemistry*, 59, 125-138.

Pelt, E., Chabaux, F., Innocent, C., Navarre-Sitchler, A.K., Sak, P.B., Brantley, S.L., (2008). Uranium–thorium chronometry of weathering rinds: Rock alteration rate and paleo-isotopic record of weathering fluids. *Earth and Planetary Science Letters*, 276, 98-105.

Pelt, E., Chabaux, F., Stille, P., Innocent, C., Ghaleb, B., Gérard, M., Guntzer, F., (2013). Atmospheric dust contribution to the budget of U-series nuclides in soils from the Mount Cameroon volcano. *Chemical Geology*, 341, 147-157.

Penney, D., (2004). The micronutrient and trace element status of forty-three soil quality benchmark sites in Alberta. *AESA Soil Quality Monitoring Program*.

Perez-Espinosa, A., Moral, R., Moreno-Caselles, J., Cortés, A., Perez-Murcia, M., Gomez, I., (2005). Co phytoavailability for tomato in amended calcareous soils. *Bioresource technology*, 96(6), 649-655.

Peters, J., Combs, S., Hoskins, B., Jarman, J., Kovar, J., Watson, M., Wolf, A., Wolf, N., (2003). *Recommended methods of manure analysis*. University of Wisconsin Cooperative Extension Publishing: Madison, WI.

Pett-Ridge, J.C., Monastra, V.M., Derry, L.A., Chadwick, O.A., (2007). Importance of atmospheric inputs and Fe-oxides in controlling soil uranium budgets and behavior along a Hawaiian chronosequence. *Chemical Geology*, 244, 691-707.

Pettygrove, G., Heinrich, A., Eagle, A., (2010). *Dairy manure nutrient content and forms.* Manure Technical Guide Series. Davis: University of California Cooperative Extension.

Plater, A.J., Dugdale, R.E., Ivanovich, M., (1988). The application of uranium series disequilibrium concepts to sediment yield determination. *Earth Surface Processes and Landforms*, 13, 171-182.

Pointurier, F., Hubert, A., Baglan, N., Hémet, P., (2008). Evaluation of a new generation quadrupole-based ICP-MS for uranium isotopic measurements in environmental samples. *Journal of Radioanalytical and Nuclear Chemistry*, 276, 505-511.

Poitrasson, F., (2017). Silicon Isotope Geochemistry. *Reviews in Mineralogy and Geochemistry*, 82(1), 289-344.

Poitrasson, F., Viers, J., Martin, F., Braun, J.-J., (2008). Limited iron isotope variations in recent lateritic soils from Nsimi, Cameroon: Implications for the global Fe geochemical cycle. *Chemical Geology*, 253(1–2), 54-63.

Pokrovsky, O. S., Viers, J., Freydier, R., (2005). Zinc stable isotope fractionation during its adsorption on oxides and hydroxides. *Journal of Colloid and Interface Science*, 291(1), 192-200.

Prabhakar, B., Jayananda, M., Shareef, M., Kano, T., (2009). Petrology and geochemistry of late archaean granitoids in the northern part of Eastern Dharwar Craton, Southern India: Implications for transitional geodynamic setting. *Journal of the Geological Society of India*, 74(3), 299-317.

Prasad, A. S., (2012). Discovery of human zinc deficiency: 50 years later. *Journal of Trace Elements in Medicine and Biology*, 26(2–3), 66-69.

Prashanth, L., Kattapagari, K. K., Chitturi, R. T., Baddam, V. R. R., Prasad, L. K., (2015). A review on role of essential trace elements in health and disease. *Journal of Dr. NTR University of Health Sciences*, 4(2), 75.

Prytulak, J., Elliott, T., Hoffmann, D.L., Coath, C.D., (2008). Assessment of USGS BCR-2 as a Reference Material for Silicate Rock U-Pa Disequilibrium Measurements. *Geostandards and Geoanalytical Research*, 32, 55-63.

Qin, L., Wang, X., (2017). Chromium Isotope Geochemistry. *Reviews in Mineralogy and Geochemistry*, 82(1), 379-414.

Ray D.K., Mueller N.D., West P.C., Foley J.A., (2013). Yield trends are insufficient to double global crop production by 2050. *PloS one*, 8, e66428.

Reeder, S., Taylor, H., Shaw, R., Demetriades, A., (2006). Introduction to the chemistry and geochemistry of the elements. T. Tarvainen, M. de Vos (Eds.), *Geochemical Atlas of Europe. Part 2. Interpretation of Geochemical Maps, Additional Tables, Figures, Maps, and Related Publications*, Geological Survey of Finland, Espoo, pp. 48-429.

Reinhard, C. T., Planavsky, N. J., Robbins, L. J., Partin, C. A., Gill, B. C., Lalonde, S. V., Bekker, A., Konhauser, K. O., Lyons, T. W., (2013). Proterozoic ocean redox and biogeochemical stasis. *Proceedings of the National Academy of Sciences*, 110(14), 5357-5362.

Renne, P. R., Deino, A. L., Hilgen, F. J., Kuiper, K. F., Mark, D. F., Mitchell, W. S., Morgan, L. E., Mundil, R., Smit, J., (2013). Time Scales of Critical Events Around the Cretaceous-Paleogene Boundary. *Science*, 339(6120), 684-687.

Retallack, G.J., (2010). Lateritization and Bauxitization Events. *Economic Geology*, 105(3), 655-667.

Reynolds, B. C., Aggarwal, J., Andre, L., Baxter, D., Beucher, C., Brzezinski, M. A., Engström, E., Georg, R. B., Land, M., Leng, M. J., (2007). An inter-laboratory

comparison of Si isotope reference materials. *Journal of Analytical Atomic Spectrometry*, 22(5), 561-568.

Rezzoug, S., Fernex, F., Michel, H., Barci-Funel, G., Barci, V., (2009). Behavior of uranium and thorium isotopes in soils of the Boréon area, Mercantour Massif (S.E. France): Leaching and weathering rate modeling. *Journal of Radioanalytical and Nuclear Chemistry*, 279, 801-809.

Richards, F. D., Hoggard, M. J., White, N. J., (2016). Cenozoic epeirogeny of the Indian peninsula. *Geochemistry, Geophysics, Geosystems*, 17(12), 4920-4954.

Robson, A. & Gilkes, R. Fertilizer responses (N, P, K, S, micronutrients) on lateritic soils in southwestern Australia—a review. International Seminar on Laterization Processes, (1980). Oxford and IBH Publishing Co. Oxford, England, 381-390.

Rosholt, J.N., Doe, B.R., Tatsumoto, M., (1966). Evolution of the isotopic composition of uranium and thorium in soil profiles. *Bulletin of the Geological Society of America* 77, 987-1004.

Roy, A., (2012). Indian Shield: insight into the pristine size, shape and tectonic framework. *Indian Journal of Geoscience*, 66, 181-192.

Rudnick, R.L., Gao, S., (2003). Composition of the Continental Crust. In: Heinrich, D.H., Karl, K.T. (Eds.), *Treatise on Geochemistry*. Pergamon, Oxford, pp. 1-64.

Sakal, R., Singh, A., Sinha, R., Bhogal, N., (1996). *Twenty five years of research on micro and secondary nutrients in soils and crops of Bihar*. RAU, Pusa, Bihar: 1-208.

Sano, T., Fujii, T., Deshmukh, S., Fukuoka, T., Aramaki, S., (2001). Differentiation processes of Deccan Trap basalts: contribution from geochemistry and experimental petrology. *Journal of Petrology*, 42(12), 2175-2195.

Savage, P.S., Armytage, R.M.G., Georg, R.B., Halliday, A.N., (2014). High temperature silicon isotope geochemistry. *Lithos*, 190, 500-519.

Savage, P.S., Georg, R.B., Armytage, R.M.G., Williams, H.M., Halliday, A.N., (2010). Silicon isotope homogeneity in the mantle. *Earth and Planetary Science Letters*, 295(1–2), 139-146.

Savage, P.S., Georg, R.B., Williams, H.M., Burton, K.W., Halliday, A.N., (2011). Silicon isotope fractionation during magmatic differentiation. *Geochimica et Cosmochimica Acta*, 75(20), 6124-6139.

Savage, P.S., Georg, R.B., Williams, H.M., Halliday, A.N., (2013). The silicon isotope composition of the upper continental crust. *Geochimica et Cosmochimica Acta*, 109, 384-399.

Schauble, E., Rossman, G.R., Taylor Jr, H.P., (2004). Theoretical estimates of equilibrium chromium-isotope fractionations. *Chemical Geology*, 205(1–2), 99-114.

Scheiderich, K., Amini, M., Holmden, C., Francois, R., (2015). Global variability of chromium isotopes in seawater demonstrated by Pacific, Atlantic, and Arctic Ocean samples. *Earth and Planetary Science Letters*, 423, 87-97.

Schellmann, W., (1986). A new definition of laterite. In: Banerji, P.K. (Ed.), Lateritisation Processes, *Memoirs of the Geological Survey of India*, 1–7.

Schmidt, P. W., Prasad, V. & Ramam, P. K., (1983). Magnetic ages of some Indian laterites. *Palaeogeography, Palaeoclimatology, Palaeoecology*, 44(3–4), 185-202.

Schoenberg, R., Merdian, A., Holmden, C., Kleinhanns, I. C., Haßler, K., Wille, M., Reitter, E., (2016). The stable Cr isotopic compositions of chondrites and silicate planetary reservoirs. *Geochimica et Cosmochimica Acta*, 183, 14-30.

Schoenberg, R., Zink, S., Staubwasser, M., von Blanckenburg, F., (2008). The stable Cr isotope inventory of solid Earth reservoirs determined by double spike MC-ICP-MS. *Chemical Geology*, 249(3-4), 294-306.

Schoene, B., Samperton, K. M., Eddy, M. P., Keller, G., Adatte, T., Bowring, S. A., Khadri, S. F. R., Gertsch, B., (2015). U-Pb geochronology of the Deccan Traps and relation to the end-Cretaceous mass extinction. *Science,* 182-184.

Schwertmann, U., Gasser, U., Sticher, H., (1989). Chromium-for-iron substitution in synthetic goethites. *Geochimica et Cosmochimica Acta*, 53(6), 1293-1297.

Schwertmann, U., Pfab, G., (1996). Structural vanadium and chromium in lateritic iron oxides: Genetic implications. *Geochimica et Cosmochimica Acta*, 60(21), 4279-4283.

Sharma, B., Mukhopadhyay, S., Katyal, J., (2006). Distribution of Total and DTPA-Extractable Zinc, Copper, Manganese, and Iron in Vertisols of India. *Communications in soil science and plant analysis*, 37(05-06), 653-672.

Shen, C.-C., Lin, H.-T., Chu, M.-F., Yu, E.-F., Wang, X., Dorale, J.A., (2006). Measurements of natural uranium concentration and isotopic composition with permil-level precision by inductively coupled plasma–quadrupole mass spectrometry. *Geochemistry, Geophysics, Geosystems* 7, n/a-n/a.

Sheth, H., Ray, J., Ray, R., Vanderkluysen, L., Mahoney, J., Kumar, A., Shukla, A., Das, P., Adhikari, S., Jana, B., (2009). Geology and geochemistry of Pachmarhi dykes and sills, Satpura Gondwana Basin, central India: problems of dyke-sill-flow correlations in the Deccan Traps. *Contributions to Mineralogy and Petrology* 158, 357-380.

Sillanpää, M., (1982). *Micronutrients and the nutrient status of soils: a global study.* Food & Agriculture Organisation (FAO).

Simonson, R.W., (1954). Morphology and classification of the Regur soils of India. *European Journal of Soil Science,* 5(2), 275-288.

Sims, K.W.W., Gill, J.B., Dosseto, A., Hoffmann, D.L., Lundstrom, C.C., Williams, R.W., Ball, L., Tollstrup, D., Turner, S., Prytulak, J., Glessner, J.J.G., Standish, J.J., Elliott, T., (2008). An Inter-Laboratory Assessment of the Thorium Isotopic Composition of Synthetic and Rock Reference Materials. *Geostandards and Geoanalytical Research* 32, 65-91.

Singh M.V., (2008). Micronutrient Deficiencies in Crops and Soils in India. In: Alloway B.J., editor. *Micronutrient Deficiencies in Global Crop Production*. Springer Netherlands, Dordrecht, 2008, 93-125.

Singh, M., (2001). Evaluation of current micronutrient stocks in different agro-ecological zones of India for sustainable crop production. *Fertiliser News*, 46(2), 25-42.

Singh, M.V., Abrol, I.P., (1986). Transformation and movement of zinc in an alkali soil and their influence on the yield and uptake of zinc by rice and wheat crops. Plant and Soil, 94(3), 445-449.

Singh, S. P., Gruissem, W., Bhullar, N. K., (2017). Single genetic locus improvement of iron, zinc and β-carotene content in rice grains. *Scientific Reports,* 7(1)**,** 6883.

Sossi, P. A., Halverson, G. P., Nebel, O., Eggins, S. M., (2015). Combined Separation of Cu, Fe and Zn from Rock Matrices and Improved Analytical Protocols for Stable Isotope Determination. *Geostandards and Geoanalytical Research,* 39(2), 129-149.

Spicer, R., Yang, J., Herman, A., Kodrul, T., Aleksandrova, G., Maslova, N., Spicer, T., Ding, L., Xu, Q., Shukla, A., Srivastava, G., Mehrotra, R., Liu, X.-Y., Jin, J.-H., (2017). Paleogene monsoons across India and South China: Drivers of biotic change. *Gondwana Research,* 49(Supplement C), 350-363.

Srinivasarao, C., Gayatri, S. R., Venkateswarlu, B., Jakkula, V., Wani, S., Kundu, S., Sahrawat, K., Rao, B. R., Marimuthu, S., Krishna, G. G., (2014). Heavy metals concentration in soils under rainfed agro-ecosystems and their relationship with soil properties and management practices. *International Journal of Environmental Science and Technology*, 11(7), 1959-1972.

Starkey H.C., Blackmon P.D., Hauff P.L., (1984*). The routine mineralogical analysis of clay-bearing samples*. US Geological Survey Bulletin 1563, 32pp.

Styles, D., Gibbons, J., Williams, A.P., Stichnothe, H., Chadwick, D.R., Healey, J.R., 2015. Cattle feed or bioenergy? Consequential life cycle assessment of biogas feedstock options on dairy farms. Gcb Bioenergy, 7(5), 1034-1049.

Suhr, N., Schoenberg, R., Chew, D., Rosca, C., Widdowson, M., Kamber, B. S., (2018a). Elemental and isotopic behaviour of Zn in Deccan basalt weathering profiles: Chemical weathering from bedrock to laterite and links to Zn deficiency in tropical soils. *Science of The Total Environment*, 619–620, 1451-1463.

Suhr, N., Widdowson, M., McDermott, F., Kamber, B.S., (2018b). Th/U and U series systematics of saprolite: importance for the oceanic 234U excess. Geochemical Perspectives Letters, 6, 17-22.

Suresh, P.O., Dosseto, A., Hesse, P.P., Handley, H.K., (2013). Soil formation rates determined from Uranium-series isotope disequilibria in soil profiles from the southeastern Australian highlands. *Earth and Planetary Science Letters*, 379, 26-37.

Taboada, T., Cortizas, A.M., García, C., García-Rodeja, E., (2006). Particle-size fractionation of titanium and zirconium during weathering and pedogenesis of granitic rocks in NW Spain. *Geoderma*, 131(1), 218-236.

Takkar, P., Singh, M., Ganeshmurthy, A., (1997). Micronutrient deficiency and fertilizer requirement by 2025, *Proceedings of national symposium on plant nutrient needs, supply, efficiency and policy issues for 2000-2025*, NAAS, New Dehli, 218-224.

Tandon, H., (1997). Organic resources: An assessment of potential supplies, their contribution to agricultural productivity and policy issues for Indian agriculture for 2000 to 2025. Plant Needs Supply, Efficiency and Policy Issues, National Academy of Agricultural Sciences, New Delhi, 15-28.

Tang, Y., Webb, S.M., Estes, E.R., Hansel, C.M., (2014). Chromium(iii) oxidation by biogenic manganese oxides with varying structural ripening. *Environmental Science: Processes & Impacts*, 16(9), 2127-2136.

Taylor, S. R. & McLennan, S. M. & McCulloch, M. T., (1983). Geochemistry of loess, continental crustal composition and crustal model ages. *Geochimica et Cosmochimica Acta*, 47(11), 1897-1905.

Taylor, S.R. & McLennan, S.M., (1995). The geochemical evolution of the continental crust. *Reviews of Geophysics*, 33, 241-265.

Them, T.R., Gill, B.C., Caruthers, A.H., Gerhardt, A.M., Gröcke, D.R., Lyons, T.W., Marroquín, S.M., Nielsen, S.G., Alexandre, J.P.T., Owens, J.D., (2018). Thallium isotopes reveal protracted anoxia during the Toarcian (Early Jurassic) associated with volcanism, carbon burial, and mass extinction. *Proceedings of the National Academy of Sciences*, 201803478.

Them, T.R., Gill, B.C., Selby, D., Gröcke, D.R., Friedman, R.M. and Owens, J.D., 2017. Evidence for rapid weathering response to climatic warming during the Toarcian Oceanic Anoxic Event. *Scientific Reports*, 7(1), 5003.

Thornton, I. & Abrahams, P., (1983). Soil ingestion—a major pathway of heavy metals into livestock grazing contaminated land. *Science of the Total Environment*, 28(1-3), 287-294.

Tréguer, P.J. & Rocha, C.L., (2013). The World Ocean Silica Cycle. *Annual Review of Marine Science*, 5(1), 477-501.

Ubide, T., McKenna, C.A., Chew, D.M., Kamber, B.S., (2015). High-resolution LA-ICP-MS trace element mapping of igneous minerals: In search of magma histories. *Chemical Geology*, 409(Supplement C), 157-168.

van den Boorn, S. H., Vroon, P. Z., van Belle, C. C., van der Wagt, B., Schwieters, J., van Bergen, M. J., (2006). Determination of silicon isotope ratios in silicate materials by high-resolution MC-ICP-MS using a sodium hydroxide sample digestion method. *Journal of Analytical Atomic Spectrometry*, 21(8), 734-742.

van den Boorn, S.H.J.M., Vroon, P.Z., van Bergen, M.J., (2009). Sulfur-induced offsets in MC-ICP-MS silicon-isotope measurements. *Journal of Analytical Atomic Spectrometry*, 24(8), 1111-1114.

Vance, D., Matthews, A., Keech, A., Archer, C., Hudson, G., Pett-Ridge, J., Chadwick, O. A., (2016). The behaviour of Cu and Zn isotopes during soil development: Controls on the dissolved load of rivers. *Chemical Geology*, 445, 36-53.

Vanderkluysen, L., Mahoney, J. J., Hooper, P. R., Sheth, H. C. & Ray, R., (2011). The Feeder System of the Deccan Traps (India): Insights from Dike Geochemistry. *Journal of Petrology*, 52(2), 315-343.

Venkatesan, T.R., Pande, K., Gopalan, K., (1993). Did Deccan volcanism pre-date the Cretaceous-Tertiary transition. *Earth and Planetary Science Letters*, 119(1-2), 181-189.

Viers, J., Oliva, P., Nonell, A., Gélabert, A., Sonke, J. E., Freydier, R., Gainville, R. & Dupré, B., (2007). Evidence of Zn isotopic fractionation in a soil–plant system of a pristine tropical watershed (Nsimi, Cameroon). *Chemical Geology*, 239(1–2), 124-137.

Viers, J. & Wasserburg, G.J., (2004). Behavior of Sm and Nd in a lateritic soil profile. *Geochimica et Cosmochimica Acta*, 68(9), 2043-2054.

Viets, F. G. J., Boawn, L. C., Crawford, C. L., (1954). Zinc contents and deficiency symptoms of 26 crops grown on a zinc-deficient soil. *Soil Science*, 78(4), 305-316.

Vigier, N., Bourdon, B., Lewin, E., Dupré, B., Turner, S., Chakrapani, G., Van Calsteren, P., Allègre, C., (2005). Mobility of U-series nuclides during basalt weathering: an example from the Deccan Traps (India). *Chemical Geology* 219, 69-91.

Wang, P., Clemens, S., Beaufort, L., Braconnot, P., Ganssen, G., Jian, Z., Kershaw, P., Sarnthein, M., (2005). Evolution and variability of the Asian monsoon system: state of the art and outstanding issues. *Quaternary Science Reviews*, 24(5), 595-629.

Wedepohl, K. H. & Correns, C. W., (1969). Handbook of geochemistry.

Welch, R. M. & Graham, R. D., (1999). A new paradigm for world agriculture: meeting human needs: productive, sustainable, nutritious. *Field crops research*, 60(1), 1-10.

Wessells, K. R. & Brown, K. H., (2012). Estimating the global prevalence of zinc deficiency: results based on zinc availability in national food supplies and the prevalence of stunting. *PloS one*, 7(11), e50568.

Widdowson, M. & Cox, K. G., (1996). Uplift and erosional history of the Deccan Traps, India: Evidence from laterites and drainage patterns of the Western Ghats and Konkan Coast. *Earth and Planetary Science Letters*, 137(1–4), 57-69.

Widdowson, M., (1997). Tertiary palaeosurfaces of the SW Deccan, Western India: implications for passive margin uplift. *Geological Society, London, Special Publications*, 120(1), 221-248.

Widdowson, M., (2007). Laterite and ferricrete. *Geochemical Sediments and Landscapes*, 45-94.

Widdowson, M., (2008). Laterite and Ferricrete, *Geochemical Sediments and Landscapes.* Blackwell Publishing Ltd, pp. 45-94.

Widdowson, M., Pringle, M. S., Fernandez, O. A., (2000). A Post K–T Boundary (Early Palaeocene) Age for Deccan-type Feeder Dykes, Goa, India. *Journal of Petrology*, 41(7), 1177-1194.

Wiederhold, J. G., (2015). Metal Stable Isotope Signatures as Tracers in Environmental Geochemistry. *Environmental Science & Technology*, 49(5), 2606-2624.

Wilding, L. P. & Lin, H., (2006). Advancing the frontiers of soil science towards a geoscience. *Geoderma*, 131(3), 257-274.

Wille, M., Babechuk, M. G., Kleinhanns, I. C., Stegmaier, J., Suhr, N., Widdowson, M., Kamber, B. S. & Schoenberg, R., (2018). Silicon and chromium stable isotopic systematics during basalt weathering and lateritisation: A comparison of variably weathered basalt profiles in the Deccan Traps, India. *Geoderma*, 314, 190-204.

Wille, M., Sutton, J., Ellwood, M. J., Sambridge, M., Maher, W., Eggins, S. & Kelly, M., (2010). Silicon isotopic fractionation in marine sponges: A new model for

understanding silicon isotopic variations in sponges. *Earth and Planetary Science Letters*, 292(3–4), 281-289.

Wimpenny, J., Gannoun, A., Burton, K., Widdowson, M., James, R. & Gíslason, S., (2007). Rhenium and osmium isotope and elemental behaviour accompanying laterite formation in the Deccan region of India. *Earth and Planetary Science Letters*, 261(1)**,** 239-258.

Xu, X. & Liu, W., (2017). The global distribution of Earth's critical zone and its controlling factors. *Geophysical Research Letters*, 44(7), 3201-3208.

Yerima, B., Van Ranst, E., Sertsu, S., Verdoodt, A., (2014). Pedogenic impacts on the distribution of total and available Fe, Mn, Cu, Zn, Cd, Pb and Co contents of vertisols and vertic inceptisols of the Bale Mountain area of Ethiopia. *African Journal of Agricultural Research*, 8(44), 5429-5439.

Yokoyama, T., Makishima, A., Nakamura, E., (1999). Separation of Thorium and Uranium from Silicate Rock Samples Using Two Commercial Extraction Chromatographic Resins. *Analytical chemistry*, 71, 135-141.

Zambardi, T. & Poitrasson, F., (2011). Precise Determination of Silicon Isotopes in Silicate Rock Reference Materials by MC-ICP-MS. *Geostandards and Geoanalytical Research*, 35(1), 89-99.

Zerkle, A. L., House, C. H., Brantley, S. L., (2005). Biogeochemical signatures through time as inferred from whole microbial genomes. *American Journal of Science*, 305(6-8), 467-502.

Zhong, L., Yang, J., Liu, L., Xing, B., (2015). Oxidation of Cr(III) on birnessite surfaces: The effect of goethite and kaolinite. *Journal of Environmental Sciences*, 37, 8-14.

Ziegler, K., Chadwick, O.A., Brzezinski, M.A., Kelly, E.F., (2005a). Natural variations of δ^{30}Si ratios during progressive basalt weathering, Hawaiian Islands. *Geochimica et Cosmochimica Acta*, 69(19), 4597-4610.

Ziegler, K., Chadwick, O.A., White, A.F., Brzezinski, M.A., (2005b). δ^{30}Si systematics in a granitic saprolite, Puerto Rico. *Geology*, 33(10), 817-820.

Zink, S., Schoenberg, R., Staubwasser, M., (2010). Isotopic fractionation and reaction kinetics between Cr(III) and Cr(VI) in aqueous media. *Geochimica et Cosmochimica Acta*, 74(20), 5729-5745.

Web reference

USGS, 1997. https://earthquake.usgs.gov/data/crust/maps.php